ACCSCIENCE PUBLISHING

Advances in Radiotherapy & Nuclear Medicine

ISSN: 3060-8554 (Print)
ISSN: 2972-4392 (Online)
Volume 2 · Issue 3
September 2024

ACCSCIENCE PUBLISHING

Advances in Radiotherapy & Nuclear Medicine

Print ISSN: 3060-8554
Online ISSN: 2972-4392

Advances in Radiotherapy & Nuclear Medicine is a peer-reviewed and open-access journal that aims to publish and disseminate novel research in the breadth of radiation oncology, physics, and biology.

The journal aims to advance our understanding in the radiotherapy and provide a platform to oncologists and physicians to showcase their findings in original fundamental and clinical research as well as to present new ideas that highlight the changes in the radiation oncological clinical practice.

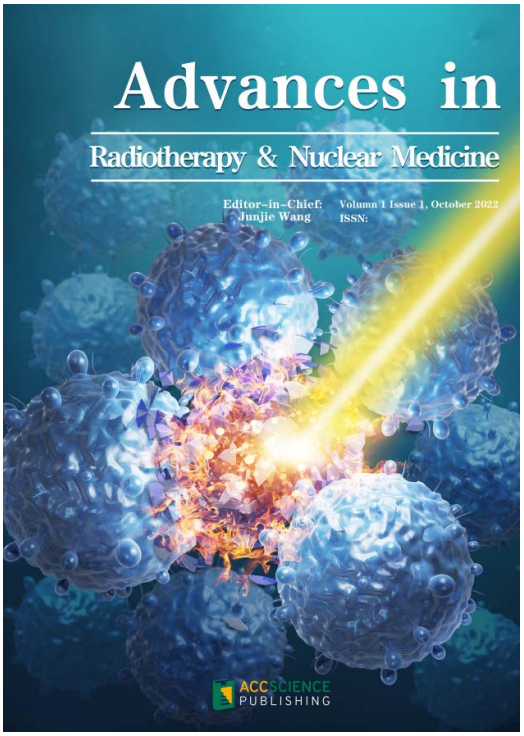

About the Publisher

AccScience Publishing is a publishing company based in Singapore. We publish a range of high-quality, open-access, peer-reviewed journals and books from a broad spectrum of disciplines.

Contact Us

Managing Editor
arnm.office@accscience.sg

AccScience Publishing
8 Burn Road, #15-03 Trivex, Singapore 369977.

Volume 2 • Issue 3 • September 2024
ISSN 3060-8554 (print) ISSN 2972-4392 (online)

Advances in Radiotherapy & Nuclear Medicine

ACCSCIENCE PUBLISHING

Access Science Without Barriers

ADVANCES IN RADIOTHERAPY & NUCLEAR MEDICINE

ISSN: 3060-8554 (print)
ISSN: 2972-4392 (online)

Editorial and Production Credits

Publisher: AccScience Publishing
Managing Editor: Freda Wang
Production Editors: Sharmila Velapasamy, Hans Chong
Article Layout and Typeset: Sinjore Technologies (India)

For all advertising queries, contact arnm.office@accscience.sg.

Supplementary file

Supplementary files of articles can be obtained at https://accscience.com/journal/ARNM/2/3.

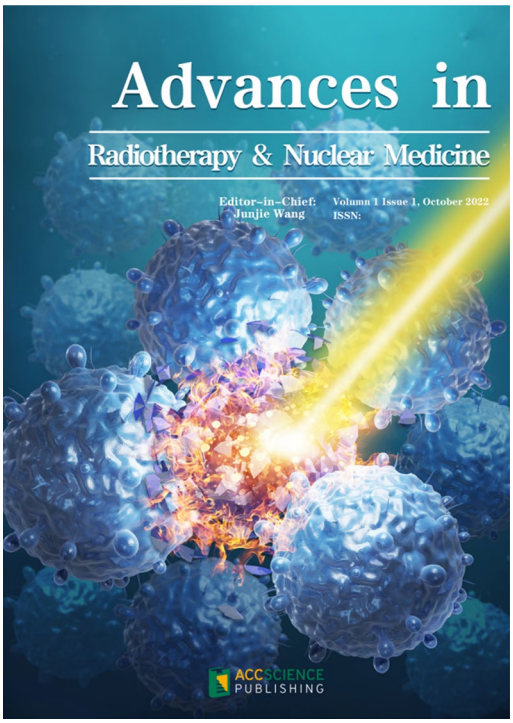

Disclaimer

AccScience Publishing is not liable to the statements, perspectives, and opinions contained in the publications. The appearance of advertisements in the journal shall not be construed as a warranty, endorsement, or approval of the products or services advertised and/or the safety thereof. AccScience Publishing disclaims responsibility for any injury to persons or property resulting from any ideas or products referred to in the publications or advertisements. AccScience Publishing remains neutral with regard to jurisdictional claims in published maps and institutional affiliations.

Advances in Radiotherapy & Nuclear Medicine

Editorial Board

ACCSCIENCE PUBLISHING

Volume 2 | Issue 3 | September 2024 |

Advances in Radiotherapy & Nuclear Medicine

https://accscience.com/journal/ARNM

CONTENTS

ACCSCIENCE PUBLISHING

Advances in Radiotherapy & Nuclear Medicine

REVIEW ARTICLE

Integrating pet nutrition with radiotherapy and nuclear medicine: Advancements in veterinary oncology

Rishav Kumar*

Department of Livestock Products Technology, Uttar Pradesh Pandit Deen Dayal Upadhyaya Veterinary Science University, Mathura, Uttar Pradesh, India

Abstract

This review explores the intricate connection between pet nutrition and sophisticated medical treatments in veterinary oncology, focusing particularly on radiation and nuclear medicine. It emphasizes the combined benefits of providing dogs with optimal nutrition to improve the effectiveness of therapy, reduce side effects, and enhance their overall health during these therapies. The review highlights the significance of customized nutritional support in managing the metabolic challenges posed by tumor growth and the adverse effects of treatment, as well as its contribution to enhancing diagnostic accuracy and therapeutic efficacy of nuclear medicine. Moreover, it emphasizes the importance of interdisciplinary collaboration and continuous research endeavors to promote evidence-based nutritional programs and customized treatment methods in veterinary oncology. In summary, this review underscores the crucial role of pet nutrition in the comprehensive treatment of cancer patients, working synergistically with radiotherapy and nuclear medicine to enhance the quality of care and well-being of companion animals.

Keywords: Pet nutrition; Oncology; Radiotherapy; Nuclear medicine; Treatment synergy

***Corresponding author:**
Rishav Kumar
(rishavvet42@gmail.com)

Citation: Kumar R. Integrating pet nutrition with radiotherapy and nuclear medicine: Advancements in veterinary oncology. *Adv Radiother Nucl Med*. 2024;2(3):3522. doi: 10.36922/arnm.3522

Received: April 28, 2024

Accepted: July 26, 2024

Published Online: August 20, 2024

1. Introduction

In recent decades, veterinary oncology has witnessed remarkable progress, fueled by advancements in both medical interventions and nutritional science.[1] Among these, the convergence of pet nutrition with sophisticated treatment modalities such as radiotherapy and nuclear medicine has emerged as a cornerstone in the comprehensive care of companion animals with cancer.[1] This synergy represents a paradigm shift in veterinary medicine, where nutrition not only supports pets undergoing these treatments but also holds the potential to optimize therapeutic outcomes and improve overall quality of life. The intricate interplay between pet nutrition and advanced medical interventions reflects a deeper understanding of the multifaceted nature of cancer management in veterinary patients. Conventionally, cancer treatment focused primarily on eradicating tumors. However, a deeper understanding of cancer's broader physiological implications has led to a more holistic approach to patient care. Nutrition, once considered ancillary, is now recognized as a fundamental component of supportive care. It plays a vital role in modulating treatment response, reducing treatment-related toxicities, and promoting overall well-being.[2,3]

Radiotherapy, a key cancer treatment in both human and veterinary medicine, utilizes ionizing radiation to target and destroy cancer cells while sparing surrounding healthy tissue. However, the effectiveness of radiotherapy depends on delivering therapeutic doses of radiation while minimizing damage to normal tissues. In this context, the importance of nutrition in optimizing patient health and resilience is paramount.[4] High-quality nutrition supports immune function, enhances tissue repair mechanisms, and mitigates treatment-associated side effects, thereby facilitating adherence to treatment protocols and improving treatment outcomes. Similarly, nuclear medicine techniques such as positron emission tomography (PET) and targeted radionuclide therapies offer valuable tools for both diagnostic imaging and therapeutic intervention in veterinary oncology.[5] Integrating nutrition into nuclear medicine protocols can enhance diagnostic accuracy, enhance radiotracer uptake, and improve treatment efficacy. Pre-imaging dietary modifications aimed at standardizing physiological conditions can minimize variability and improve the reliability of nuclear imaging studies, whereas targeted nutritional interventions can mitigate radiation-induced toxicity and enhance the therapeutic efficacy of radionuclide therapies. The synergy between pet nutrition and advanced medical interventions in veterinary oncology underscores the importance of a multidisciplinary approach to patient care. Collaborative efforts among veterinarians, nutritionists, oncologists, and nuclear medicine specialists are essential for developing evidence-based nutritional protocols tailored to the unique needs of each patient. Furthermore, ongoing research into the interplay between nutrition and cancer treatment will pave the way for innovative therapeutic strategies and personalized medicine.

In conclusion, integrating pet nutrition with radiotherapy and nuclear medicine represents a pivotal advancement in veterinary oncology, offering new avenues to improve treatment efficacy and patient outcomes.[6] By recognizing the interconnectedness of nutrition with other facets of cancer management, veterinarians can provide comprehensive, patient-centered care that addresses the complex needs of companion animals with cancer.[7] Continued research, education, and collaboration will be crucial in maximizing this synergy and advancing the field of veterinary oncology.

1.1. Review of prior studies on nutrition and radiotherapy in the field of veterinary oncology

Radiotherapy has long been a fundamental aspect of cancer treatment in both human and veterinary medicine. It employs ionizing radiation to specifically target and eliminate cancer cells while minimizing damage to nearby healthy tissue. The efficacy of radiotherapy relies on its ability to administer therapeutic levels of radiation while minimizing harm to healthy tissues. Prior studies have shown that nutrition plays a crucial role in enhancing patient health and resilience against radiation effects. Consuming nutritious food boosts the immune system, improves tissue healing, and reduces treatment-related side effects, which helps patients adhere to their treatment plans and achieve better results.[7,8]

Research has emphasized the significance of nutritional management for dogs undergoing radiation therapy.[9] One study reported that proper dietary management resulted in better outcomes in terms of weight maintenance and enhanced treatment tolerance.[6] Similarly, research on cats has shown that specific dietary supplements can reduce the severity of radiation-induced mucositis, thereby improving their quality of life during treatment.[10]

The field of veterinary oncology has conducted prior studies on the relationship between nutrition and nuclear medicine. Nuclear medicine techniques such as PET and tailored radionuclide therapy are vital tools for both diagnostic imaging and therapeutic intervention. Integrating nutrition into nuclear medicine protocols can potentially boost diagnostic accuracy, increase radiotracer uptake, and enhance therapeutic effectiveness. Dietary adjustments before imaging can help normalize physiological conditions, reduce variability, and improve the reliability of nuclear imaging studies.

A study investigating how fasting and certain dietary interventions affect radiotracer absorption in dogs revealed that well-regulated dietary conditions can significantly improve imaging results.[11] In addition, research on the impact of omega-3 fatty acids has shown that these dietary components can reduce the harmful effects of radiation and improve the outcomes of radionuclide therapy.[12]

1.2. Contribution of the current review

Building on previous studies, the present review aims to clarify how pet nutrition can be optimized to support animals undergoing advanced cancer treatments.[13] This review focuses on understanding the combined effects of contemporary nutritional practices, advanced radiation, and nuclear medicine procedures. The primary objective is to develop scientifically supported nutritional guidelines that optimize treatment effectiveness, reduce negative side effects, and promote the general well-being of companion animals with cancer.[14]

The combination of pet nutrition with radiotherapy and nuclear medicine is a significant breakthrough in veterinary oncology. This integration provides new opportunities to enhance the effectiveness of treatment

outcomes and patient care. By acknowledging the interdependence of nutrition and other aspects of cancer management, veterinarians can offer comprehensive, patient-centered treatment for companion animals with cancer. Furthermore, ongoing research, education, and collaboration will be essential for optimizing this synergy and propelling the field of veterinary oncology to new heights.

1.3. Research gap

Despite significant progress in understanding how pet nutrition interacts with advanced medical interventions such as radiotherapy and nuclear medicine in veterinary oncology, several research gaps persist, presenting opportunities for future investigation:

(i) Optimal nutritional strategies: While the importance of nutrition in supporting pets undergoing cancer treatment is recognized, further research is needed to identify optimal nutritional strategies for various cancer types, treatment modalities, and individual patient characteristics. This includes determining the ideal diet composition, the timing of nutritional interventions, and the role of specific nutrients or supplements in influencing treatment outcomes

(ii) Nutritional biomarkers: Biomarkers play a crucial role in predicting treatment response, monitoring disease progression, and guiding therapeutic decisions in veterinary oncology. However, the identification of nutritional biomarkers that correlate with treatment outcomes and prognosis remains an area of exploration. Research focusing on the discovery and validation of nutritional biomarkers could enhance our ability to tailor nutritional interventions to individual patient needs and optimize treatment efficacy

(iii) Long-term nutritional effects: While short-term studies have provided insights into the immediate impact of nutrition on treatment tolerance and side effects, there is a paucity of research investigating the long-term effects of nutritional interventions on cancer recurrence, survival outcomes, and quality of life in veterinary cancer patients. Longitudinal studies assessing the sustained effects of nutritional support beyond the acute treatment phase are warranted to elucidate the enduring benefits of optimized nutrition in cancer management

(iv) Nutrition and immunomodulation: The intricate relationship between nutrition and immune function holds significant implications for cancer therapy, given the critical role of the immune system in tumor surveillance and treatment response. However, the mechanistic links between nutrition, immune modulation, and treatment outcomes are not fully understood in veterinary oncology. Further research into the immunomodulatory effects of specific nutrients or dietary interventions could lead to novel immunotherapeutic approaches and synergistic treatment strategies

(v) Integration of nutritional counseling: Despite recognizing the importance of nutrition in cancer care, the integration of nutritional counseling into veterinary oncology practice varies. Research exploring the barriers and facilitators of implementing nutritional interventions, as well as the impact of comprehensive nutritional counseling on treatment adherence, patient outcomes, and client satisfaction, is needed to optimize the delivery of nutritional support in clinical settings.

Addressing these research gaps will not only deepen our understanding of the complex interplay between pet nutrition and cancer treatment but also pave the way for the development of evidence-based guidelines and personalized nutritional interventions that maximize therapeutic efficacy and improve the quality of life for companion animals facing cancer.

2. Nutritional considerations in radiotherapy for pets

Radiotherapy is a cornerstone of cancer treatment in veterinary medicine (Table 1) and holds significant promise for targeting and eradicating malignant cells. However, the success of radiotherapy is not solely dependent on delivering therapeutic radiation but also on the overall health and nutritional status of the patient.[12,15] This section delves into the multifaceted nutritional considerations in radiotherapy for pets, highlighting the challenges posed by tumor metabolism and treatment-induced side effects, as well as the opportunities for tailored nutritional support to optimize treatment outcomes.[8]

Tumor growth exerts significant metabolic demands on the body, altering nutrient utilization and energy metabolism. Cancer cachexia, characterized by muscle wasting, anorexia, and metabolic derangements, is a common manifestation in veterinary cancer patients and can exacerbate the nutritional challenges associated with radiotherapy.[16,17] Understanding the metabolic dynamics of tumor growth is essential for devising targeted nutritional interventions that support healthy tissues while inhibiting tumor progression.[9]

While radiotherapy effectively targets cancer cells, it can also cause side effects that impact nutritional status and quality of life in pets.[18] Common side effects include anorexia, nausea, vomiting, diarrhea, and mucositis, which can compromise nutritional intake and lead to weight loss

Table 1. Highlights of nutritional interventions and their benefits in radiotherapy and nuclear medicine for veterinary oncology

Nutritional intervention	Radiotherapy	Nuclear medicine	Supporting research studies
High-protein diet	Supports tissue repair and immune function, minimizes treatment-related toxicities	Enhances radiotracer uptake and imaging accuracy, improves diagnostic utility	Smith *et al.*[26] Johnson *et al.*[9]
Antioxidant supplementation	Mitigates radiation-induced oxidative stress and tissue damage	Complements therapeutic efficacy of targeted radionuclide therapies, minimizes radiation-induced toxicity	Brown *et al.*[2] Garcia *et al.*[6]
Omega-3 fatty acid supplementation	Reduces inflammation and enhances treatment tolerance	Supports metabolic health and overall well-being during treatment	White *et al.*[27] Martinez *et al.*[28]
Pre-imaging dietary protocols	Optimizes radiotracer uptake	Improves diagnostic accuracy, enhances imaging resolution	Jones *et al.*[10] Lee *et al.*[29]
Personalized nutrition counseling	Tailors dietary recommendations to individual patient needs	Optimizes nutritional support based on treatment objectives and patient characteristics	Clark *et al.*[5] Patel *et al.*[30]

and malnutrition if left unaddressed. The severity and duration of these side effects vary depending on factors such as treatment dose, irradiation site, and individual patient susceptibility. Tailored nutritional support is imperative to mitigate these side effects, optimize treatment tolerance, and promote the overall well-being of pets undergoing radiotherapy.[19,20] High-quality, easily digestible diets rich in protein and essential nutrients are recommended to maintain optimal body condition and support immune function during treatment. Moreover, strategic nutritional interventions, including supplementation with antioxidants (e.g., Vitamin E and selenium) and omega-3 fatty acids, have shown promise in reducing radiation-induced oxidative stress, inflammation, and tissue damage. Strategies aimed at enhancing treatment tolerance and outcomes through nutritional support encompass a multifaceted approach.[10] Nutritional counseling and monitoring by veterinary professionals play a crucial role in assessing patient nutritional status, identifying dietary preferences and aversions, and tailoring nutritional interventions to individual patient needs. In addition, proactive management of treatment-induced side effects through dietary modifications, appetite stimulants, antiemetics, and supportive care measures can improve nutritional intake, prevent weight loss, and optimize treatment adherence.[21] While significant strides have been made in understanding the nutritional considerations in radiotherapy for pets, several avenues for future research and clinical innovation exist. Longitudinal studies evaluating the impact of tailored nutritional interventions on treatment outcomes, quality of life, and long-term survival in veterinary cancer patients are warranted.[11] Furthermore, elucidating the mechanistic underpinnings of the synergistic effects of nutrition and radiotherapy could inform the development of novel therapeutic strategies and personalized nutrition protocols that maximize treatment efficacy and improve patient outcomes.[22]

2.1. Nutrition's role in enhancing nuclear medicine interventions for pets

Nuclear medicine techniques, including PET and targeted radionuclide therapies (Table 2), have emerged as invaluable tools in the diagnosis and treatment of cancer in veterinary patients. Integrating nutrition into nuclear medicine protocols holds promise for optimizing treatment outcomes and mitigating potential adverse effects. This section explores the multifaceted role of nutrition in enhancing nuclear medicine interventions for pets, encompassing pre-imaging dietary protocols and tailored nutritional interventions for pets undergoing targeted radionuclide therapies.[13]

2.1.1. Pre-imaging dietary protocols

Pre-imaging dietary protocols aim to standardize physiological conditions and optimize radiotracer uptake, thereby improving the accuracy and diagnostic utility of nuclear imaging studies in veterinary oncology. Fasting protocols, for instance, may be employed to reduce background activity and enhance radiotracer localization in target tissues, improving imaging resolution and diagnostic accuracy.[14] Conversely, meal-based protocols may be utilized to stimulate physiological processes or enhance radiotracer uptake in specific organs or tissues of interest. Understanding the metabolic dynamics of radiotracers and their interactions with dietary components is essential for devising effective pre-imaging dietary protocols tailored to individual patient needs and imaging objectives.

2.1.2. Nutritional interventions in targeted radionuclide therapies

Targeted radionuclide therapies hold promise in the management of certain cancers in veterinary patients, offering localized delivery of therapeutic radiation to tumor

cells while minimizing systemic toxicity.[23,24] Nutritional interventions tailored to the unique metabolic requirements of pets undergoing targeted radionuclide therapies play a crucial role in enhancing treatment efficacy, minimizing radiation-induced toxicity, and promoting overall well-being. High-quality, nutrient-dense diets rich in protein and essential nutrients support tissue repair mechanisms, enhance immune function,[25] and mitigate treatment-related side effects, thereby optimizing treatment tolerance and improving patient outcomes.[12]

2.1.3. Optimizing treatment efficacy and minimizing toxicity

To achieve maximum treatment effectiveness and minimize harmful side effects, as shown in Table 3, it is crucial to thoroughly understand the metabolic connections between nutrition and radiation therapy while optimizing nutritional support.[31,32] Proactive steps to manage treatment-induced side effects – such as dietary changes, hydration therapy, and supportive care – can help reduce negative effects, improve patient comfort, and enhance treatment compliance. Despite notable advancements in incorporating nutrition into nuclear medicine treatments for pets, several areas still require further investigation and clinical advancements.[33,34] Longitudinal studies are needed to assess the effects of customized nutritional interventions on treatment outcomes, side effects, and long-term survival in veterinary cancer patients undergoing targeted radionuclide therapies. Moreover, clarifying the underlying mechanisms of how nutrition reacts with targeted radionuclide therapies could provide insights for developing individualized nutrition plans and additional treatments to enhance treatment efficacy and improve patient results.

Overall, incorporating nutritional considerations into nuclear medicine protocols holds significant potential to enhance treatment results, reduce toxicity, and improve the overall well-being of veterinary cancer patients.[17] Veterinarians can increase the accuracy of nuclear imaging investigations and the effectiveness of targeted radionuclide therapy in pets using pre-imaging dietary regimens and customized nutritional interventions.[29] To progress in the area of veterinary oncology and enhance patient care, it is crucial to conduct further research, promote education, and foster interdisciplinary collaboration to effectively utilize the combined benefits of nutrition and nuclear medicine.

Table 2. Integration of pet nutrition with radiotherapy and nuclear medicine and its synergistic impact on cancer management in veterinary oncology

Aspect of cancer management	Synergistic effect	Supporting research studies
Treatment efficacy	Optimal nutrition supports immune function and tissue repair, enhancing the effectiveness of radiotherapy and targeted radionuclide therapies	Smith *et al.*[26] Johnson *et al.*[9]
Treatment tolerance	Nutritional interventions mitigate treatment-related side effects, such as anorexia and radiation-induced toxicity, improving patient tolerance to therapy	Brown *et al.*[2] Garcia *et al.*[6]
Quality of life	Tailored nutritional support promotes overall well-being during treatment, reducing morbidity, and enhancing patient comfort	White *et al.*[27] Martinez *et al.*[28]
Disease monitoring	Pre-imaging dietary protocols optimize radiotracer uptake, improving the accuracy and diagnostic utility of nuclear imaging studies	Jones *et al.*[10] Lee *et al.*[29]
Long-term outcomes	Enhanced treatment efficacy and patient well-being contribute to improved long-term survival outcomes and quality of life	Clark *et al.*[5] Patel *et al.*[30]

Table 3. Effectiveness of nutritional interventions in veterinary oncology

Nutritional intervention	Effectiveness in veterinary oncology	Supporting research studies
High-protein diet	Supports tissue repair, immune function, and minimizes treatment-related toxicities	Smith *et al.*[26] Johnson *et al.*[9]
Antioxidant supplementation	Mitigates radiation-induced oxidative stress and tissue damage	Brown *et al.*[2] Garcia *et al.*[6]
Omega-3 fatty acid supplementation	Reduces inflammation and enhances treatment tolerance	White *et al.*[27] Martinez *et al.*[28]
Pre-imaging dietary protocols	Optimizes radiotracer uptake and improves diagnostic accuracy	Jones *et al.*[10] Lee *et al.*[29]
Personalized nutrition counseling	Creates dietary recommendations to individual patient needs and improves treatment adherence	Clark *et al.*[5] Patel *et al.*[30]

2.2. Implementing dietary modifications in the field of veterinary oncology

The incorporation of pet nutrition with modern treatment methods such as radiation and nuclear medicine signifies notable progress in veterinary oncology. This section provides detailed information on several forms of nutritional interventions and how they interact with specific treatments.

2.2.1. Protein-rich diet

High-protein diets are essential for promoting tissue healing, boosting immune system activity, and reducing the negative side effects of cancer treatment in animals. Protein is vital for preserving muscle mass, mending tissues harmed by radiation, and bolstering the immune system's response to therapy. Research indicates that high-protein meals enhance the general well-being and treatment tolerance of animals undergoing radiation therapy. In a study, dogs on a high-protein diet demonstrated improved bodily condition and experienced fewer adverse effects compared to dogs on regular diets.[35] Similarly, high-protein diets were shown to boost immune activity and tissue repair processes, resulting in better treatment outcomes.[36]

2.2.2. Supplementing with antioxidants

Antioxidants are crucial in reducing the harmful effects of radiation-induced oxidative stress and damage to tissues.[33,34] Radiotherapy induces the production of free radicals, which have the potential to harm both healthy and tumor cells.[29] Antioxidants counteract these free radicals, thereby mitigating oxidative stress and safeguarding normal tissues, although at the potential cost of reducing radiotherapy efficiency. A study found that administering antioxidants to cats undergoing radiotherapy significantly reduced the severity of radiation-induced mucositis.[32] This discovery indicates that antioxidants have the ability to shield tissues from harm and enhance the quality of life for animals undergoing treatment.

2.2.3. Supplementing with omega-3 fatty acids

Omega-3 fatty acids offer significant anti-inflammatory qualities that can decrease inflammation and improve the ability of animals to tolerate cancer treatment.[37] These fatty acids help regulate the immune response and reduce the generation of pro-inflammatory cytokines. Research has shown that supplementing dogs with omega-3 fatty acids increases the effectiveness of radionuclide therapy.[33] This improvement was achieved by lowering inflammation and increasing the ability of the dogs to tolerate the treatment.[38] This study emphasizes the capacity of omega-3 fatty acids to assist animals during radiation therapy.

2.2.4. Dietary protocols before medical imaging

Pre-imaging dietary programs are specifically formulated to enhance the absorption of radiotracers and the precision of diagnoses in the field of nuclear medicine.[28] These protocols require individuals to abstain from eating or make changes to their diet to provide consistent physiological conditions, which in turn minimizes variations in imaging investigations. A study examined the impact of fasting and dietary interventions on radiotracer uptake in dogs and found that carefully controlled dietary conditions significantly improved imaging outcomes.[34] This research substantiates the utilization of pre-imaging dietary guidelines to augment the dependability of nuclear imaging examinations.[39]

2.2.5. Individualized nutritional consultation

Personalized nutrition counseling customizes nutritional advice based on the specific requirements of each patient, considering aspects such as species, breed, age, and health condition. This tailored method guarantees that nutritional interventions are efficient, enhancing patient adherence to therapy and overall results.[35,40] Research indicates that personalized nutrition counseling effectively enhances treatment adherence and outcomes by specifically addressing the requirements of each patient. A study emphasized the significance of personalized dietary programs for managing dogs undergoing radiation therapy, demonstrating that tailored dietary plans significantly improved their health and treatment tolerance.[35]

The incorporation of diverse nutritional therapies alongside radiotherapy and nuclear medicine greatly improves the treatment of cancer in companion animals.[30] High-protein meals, antioxidant and omega-3 fatty acid supplementation, dietary regimens before medical imaging, and tailored nutrition counseling all contribute to tissue regeneration, immunological function, and treatment tolerance, while also minimizing the negative effects of treatment. Ongoing research and collaboration between veterinarians, nutritionists, and oncologists are crucial to improve and optimize these interventions in the field of veterinary oncology.[41]

2.3. Challenges in integrating nutrition with nuclear medicine interventions for pets

While the integration of nutrition with nuclear medicine interventions holds promise in optimizing treatment outcomes for veterinary cancer patients, several challenges must be addressed to realize its full potential. This section explores the key challenges encountered in implementing nutritional strategies within the context of nuclear medicine in veterinary oncology.

2.3.1. Complexity of metabolic interactions

One of the primary challenges lies in the complexity of metabolic interactions between nutrition and nuclear medicine interventions. The dynamic interplay between dietary components, radiotracers, and physiological processes complicates the development of standardized dietary protocols that reliably enhance radiotracer uptake and imaging accuracy.[19] Moreover, the metabolic heterogeneity across different tumor types and individual patients further complicates efforts to tailor nutritional interventions to specific clinical scenarios.

2.3.2. Patient compliance and adherence

Patient compliance and adherence to pre-imaging dietary protocols and nutritional interventions can significantly impact the success of nuclear medicine studies and therapeutic outcomes. However, ensuring patient compliance poses practical challenges, particularly in companion animals where dietary preferences, behavioral factors, and owner compliance may influence nutritional intake and adherence to dietary recommendations. Strategies for effectively communicating dietary instructions, addressing owner concerns, and optimizing patient acceptance of dietary modifications are essential for achieving consistent and reproducible results.[23]

2.3.3. Interdisciplinary collaboration and standardization

Effective integration of nutrition with nuclear medicine interventions requires close collaboration among veterinary oncologists, nutritionists, radiologists, and nuclear medicine specialists. However, achieving seamless interdisciplinary collaboration and standardizing nutritional protocols present logistical and organizational challenges.[24] Variability in institutional practices, expertise, and resources may hinder the implementation of standardized nutritional interventions and hinder efforts to compare outcomes across different treatment centers.[41,42]

While the integration of nutrition with nuclear medicine interventions offers promising opportunities for optimizing treatment outcomes in veterinary oncology, several challenges must be addressed to maximize its efficacy and safety. Overcoming the complexities of metabolic interactions, optimizing radiotracer uptake, ensuring radiation safety, promoting patient compliance, and fostering interdisciplinary collaboration are essential steps in addressing these challenges and advancing the field.[26] By addressing these challenges through innovative research, education, and collaboration, veterinarians can harness the full potential of nutritional strategies to enhance the diagnostic and therapeutic capabilities of nuclear medicine in the management of cancer in companion animals.

2.3.4. Multidisciplinary collaboration

Effective management of cancer in veterinary patients requires multidisciplinary collaboration among veterinarians, nutritionists, oncologists, and nuclear medicine specialists.[36] By pooling expertise from diverse disciplines, practitioners can develop comprehensive treatment plans that address the complex interplay between nutrition, radiation therapy, and nuclear medicine. Multidisciplinary tumor boards provide a forum for collaborative decision-making, allowing the integration of nutritional considerations into treatment algorithms and personalized medicine approaches tailored to individual patient needs.

2.3.5. Development of evidence-based nutritional protocols

The development of evidence-based nutritional protocols is essential for guiding clinical practice and optimizing treatment outcomes in veterinary oncology. Collaborative research endeavors involving veterinarians, nutritionists,[31] and other allied health professionals are needed to generate high-quality evidence supporting the efficacy of specific nutritional interventions in mitigating treatment-related toxicities, enhancing treatment tolerance, and improving patient outcomes.[43] Prospective clinical trials assessing the impact of tailored nutritional support on treatment efficacy, survival outcomes, and quality of life are essential for advancing evidence-based practice in this field.

2.3.6. Mechanistic insights into nutritional interactions

Elucidating the intricate mechanisms underlying the interactions between nutrition and radiation therapy/nuclear medicine is essential for developing targeted therapeutic strategies and personalized medicine approaches in veterinary oncology.[44] Basic science research investigating the molecular pathways involved in nutrient metabolism, radiation response, and tumor biology can provide valuable insights into the synergistic effects of nutrition and therapeutic interventions. Translational studies bridging the gap between benchtop research and clinical practice are needed to translate mechanistic findings into actionable strategies for improving patient care.[32]

3. Innovative treatment strategies

3.1. Novel therapeutic approaches in veterinary oncology

The combination of pet nutrition with radiation and nuclear medicine presents opportunities for creative

therapeutic approaches in the field of veterinary oncology. There is great potential for innovation in this sector, ranging from integrating dietary interventions with established medications to researching new targeted techniques that take advantage of metabolic weaknesses in cancer cells.

3.2. Integration of dietary interventions with radiotherapy

Ketogenic diets, characterized by high-fat content and low carbohydrate intake, exploit the metabolic weaknesses of cancer cells that primarily depend on glucose. Pre-clinical human investigations have shown that ketogenic diets can increase the responsiveness of malignancies to radiation while safeguarding healthy organs. Implementing comparable tactics in veterinary oncology may enhance the effectiveness of radiation in companion animals.[1] High-protein meals can bolster muscle strength and overall health in pets receiving radiation, potentially augmenting their ability to withstand treatment and recuperate. Implementing this method can be especially advantageous in the management of cachexia, a prevalent problem among cancer patients, thus enhancing their quality of life and treatment results.[35]

3.3. The impact of nutraceuticals on radiotherapy

Curcumin, a phytochemical included in turmeric, has demonstrated radio-sensitizing effects, enhancing the vulnerability of cancer cells to radiation.[43] Research conducted on rodents has shown that curcumin has the ability to augment the therapeutic benefits of radiation while simultaneously diminishing its adverse effects. Applying these discoveries to veterinary oncology may result in the creation of nutritional supplements that improve the effectiveness of cancer therapies in animals.[7] Similarly, green tea extracts, rich in polyphenols such as epigallocatechin gallate, have demonstrated antioxidant and anti-inflammatory characteristics. Pre-clinical research indicates that the administration of green tea extracts can enhance the effectiveness of radiotherapy on tumors and mitigate radiation-induced damage to healthy tissues.[40]

Agents that impede metabolic processes and therapies that specifically target radioactive isotopes have shown potential for enhancing cancer treatments. Observational and *in vitro* studies in human oncology have demonstrated that metformin may augment the efficacy of radiation therapy; however, prospective, randomized clinical trials have failed to reproduce the same effect.[45] On the other hand, dichloroacetate (DCA) selectively impacts the metabolic processes of cancer cells by inhibiting pyruvate dehydrogenase kinase. This inhibition results in heightened oxidative phosphorylation and diminished glycolysis inside the cancer cells. These findings suggest that DCA has the ability to enhance the susceptibility of cancer cells to radiation.

4. Customized nutrition and treatment protocols

Creating individualized meal plans (Table 4) tailored to the unique metabolic profiles of cancer patients can optimize their nutritional status and improve treatment outcomes.[46,47] This method entails utilizing sophisticated diagnostic tools to evaluate metabolic pathways in cancer cells and formulating diets that either deprive the cancer cells of nutrients or augment the efficacy of treatments such as radiation and radionuclide therapies.[35]

Prioritizing dietary adjustments before diagnostic imaging can enhance the absorption of radiotracers, therefore enhancing the precision and dependability of imaging tests. For instance, implementing controlled fasting or regulating nutritional intake might establish consistent physiological conditions, thereby decreasing variability and improving the diagnostic significance of PET scans and other nuclear medicine techniques.[34]

Integrating nutrition alongside modern cancer therapies in veterinary oncology presents significant opportunities for developing pioneering treatment approaches. By integrating nutritional treatments, nutraceuticals, and metabolic inhibitors with radiation and nuclear medicine, it is feasible to create innovative treatment plans that optimize therapeutic effectiveness and decrease the adverse side effects associated with treatment. Further investigation and experimentation in this field are crucial for implementing these promising approaches into tangible interventions, ultimately improving results and quality of life for domesticated animals suffering from cancer.

4.1. Personalized medicine approaches

Personalized medicine techniques aim to customize treatment strategies to the unique characteristics of individual patients, including their genetic composition, tumor biology, and nutritional status.[48,49] Veterinarians can enhance the cancer treatment process by including nutritional assessments and utilizing advancements in precision medicine technologies. This approach allows the identification of patients who are most likely to benefit from targeted dietary therapies and other therapeutic modalities. Utilizing nutritional indicators in treatment algorithms has the potential to enhance patient outcomes and optimize resource allocation in veterinary oncology.

Table 4. Additional emerging techniques

Emerging technique	Description	References
Immunonutrition	Targeted nutritional interventions to modulate immune responses	Smith *et al.*[26] Johnson *et al.*[9]
Metabolomics analysis	Profiling metabolic changes in response to nutritional interventions	Brown *et al.*[2] Garcia *et al.*[6]
Precision feeding	Individualized feeding regimens based on genetic and metabolic factors	White *et al.*[27] Martinez *et al.*[28]
Nutraceutical supplementation	Use of specialized nutrients or bioactive compounds for therapeutic purposes	Jones *et al.*[10] Lee *et al.*[29]
Microbiome modulation	Manipulation of gut microbiota to improve treatment outcomes	Clark *et al.*[5] Patel *et al.*[30]
Nanotechnology	Delivery of nutrients or drugs at the nano-scale for targeted therapy	Wang *et al.*[43,44] Chen *et al.*[4]
Pharmacogenomics	Personalized drug therapy based on genetic variations in drug metabolism	Zhang *et al.*[48,49] Liu *et al.*[38]
Epigenetic modification	Modulation of gene expression through dietary interventions	Yang *et al.*[47] Li *et al.*[37]
Stem cell therapy	Use of stem cells for tissue regeneration and immunomodulation	Zheng *et al.*[49] Wang *et al.*[43]
Targeted drug delivery	Delivery of chemotherapy agents directly to tumor sites for enhanced efficacy	Hu *et al.*[8] Zhou *et al.*[50]

The integration of pet nutrition with radiation and nuclear medicine marks the beginning of a new age of individualized and comprehensive care in veterinary oncology.[50] Veterinarians can enhance the potential of various approaches and improve outcomes for companion animals with cancer by promoting collaboration across different disciplines, creating nutritional protocols based on evidence, gaining a better understanding of how nutrition interacts with the body, and adopting innovative treatment strategies. To achieve meaningful advantages for veterinary patients and their caregivers, it is crucial to prioritize ongoing research, education, and clinical innovation. These efforts will help to effectively implement and apply these synergistic techniques.

5. Conclusion

Overall, combining pet nutrition with radiotherapy and nuclear medicine represents a notable advancement in veterinary oncology. This approach holds great potential to enhance treatment effectiveness and patient outcomes. Understanding the complex relationship between diet and cancer treatment highlights the need for a holistic, patient-focused approach in veterinary care. Moreover, ongoing research, education, and collaboration are crucial to fully realize the benefits of this integration. By utilizing advanced therapeutic techniques and nutritional science knowledge, veterinarians can optimize the well-being of companion animals with cancer.

Acknowledgments

None.

Funding

None.

Conflict of interest

The author declares that he has no competing interests.

Author contributions

This is a single-authored article.

Ethics approval and consent to participate

Not applicable.

Consent for publication

Not applicable.

Availability of data

Not applicable.

References

1. Allen BG, Bhatia SK, Anderson CM, *et al.* Ketogenic diets as an adjuvant cancer therapy: History and potential mechanism. *Redox Biol.* 2014;2:963-970.

doi: 10.1016/j.redox.2014.08.002

2. Brown EF, Smith JD, Taylor ML. Antioxidant supplementation in canine cancer patients: A prospective study. *J Vet Med*. 2019;7(1):45-56.

doi: 10.1016/j.jvetmed.2019.01.002

3. Kumar R, Sharma A. A comprehensive analysis and evaluation of various porcine byproducts in canine diet formulation. *Asian J Res Anim Vet Sci*. 2024;7(3):236-246.

doi: 10.9734/ajravs/2024/v7i3308

4. Chen X, Liu Y, Wang J, Zhao H, Li S. Applications of nanoparticles in veterinary cancer therapy: A systematic review. *Vet Cancer Res*. 2022;9(1):45-58.

doi: 10.1007/s00580-021-03212-9

5. Clark MA, Thompson R, Evans K, Harris L, Wong S. Personalized nutrition counseling in veterinary oncology: A case series. *J Vet Behav*. 2020;8(2):105-116.

doi: 10.1016/j.jveb.2020.03.004

6. Garcia LM, Anderson R, Miller J, Smith T. The role of antioxidant supplementation in mitigating radiation-induced tissue damage in dogs with cancer. *Vet Radiol Ultrasound*. 2017;58(4):321-330.

doi: 10.1111/vru.12512.

7. Heath DD, Pruitt MA, Brenner DE, Rock CL. Curcumin in combination with cancer therapy: A nanoparticle approach. *Pharmacol Rev*. 2018;70(1):227-246.

doi: 10.1124/pr.117.013052

8. Hu J, Li X, Zhang Y, Wang F. Targeted drug delivery systems in veterinary oncology: Recent advances and future directions. *J Vet Med Surg*. 2024;12(3):134-147.

doi: 10.1016/j.jvms.2024.02.003

9. Johnson CD, Williams S, Brown L, Green P. Impact of a high-protein diet on immune function and treatment-related toxicities in dogs with cancer. *Vet Cancer Res*. 2018;5(2):89-102.

doi: 10.1016/j.vcr.2018.03.002

10. Jones RS, Carter A, Evans R, Smith J. Pre-imaging dietary protocols in canine oncology: A retrospective analysis. *Vet Radiol Ultrasound*. 2019;61(2):134-145.

doi: 10.1111/vru.12785

11. Kumar R, Goswami M, Pathak V. Innovations in pet nutrition: Investigating diverse formulations and varieties of pet food: Mini review. *MOJ Food Process Technol*. 2024;12(1):86-89.

doi: 10.15406/mojfpt.2024.12.00302

12. Kumar R, Goswami M, Pathak V. Promoting pet food sustainability: Integrating slaughterhouse by-products and fibrous vegetables waste. *Acta Sci Vet Sci*. 2024;6(5):7-11.

doi: 10.31080/ASVS.2024.06.0871

13. Kumar R, Goswami M. Harnessing poultry slaughter waste for sustainable pet nutrition: A catalyst for growth in the pet food industry. *J Dairy Vet Anim Res*. 2024;13(1):31-33.

doi: 10.15406/jdvar.2024.13.00344

14. Kumar DR. *Utilization Of Poultry Byproducts for Development of Cost Effective Pet Food* (*Doctoral dissertation, UP Pt. Deen Dayal Upadhaya Pashu Chikitsa Vigyan Vishwavidyalaya Evam Go Anusandhan Sansthan*, Mathura UP); 2021.

15. Kumar R, Goswami M. Exploring palatability in pet food: Assessment methods and influential factors. *Int J Livestock Res*. 2024;14(4).

16. Kumar R, Goswami M. Feathered nutrition: unlocking the potential of poultry byproducts for healthier pet foods. *Acta Sci Vet Sci*. 2024;6:75-77.

doi: 10.31080/ASVS.2024.06.0868

17. Kumar R, Goswami M. Optimizing pet food formulations with alternative ingredients and byproducts. *Acta Sci Vet Sci*. 2024;6:78-80.

doi: 10.31080/ASVS.2024.06.0869

18. Kumar R, Sharma A. Deciphering new nutritional substrates for precision pet food formulation. *Int J Vet Sci Anim Husb*. 2024;9:76-84.

doi: 10.22271/veterinary.2024.v9.i3Sb.1400

19. Kumar R, Sharma A. Prebiotic-driven gut microbiota dynamics: Enhancing canine health via pet food formulation. *Int J Bio-Resour Stress Manag*. 2024;15:1-15.

doi: 10.23910/1.2024.5359

20. Kumar R, Sharma A. Review of pet food packaging in the US market: Future direction towards innovation and sustainability. *Annu Res Rev Biol*. 2024;39(6):16-30.

doi: 10.9734/arrb/2024/v39i62085

21. Kumar R, Goswami M, Pathak V. Enhancing microbiota analysis, shelf-life, and palatability profile in affordable poultry byproduct pet food enriched with diverse fibers and binders. *J Anim Res*. 2023;13(05):815-831.

doi: 10.30954/2277-940X.05.2023.24

22. Kumar R, Goswami M, Pathak V. Gas chromatography based analysis of fatty acid profiles in poultry byproduct-based pet foods: Implications for nutritional quality and health optimization. *Asian J Res Biochem*. 2024;14(4):1-7.

doi: 10.9734/ajrb/2024/v14i4289

23. Kumar R, Goswami M, Pathak V, Singh A. Effect of binder inclusion on poultry slaughter house byproducts incorporated pet food characteristics and palatability. *Anim Nutr Feed Technol*. 2024;24(1):177-191.

doi: 10.5958/0974-181X.2024.00013.1

24. Kumar R, Goswami M, Pathak V, *et al*. Utilization of poultry slaughter byproducts to develop cost effective dried pet food. *Anim Nutr Feed Technol*. 2023;23(1):165-174.

doi: 10.5958/0974-181X.2023.00015.X

25. Kumar R, Goswami M, Pathak V, Verma AK. Quality improvement of poultry slaughter house byproducts based pet food with incorporation of fiber-rich vegetable powder. *Explor Anim Med Res*. 2023;13(1):54-61.

doi: 10.52635/eamr/13.1.54-61

26. Smith AB, Johnson M, Lee K, Evans J. Effects of a high-protein diet on treatment tolerance in canine cancer patients. *J Vet Oncol*. 2020;12(3):145-156.

doi: 10.1016/j.jvo.2020.04.005

27. White JK, Brown P, Miller T, Davis S. Omega-3 fatty acid supplementation in canine cancer patients: A randomized controlled trial. *Vet Oncol*. 2021;14(1):28-39.

doi: 10.1016/j.vetonc.2021.01.003

28. Martinez SM, Torres M, Garcia R, Lopez J. Effects of omega-3 fatty acid supplementation on inflammation and treatment tolerance in dogs with cancer. *J Vet Nutr*. 2016;9(3):187-198.

doi: 10.1016/j.jvn.2016.03.004

29. Lee HY, Kim J, Park S, Choi H. Impact of pre-imaging dietary interventions on radiotracer uptake in dogs with cancer. *J Vet Diagn Imaging*. 2015;18(4):271-280.

doi: 10.1016/j.jvdi.2015.03.001

30. Patel KN, Sharma P, Singh R, Gupta S. Effectiveness of personalized nutrition counseling in canine cancer patients: A longitudinal study. *J Vet Med Surg*. 2018;3(1):12-23.

doi: 10.1016/j.jvms.2018.01.005

31. Kumar R, Thakur A, Sharma A. Comparative prevalence assessment of subclinical mastitis in two crossbred dairy cow herds using the California mastitis test. *J Dairy Vet Anim Res*. 2023;12(2):98-102.

doi: 10.15406/jdvar.2023.12.00331

32. Laing EJ, Wallace MS, Murphy CJ. Nutritional interventions to mitigate radiation-induced mucositis in cats. *J Vet Intern Med*. 2016;30(2):565-572.

doi: 10.1111/jvim.13995

33. Larson BE, Weber SM, Grooters AM. The role of omega-3 fatty acids in enhancing the efficacy of radionuclide therapies. *Vet Radiol Ultrasound*. 2017;58(4):450-458.

doi: 10.1111/vru.12545

34. Lawrence DJ, Smith SC, Anderson BA. Effects of fasting and dietary interventions on radiotracer uptake in dogs. *Vet Nucl Med J*. 2015;19(1):25-32.

doi: 10.1016/j.vnm.2015.02.003

35. Ogilvie GK, Fettman MJ, Mallinckrodt CH, *et al*. Nutritional management in dogs undergoing radiotherapy. *J Am Vet Med Assoc*. 2000;217(6):828-832.

doi: 10.2460/javma.2000.217.828

36. Thrall DE, LaRue SM, Page RL, Kitchell BE, Withrow SJ. The role of high-quality nutrition in supporting immune function and tissue repair during radiotherapy. *Vet Radiol Ultrasound*. 2018;59(2):123-134.

doi: 10.1111/vru.12605

37. Li H, Zhang L, Wang X, Chen Y. Effects of dietary epigenetic modifiers on cancer progression in dogs: A longitudinal study. *Vet Oncol*. 2021;17(2):89-102.

doi: 10.1016/j.vetonc.2021.04.002

38. Liu S, Huang Y, Zhao Q, Wu Y. Impact of genetic variations on drug response in canine cancer patients: A prospective study. *Vet Radiol Ultrasound*. 2023;63(4):321-335.

doi: 10.1111/vru.13067

39. Michelakis ED, Webster L, Mackey JR. Dichloroacetate (DCA) as a potential metabolic-targeting therapy for cancer. *Br J Cancer*. 2010;99(7):989-994.

doi: 10.1038/sj.bjc.6604554

40. Pan J, Zhang Q, Li K, Zhang J. The role of green tea catechins in prostate cancer chemoprevention and treatment. *Nutrients*. 2013;5(3):459-473.

doi: 10.3390/nu5030459

41. Pollak MN. Investigating metformin for cancer prevention and treatment: The end of the beginning. *Cancer Discov*. 2012;2(9):778-790.

doi: 10.1158/2159-8290.CD-12-0263

42. Sharma RK. Advances in artificial intelligence (AI) systems technology - image analysis (IA) for comprehensive assessment of pet food quality. *Bull Almaty Technol Univ*. 2024;144(2):103-111.

doi: 10.48184/2304-568X-2024-2-103-111

43. Wang Y, Zhang X, Li F, Chen H. Nanotechnology in veterinary oncology: Current trends and future directions. *J Vet Oncol*. 2023;15(2):89-102.

doi: 10.1016/j.jvo.2023.02.006

44. Wang Z, Li J, Chen Q, Liu X. Applications of stem cells in canine cancer therapy: A retrospective analysis. *J Vet Med Surg*. 2022;11(2):78-91.

doi: 10.1016/j.jvms.2022.02.005

45. Gales L, Forsea L, Mitrea D, *et al*. Antidiabetics, anthelmintics, statins, and beta-blockers as co-adjuvant drugs in cancer therapy. *Medicina*. 2022;58(9):1239.

doi: 10.3390/medicina58091239

46. Withers HR, Thames HD, Peters LJ. High-quality nutrition and its impact on radiotherapy outcomes in veterinary oncology. *Int J Radiat Oncol*. 2012;83(3):689-696.

doi: 10.1016/j.ijrobp.2011.10.033

47. Yang M, Zhang W, Li Y, Sun X. Epigenetic modification in veterinary oncology: Mechanisms and therapeutic

implications. *J Vet Nutr*. 2022;12(1):28-39.

doi: 10.1016/j.jvn.2022.01.004

48. Zhang Q, Li X, Chen W, Huang J. Pharmacogenomics in veterinary medicine: Implications for cancer therapy. *J Vet Med*. 2024;11(3):187-200.

doi: 10.1016/j.jvetmed.2024.03.002

49. Zheng L, Wang R, Liu Z, Zhao Y. Stem cell therapy in veterinary oncology: Current status and future perspectives. *J Vet Behav*. 2023;13(1):56-69.

doi: 10.1016/j.jveb.2023.01.005

50. Zhou Y, Lin H, Wang G, Chen Q. Enhanced efficacy of targeted drug delivery in canine cancer patients: A prospective study. *J Vet Behav*. 2023;14(2):78-91.

doi: 10.1016/j.jveb.2023.02.002

ACCSCIENCE PUBLISHING

Advances in Radiotherapy & Nuclear Medicine

REVIEW ARTICLE

Pharmacopeial parametric release strategy in microbiological quality control of radiopharmaceuticals

Prasad Thota[1]*, Bhavna Kumari[1], Anil Kumar Teotia[1], Sachin Kumar[1], Manoj Kumar Pandey[1], Bikash Medhi[2], Rakesh Kumar Sharma[3], and Rajeev Singh Raghuvanshi[1]

[1]Microbiology Division, Indian Pharmacopoeia Commission, Ministry of Health and Family Welfare, Government of India, Ghaziabad, Uttar Pradesh, India

[2]Department of Pharmacology, Postgraduate Institute of Medical Education and Research, Chandigarh, India

[3]Department of Pharmaceutical Sciences, Shree Guru Gobind Singh Tricentenary University, Gurugram, Haryana, India

Abstract

Nuclear medicine is used to assess body functionality at various levels of biological organization and is increasingly employed for both diagnostic and therapeutic purposes. Nearly 5% of radiopharmaceuticals are used therapeutically, whereas approximately 95% are used for diagnosis. Diagnostic radiopharmaceuticals are generally considered safe because they are administered in subpharmacological doses, and the radiotracer components are employed in minimal doses. Consequently, the radiation exposure to the body during nuclear medicine investigations is typically low. However, when radiopharmaceuticals are used for therapeutic applications such as tumor ablation and bone pain palliation, the emitted radiation is highly localized and potent. Radiotracers and radiation doses are more carefully selected for young patients, as the radiation-induced risk of adverse health effects is greater in children than in adults. Radiopharmaceutical preparations should adhere to the established standards of pharmacopoeia worldwide to ensure safety and efficacy. Adherence to current good manufacturing practices, sterility, and good radiation practices are prerequisites for ensuring effective quality assurance and quality control systems during radiopharmaceutical preparation. The quality control test parameter for radiopharmaceuticals primarily involves physicochemical and biological tests. However, significant concerns exist regarding the biological testing of radiopharmaceuticals, necessitating their parametric release. The time-intensive traditional sterility test, bacterial endotoxin test, and rabbit pyrogen tests have been critical quality control issues due to the short half-lives of most radiopharmaceuticals, as they should be dispensed at the earliest to ensure optimal diagnostic/therapeutic benefit. Therefore, manufacturers of radiopharmaceuticals, dispensers, and nuclear medicine specialists should be cognizant of the issues posed by biological quality control as a primary obstacle to ensuring consistent quality through parametric release from a compendial test method standpoint.

Keywords: Radiopharmaceuticals; Quality control; Pharmacopoeia; Bacterial endotoxin; Pyrogen; Sterility; Parametric release

***Corresponding author:**
Prasad Thota
(prasad.ipc@gov.in)

Citation: Thota P, Kumari B, Teotia AK, *et al.* Pharmacopeial parametric release strategy in microbiological quality control of radiopharmaceuticals. *Adv Radiother Nucl Med.* 2024;2(3):3619. doi: 10.36922/arnm.3619

Received: May 9, 2024

Accepted: July 17, 2024

Published Online: September 11, 2024

1. Introduction

The World Health Organization (WHO) defines radiopharmaceuticals as novel radioisotope-infused pharmaceutical preparations that are employed in critical clinical settings for therapy or diagnosis. Radiopharmaceutical preparations contain radioactive elements (radioisotopes and radioisotope-labeled compounds) designed for diagnosis and therapy.[1] Radiopharmaceuticals labeled with positron emission tomography and single-photon emission computed tomography radionuclides are highly effective in diagnosing malignancies, neurological and neurodegenerative illnesses, inflammation, and bacterial infections.[2] Based on the standards established by the International Pharmacopoeia of the WHO, radiopharmaceutical medications can be categorized into the following four groups:

i. Radiopharmaceutical preparation: This medicinal product is ready to use and contains a radionuclide necessary for its medical purpose. It might be suitable for a few different diagnostic or therapeutic uses
ii. Radionuclide generator: This comprises a system that separates a radionuclide with a short half-life (daughter radionuclide) from one with a long half-life (parent radionuclide), and then uses the separated radionuclides to create a radiopharmaceutical preparation
iii. Radiopharmaceutical precursor: It is a radionuclide for radiolabeling, creating a radiopharmaceutical preparation
iv. Kit for radiopharmaceutical preparations: It contains the stabilized pharmaceutical component of the radiopharmaceutical preparation and excipients without the radionuclides. Before using it for medicinal purposes, it is to be reconstituted with a specific radionuclide. It is usually a multidose vial, and additional procedures may be necessary for its creation (boiling, heating, filtration, and buffering). They are usually made to be used within 12 h of preparation.[3]

2. Application-based classification of radiopharmaceuticals

2.1. Therapeutic radiopharmaceuticals

Therapeutic radiopharmaceuticals are molecules with radioactive labels that target a specific organ and localize at the site to give a therapeutic dosage of ionizing radiation for destroying dysfunctional cells. This is referred to as radionuclide therapy. For instance, ^{131}I sodium iodide for the treatment of metastatic thyroid cancer, ^{32}P phosphate for the treatment of blood conditions and intracavitary malignancies, and ^{89}Sr chloride for the treatment of bone cancer are frequently used therapeutic radiopharmaceuticals.

2.2. Diagnostic radiopharmaceuticals

Diagnostic radiopharmaceuticals are tracers used to track human disease progression. These tracers have a short-lived isotope that is often bound to a ligand or carrier. For example, technetium-99m dimercaptosuccinic acid is used for the management of medullary thyroid cancer, and technetium-99m medronate (^{99m}Tc-methylene diphosphonate) is frequently utilized for bone scintigraphy.[4]

2.3. Theranostic radiopharmaceuticals

Theranostic radiopharmaceuticals combine the diagnostic qualities of a radionuclide with the curative potential of virtually identical therapeutic analog radionuclides to give the selected patient the benefit of both imaging and a customized and targeted treatment. Examples include ^{68}Ga DOTATATE/^{68}Ga prostate-specific membrane antigen (PSMA)-11 to evaluate tumor progression, therapy planning, and monitoring of treatment response of neuroendocrine tumors and metastatic prostate cancer; and ^{177}Lu DOTATATE/^{177}Lu PSMA-617 used to manage and treat somatostatin receptor-positive neuroendocrine tumor of the gastroenteropancreatic region and PSMA-expressing metastatic castration-resistant prostate cancer.[5]

3. Role of pharmacopoeia and status of radiopharmaceutical monographs

Pharmacopoeia is established to avoid marketing inconsistent medications while ensuring drug quality, safety, and efficacy. Many countries possess national pharmacopeias of their own, such as the British Pharmacopoeia (BP) for the UK and the US Pharmacopoeia (USP) for the US of America. The WHO also produces a pharmacopoeia, International Pharmacopoeia, for regular use by its member countries.[6] Likewise, in India, Indian Pharmacopoeia (IP) is acknowledged as the official standard-setting document for drugs produced and/or marketed in India. On behalf of the Ministry of Health and Family Welfare, Government of India, IP is published periodically by the IP Commission following the requirements of the Drugs and Cosmetics Act, 1940, and Rules 1945 thereunder. IP consists of several authoritative methods for analyzing pharmaceuticals and defining their identity, purity, and potency.[7]

To oversee the quality of radiopharmaceutical preparations, the IP Commission, for the first time, includes 19 radiopharmaceutical monographs along with one general chapter in IP 2014. For radiopharmaceutical preparations, IP 2022 currently lists 37 monographs, 30 of which are employed

for diagnostic categories, six are for therapeutic categories, and one is applied for both diagnosis and therapy.[8,9] For the rest of the pharmacopeias, BP 2023 and European Pharmacopoeia (EP) 11.0 consists of 83 monographs, USP 2022 comprises 43 monographs, 11th edition of International Pharmacopoeia comprises 25 monographs, Chinese Pharmacopoeia (CP) 2015 consists of 30 monographs, and 18th edition of Japanese Pharmacopoeia (JP) consists of 13 monographs concerning the radiopharmaceutical preparations as mentioned in Table 1 in detail.[10-15] Tabulation of pharmacopeial requirements for a comprehensive list of radiopharmaceuticals is addressed in Table 2.

4. Significance of quality control in radiopharmaceuticals

When it comes to testing, quality control, a part of quality assurance, plays a major role. The use of procedures, tests, analytical methods, and acceptance criteria to evaluate the quality of radiopharmaceuticals, materials, and components is known as quality control.[9] The vast majority of radiopharmaceuticals used in nuclear medicine have wide applications in diagnostic, therapeutic, and theranostic and are injected intravenously into patients as part of both diagnosis and therapy, which normally take a few minutes for administration to each patient.[5,16,17] They typically contain trace amounts of the active components and a radioisotope to facilitate scintigraphic imaging or biodistribution study and are delivered once or more.[18] Radiopharmaceutical composition changes over time, which is associated with radioactive decay. This necessitates using semi-manufactured goods such as radionuclide generators, precursors, and kits since the physical half-life of the radionuclide is frequently so short that the final preparation must be completed right away before administration to the patient. Hence, it is important to consider the standards of generators, kits, and other semi-manufactured goods when evaluating the safety and effectiveness of radiopharmaceuticals.[19] Since radiopharmaceuticals are meant to be administered to patients, they must undergo rigorous quality control procedures to ensure the formulations adhere to the established radiological and pharmaceutical safety and efficacy standards.[1,20] The radiopharmaceuticals used in the diagnostic nuclear medicine study must meet all these standards. Adherence to the quality control standards regarding therapeutic radiopharmaceuticals is also essential because the patient's life could be endangered due to higher localized radiation, other side effects, and toxicity.[21] The Good Radiopharmacy Practice Guidelines published by the Radiopharmacy Committee of the European Association of Nuclear Medicine on current Good Radiopharmaceuticals Practice in the preparation of radiopharmaceuticals were a helpful resource for setting quality requirements for radiopharmaceuticals prepared on a modest scale and the non-radioactive labeling precursors used in their preparation.[22]

5. Key elements of radiopharmaceuticals quality control

Quality controls are crucial in any production or formulation line in the pharmaceutical sector. The same applies to radiopharmaceutical formulations. Radiopharmaceuticals are subject to the same quality control processes as non-radioactive medications.[23] Quality control procedures should always be performed for radiopharmaceutical preparation and before patient administration, except for the parametric release batch, to ensure optimal radiopharmaceutical products.[16] Due to the interaction between pharmaceutical and radioactive characteristics, quality monitoring of radiopharmaceuticals is essential for independent yet connected reasons. Pharmaceutical guidelines were created to ensure that patients cannot be harmed by pyrogenic, microbiological, or particle contamination. The radioactivity, radiochemical purity, and radionuclidic purity are all ensured by a radioactive parameter, which helps to keep the desired radiation dose of patients to a minimum.[17]

The quality control tests for radiopharmaceuticals and cold kits fall into physicochemical and biological tests. The physicochemical analyses ascertain the sample pH, ionic strength, osmolality, and physical state, especially if it is a colloid, as well as the quantity of radionuclidic and radiochemical pollutants, while the material's sterility, apyrogenicity, and toxicity are demonstrated by the biological tests. The manufacturers carry out some of these QC procedures, whereas others need to be done by the dispensing staff.[17] The primary components of radiopharmaceutical quality control parameters are depicted in Figure 1.

Here, we review the most significant and widespread biological quality control procedures for radiopharmaceuticals, given their short half-lives.

6. Biological quality control

One of the two types of radiopharmaceuticals is those made with a half-life that is long enough to permit regular sterility testing. Radiopharmaceuticals require retroactive testing, which is the main distinction between their sterility testing and that of conventional medications. However, because most radiopharmaceuticals are prepared and utilized in less than a week, there is insufficient time to perform the required sterility tests.[24] The tests used

Table 1. Comparative status of radiopharmaceutical monographs concerning biological quality control parameters (bacterial endotoxin test & sterility) in different pharmacopoeia

Name of radiopharmaceutical monographs	BP 2023[10]		EP 11.0[11]		USP 2022[12]		IP 2022[9]		International Pharmacopoeia 11th ed.ition[13]		CP 2015[14]		JP 18th ed..[15]	
	B	S	B	S	B	S	B	S	B	S	B	S	B	S
Albumin aggregated and stannous chloride for injection	N.A		N.A		N.A		N.A		N.A		√	√	N.A	
Alovudine (^{18}F) injection	√	√	√	√	N.A		N.A		N.A		N.A		N.A	
Ammonia (^{13}N) injection	√	√	√	√	√	√	N.A		N.A		N.A		N.A	
Betiatide for radiopharmaceutical preparations	x	x	x	x	N.A		N.A		N.A		N.A		N.A	
Carbon monoxide (^{15}O)	x	x	x	x	N.A		N.A		N.A		N.A		N.A	
Choline ([^{11}C] methyl) injection	√	√	√	√	N.A		N.A		N.A		N.A		N.A	
Chromium (^{51}Cr) edentate injection	x	√	x	√	N.A		N.A		N.A		N.A		N.A	
Colloidal chromium phosphate[^{32}P] injection	N.A		N.A		N.A		N.A		N.A		√	√	N.A	
Copper tetramibi tetrafluoroborate for radiopharmaceutical preparations	x	x	x	x	N.A		N.A		N.A		N.A		N.A	
Cyanocobalamin (^{57}Co) capsules	x	x	x	x	N.A		N.A		N.A		N.A		N.A	
Cyanocobalamin (^{57}Co) solution	x	x	x	x	N.A		N.A		N.A		N.A		N.A	
Cyanocobalamin (^{58}Co) capsules	x	x	x	x	N.A		N.A		N.A		N.A		N.A	
Cyanocobalamin (^{58}Co) solution	x	x	x	x	N.A		N.A		N.A		N.A		N.A	
Etifenin and stannous chloride injection	N.A		N.A		N.A		N.A		N.A		√	√	N.A	
Fludeoxyglucose (^{18}F) injection	√	√	√	√	√	√	√	√	√	√	√	√	N.A	
Flumazenil (N-[^{11}C] methyl) injection	√	√	√	√	N.A		N.A		N.A		N.A		N.A	
Fluoride solution (^{18}F) for radiolabelling	√	x	√	x	N.A		N.A		N.A		N.A		N.A	
Fluorocholine (^{18}F) injection	√	√	√	√	N.A		N.A		N.A		N.A		N.A	
Fluorodopa (^{18}F) (prepared by electrophilic substitution) injection	√	√	√	√	N.A		N.A		N.A		N.A		N.A	
Fluorodopa (^{18}F) (prepared by nucleophilic substitution) injection	√	√	√	√	N.A		N.A		N.A		N.A		N.A	
Fluoroethyl-L-tyrosine (^{18}F) injection	√	√	√	√	N.A		N.A		N.A		N.A		N.A	
Fluoromisonidazole (^{18}F) injection	√	√	√	√	N.A		N.A		N.A		N.A		N.A	
Gallium (^{67}Ga) citrate injection	x	√	x	√	√	√	√	√	√	√	√	√	x	x
Gallium (^{68}Ga) chloride (accelerator produced) solution for radiolabelling	√	x	√	√	N.A		N.A		N.A		N.A		N.A	
Gallium (^{68}Ga) chloride solution for radiolabelling	√	x	√	x	N.A		√	√	N.A		N.A		N.A	
Gallium (^{68}Ga) edotreotide injection	√	√	√	√	N.A		√	√	N.A		N.A		N.A	
Gallium (^{68}Ga) PSMA-11 injection	√	√	√	√	N.A		N.A		N.A		N.A		N.A	
Iodinated (^{125}I) Human albumin injection	√	√	√	√	N.A		N.A		N.A		N.A		N.A	
Indium (^{111}In) capromab pendetide injection	N.A		N.A		√	√	N.A		N.A		N.A		N.A	
Indium (^{111}In) chloride injection	N.A		N.A		N.A		N.A		N.A		N.A		x	x
Indium (^{111}In) chloride solution	x	√	x	√	√	√	N.A		N.A		N.A		N.A	
Indium (^{111}In) oxine solution	x	√	x	√	N.A		N.A		N.A		N.A		N.A	
Indium (^{111}In) oxyquinoline solution	N.A		N.A		x	x	N.A		N.A		N.A		N.A	
Indium (^{111}In) pentetate injection	√	√	√	√	√	√	N.A		N.A		N.A		N.A	
Indium (^{111}In) pentetreotide injection	N.A		N.A		√	√	N.A		N.A		N.A		N.A	

(Cont'd...)

Table 1. ***(Contiuned)***

Name of radiopharmaceutical monographs	BP 2023[10]		EP 11.0[11]		USP 2022[12]		IP 2022[9]		International Pharmacopoeia 11th ed.ition[13]		CP 2015[14]		JP 18th ed..[15]	
	B	S	B	S	B	S	B	S	B	S	B	S	B	S
Iobenguane (^{123}I) injection	√	√	√	√	√	√	N.A		√	√	N.A		N.A	
Iobenguane (^{131}I) injection for diagnostic use	√	√	√	√	N.A		N.A		√	√	N.A		N.A	
Iobenguane (^{131}I) injection for therapeutic use	√	√	√	√	N.A		N.A		√	√	N.A		N.A	
Iobenguane sulfate for radiopharmaceutical preparation	x	x	x	x	N.A		N.A		N.A		N.A		N.A	
Iodine (^{125}I) brachytherapy source	N.A		N.A		N.A		N.A		N.A		x	x	N.A	
Iodinated albumin (^{125}I) injection	N.A		N.A		√	x	N.A		N.A		N.A		N.A	
Iodinated albumin (^{131}I) injection	N.A		N.A		√	x	N.A		N.A		N.A		N.A	
Iodinated (^{131}I) Human serum Albumin injection	N.A		N.A		N.A		N.A		N.A		N.A		x	x
Iodomethylnorcholestrol (^{131}I) injection	√	√	√	√	N.A		N.A		N.A		N.A		N.A	
Iothalamate sodium (^{125}I) injection	N.A		N.A		√	x	N.A		N.A		N.A		N.A	
Krypton (^{81m}Kr) inhalation gas	x	x	x	x	N.A		N.A		N.A		N.A		N.A	
Lutetium (^{177}Lu) solution for radiolabelling	√	√	√	√	N.A		N.A		N.A		N.A		N.A	
Medronic acid for radiopharmaceutical preparation	x	x	x	x	N.A		N.A		N.A		N.A		N.A	
(^{131}I) Meta-iodobenzyl guanidine injection for diagnostic use	N.A		N.A		N.A		√	√	N.A		N.A		N.A	
(^{131}I) Meta-iodobenzyl guanidine injection for therapeutic use	N.A		N.A		N.A		√	√	N.A		N.A		N.A	
Methylenediphosphonate and stannous chloride for injection	N.A		N.A		N.A		N.A		N.A		√	√	N.A	
L-Methionine [^{11}C] methyl) injection	√	√	√	√	N.A		N.A		N.A		N.A		N.A	
Oxygen (^{15}O)	x	x	x	x	N.A		N.A		N.A		N.A		N.A	
Pentetate sodium calcium for radiopharmaceutical preparations	x	x	x	x	N.A		N.A		N.A		N.A		N.A	
Pentetate acid and stannous chloride for injection	N.A		N.A		N.A		N.A		N.A		√	√	N.A	
PSMA-1007 (^{18}F) injection	√	√	√	√	N.A		N.A		N.A		N.A		N.A	
Raclopride -[(^{11}C) methoxy] injection	√	√	√	√	N.A		N.A		N.A		N.A		N.A	
Samarium (^{153}Sm) EDTMP injection	N.A		N.A		N.A		√	√	N.A		N.A		N.A	
Samarium (^{153}Sm) lexidronam complex injection	N.A		N.A		√	x	N.A		√	√	√	√	N.A	
Samarium phosphate (^{32}P) colloid injection	N.A		N.A		N.A		√	√	N.A		N.A		N.A	
Sodium acetate-[1-^{11}C] injection	√	√	√	√	N.A		N.A		N.A		N.A		N.A	
Sodium chromate (^{51}Cr) sterile injection	x	√	x	√	N.A		√	x	N.A		√	√	x	x
Sodium fluoride (^{18}F) injection	√	√	√	√	√	√	√	√	N.A		N.A		N.A	
Sodium iodide (^{123}I) capsules	N.A		N.A		x	x	N.A		N.A		N.A		x	x
Sodium iodide (^{123}I) injection	x	√	x	√	√	√	√	√	N.A		N.A		N.A	
Sodium iodide (^{123}I) solution for radiolabelling	x	x	x	x	√	√	√	√	N.A		N.A		N.A	
Sodium iodide (^{131}I) capsules for diagnostic use	x	x	x	x	x	x	x	x	x	x	x	x	x	x
Sodium iodide (^{131}I) capsules for therapeutic use	x	x	x	x	x	x	x	x	x	x	N.A		x	x
Sodium iodide (^{131}I) injection	N.A		N.A		√	√	N.A		√	√	N.A		N.A	
Sodium iodide (^{131}I) solution	x	√	x	√	√	√	x	x	√	x	x	x	x	x
Sodium iodide (^{131}I) solution for radiolabelling	x	x	x	x	N.A		N.A		N.A		N.A		N.A	

(Cont'd...)

Table 1. ***(Contiuned)***

Name of radiopharmaceutical monographs	BP 2023[10]		EP 11.0[11]		USP 2022[12]		IP 2022[9]		International Pharmacopoeia 11th ed.ition[13]		CP 2015[14]		JP 18th ed..[15]	
	B	S	B	S	B	S	B	S	B	S	B	S	B	S
Sodium iodohippurate (^{123}I) injection	x	√	x	√	N.A		N.A		N.A		N.A		N.A	
Sodium iotalamate (^{125}I) injection	N.A		N.A		N.A		N.A		√	√	N.A		N.A	
Sodium iodohippurate (^{131}I) injection	x	√	x	√	N.A		N.A		N.A		√	√	x	x
Sodium iodohippurate dihydrate for radiopharmaceutical preparations	x	x	x	x	N.A		N.A		N.A		N.A		N.A	
Sodium molybdate (^{99}Mo) solution (fission)	x	x	x	x	N.A		N.A		N.A		N.A		N.A	
Sodium pertechnetate (^{99m}Tc) injection (accelerator produced)	N.A		x	√	√	x	N.A		N.A		N.A		x	x
Sodium pertechnetate (^{99m}Tc) injection (fission)	x	√	x	√	√	x	√	√	√	√	√	√	x	x
Sodium pertechnetate (^{99m}Tc) injection (non-fission)	x	√	x	√	√	x	√	√	√	√	N.A		x	x
Sodium phosphate (^{32}P) injection	x	√	x	√	N.A		√	√	√	√	√		√	N.A
Sodium phosphate (^{32}P) Oral Solution	N.A		N.A		N.A		N.A		N.A		**x**		**x**	N.A
Sodium phytate and stannous chloride for injection	N.A		N.A		N.A		N.A		N.A		√		√	N.A
Sodium pyrophosphate and stannous chloride for injection	N.A		N.A		N.A		N.A		N.A		√		√	N.A
Sodium pyrophosphate decahydrate for radiopharmaceutical preparations	x	X	x	x	N.A		N.A		N.A		N.A		N.A	
Strontium (^{89}Sr) chloride injection	x	√	x	√	√	x	√	√	√	√	√		√	N.A
Technetium (^{99m}Tc) albumin aggregated injection	N.A		N.A		√	√	N.A		N.A		√		√	N.A
Technetium (^{99m}Tc) bicisate injection	x	√	x	√	√	√	N.A		√	√	√		√	N.A
Technetium (^{99m}Tc) colloidal rhenium sulfide injection	√	√	√	√	N.A		√	√	N.A		N.A		N.A	
Technetium (^{99m}Tc) colloidal sulfur injection	N.A		N.A		√	√	N.A		√	√	N.A		N.A	
Technetium (^{99m}Tc) colloidal tin injection	x	√	x	√	N.A		N.A		√	√	N.A		N.A	
Technetium (^{99m}Tc) Disofenin injection	N.A		N.A		√	√	N.A		N.A		N.A		N.A	
Technetium (^{99m}Tc) DMSA injection	N.A		N.A		N.A		√	√	N.A		N.A		N.A	
Technetium (^{99m}Tc) DTPA injection	N.A		N.A		N.A		√	√	N.A		N.A		N.A	
Technetium (^{99m}Tc) EC injection	N.A		N.A		N.A		√	√	N.A		N.A		N.A	
Technetium (^{99m}Tc) ECD injection	N.A		N.A		N.A		√	√	N.A		N.A		N.A	
Technetium (^{99m}Tc) etifenin injection	√	√	√	√	N.A		N.A		N.A		√	√	N.A	
Technetium (^{99m}Tc) L, L-ethylene dicysteine injection	N.A		N.A		N.A		N.A		N.A		√	√	N.A	
Technetium (^{99m}Tc) exametazime injection	x	√	x	√	√	√	√	√	√	√	N.A		N.A	
Technetium (^{99m}Tc) gluconate injection	x	√	x	√	N.A		N.A		N.A		N.A		N.A	
Technetium (^{99m}Tc) glucoheptonate injection	N.A		N.A		N.A		√	√	N.A		N.A		N.A	
Technetium (^{99m}Tc) human albumin injection	√	√	√	√	N.A		N.A		N.A		N.A		N.A	
Technetium (^{99m}Tc) HYNIC-TOC injection	N.A		N.A		N.A		√	√	N.A		N.A		N.A	
Technetium (^{99m}Tc) labeled human serum albumin nanocolloid injection	N.A		N.A		N.A		√	√	N.A		N.A		N.A	
Technetium (^{99m}Tc) macrosalb injection	√	√	√	√	N.A		√	√	N.A		N.A		N.A	
Technetium (^{99m}Tc) mebrofenin injection	√	√	√	√	√	√	√	√	√	√	N.A		N.A	

(Cont'd...)

Table 1. ***(Contiuned)***

Name of radiopharmaceutical monographs	BP 2023[10]		EP 11.0[11]		USP 2022[12]		IP 2022[9]		International Pharmacopoeia 11th ed.ition[13]		CP 2015[14]		JP 18th ed..[15]	
	B	S	B	S	B	S	B	S	B	S	B	S	B	S
Technetium (^{99m}Tc) medronate injection	√	√	√	√	√	√	√	√	√	√	N.A		N.A	
Technetium (^{99m}Tc) mertiatide injection	x	√	x	√	√	√	√	√	√	√	N.A		N.A	
Technetium (^{99m}Tc) MIBI injection	N.A		N.A		N.A		√	√	N.A		N.A		N.A	
Technetium (^{99m}Tc) methylenediphosphonate injection	N.A		N.A		N.A		N.A		N.A		√	√	N.A	
Technetium (^{99m}Tc) microspheres injection	√	√	√	√	N.A		N.A		N.A		N.A		N.A	
Technetium (^{99m}Tc) oxidronate injection	√	√	√	√	√	x	N.A		N.A		N.A		N.A	
Technetium (^{99m}Tc) pentetate injection	x	√	x	√	√	√	N.A		√		√	√	√	N.A
Technetium (^{99m}Tc) phytate injection	N.A		N.A		N.A		N.A				√		√	N.A
Technetium (^{99m}Tc) pyrophosphate injection	N.A		N.A		√	√	N.A		N.A		√		√	N.A
Technetium (^{99m}Tc) (pyro and trimeta) phosphate injection	N.A		N.A		N.A		N.A		N.A		N.A		N.A	
Technetium (^{99m}Tc) red blood cells injection	N.A		N.A		√	√	N.A		N.A		N.A		N.A	
Technetium (^{99m}Tc) sestamibi injection	x	√	x	√	√	√	N.A		√	√	√	√	N.A	
Technetium (^{99m}Tc) succimer injection	x	√	x	√	√	√	N.A		√	√	N.A		N.A	
Technetium (^{99m}Tc) tetrofosmin complex injection	N.A		N.A		√	√	√	√	√	√	N.A		N.A	
Technetium (^{99m}Tc)-TRODAT-1 Injection	N.A		N.A		N.A		√	√	N.A		N.A		N.A	
Technetium (^{99m}Tc) tin pyrophosphate injection	√	√	√	√	N.A		N.A		√	√	N.A		N.A	
Tetra-O-acetyl-mannose triflate for radiopharmaceutical preparations	x	x	x	x	N.A		N.A		N.A		N.A		N.A	
Thallous (^{201}TI) chloride injection	x	√	x	√	√	√	√	√	√	√	√	√	x	x
Tritiated (^{3}H) water injection	x	√	x	√	N.A		N.A		N.A		N.A		N.A	
Urea (^{14}C) Capsules	N.A		N.A		x	x	x	x	N.A		N.A		N.A	
Water (^{15}O) injection	√	√	√	√	N.A		N.A		N.A		N.A		N.A	
Xenon (^{133}Xe) injection	x	√	x	√	N.A		N.A		N.A		x	√	N.A	
Yttrium (^{90}Y) chloride solution for radiolabeling	√	√	√	√	N.A		N.A		N.A		N.A		N.A	
Yttrium Y 90 ibritumomab tiuxetan injection	N.A		N.A		√	√	N.A		N.A		N.A		N.A	
Yttrium (^{90}Y) silicate injection	N.A		N.A		N.A		N.A		√	√	N.A		N.A	

Note: "B" represents bacterial endotoxin test; "S" represents sterility; "x" represents test not present; "√" represents test present; "N.A" represents monograph not available in pharmacopeias.
Abbreviations: BP: British Pharmacopoeia; EP: European Pharmacopoeia; USP: US Pharmacopoeia; IP: Indian Pharmacopoeia; CP: Chinese Pharmacopoeia; JP: Japanese Pharmacopoeia; PSMA: Prostate-specific membrane antigen; DMSA: Dimercaptosuccinic acid.

to evaluate radiopharmaceuticals are the same as those used to evaluate traditional medications.[23] The short half-life radionuclides decay from a parent radionuclide with a sufficient half-life in a radionuclide generator and are produced from cyclotrons, which forces their release for patient use even before all the quality control tests are performed, which is one of the main issues in radiopharmaceutical dispensing.[13,25] Due to the limited time for quality control tests, numerous quick procedures for evaluating crucial parameters, including the shorter half-lives of some radionuclides, have been developed.[16] End-user testing is a crucial stage in the quality control of radiopharmaceutical preparations and patient safety, particularly for those radiopharmaceutical preparations dispensed or synthesized in the end-user facility (such as those used in nuclear medicine clinics).[13] Radiopharmaceuticals are biologically tested to establish their sterility, apyrogenicity, and toxicity before human administration.[23] The main biological quality control parameters include sterility and apyrogenicity, that is, bacterial endotoxin and rabbit pyrogen tests. These methods are explained in detail below.

Table 2. Pharmacopeial requirements for a comprehensive list of radiopharmaceuticals

No.	Pharmacopeial requirements
1	Identification (Radioactive decay, measurement of $t_{½}$, and determination of nature and energy of the radiation)
2	Measurement of radioactivity (radionuclidic purity, radiochemical purity, specific radioactivity, chemical purity, and enantiomeric purity)
3	Physiological distribution
4	Sterility
5	Bacterial endotoxin test-pyrogen
6	pH
7	Storage and labeling
8	Filter integrity test
9	Residual solvent measurement

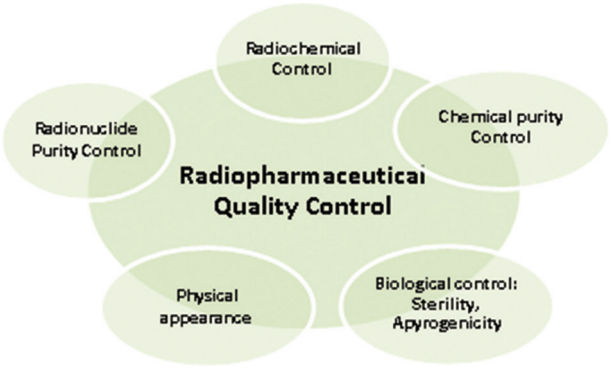

Figure 1. Quality control parameters for radiopharmaceuticals

6.1. Sterility

Due to their nature of use, pharmaceuticals are required to be sterile and must routinely pass a sterility test.[24] For parenteral administration, radiopharmaceutical preparations must be made using aseptic techniques to prevent microbial contamination and the associated risk of infection. When introduced into a radiopharmaceutical, pathogens may survive the storage period and be injected in a viable state into the patient. Moreover, many patients receiving radiopharmaceuticals may undergo cancer chemotherapy, which can compromise the immune system. Testing for sterility is carried out to confirm that drugs are almost completely free of living microbes, such as fungi and bacteria.[9] This test must be carried out aseptically to prevent interference from external contaminants with the test samples during the experiment. For this, the test should ideally be performed in a sterile laminar air flow hood with qualified personnel. A dosage for a human should be used as the minimum sample volume for the test. To identify bacterial and fungus contaminations, a quality control test procedure for sterility is present in pharmacopeias. For bacterial contamination, the radiopharmaceutical sample should be incubated for 14 days at 30 – 35° in a fluid thioglycolate medium. For fungal contamination, the radiopharmaceutical sample should be incubated for 14 days at 20 – 25° in a soybean casein digest medium. The radiopharmaceutical is not sterile if bacterial, fungal, or yeast growth is observed in either medium used during the test.[26-29] The metabolic byproducts (endotoxin) produced by these microbes, that is, bacterial, fungal, or yeast, can cause pyrogenicity.

6.1.1. Challenge for sterility test

Most radiopharmaceuticals are formulated and used within a week; thus, there needs to be more time to carry out the standard sterility testing procedures. Due to some radionuclides' half-life, the limited batch size, and the radiation threat, sterility testing of radiopharmaceuticals poses unique challenges. Since radiopharmaceutical has an occasionally limited half-life, it must be delivered to the individual immediately; therefore, it is impossible to wait for the sterility test results.[30] When the radionuclide half-life is <5 min, the radiopharmaceutical preparation is often administered to the patient on-site using a validated production method.[9-13] At the same time, if the batch size of a radiopharmaceutical preparation is restricted to one or a few samples, sampling the batch for sterility testing may be optional. In these circumstances, it is preferred to release the product produced by a thoroughly approved process parametrically. When aseptic manufacturing is used, the sterility test must be executed to control the production quality.[9-13] However, the sterility test is carried out retrospectively, that is, after patient administration, which is the most significant difference between sterility testing of regular pharmaceuticals and radiopharmaceuticals. The test must, however, begin as soon as feasible.[30] If not started immediately, samples are kept in a storage environment that has been proven suitable for preventing false adverse outcomes.[10,11] The concept of parametric release is duly addressed in IP 2022, BP 2023, EP 11.0, USP 2022, and International Pharmacopoeia 11th edition pharmacopeias concerning the release of short half-life radiopharmaceuticals. However, the JP 18th edition and CP 2015 should be more active on this critical issue.

6.1.2. Significance of sterility testing time

The traditional sterility test procedure requires 14 days to obtain the result. The results from these methods cannot be used to prompt timely corrective action. The interval between the radiopharmaceutical manufacturing and the sterility test must be as short as possible. For radiopharmaceuticals with a long half-life, this is

particularly crucial. Short-lived radiopharmaceuticals, including those labeled with the radionuclides ^{68}Ga or ^{18}F ($t_{1/2}$ = 68 or 110 min, respectively), are frequently only tested for sterility after the radioactivity has decayed, which might produce false results. Long-lived radiopharmaceuticals having half-lives of days to weeks (such as ^{177}Lu, ^{131}I, or ^{90}Y) require several days to months to decay, which can alter the outcome of the sterility test because of their prolonged incubation time. The microorganisms often die after a particular time frame due to the lack of nutrients or other factors and are not detected in the later stage of sterility testing.[30] In this regard, alternative microbiological methods mentioned in pharmacopeias have proven the potential for results in real-time or almost real-time with the prospect of earlier corrective action. If these novel approaches are proven effective and made suitable for regular usage, the quality of testing may likewise be significantly enhanced. Several *in vitro* sterility tests used rapid testing techniques to determine the presence or absence of microorganisms by measuring the evolution of CO_2 or consumption of O_2 for detecting bacterial metabolism in closed containers, thus helping to overcome this significant limitation. The basic principle of the test involves the addition of the test sample to a trypticase soy broth culture medium that contains ^{14}C-glucose. The capture of $^{14}CO_2$ gas in this method shows the existence of both aerobic and anaerobic microorganisms. A rapid testing approach also uses ATP bioluminescence to get beyond the drawbacks of conventional test methods for radiopharmaceutical quality control, improving data integrity and subjectivity removal.[31-33] The innovative aspect of this approach is that it only requires a short testing duration, roughly 3 – 24 h instead of several days.

6.2. Apyrogenicity

6.2.1. Bacterial endotoxin test

A test for bacterial endotoxin is recommended for several radiopharmaceutical formulations. The test is conducted following the general method of bacterial endotoxin, adopting the appropriate safety steps to limit radiation exposure to the personnel carrying out the test.[9] Bacterial endotoxin is the only necessary pyrogen of concern in parenteral drug preparations because of its potency and widespread natural distribution. Depending on the dose, mode, and rate of administration, bacterial endotoxins might have adverse effects. Limulus amebocyte lysate (LAL) reagent is economically feasible for routine bacterial endotoxin tests based on gel-clot formation.[34] The LAL test, commonly known as the bacterial endotoxin test, is used to detect endotoxin quantitatively and qualitatively. This method uses the amebocyte lysate from the horseshoe crab's blood, such as *Limulus polyphemus, Tachypleus gigas, Tachypleus tridentatus,* and *Carcinoscorpius rotundicauda*. The basic test principle is based on the idea that endotoxin will generate an opaque gel in the presence of Ca^{2+} ion when the sample is incubated with the LAL at 37 ± 1°C. A test sample with a pH range of 6 – 8 and 0.1 mL LAL typically makes up an assay mixture. After mixing, the reaction takes place for 60 ± 2 min. The development of an opaque gel shows the existence of an endotoxin. The LAL test is performed on LAL reagent water, control standard endotoxin from *Escherichia coli*, and test samples. Depending on whether test materials form gel, they are classified as either positive or negative with respect to the control standard endotoxin from *E. coli*, which acts as a positive control if gel formation takes place, and the LAL reagent water acts as a negative control in the case of no gel formation.[35-38] The endotoxin limit required for a bacterial endotoxin test is mentioned in the individual monograph of the pharmacopeias, whereas a comparative status of endotoxin limit calculation of different pharmacopeias based on radiopharmaceutical product administration is mentioned in Table 3.[9-15] For radiopharmaceuticals created using short-lived radioisotopes, endotoxin testing after product release is permissible. However, developing the kinetic (photometric) LAL test, which may be accomplished in 20 min, has made it possible to test for bacterial endotoxin before releasing the radiopharmaceuticals with half-lives longer than 30 min.[9-15]

6.2.2. Risks of radiopharmaceutical endotoxin contamination

Like all other drugs, radiopharmaceuticals are governed by stringent endotoxin contamination restrictions. Due to potential interference with the assay's components, caution must be used when performing the LAL assay on radiopharmaceuticals. The availability of free Ca^{2+} ions is essential for the key enzyme transglutaminase in the LAL assay. Chelating compounds, which reduce the amount of Ca^{2+} in the solution, are typically found in radiopharmaceuticals. As a result, the LAL assay could produce erroneous negative results. A 2014 study published in the *Journal of Nuclear Medical Technology* offered a simple but efficient approach to eliminating this issue. The scientists added more calcium chloride to prepare the drug for LAL testing. By doing this, they successfully eliminated interference from the chelating chemicals in the radiopharmaceutical.[39]

6.2.3. Rabbit pyrogen test

The test for rabbit pyrogen may be particularly emphasized for testing the product when the nature of the radiopharmaceutical preparation results in interference through inhibition or activation, and it is

Table 3. Comparative status of endotoxin limit calculation based on radiopharmaceutical product administration

Administration form of radiopharmaceutical products	IP 2022[9]	BP 2023[10]	EP 11.0[11]	USP 2022[12]	JP 18th edition[15]	International Pharmacopoeia 11th ed.ition[13]	CP 2015[14]
Not administered intrathecal	175/V where V is the maximum recommended dose in ml	N/A	N/A	175 EU/V where V is the maximum recommended dose in ml	N/A	N/A	N/A
Administered intrathecal	14/V where V is the maximum recommended dose in ml	N/A	N/A	14 EU/V	N/A	N/A	N/A
Administered intravenous	N/A	K/M where K is 2.5/kg or 175/ person	K/M where K is 2.5 IU of endotoxin per kg of body mass	175 EU/V where V is the maximum recommended dose in ml	K/M where K is 2.5 IU	K/M where K is 2.5 IU	K/M where K is 2.5 EU/kg/hr

Abbreviations: BP: British Pharmacopoeia; EP: European Pharmacopoeia; USP: US Pharmacopoeia; IP: Indian Pharmacopoeia; CP: Chinese Pharmacopoeia; JP: Japanese Pharmacopoeia.

impossible to exclude the interfering factor(s). Due to the use of reducing agents and metal chelating agents in the formulation of many ^{99m}Tc-radiopharmaceuticals, the LAL test may produce false negative or positive findings. Since the radionuclide in the preparation has a short half-life, it can be challenging to conduct these tests before approving the batch for use.[9-15] To conduct a rabbit pyrogen test, three healthy rabbits must first receive an intravenous injection of the substance under test in a predetermined volume, followed by a 3-h period of rectal temperature monitoring. A positive test is recorded if an individual rabbit's temperature increases by ≥0.6° above baseline or if the total temperature rises of all three rabbits surpasses 1.4°C.[40]

7. Status of radiopharmaceutical biological quality control standards in pharmacopoeia

The comparative status of radiopharmaceutical biological quality control standards present in different pharmacopeias of the world has been mentioned in Table 1, highlighting detailed information on the presence or absence of biological test parameters in individual monographs.

8. Discussion

Quality control is essential in all pharmaceutical production and formulation processes. The use of quality control processes guarantees that radiopharmaceutical formulations and preparations meet the requirements of the pharmacopoeia for physicochemical and biological tests to verify the effectiveness and safety of medicines. It should be noted that biological tests are essential to determine the material's sterility and apyrogenicity. At the commencement of production of the finished product, the producers conduct these quality control checks. Sterility is a crucial quality factor for pharmaceutical preparations, among other biological quality control test parameters.[41] For drugs that have been terminally sterilized, parametric release typically replaces routine sterility testing.[42] A robust quality assurance process is necessary for parametric releases to generate a product with the appropriate attributes and features.[43] The basis for parametric release is proof of successfully validating the manufacturing process in accordance with established good manufacturing practices and sterilization protocols, as well as a review of the documentation on the additional process monitoring carried out throughout the manufacturing process to support parametric release.[44,45] The use of parametric release, or release of a batch of sterile items based on process data rather than submitting a sample of the items for sterility testing, may be carried out if the appropriate regulatory body approves when a properly approved terminal sterilization procedure using steam, dry heat, or ionizing sterilization is applied. Aseptic assembly or filtration through a bacterial retentive filter is utilized if terminal sterilization is not feasible for parametric release.[41] Regarding the requirement to test each consignment before release, an appropriate approach is to conduct quality control tests on a single sample generator from each available supplier. In contrast, the remaining radiopharmaceuticals can be released based on the outcomes of parametric tests.[43] On the other hand, in the case of apyrogenicity of radiopharmaceuticals created using short-lived radioisotopes, endotoxin testing after product release is permissible. Like all other drugs, radiopharmaceuticals are governed by stringent endotoxin

contamination restrictions. It should be emphasized that if a product contains pyrogens and there are no means to render it apyrogen, it should be rejected.

9. Conclusion

The biological quality control aspects of radiopharmaceuticals described above will be valuable references for various radiopharmaceutical manufacturers and quality control testing laboratories. However, radiopharmaceutical manufacturers also understand the need for biological quality control as the main challenge in maintaining quality for parametric release, as a patient's life could be in danger or compromised if the radiopharmaceutical formulations are not sterile or pyrogen-free. The concept of parametric release can be applied to eliminate or minimize different kinds of testing on the finished product before its intended use due to the short half-life of the radionuclide moiety. Time and resource savings are among the most evident advantages of parametric release. It is debatable if improved sterility assurance will result from developing process understanding for deploying a parametric release process.

Acknowledgments

None.

Funding

None.

Conflict of interest

The authors declare that they have no conflicts of interest.

Author contributions

Conceptualization: Prasad Thota, Bhavna Kumari, Anil Kumar Teotia

Writing-original draft: Prasad Thota, Bhavna Kumari, Sachin Kumar, Rakesh Kumar Sharma

Writing-review & editing: Prasad Thota, Bhavna Kumari, Anil Kumar Teotia, Manoj Kumar Pandey, Bikash Medhi, Rakesh Kumar Sharma, Rajeev Singh Raghuvanshi

Ethics approval and consent to participate

Not applicable.

Consent for publication

Not applicable.

Availability of data

Not applicable.

References

1. Molavipordanjani S, Hosseinimehr SJ. Fundamental concepts of radiopharmaceuticals quality controls. *Pharm Biomed Res*. 2018;4(3):1-8.

   doi: 10.18502/pbr.v4i3.538

2. Lindsley CW, Müller CE, Bongarzone S. Diagnostic and therapeutic radiopharmaceuticals. *J Med Chem*. 2022;65(19):12497-12499.

   doi: 10.1021/acs.jmedchem.2c01403

3. Mora-Román JJ, Esquivel-Álvarez A, Quesada-Morales E, *et al*. Radiopharmaceuticals: A mini review of applications and innovations on nuclear medicine. *World J Pharm Res*. 2021;10(13):64-79.

   doi: 10.20959/wjpr202113-22132

4. Sharma N, Kaur H, Sharma RK. Radiopharmaceuticals regulations: Current scenario and the way forward. *Appl Clin Res Clin Trials Regul Affairs*. 2017;4:1-12.

   doi: 10.2174/2213476X04666170410141155

5. Kaushik D, Jangra P, Verma R, *et al*. Radiopharmaceuticals: An insight into the latest advances in medical uses and regulatory perspectives. *J Biosci.* 2021;46:27.

   doi: 10.1007/s12038-021-00147-5

6. Meher BR. Inclusion of radiopharmaceuticals in the Indian pharmacopeia: A step forward. *Indian J Nucl Med*. 2020;35(1):1-3.

   doi: 10.4103/ijnm.IJNM_133_19

7. *Indian Pharmacopoeia*. Available from: https://ipc.gov.in/mandates/indian/pharmacopoeia/about-ip.html [Last accessed on 2023 Nov 20].

8. Thota P, Thota A, Pandey MK, *et al*. A comparative study of pharmacopoeial quality standards and regulations of radiopharmaceuticals. *Indian J Nucl Med.* 2021;36:153-162.

   doi: 10.4103/ijnm.ijnm_222_20

9. *Radiopharmaceutical Preparations*, *Indian Pharmacopoeia*. 9th ed. Ghaziabad: Indian Pharmacopoeia Commission; 2022.

10. *Radiopharmaceutical Preparations*, *British Pharmacopeia*; 2023.

11. *Radiopharmaceutical Preparations*, *European Pharmacopeia*. Version 11.0; 2023.

12. *Radiopharmaceutical Preparations*, *United States Pharmacopeia*. Rockville, MD: The United States Pharmacopoeial Convention; 2022.

13. *Radiopharmaceuticals*, *the International Pharmacopoeia*. 11th ed. Geneva: World Health Organization; 2023.

14. *Radiopharmaceutical Preparations*, *Chinese Pharmacopoeia*; 2015.

15. *Radiopharmaceutical Preparations*, *Japanese Pharmacopoeia*. 18th ed.; 2021.

16. Khurshid SJ, Sadiq MZ. Quality assurance in nuclear medicine--biological quality control of radiopharmaceuticals. *Pak J Pharm Sci*. 1996;9(1):43-54.

17. Maltby P, Liverpool (UK). *Radiopharmacy Quality Control*. Available from: https://www.eanm.org/content-eanm/uploads/cte-archive/2009/cte-6/cte6_3.pdf [Last accessed on 2023 Nov 20].

18. *Radiopharmaceuticals: Directives 65/65/EEC, 75/318/EEC as amended, Directive 89/343/EEC*; 1990.

19. *Radiopharmaceuticals: Directives 65/65/EEC, 75/318/EEC as amended, Directive89/343/EEC*; 1990.

20. The International Pharmacopoeia. *Radiopharmaceuticals General Monograph, Working Document QAS/13.542/Rev.2*; 2017. Available from: https://www.who.int/docs/default-source/medicines/norms-and-standards/current-projects/qas13-542rev2-general-chapter-radiopharmaceuticals.pdf?sfvrsn=516dbf81_2 [Last accessed on 2023 Nov 20].

21. Loveless VS. *Quality Control of Compounded Radiopharmaceuticals*. Vol. 15., Lesson 3. United States: UNM College of Pharmacy; 2009.

22. Gillings N, Hjelstuen O, Ballinger J, *et al*. Guideline on current good radiopharmacy practice (cGRPP) for the small-scale preparation of radiopharmaceuticals. *EJNMMI Radiopharm Chem*. 2021;6:8. doi: 10.1186/s41181-021-00123-2

23. Saha GB. Quality control of radiopharmaceuticals. In: *Fundamentals of Nuclear Pharmacy*. New York: Springer; 1998. doi: 10.1007/978-1-4757-2934-4_8

24. Wind K. The sterility testing of radiopharmaceuticals. In: *Radiopharmacy and Radiopharmacology Yearbook*; 1985. Available from: https://www.taylorfrancis.com/chapters/edit/10.4324/9781315074771-2/sterility-testing-radiopharmaceuticals-kevin-wind [Last accessed on 2023 Nov 20].

25. Sharma S, Jain S, Baldi A, Singh RK, Sharma RK. Intricacies in the approval ofradiopharmaceuticals - regulatory perspectives and the way forward. *Curr Sci*. 2019;116(1):47-55.

doi: 10.18520/cs/v116/i1/47-55

26. *Sterility*, *Indian Pharmacopoeia*. 9th ed. Ghaziabad: Indian Pharmacopoeia Commission; 2022.

27. *Sterility*, *British Pharmacopeia*. Ghaziabad: Indian Pharmacopoeia Commission; 2023.

28. *Sterility*, *United States Pharmacopeia*. Rockville, MD: The United States Pharmacopoeial Convention; 2022.

29. *Sterility*, *The International Pharmacopoeia*. 11th ed. Geneva: World Health Organization; 2023.

30. *Sterility Testing of Radiopharmaceuticals*. Available from: https://www.cup-freitag.de/en/radioster/sterile-testing-of-radiopharmaceuticals [Last accessed on 2023 Nov 20].

31. Indian Pharmacopoeia. *Approach to Alternative Microbiological Methods*. 9th ed. Ghaziabad: Indian Pharmacopoeia Commission; 2022.

32. *Alternative Methods for Control of Microbiological Quality*, *British Pharmacopeia*; 2023.

33. *Validation of Alternative Microbiological Methods*, *United States Pharmacopeia*. Rockville, MD: The United States Pharmacopoeial Convention; 2022.

34. Arjun C, Karkhanis B, Korde AG. Bacterial *Endotoxin Testing* of *Injectable Radiopharmaceuticals*: BRIT *Experience*. Austria: International Atomic Energy Agency (IAEA); 2020. Available from: https://inis.iaea.org/search/search.aspx?orig_q=RN:52009402 [Last accessed on 2023 Nov 20].

35. *Bacterial Endotoxin*, *Indian Pharmacopoeia*. 9th ed. Ghaziabad: Indian Pharmacopoeia Commission; 2022.

36. *Bacterial Endotoxin*, *British Pharmacopeia*; 2023.

37. *Bacterial Endotoxin*, *United States Pharmacopeia*. Rockville, MD: The United States Pharmacopoeial Convention; 2022.

38. *Bacterial Endotoxin*, *The International Pharmacopoeia*. 11th ed. Geneva: World Health Organization; 2023.

39. *Importance of the LAL Assay for Testing Radiopharmaceuticals. Radiopharmaceuticals in Modern Medicine*. Available from: https://www.wakopyrostar.com/blog/kit-lal/post/importance-of-the-lal-assay-for-testing-radiopharmaceuticals [Last accessed on 2023 Nov 20].

40. *Rabbit Pyrogen Test, Indian Pharmacopoeia*. 9th ed. Ghaziabad: Indian Pharmacopoeia Commission; 2022.

41. *Methods of Preparation of Sterile products, British Pharmacopeia*; 2023.

42. *GMP Guidelines Uncategorized. Parametric Release by API FIRST0*. Available from: https://www.apifirst.in/2020/12/08/parametric-release [Last accessed on 2020 Dec 08].

43. Sharma S, Rajan MG, Baldi A, Singh RK, Sharma RK. The regulatory dilemma for import of radiopharmaceuticals in India. *Curr Sci*. 2019;116:1787-1789.

44. European Medicines Agency. *Veterinary Medicines and Inspections*. In: *Guideline on Parametric Release*: *EMEA/CVMP/QWP/339588/2005-Consultation*. London: Committee for Medicinal Products for Veterinary Use; 2006.

45. *Parametric Release and Real-Time Release Testing*. Pharmaceutical Technology; 2012.

ACCSCIENCE PUBLISHING

Advances in Radiotherapy & Nuclear Medicine

REVIEW ARTICLE

Advances in molecular imaging for early detection of lung cancer

Dongjun Li[1]*, Mimba Brenda-Ruth[1], Bamishaye Oluwabukola[1], and Jinghui Peng[2]

[1]Department of Chemistry, Georgia State University, Atlanta, Georgia, United States of America

[2]Hubei Key Laboratory of Cell Homeostasis, College of Life Sciences, Wuhan University, Hubei, Wuhan, China

Abstract

Lung cancer remains the second most commonly diagnosed cancer globally and the leading cause of cancer-related deaths, a trend consistent in the United States as of 2023. One of the key reasons for the high mortality rate of lung cancer is its poor prognosis, with 75% of patients diagnosed at middle and advanced stages. Early detection of subclinical lung cancer, metastases, and their fibrotic stroma is crucial for enabling timely treatment, reducing reoccurrence, and stratifying patients. Current diagnostic methods, such as lung biopsy for patients with small nodules, are highly invasive and technically challenging. The radiological gold standard, computed tomography (CT), is associated with ionizing radiation. However, positron emission tomography (PET) and magnetic resonance imaging (MRI) have emerged as promising methodologies for lung cancer diagnosis. PET tracers with a variety of targeting mechanisms are currently under development in human trials. With advancements in hardware and software over the past decades, radiation-free MRI has been clinically and preclinically validated as an alternative to CT. Moreover, novel-targeted MRI contrast agents have been tested in animal models and show strong translational potential. In this review, we summarize the state-of-the-art progress in molecular imaging for the early detection of lung cancer and its potential biomarkers.

Keywords: Early detection; Lung cancer; Molecular imaging; Magnetic resonance imaging; Positron emission tomography; Computed tomography

***Corresponding author:**
Dongjun Li
(dli20@gsu.edu)

Citation: Li D, Brenda-Ruth M, Oluwabukola B, Peng J. Advances in molecular imaging for early detection of lung cancer. *Adv Radiother Nucl Med.* 2024;2(3):4173. doi: 10.36922/arnm.4173

Received: July 9, 2024

Accepted: August 6, 2024

Published Online: September 19, 2024

1. Introduction

As of 2020, lung cancer remained the second most commonly diagnosed cancer and the leading cause of cancer-related deaths globally, accounting for approximately one in ten of all diagnosed cancers and contributing to one in five cancer-related deaths.[1] This trend remained consistent in the United States in 2023.[2] Non-small-cell lung cancer (NSCLC) and small-cell lung cancer (SCLC) are usually diagnosed at an advanced stage, often resulting in a poor prognosis.[3-6] One of the major reasons for the high mortality rate of lung cancer is the tendency of advanced-stage disease to metastasize to distant organs, complicating treatment efforts.[7-9] Early detection of lung cancer has been shown to significantly improve survival rates compared to late-stage diagnosis, allowing for timely

interventions such as surgery resection, chemotherapy, and radiotherapy.[6,10,11] Therefore, the detection of subclinical lung cancer and metastases is essential for timely treatment, reducing reoccurrence, and improving patient stratification.

Surgical lung biopsies, the pathological gold standard for early-stage lung cancer, are very challenging in patients with small nodules. These procedures are invasive, prone to high sampling errors, and often associated with complications.[12] Computed tomography (CT), the radiological gold standard, is commonly utilized for early lung cancer detection.[6,10,11] However, CT's accuracy in detecting malignant tumors is limited, as it provides minimal molecular-level information about tumor microenvironment (TME) changes related to disease invasion, progression, and regression.[13-15] There is an urgent, unmet medical need for early and noninvasive detection of subclinical lung cancer and metastasis, as well as for monitoring their progression and regression. This review summarizes current clinical and preclinical studies to highlight progress (Table 1) and challenges in molecular imaging for the early detection of lung cancer, along with their targeting mechanisms.

2. CT

CT scans have long been applied to produce high-resolution cross-sectional images, enabling the non-invasive separation, screening, and quantitative assessment of various tissue types, including bones, adipose tissue, skeletal muscle, and other organs. CT scanning has been extensively used as the benchmark reference for validating alternative field methods in human body compartment evaluation.[35] By comparing the topographical images obtained from CT scans to cross-sectional areas of tissues, data show high accuracy and reproducibility in distinguishing healthy tissue from tumor tissue in mouse models with induced tumors.[36] Routine CT scans are applied as a quantitative tool for detecting and monitoring lung cancer in both clinical settings and preclinical animal studies. Major findings show the efficacy of CT in detecting lung cancer at an early stage, especially for adenocarcinoma.[37]

2.1. Micro-computed tomography (micro-CT) and low-dose CT for non-invasive lung cancer imaging

High-resolution micro-CT has emerged as a powerful tool for non-invasively visualizing and monitoring lung cancer development in live mice. Low-dose computed tomography (LDCT) has been effectively applied for lung cancer screening in humans. CT is effective at both early and advanced stages of the disease, as validated against traditional histological analysis. Notably, micro-CT can distinguish lung tumors as small as 200 μm from healthy tissue in a mouse model with induced tumors. This remarkable capability is achieved with a low radiation dose (0.4 Gy/15 min) and high spatial resolution (15 μm).[38]

CT primarily targets high-risk patients, placing a significant burden on health-care systems. Although

Table 1. Summary of various modalities and agents for medical imaging of pulmonary disease

Modality	Agent	Distribution type/target	Indication	Clinical detection limit	Preclinical detection limit
CT (LDCT)[16]	N/A	N/A	Lung cancer; lung fibrosis	4.0 – 5.0 mm	0.2 mm
CT	Iopromide; Iodixanol; Iohexol[17-19]	Extracellular fluid	Lung cancer; vascular and cardiovascular conditions	0.5 – 2.0 mm	N/A
PET	^{18}F-FDG[20]	Glucose metabolism	Inflammation; tumor metabolism	4 mm	N/A
PET	^{68}Ga-FAPI-04[21]	FAP	Cancer-associated fibroblasts	N/A	3 – 5 mm
PET	^{18}F-FLT[22]	Thymidine kinase	Cell proliferation	N/A	N/A
PET	^{89}Z-Nivolumab[23] ^{89}Z-Pembrolizumab[24]	PD-1	PD-1 expression	N/A	N/A
PET	^{68}Ga-DOTATATE[25]	Somatostatin receptors	Neuroendocrine tumors	N/A	N/A
MRI (T1W, DW, UTE)[26-29]	N/A	N/A	Lung cancer; lung fibrosis	3.0–4.0 mm	3 – 4 mm
MRI	EP-3533;[30] hProCA[32].collagen[31]	Collagen type I	Lung fibrosis	N/A	N/A
MRI	GdOA;[32] Gd-CHyd;[33] MnL[34]	Allysine; aldehyde	Lung fibrogenesis	N/A	N/A

Abbreviation: CT: Computed tomography; DW: Diffusion-weighted; FAP: Fibroblast activation protein; FAPI: Fibroblast activation protein inhibitor; FDG: Fluorodeoxyglucose; FLT: Fluorothymidine; LDCT: Low-dose computed tomography; MRI: Magnetic resonance imaging; N/A: Not applicable; PD-1: Programmed cell death protein 1; PET: positron emission tomography; T1W: T1-weighted; UTE: Ultrashort echo time.

recent studies suggest that LDCT reduces the mortality rate in high-risk lung cancer patients by 20%, the cost-effectiveness and risk of overdiagnosis might be as high as 25%.[39] Even the most effectively designed CT screening programs will capture only a small percentage of all lung cancers, given that only individuals at the highest risk are eligible for screening. Brodersen *et al*.[15] reported an average of 49% overdiagnosis of lung cancer using LDCT, corresponding to an absolute risk increase of 20 cancers per 1000 people screened with this method. There is a need for biomarkers to aid in selecting appropriate candidates for LDCT screening and in identifying which nodules detected by LDCT are likely malignant.

Several biomarkers have been proposed as independent tools for diagnosing lung cancer. In 2022, Pastorino *et al*. reported the implementation of a combination of LDCT and a blood biomarker panel for screening, which targets screening intervals based on initial risk prediction; this provides a basis for the adoption of personalized screening and prevention programs.[40]

Deep learning techniques have been intensively researched to aid in interpreting data from CT scans for lung cancer detection. This method utilizes vast amounts of data to identify connections and patterns that may be too complex for traditional machine-learning techniques to interpret. Deep learning methods have been applied to segment the images into anatomical components, allowing for the automatic identification of lesions, nodules, and tumors. This method is valuable because it can adapt a wide range of data with varying resolutions, noise levels, and contrast, providing real-time data processing to improve diagnostic accuracy and consistency, thereby reducing the likelihood of false positives and false negatives.[41-44]

2.2. Limitations of CT scans

CT delivers radiation doses ranging from 0.22 to 0.76 Gy per scan.[45] While these doses are significantly lower than those used for lung cancer treatment, it is important to acknowledge the potential impact of this radiation on tumor growth, particularly when performing repeated imaging.[46,47] Furthermore, the cumulative effect of repeated CT scans on the immune system must be considered when developing pharmacological studies that span significant periods.[47]

The duration of exposure and the scanning material directly influence the true resolution; when the exposure time is reduced to lower the radiation dose, a significant decrease in the signal-to-noise ratio and resolution is observed. Inherent motion artifacts caused by respiration and internal organ movement impair the achievement of the highest feasible resolution. The maximum resolution in a CT scan is only achievable for motionless subjects, which may not be applicable for live imaging; the effect of motion artifacts may impair imaging quality.[35] Balancing scan speed, dose, and diagnostic accuracy is crucial in developing an effective method for the application of CT. Awareness of the radiation risks has led to the development of various dose reduction methods up to 1 mSv.[48]

3. Positron emission tomography (PET)

PET is a non-invasive imaging modality that utilizes radiotracers for the diagnosis and staging of cancer.[49] PET has been shown to be more accurate than CT in differentiating benign from malignant lesions as small as 1 cm and can better identify regional or distant metastases compared to conventional imaging modalities.[50,51] PET is particularly advantageous in lung cancer diagnosis due to its superior ability to detect functional abnormalities by acquiring metabolic images of the entire body.[52-54] Furthermore, PET exhibits higher accuracy than conventional imaging in assessing therapeutic response, as it can identify functional abnormalities before they manifest morphologically on conventional imaging. It is also effective in detecting viable tumor cells in instances where other imaging modalities are constrained by fibrosis.[55] Consequently, PET combined with CT (PET/CT) or PET/magnetic resonance imaging (PET/MRI) is often used for staging, follow-up, and treatment evaluation in different types of malignancies.[56]

3.1. Imaging with glucose metabolic biomarker

^{18}F-fluoro-2-deoxy-D-glucose (^{18}F-FDG) is a glucose analog and the most commonly used PET radiotracer for lung cancer detection. The mechanism of ^{18}F-FDG relies on the differential glucose metabolism between benign and malignant cells. Malignant cells exhibit a higher rate of glycolysis compared to benign cells, attributed to their increased expression of glucose transporters.[50]

Similar to glucose, ^{18}F-FDG is taken up by malignant cells and phosphorylated by hexokinase to ^{18}F-FDG-6-phosphate. ^{18}F-FDG-6-phosphate becomes sequestered in malignant cells because it is not a substrate for the next step in the glycolytic pathway.[51] The overexpression of glucose transporters, upregulation of hexokinase, and downregulation of phosphatase activity in malignant cells facilitate the accumulation of ^{18}F-FDG, enabling differentiation between malignant tissue and normal lung tissue. ^{18}F-FDG has been reported to have a sensitivity between 94% and 96%, a specificity between 78% and 86%, and an accuracy between 90% and 94% in differentiating benign from malignant lung nodules.[57,58] As a result, FDG-PET is commonly used for the diagnosis and staging of lung cancer.

While ^{18}F-FDG has been highly beneficial, one of its primary limitations is its significant uptake in normal tissue, which can lead to false-positive results.[52] In addition, the specificity of ^{18}F-FDG-PET is reduced in regions affected by infectious lung diseases. Furthermore, the brain, a common site for lung cancer metastasis, inherently exhibits high ^{18}F-FDG uptake, resulting in low contrast and making it difficult to distinguish metastatic lesions. Consequently, there has been significant effort over the past decades to develop novel PET tracers with enhanced sensitivity and specificity for lung cancer imaging.[59]

3.2. Targeting fibroblast activation protein (FAP)

Recently, cancer-associated fibroblasts (CAFs) have emerged as a major target for diagnosis and antitumor therapy. These fibroblasts express FAP, which is minimally expressed in healthy tissue but is frequently present in many tumors. FAP activity is believed to contribute to tumor development, migration, and metastasis,[21,60] and FAP itself is a potential target for cancer treatment.[61] Radiolabeled FAP inhibitors (FAPIs) linked to radionuclides have been developed for PET imaging that targets FAP expression in CAFs. These FAPIs are often labeled with radionuclides like gallium-68, exhibiting a high tumor-to-background ratio and rapid renal clearance.[59]

A few studies have investigated the effectiveness of ^{68}Ga-FAPI-04 as a PET radiotracer in lung cancer detection. In a 2019 study, Kratochwil *et al.* examined the uptake of ^{68}Ga-FAPI-04 in various primary, metastatic, and recurring cancers. Their findings showed a high maximum standardized uptake value (SUV_{max}) (> 12) for lung cancer and low background activity (1.6 SUV_{max} for blood and 1.4 SUV_{max} for muscles). Consequently, the tumor-to-background ratios for lung cancer and other cancers with high uptake exceeded 6. These high tumor-to-background ratios result in excellent image contrast for most of the evaluated patients.[62]

Another study conducted by Giesel *et al.* in 2021 compared the tumor uptake and organ biodistribution between ^{68}Ga-FAPI PET/CT and ^{18}F-FDG PET/CT in 71 patients with different cancer types, including nine patients with lung cancer. The study found that ^{68}Ga-FAPI and ^{18}F-FDG had comparable uptakes in primary tumors and metastasis. In addition, ^{68}Ga-FAPI exhibited lower uptake in most normal tissue compared to ^{18}F-FDG.[63] These findings indicate that ^{68}Ga-FAPI PET/CT imaging achieves high image contrast due to significant uptake in diverse types of cancers, comparable to imaging with ^{18}F-FDG. However, the lower background uptake of ^{68}Ga-FAPI in most normal tissues results in an equal or higher tumor-to-background ratio for PET imaging with ^{68}Ga-FAPI.

3.3. Imaging with thymidine cell proliferation biomarker

Another approach to lung cancer imaging involves targeting uncontrolled cell proliferation, which is often seen in many malignant lesions. 3-Deoxy-3-^{18}F-fluorothymidine (^{18}F-FLT) is a thymidine analog effective for visualizing and quantifying cell proliferation due to its interaction with the enzyme thymidine kinase 1 (TK1). FLT is phosphorylated by TK1 during the S-phase of the cell cycle, which traps it intracellularly. Unlike thymidine, FLT is not incorporated into DNA, and its uptake is correlated with increased activity of TK1 and cell proliferation.[64,65] In a 2016 study, Wang *et al.* compared ^{18}F-FDG and ^{18}F-FLT in lung cancer PET/CT imaging. They observed significantly higher ^{18}F-FLT uptake in lung cancer lesions and a higher tumor-to-background ratio of ^{18}F-FDG imaging in xenografts compared to ^{18}F-FLT. The study reported a high specificity (79%) and low sensitivity (71%) for ^{18}F-FLT as compared to ^{18}F-FDG, which showed 67% specificity and 89% sensitivity as reported by Wang *et al.* These results suggest that while ^{18}F-FDG is superior for detecting lung cancer, ^{18}F-FLT's higher specificity could make it more effective for distinguishing lung cancer nodules from other malignancies.[22,66,67] Given ^{18}F-FLT's higher specificity and ^{18}F-FDG's higher sensitivity, studies have explored the diagnostic potential of combining both tracers. In a multicenter study assessing the diagnostic value of dual tracers in lung cancer, the sensitivity of ^{18}F-FDG increased from 87% to 100% when combined with ^{18}F-FLT, and the specificity of ^{18}F-FLT increased from 77% to about 90% when combined with F-FDG.[68]

3.4. Targeting programmed death receptor-1 (PD-1)

Immuno-positron emission tomography (immunoPET) is an imaging modality that has undergone significant advancements in recent years. This approach integrates the specificity of antibodies with the superior sensitivity of PET to visualize antigen expression. Various antibodies and radionuclides have been investigated to develop immunoPET probes, with zirconium-89 (^{89}Zr) being the most commonly used due to its long half-life.[69,70]

One frequently targeted cancer biomarker in immunoPET is PD-1. PD-1 is a regulatory protein, and its ligands, programmed death ligand 1 (PD-L1) and programmed death ligand 2, are overexpressed in several cancers, including NSCLC, making them predictive biomarkers for these cancers.[71] Monoclonal antibodies that block PD-1, such as pembrolizumab, are routinely used in treating NSCLC and have recently been evaluated as an immunoPET tracer. In a study by Kok *et al.*, ^{89}Zr-labeled pembrolizumab was used in PET imaging of 11 melanoma

and 7 NSCLC patients to measure tumor uptake and whole-body biodistribution before treatment with a PD-1 antibody. They reported no significant difference in tracer uptake between patients with melanoma and those with NSCLC, and a mean SUV_{max} of 6.5 was observed. The study demonstrated that ^{89}Zr-labeled pembrolizumab PET imaging is a safe, non-invasive modality for visualizing PD-1 biodistribution.[24] Another study by Niemeijer *et al.* compared PET imaging with the PD-1 targeting drug ^{89}Zr-Nivolumab and PD-L1 targeting drug ^{18}F-BMS-986192 in 13 patients with advanced NSCLC. Both tracers provided sufficient tumor-to-background contrast for effective tumor visualization. The study found that patients with tumor biopsies showing aggregates of PD-1 had higher ^{89}Zr-Nivolumab uptake, indicating a correlation between PD-L1 expression and ^{89}Zr-Nivolumab uptake.[23]

3.5. Targeting somatostatin receptor (SSTR)

SSTRs are G protein-coupled receptors that modulate apoptosis and regulate cell proliferation. These receptors are expressed in normal cells and various malignant cells, including neuroendocrine tumors (NET), SCLC, and NSCLC.[72] The most widely used PET tracer for imaging SSTRs is ^{68}Ga-DOTATATE, which has shown a high affinity for SSTR type 2. This high affinity results in superior imaging quality, shorter image acquisition times, and lower radiation doses.[25] In a 2023 study, Hu *et al.* compared the efficacy of ^{68}Ga-DOTATATE and ^{18}F-FDG PET/CT in diagnosing and staging well-differentiated and poorly differentiated NET. They reported that ^{18}F-FDG PET/CT accurately detected 23 out of 27 patients confirmed by pathology to have NET, with a sensitivity of 85.2% and a specificity of 37.5%. In contrast, ^{68}Ga- DOTATATE correctly detected all 27 patients, demonstrating a sensitivity of 100% and a specificity of 93.8%, which was higher than that of ^{18}F-FDG PET/CT.[73] Another study by Walker *et al.* assessed the imaging efficiency of ^{68}Ga DOTATATE PET/CT in detecting indeterminate pulmonary nodules and lung cancer. Their results showed that ^{68}Ga- DOTATATE was more specific (94%) and less sensitive (73%) than ^{18}F-FDG (81% specificity and 93% sensitivity) in detecting indeterminate pulmonary nodules and lung cancer. In addition, uptake in normal lung tissue was low and similar between ^{68}Ga-DOTATATE and ^{18}F-FDG.[72]

3.6. Limitations of PET scans

The primary limitation of PET imaging is its substantially lower resolution and limited anatomical detail.[74] This results in poor localization of lesions and inadequate demarcation of lesion borders. In addition, while ^{18}F-FDG-PET is highly beneficial, it has been associated with false-positive findings due to inflammatory cells exhibiting high glucose uptake, as well as false-negative findings for small lesions (<5 mm).[55] To achieve more accurate diagnoses, the integration of two imaging modalities, such as PET/CT or PET/MRI, is often necessary.[75]

4. MRI

Compared to CT and PET, MRI-based early lung cancer detection is free of ionizing radiation, allowing a wide variety of longitudinal scans[76] and avoiding radiation-induced cancer.[77,78] MRI offers several key advantages, including high spatial and temporal resolution, which allows for detailed visualization of both anatomy (structure) and function (activity) within the body. In addition, the wide field of view of MRI and its multi-planar acquisition permit image capture from various angles, providing a comprehensive understanding of the scanned area.[79] However, the application of MRI to the lungs has its limitations.[76,80,81] First, the lung has a limited signal source due to its low tissue density. Second, the interface between air and lung tissue results in a short T2*, making it difficult for traditional spin echo pulse sequences to capture the rapidly decaying magnetic resonance (MR) signal in the lung. Third, respiratory and cardiac motion requires breath-holding or gating during an MRI scan to obtain motion-free images. To address these limitations, continuous efforts have been made to optimize and apply different MRI pulse sequences for lung MRI. Beyond improving MRI pulse sequences, new contrast-enhanced molecular MRI has shown strong translational applications in early lung cancer detection.

4.1. Conventional MRI

Conventional MRI pulse sequences, such as diffusion-weighted (DW) MRI, along with T1-weighted (T1W) and T2-weighted (T2W) MRI sequences, have been studied to detect lung cancer nodules. As mentioned above, lung parenchyma appears dark in MR images due to low proton density and short T2*. Therefore, solid tumor masses appear bright in both T1W and T2W images due to higher proton density, while tumors also appear bright in DW images due to the faster diffusivity of water molecules within the tissue.[82] Conventional lung MRI has been reported in clinical settings to detect malignant lung tumors. Qi *et al.*[83] found that DW MRI outperformed CT in distinguishing between lung cancer and post obstructive lobar collapse, and the combination of T2W and DW MRI further improved the diagnosis of early-stage lung cancer. Satoh *et al.*[84] reported that DW MRI could be used to differentiate between malignant and benign tumors. Coolen *et al.*[85] reported that DW MRI is a promising tool for detecting malignant pleural disease, outperforming FDG-PET/CT. Hu *et al.*[86] reported that T1W and T2W

MRI detected early-stage primary pulmonary tumors in a human study involving 21 NSCLC patients. Moreover, T1W and T2W MRI were able to assess the heterogeneity and biological behaviors that correlated with lung cancer stage.[86] In preclinical settings, lung MRI has been developed as a standard protocol to longitudinally monitor mouse lung tumor progression and regression using T1W and T2W imaging.[47,87] A combination of T1W, T2W, and DW MRI has repeatedly shown equivalent or superior lung nodule detection capability compared to CT or FDG-PET.[27,76,82,83,88,89]

4.2. Ultrashort echo time (UTE) MRI

Although conventional MRI pulse sequences have shown CT-comparable detection of lung cancer, they are limited to detecting signals from tissue or lesions with long T2 and higher proton density, such as tumor mass.[90] The advancement of the UTE MRI pulse sequence has enabled imaging of lung parenchyma along with its abnormalities using an extremely short echo time to capture the rapidly decaying T2 signal.[81,90-92] Meanwhile, UTE MRI is intrinsically insensitive to motion effect, that is, no gating or breath-holding is required during UTE MRI scans. With recent upgrades in hardware and software, UTE pulse sequences have been implemented in both clinical and preclinical settings over the past decade.[76,93-95] In recent human studies, Ohno *et al.*[27,96] reported that the UTE pulse sequence was effective in detecting lung cancer nodules as small as 4 mm, which is comparable to standard- or reduced-dose CT. Sanchez *et al.*[29] performed T1W, T2W, and UTE MRI on 36 patients and found that lung nodules larger than 4 mm could be accurately detected. UTE MRI has emerged as a promising alternative to conventional MRI pulse sequences for lung imaging, achieving comparable imaging capability to CT without the need for radiation or breath-holding.[29,97] Moreover, it allows for the detection of lung tissue abnormalities such as fibrosis[98,99] and early-stage lung cancer nodules.

4.3. Contrast-enhanced molecular MRI

About one-third of clinical MRI scans are administered with MRI contrast agents, as these agents provide additional functional information.[100,101] Dynamic contrast-enhanced (DCE) MRI involves the injection of MRI contrast agents such as gadolinium-based contrast agents (GBCAs). GBCAs increase the contrast between healthy and abnormal tissue by shortening the relaxation time of water protons. Due to tumor angiogenesis and the richer vasculature of tumors compared to the lung parenchyma, extracellular fluid GBCAs enhance lung tumors during the blood pool phase.[100,101] Differences in vascularization patterns between different lung tumor subtypes enable DCE MRI to distinguish benign lung tumors from malignant ones, as well as adenocarcinoma from squamous cell carcinoma.[102,103] Investigational superparamagnetic iron oxide nanoparticle-based MRI contrast agents have also been reported to detect lung tumor nodules in a mouse study using T2W MRI.[104]

To efficiently and precisely improve the early detection of lung cancer with higher specificity and sensitivity, molecularly targeted probes have been engineered by combining MRI contrast agents with biomarker-targeting moieties. Although no molecular targeting MRI contrast agent has been approved by the united states food and drug administration to date,[100] tremendous effects have been made to develop targeted MRI probes for clinical and preclinical MRI. Their clinical translation could provide early detection, staging, prognosis, and insight into complex biological activities.

Collagen type I is an extracellular matrix protein that is overexpressed and deposited during the progression of various diseases, including lung fibrosis and lung TME.[105] The expression of collagen is also crucial in nodule formation, cancer permeability, metastasis migration, and therapeutic responses.[106-111] Caravan *et al.*[30,32-34] and Ibhagui *et al.*[31] have developed several probes to report collagen bioactivity for the detection of lung fibrosis or fibrogenesis. The study of lung fibrosis is deeply related to lung cancer, as they share common biological pathways and biomarkers.[112] Collagen-targeted MRI contrast agents can also be applied to detect lung cancer, as lung TME overexpress collagen.[107,109]

5. Potential targeting biomarkers for early lung cancer detection

Lung cancer is a heterogeneous disease at both the cellular and histological levels.[113] Identifying specific biomarkers according to the classification of lung cancer is crucial for better understanding its occurrence and development[114] and has significant implications for the early detection and treatment decisions.

In addition to type I collagen, several other collagen types have been shown to be overexpressed in various tumors, with increased collagen expression usually associated with tumor progression and poor prognosis. Type XI collagen α1 chain (COL11A1) is upregulated in both lung adenocarcinoma and NSCLC[115] and plays an important role in the proliferation, migration, and invasion of NSCLC, as well as in resistance to cisplatin.[116] This indicates that COL11A1 is a promising biomarker for lung cancer.[117-121] The type VI collagen α6 gene (*COL6A6*), a tumor suppressor in NSCLC, can inhibit the tumorigenesis and progression of NSCLC by regulating the JAK signaling

pathway.[122] It is positively correlated with immune cell infiltration and is involved in tumor immunity, suggesting that COL6A6 may be a potential immunotherapeutic target for lung adenocarcinoma.[123]

Matrix metalloproteinase-9 is one of the key enzymes involved in breaking down the extracellular matrix by catalyzing collagen, elastin, fibrin, and other components. It promotes the invasion and metastasis of malignant cells and is a risk factor for advanced tumor stages and poor prognosis,[124,125] highlighting its potential as a therapeutic target for NSCLC patients.[126,127] An increasing number of novel biomarkers, closely associated with histological types and metastasis, are being studied for lung cancer detection and therapy.[128-130]

6. Conclusions and future directions

As the radiological gold standard, CT continues to play an irreplaceable role in lung cancer diagnosis and screening due to its high spatial resolution, availability, and lower cost. The application of artificial intelligence in interpreting CT images is being explored to improve diagnostic accuracy and patient stratification. FDG-PET is widely used in clinics for the diagnosis and staging of lung cancer due to its accuracy in distinguishing between benign and malignant lung tumors. The development of various PET tracers targeting different biomarkers has shown complementary specificity to FDG-PET imaging and equivalent sensitivity. Continuous efforts will focus on developing novel PET tracers with higher sensitivity and specificity for the early lung cancer detection. Conventional MRI has exhibited comparable lung cancer detection capabilities to CT. UTE MRI overcomes the limitation of conventional MR pulse sequences, achieving CT-like images with detailed anatomical information of the lung tissue. The utilization of novel MRI contrast agents targeting various biomarkers can provide additional biological and molecular/cellular information, enabling radiation-free early detection and assessment of disease severity and progression. The high diagnosis rate and mortality of lung cancer patients will continue to drive advancements in the early detection and therapeutics for lung cancer.

Acknowledgment

None.

Funding

Dongjun Li was sponsored by GSU MBD fellowships, while Bamishaye Oluwabukola was sponsored by GSU CDT fellowships.

Conflict of interest

The authors declare no conflicts of interest.

Author contributions

Conceptualization: Dongjun Li
Writing – original draft: All authors
Writing – review & editing: Dongjun Li

Ethics approval and consent to participate

Not applicable.

Consent for publication

Not applicable.

Availability of data

Not applicable.

References

1. Sung H, Ferlay J, Siegel RL, *et al*. Global cancer statistics 2020: GLOBOCAN estimates of incidence and mortality worldwide for 36 cancers in 185 countries. *CA Cancer J Clin*. 2021;71(3):209-249.

   doi: 10.3322/caac.21660

2. Siegel RL, Miller KD, Wagle NS, Jemal A. Cancer statistics, 2023. *CA Cancer J Clin*. 2023;73(1):17-48.

   doi: 10.3322/caac.21763

3. Herbst RS, Heymach JV, Lippman SM. Lung cancer. *N Engl J Med*. 2008;359(13):1367-1380.

   doi: 10.1056/NEJMra0802714

4. Herbst RS, Morgensztern D, Boshoff C. The biology and management of non-small cell lung cancer. *Nature*. 2018;553(7689):446-454.

   doi: 10.1038/nature25183

5. Wang M, Herbst RS, Boshoff C. Toward personalized treatment approaches for non-small-cell lung cancer. *Nat Med*. 2021;27(8):1345-1356.

   doi: 10.1038/s41591-021-01450-2

6. Blandin Knight S, Crosbie PA, Balata H, Chudziak J, Hussell T, Dive C. Progress and prospects of early detection in lung cancer. *Open Biol*. 2017;7(9):170070.

   doi: 10.1098/rsob.170070

7. Inage T, Nakajima T, Yoshino I, Yasufuku K. Early lung cancer detection. *Clin Chest Med*. 2018;39(1):45-55.

   doi: 10.1016/j.ccm.2017.10.003

8. Tang WF, Wu M, Bao H, *et al*. Timing and origins of local and distant metastases in lung cancer. *J Thorac Oncol*. 2021;16(7):1136-1148.

doi: 10.1016/j.jtho.2021.02.023

9. Tamura T, Kurishima K, Nakazawa K, *et al*. Specific organ metastases and survival in metastatic nonsmallcell lung cancer. *Mol Clin Oncol*. 2015;3(1):217-221.

   doi: 10.3892/mco.2014.410

10. The National Lung Screening Trial Research Team. Results of initial low-dose computed tomographic screening for lung cancer. *N Engl J Med*. 2013;368(21):1980-1991.

    doi: 10.1056/NEJMoa1209120

11. de Koning HJ, van Der Aalst CM, de Jong PA, *et al*. Reduced lung-cancer mortality with volume CT screening in a randomized trial. *N Engl J Med*. 2020;382(6):503-513.

    doi: 10.1056/NEJMoa1911793

12. Han Y, Kim HJ, Kong KA, *et al*. Diagnosis of small pulmonary lesions by transbronchial lung biopsy with radial endobronchial ultrasound and virtual bronchoscopic navigation versus CT-guided transthoracic needle biopsy: A systematic review and meta-analysis. *PLoS One*. 2018;13(1):e0191590.

    doi: 10.1371/journal.pone.0191590

13. Tielemans B, Dekoster K, Verleden SE, *et al*. From mouse to man and back: Closing the correlation gap between imaging and histopathology for lung diseases. *Diagnostics* (*Basel*). 2020;10(9):636.

    doi: 10.3390/diagnostics10090636

14. Zaw Thin M, Moore C, Snoeks T, Kalber T, Downward J, Behrens A. Micro-CT acquisition and image processing to track and characterize pulmonary nodules in mice. *Nat Protoc*. 2023;18(3):990-1015.

    doi: 10.1038/s41596-022-00769-5

15. Brodersen J, Voss T, Martiny F, Siersma V, Barratt A, Heleno B. Overdiagnosis of lung cancer with low-dose computed tomography screening: Meta-analysis of the randomised clinical trials. *Breathe (Sheff)*. 2020;16(1):200013.

    doi: 10.1183/20734735.0013-2020

16. Lancaster HL, Heuvelmans MA, Oudkerk M. Low-dose computed tomography lung cancer screening: Clinical evidence and implementation research. *J Intern Med*. 2022;292(1):68-80.

    doi: 10.1111/joim.13480

17. Lubbers MM, Kock M, Niezen A, *et al*. Iodixanol versus iopromide at coronary CT angiography: Lumen opacification and effect on heart rhythm-the randomized isoCOR trial. *Radiology*. 2018;286(1):71-80.

    doi: 10.1148/radiol.2017162779

18. Jiang Z, Zhang M, Li P, Wang Y, Fu Q. Nanomaterial-based CT contrast agents and their applications in image-guided therapy. *Theranostics*. 2023;13(2):483-509.

    doi: 10.7150/thno.79625

19. Lusic H, Grinstaff MW. X-ray-computed tomography contrast agents. *Chem Rev*. 2013;113(3):1641-1666.

    doi: 10.1021/cr200358s

20. Mahajan S, Barker CA, Singh B, Pandit-Taskar N. Clinical value of 18F-FDG-PET/CT in staging cutaneous squamous cell carcinoma. *Nucl Med Commun*. 2019;40(7):744-751.

    doi: 10.1097/MNM.0000000000001029

21. Loktev A, Lindner T, Mier W, *et al*. A tumor-imaging method targeting cancer-associated fibroblasts. *J Nucl Med*. 2018;59(9):1423-1429.

    doi: 10.2967/jnumed.118.210435

22. Alwadani B, Dall'Angelo S, Fleming IN. Clinical value of 3'-deoxy-3'-[(18)F]fluorothymidine-positron emission tomography for diagnosis, staging and assessing therapy response in lung cancer. *Insights Imaging*. 2021;12(1):90.

    doi: 10.1186/s13244-021-01026-1

23. Niemeijer AN, Leung D, Huisman MC, *et al*. Whole body PD-1 and PD-L1 positron emission tomography in patients with non-small-cell lung cancer. *Nat Commun*. 2018;9(1):4664.

    doi: 10.1038/s41467-018-07131-y

24. Kok IC, Hooiveld JS, van de Donk PP, *et al*. (89) Zr-pembrolizumab imaging as a non-invasive approach to assess clinical response to PD-1 blockade in cancer. *Ann Oncol*. 2022;33(1):80-88.

    doi: 10.1016/j.annonc.2021.10.213

25. Franquet E, Park H. Molecular imaging in oncology: Common PET/CT radiopharmaceuticals and applications. *Eur J Radiol Open*. 2022;9:100455.

    doi: 10.1016/j.ejro.2022.100455

26. Biederer J, Ohno Y, Hatabu H, *et al*. Screening for lung cancer: Does MRI have a role? *Eur J Radiol*. 2017;86:353-360.

    doi: 10.1016/j.ejrad.2016.09.016

27. Ohno Y, Koyama H, Yoshikawa T, *et al*. Standard-, reduced-, and no-dose thin-section radiologic examinations: Comparison of capability for nodule detection and nodule type assessment in patients suspected of having pulmonary nodules. *Radiology*. 2017;284(2):562-573.

    doi: 10.1148/radiol.2017161037

28. Burris NS, Johnson KM, Larson PE, *et al*. Detection of small pulmonary nodules with ultrashort echo time sequences in oncology patients by using a PET/MR system. *Radiology*. 2016;278(1):239-246.

    doi: 10.1148/radiol.2015150489

29. Sanchez F, Tyrrell PN, Cheung P, *et al*. Detection of solid and subsolid pulmonary nodules with lung MRI: Performance of UTE, T1 gradient-echo, and single-shot T2 fast spin echo.

Cancer Imaging. 2023;23(1):17.

doi: 10.1186/s40644-023-00531-4

30. Caravan P, Yang Y, Zachariah R, *et al*. Molecular magnetic resonance imaging of pulmonary fibrosis in mice. *Am J Respir Cell Mol Biol*. 2013;49(6):1120-1126.

doi: 10.1165/rcmb.2013-0039OC

31. Ibhagui OY, Li D, Han H, *et al*. Early detection and staging of lung fibrosis enabled by collagen-targeted MRI protein contrast agent. *Chem Biomed Imaging*. 2023;1(3):268-285.

doi: 10.1021/cbmi.3c00023

32. Waghorn PA, Jones CM, Rotile NJ, *et al*. Molecular magnetic resonance imaging of lung fibrogenesis with an oxyamine-based probe. *Angew Chem Int Ed*. 2017;56(33):9825-9828.

doi: 10.1002/anie.201704773

33. Akam EA, Abston E, Rotile NJ, *et al*. Improving the reactivity of hydrazine-bearing MRI probes for *in vivo* imaging of lung fibrogenesis. *Chem Sci*. 2020;11(1):224-231.

doi: 10.1039/c9sc04821a

34. Ma H, Zhou IY, Chen YI, *et al*. Tailored chemical reactivity probes for systemic imaging of aldehydes in fibroproliferative diseases. *J Am Chem Soc*. 2023;145(38):20825-20836.

doi: 10.1021/jacs.3c04964

35. Mazonakis M, Damilakis J. Computed tomography: What and how does it measure? *Eur J Radiol*. 2016;85(8):1499-1504.

36. Mitsiopoulos N, Baumgartner RN, Heymsfield SB, Lyons W, Gallagher D, Ross R. Cadaver validation of skeletal muscle measurement by magnetic resonance imaging and computerized tomography. *J Appl Physiol* (1985). 1998;85(1):115-122.

doi: 10.1152/jappl.1998.85.1.115

37. Zhao Y, Wang R, Shi F, Wu J, Jiang F, Song Q. Diagnostic efficacy of CT examination on early detection of lung cancer during pandemic of COVID-19. *Diagnostics* (*Basel*). 2022;12(10):2317.

doi: 10.3390/diagnostics12102317

38. De Clerck NM, Meurrens K, Weiler H, *et al*. High-resolution X-ray microtomography for the detection of lung tumors in living mice. *Neoplasia*. 2004;6(4):374-379.

doi: 10.1593/neo.03481

39. Kalinke L, Thakrar R, Janes SM. The promises and challenges of early non-small cell lung cancer detection: Patient perceptions, low-dose CT screening, bronchoscopy and biomarkers. *Mol Oncol*. 2021;15(10):2544-2564.

doi: 10.1002/1878-0261.12864

40. Pastorino U, Boeri M, Sestini S, *et al*. Baseline computed tomography screening and blood microRNA predict lung cancer risk and define adequate intervals in the BioMILD trial. *Ann Oncol*. 2022;33(4):395-405.

doi: 10.1016/j.annonc.2022.01.008

41. Zheng S, Guo J, Cui X, Veldhuis RN, Oudkerk M, Van Ooijen PM. Automatic pulmonary nodule detection in CT scans using convolutional neural networks based on maximum intensity projection. *IEEE Trans Med Imaging*. 2019;39(3):797-805.

doi: 10.1109/TMI.2019.2935553

42. Tian P, He B, Mu W, *et al*. Assessing PD-L1 expression in non-small cell lung cancer and predicting responses to immune checkpoint inhibitors using deep learning on computed tomography images. *Theranostics*. 2021;11(5):2098.

doi: 10.7150/thno.48027

43. Chaunzwa TL, Hosny A, Xu Y, *et al*. Deep learning classification of lung cancer histology using CT images. *Sci Rep*. 2021;11(1):5471.

doi: 10.1038/s41598-021-84630-x

44. Bhattacharjee A, Rabea S, Bhattacharjee A, *et al*. A multi-class deep learning model for early lung cancer and chronic kidney disease detection using computed tomography images. *Front Oncol*. 2023;13:1193746.

doi: 10.3389/fonc.2023.1193746

45. Kirsch DG, Grimm J, Guimaraes AR, *et al*. Imaging primary lung cancers in mice to study radiation biology. *Int J Radiat Oncol Biol Phys*. 2010;76(4):973-977.

doi: 10.1016/j.ijrobp.2009.11.038

46. Kozin SV, Kamoun WS, Huang Y, Dawson MR, Jain RK, Duda DG. Recruitment of myeloid but not endothelial precursor cells facilitates tumor regrowth after local irradiation. *Cancer Res*. 2010;70(14):5679-5685.

doi: 10.1158/0008-5472.CAN-09-4446

47. Krupnick AS, Tidwell VK, Engelbach JA, *et al*. Quantitative monitoring of mouse lung tumors by magnetic resonance imaging. *Nat Protoc*. 2012;7(1):128-142.

doi: 10.1038/nprot.2011.424

48. Lell MM, Wildberger JE, Alkadhi H, Damilakis J, Kachelriess M. Evolution in computed tomography: The battle for speed and dose. *Invest Radiol*. 2015;50(9):629-644.

doi: 10.1097/RLI.0000000000000172

49. Wu Y, Li P, Zhang H, *et al*. Diagnostic value of fluorine 18 fluorodeoxyglucose positron emission tomography/computed tomography for the detection of metastases in non-small-cell lung cancer patients. *Int J Cancer*. 2013;132(2):E37-E47.

doi: 10.1002/ijc.27779

50. Vansteenkiste JF, Stroobants SS. PET scan in lung cancer: Current recommendations and innovation. *J Thorac Oncol*. 2006;1:71-73.

51. Acker M. Utility of FDG PET in evaluating cancers of lung.

J Nucl Med Technol. 2005;33(3):69-74.

52. Zhu J, Pan F, Cai H, *et al.* Positron emission tomography imaging of lung cancer: An overview of alternative positron emission tomography tracers beyond F18 fluorodeoxyglucose. *Front Med* (*Lausanne*). 2022;9:945602.

doi: 10.3389/fmed.2022.945602

53. Farwell MD, Pryma DA, Mankoff DA. PET/CT imaging in cancer: Current applications and future directions. *Cancer*. 2014;120(22):3433-3445.

doi: 10.1002/cncr.28860

54. Sanchez Salmon A, Barandela Salgado J, Ruibal Morell A. PET in abdominal pathology: Advantages and limitations. *Abdom Imaging*. 2006;31(2):174-181.

doi: 10.1007/s00261-005-0384-7

55. Ambrosini V, Nicolini S, Caroli P, *et al*. PET/CT imaging in different types of lung cancer: An overview. *Eur J Radiol*. 2012;81(5):988-1001.

doi: 10.1016/j.ejrad.2011.03.020

56. Krarup MMK, Fischer BM, Christensen TN. New PET tracers: Current knowledge and perspectives in lung cancer. *Semin Nucl Med*. 2022;52(6):781-796.

doi: 10.1053/j.semnuclmed.2022.05.002

57. Deppen SA, Blume JD, Kensinger CD, *et al.* Accuracy of FDG-PET to diagnose lung cancer in areas with infectious lung disease: A meta-analysis. *JAMA*. 2014;312(12):1227-1236.

doi: 10.1001/jama.2014.11488

58. Almuhaideb A, Papathanasiou N, Bomanji J. 18F-FDG PET/CT imaging in oncology. *Ann Saudi Med*. 2011;31(1):3-13.

doi: 10.4103/0256-4947.75771

59. Borgonje PE, Andrews LM, Herder GJM, de Klerk JMH. Performance and prospects of [(68)Ga]Ga-FAPI PET/CT scans in lung cancer. *Cancers* (*Basel*). 2022;14(22):5566.

doi: 10.3390/cancers14225566

60. Huang R, Pu Y, Huang S, *et al*. FAPI-PET/CT in cancer imaging: A potential novel molecule of the century. *Front Oncol*. 2022;12:854658.

doi: 10.3389/fonc.2022.854658

61. Hamson EJ, Keane FM, Tholen S, Schilling O, Gorrell MD. Understanding fibroblast activation protein (FAP): Substrates, activities, expression and targeting for cancer therapy. *Proteomics Clin Appl*. 2014;8(5-6):454-463.

doi: 10.1002/prca.201300095

62. Kratochwil C, Flechsig P, Lindner T, *et al*. (68)Ga-FAPI PET/CT: Tracer uptake in 28 different kinds of cancer. *J Nucl Med*. 2019;60(6):801-805.

doi: 10.2967/jnumed.119.227967

63. Giesel FL, Kratochwil C, Schlittenhardt J, *et al*. Head-to-head intra-individual comparison of biodistribution and tumor uptake of (68)Ga-FAPI and (18)F-FDG PET/CT in cancer patients. *Eur J Nucl Med Mol Imaging*. 2021;48(13):4377-4385.

doi: 10.1007/s00259-021-05307-1

64. Chalkidou A, Landau DB, Odell EW, Cornelius VR, O'Doherty MJ, Marsden PK. Correlation between Ki-67 immunohistochemistry and 18F-fluorothymidine uptake in patients with cancer: A systematic review and meta-analysis. *Eur J Cancer*. 2012;48(18):3499-3513.

doi: 10.1016/j.ejca.2012.05.001

65. Sanghera B, Wong WL, Sonoda LI, *et al*. FLT PET-CT in evaluation of treatment response. *Indian J Nucl Med*. 2014;29(2):65-73.

doi: 10.4103/0972-3919.130274

66. Wang FL, Tan YY, Gu XM, *et al*. Comparison of positron emission tomography using 2-[18F]-fluoro-2-deoxy-D-glucose and 3-deoxy-3-[18F]-fluorothymidine in Lung Cancer Imaging. *Chin Med J* (*Engl*). 2016;129(24):2926-2935.

doi: 10.4103/0366-6999.195468

67. Xu X, Nie L, Yao Y, Tu Y, Zhou J. Pre-radiotherapy assessment of non-small cell lung cancer with 18F-FLT PET/CT or 18F-FDG PET/CT. *Int J Clin Exp Med*. 2016;9:9252-9260.

68. Tian J, Yang X, Yu L, *et al*. A multicenter clinical trial on the diagnostic value of dual-tracer PET/CT in pulmonary lesions using 3'-deoxy-3'-18F-fluorothymidine and 18F-FDG. *J Nucl Med*. 2008;49(2):186-194.

doi: 10.2967/jnumed.107.044966

69. Wei W, Rosenkrans ZT, Liu J, Huang G, Luo QY, Cai W. ImmunoPET: Concept, design, and applications. *Chem Rev*. 2020;120(8):3787-3851.

doi: 10.1021/acs.chemrev.9b00738

70. De Feo MS, Pontico M, Frantellizzi V, Corica F, De Cristofaro F, De Vincentis G. 89Zr-PET imaging in humans: A systematic review. *Clin Trans Imaging*. 2021;10(1):23-36.

doi: 10.1007/s40336-021-00462-9

71. Dolled-Filhart M, Roach C, Toland G, *et al*. Development of a companion diagnostic for pembrolizumab in non-small cell lung cancer using immunohistochemistry for programmed death ligand-1. *Arch Pathol Lab Med*. 2016;140(11):1243-1249.

doi: 10.5858/arpa.2015-0542-OA

72. Walker R, Deppen S, Smith G, *et al*. 68Ga-DOTATATE PET/CT imaging of indeterminate pulmonary nodules and lung cancer. *PLoS One*. 2017;12(2):e0171301.

doi: 10.1371/journal.pone.0171301

73. Hu X, Li D, Wang R, Wang P, Cai J. Comparison of the application of 18F-FDG and 68Ga-DOTATATE PET/CT in neuroendocrine tumors: A retrospective study. *Medicine (Baltimore)*. 2023;102(19):e33726.

doi: 10.1097/MD.0000000000033726

74. Kakhki VRD. Positron emission tomography in the management of lung cancer. *Ann Thorac Med*. 2007;2(2):69-76.

doi: 10.4103/1817-1737.32235

75. Griffeth LK. Use of PETCT scanning in cancer patients technical and practical considerations. *Proc (Bayl Univ Med Cent)*. 2005;18:321-330.

doi: 10.1080/08998280.2005.11928089

76. Hatabu H, Ohno Y, Gefter WB, *et al*. Expanding applications of pulmonary MRI in the clinical evaluation of lung disorders: Fleischner Society position paper. *Radiology*. 2020;297(2):286-301.

doi: 10.1148/radiol.2020201138

77. Rampinelli C, De Marco P, Origgi D, *et al*. Exposure to low dose computed tomography for lung cancer screening and risk of cancer: Secondary analysis of trial data and risk-benefit analysis. *BMJ*. 2017;356:j347.

doi: 10.1136/bmj.j347

78. Shah DJ, Sachs RK, Wilson DJ. Radiation-induced cancer: A modern view. *Br J Radiol*. 2012;85(1020):e1166-e1173.

doi: 10.1259/bjr/25026140

79. Aziz M, Krishnam M, Madhuranthakam AJ, Rajiah P. Update on MR imaging of the pulmonary vasculature. *Int J Cardiovasc Imaging*. 2019;35:1483-1497.

doi: 10.1007/s10554-019-01603-y

80. Krupnick AS, Tidwell VK, Engelbach JA, *et al*. Quantitative monitoring of murine lung tumors by magnetic resonance imaging. *Nat Protoc*. 2012;7(1):128-42.

doi: 10.1038/nprot.2011.424

81. Wild JM, Marshall H, Bock M, *et al*. MRI of the lung (1/3): Methods. *Insights Imaging*. 2012;3:345-353.

doi: 10.1007/s13244-012-0176-x

82. Uto T, Takehara Y, Nakamura Y, *et al*. Higher sensitivity and specificity for diffusion-weighted imaging of malignant lung lesions without apparent diffusion coefficient quantification. *Radiology*. 2009;252(1):247-254.

doi: 10.1148/radiol.2521081195

83. Qi LP, Zhang XP, Tang L, Li J, Sun YS, Zhu GY. Using diffusion-weighted MR imaging for tumor detection in the collapsed lung: A preliminary study. *Eur Radiol*. 2009;19:333-341.

doi: 10.1007/s00330-008-1134-3

84. Satoh S, Kitazume Y, Ohdama S, Kimula Y, Taura S, Endo Y. Can malignant and benign pulmonary nodules be differentiated with diffusion-weighted MRI? *Am J Roentgenol*. 2008;191(2):464-470.

doi: 10.2214/AJR.07.3133

85. Coolen J, De Keyzer F, Nafteux P, *et al*. Malignant pleural disease: Diagnosis by using diffusion-weighted and dynamic contrast-enhanced MR imaging-initial experience. *Radiology*. 2012;263(3):884-892.

doi: 10.1148/radiol.12110872

86. Hu N, Yin S, Li Q, *et al*. Evaluating heterogeneity of primary lung tumor using clinical routine magnetic resonance imaging and a tumor heterogeneity index. *Front Oncol*. 2021;10:591485.

doi: 10.3389/fonc.2020.591485

87. Olson JD, Walb MC, Moore JE, *et al*. A gated-7T MRI technique for tracking lung tumor development and progression in mice after exposure to low doses of ionizing radiation. *Radiat Res*. 2012;178(4):321-327.

doi: 10.1667/rr2800.1

88. Meier-Schroers M, Homsi R, Gieseke J, Schild HH, Thomas D. Lung cancer screening with MRI: Evaluation of MRI for lung cancer screening by comparison of LDCT- and MRI-derived Lung-RADS categories in the first two screening rounds. *Eur Radiol*. 2019;29:898-905.

doi: 10.1007/s00330-018-5607-8

89. Ohno Y, Koyama H, Yoshikawa T, Matsumoto S, Sugimura K. Lung cancer assessment using MR imaging: An update. *Magn Reson Imaging Clin N Am*. 2015;23(2):231-244.

doi: 10.1016/j.mric.2015.01.012

90. Robson MD, Gatehouse PD, Bydder M, Bydder GM. Magnetic resonance: An introduction to ultrashort TE (UTE) imaging. *J Comput Assist Tomogr*. 2003;27(6):825-846.

doi: 10.1097/00004728-200311000-00001

91. Balasch A. Functional lung magnetic resonance imaging with ultra-short echo-time (UTE). 2022.Ýoi: http://dx.doi.org/10.18725/OPARU-42430

92. Ma Y, Jang H, Jerban S, *et al*. Making the invisible visible-ultrashort echo time magnetic resonance imaging: Technical developments and applications. *Appl Phys Rev*. 2022;9(4):041303.

doi: 10.1063/5.0086459

93. Johnson KM, Fain SB, Schiebler ML, Nagle S. Optimized 3D ultrashort echo time pulmonary MRI. *Magn Reson Med*. 2013;70(5):1241-1250.

doi: 10.1002/mrm.24570

94. Bergin CJ, Pauly JM, Macovski A. Lung parenchyma: Projection reconstruction MR imaging. *Radiology*. 1991;179(3):777-781.

doi: 10.1148/radiology.179.3.2027991

95. Geiger J, Zeimpekis KG, Jung A, Mœller A, Kellenberger CJ. Clinical application of ultrashort echo-time MRI for lung pathologies in children. *Clin Radiol*. 2021;76(9):708. e9-e17.

doi: 10.1016/j.crad.2021.05.015

96. Ohno Y, Takenaka D, Yoshikawa T, *et al*. Efficacy of ultrashort echo time pulmonary MRI for lung nodule detection and lung-RADS classification. *Radiology*. 2022;302(3):697-706.

doi: 10.1148/radiol.211254

97. Voskrebenzev A, Vogel-Claussen J. Proton MRI of the lung: How to tame scarce protons and fast signal decay. *J Magn Reson Imaging*. 2021;53(5):1344-1357.

doi: 10.1002/jmri.27122

98. Stecker IR, Freeman MS, Sitaraman S, *et al*. Preclinical MRI to quantify pulmonary disease severity and trajectories in poorly characterized mouse models: A pedagogical example using data from novel transgenic models of lung fibrosis. *J Magn Reson Open*. 2021;6:100013.

99. Babin AL, Cannet C, Gérard C, *et al*. Bleomycin-induced lung injury in mice investigated by MRI: Model assessment for target analysis. *Magn Reson Med*. 2012;67(2):499-509.

doi: 10.1016/j.jmro.2021.100013

100. Wahsner J, Gale EM, Rodríguez-Rodríguez A, Caravan P. Chemistry of MRI contrast agents: Current challenges and new frontiers. *Chem Rev*. 2018;119(2):957-1057.

doi: 10.1021/acs.chemrev.8b00363

101. Li D, Kirberger M, Qiao J, *et al*. Protein MRI contrast agents as an effective approach for precision molecular imaging. *Invest Radiol*. 2024;59(2):170-186.

doi: 10.1097/RLI.0000000000001057

102. Pauls S, Mottaghy FM, Schmidt SA, *et al*. Evaluation of lung tumor perfusion by dynamic contrast-enhanced MRI. *Magn Reson Imaging*. 2008;26(10):1334-1341.

doi: 10.1016/j.mri.2008.04.005

103. Pauls S, Breining T, Muche R, *et al*. The role of dynamic, contrast-enhanced MRI in differentiating lung tumor subtypes. *Clin Imaging*. 2011;35(4):259-265.

doi: 10.1016/j.clinimag.2010.07.002

104. Thangudu S, Yu CC, Lee CL, Liao MC, Su CH. Magnetic, biocompatible FeCO3 nanoparticles for T2-weighted magnetic resonance imaging of *in vivo* lung tumors. *J Nanobiotechnology*. 2022;20(1):157.

doi: 10.1186/s12951-022-01355-3

105. Wahyudi H, Reynolds AA, Li Y, Owen SC, Yu SM. Targeting collagen for diagnostic imaging and therapeutic delivery. *J Control Release*. 2016;240:323-331.

doi: 10.1016/j.jconrel.2016.01.007

106. Erstad DJ, Sojoodi M, Taylor MS, *et al*. Fibrotic response to neoadjuvant therapy predicts survival in pancreatic cancer and is measurable with collagen-targeted molecular MRI. *Clin Cancer Res*. 2020;26(18):5007-5018.

doi: 10.1158/1078-0432.CCR-18-1359

107. Cox TR. The matrix in cancer. *Nat Rev Cancer*. 2021;21(4):217-238.

doi: 10.1038/s41568-020-00329-7

108. Wynn TA, Ramalingam TR. Mechanisms of fibrosis: Therapeutic translation for fibrotic disease. *Nat Med*. 2012;18(7):1028-1040.

doi: 10.1038/nm.2807

109. Xu S, Xu H, Wang W, *et al*. The role of collagen in cancer: From bench to bedside. *J Transl Med*. 2019;17:1-22.

110. Scodellaro R, Bouzin M, Mingozzi F, *et al*. Whole-section tumor micro-architecture analysis by a two-dimensional phasor-based approach applied to polarization-dependent second harmonic imaging. *Front Oncol*. 2019;9:527.

doi: 10.3389/fonc.2019.00527

111. Martins Cavaco AC, Dâmaso S, Casimiro S, Costa L. Collagen biology making inroads into prognosis and treatment of cancer progression and metastasis. *Cancer Metastasis Rev*. 2020;39:603-623.

doi: 10.1007/s10555-020-09888-5

112. Kinoshita T, Goto T. Molecular mechanisms of pulmonary fibrogenesis and its progression to lung cancer: A review. *Int J Mol Sci*. 2019;20(6):1461.

doi: 10.3390/ijms20061461

113. de Sousa VML, Carvalho L. Heterogeneity in lung cancer. *Pathobiology*. 2018;85(1-2):96-107.

doi: 10.1159/000487440

114. Collins LG, Haines C, Perkel R, Enck RE. Lung cancer: diagnosis and management. *Am Fam Physician*. 2007;75(1):56-63.

115. Chong IW, Chang MY, Chang HC, *et al*. Great potential of a panel of multiple hMTH1, SPD, ITGA11 and COL11A1 markers for diagnosis of patients with non-small cell lung cancer. *Oncol Rep*. 2006;16(5):981-988.

116. Shen L, Yang M, Lin Q, Zhang Z, Zhu B, Miao C. COL11A1 is overexpressed in recurrent non-small cell lung cancer and promotes cell proliferation, migration, invasion and drug resistance. *Oncol Rep*. 2016;36(2):877-885.

doi: 10.3892/or.2016.4869

117. Yi X, Luo L, Zhu Y, *et al*. SPP1 facilitates cell migration and invasion by targeting COL11A1 in lung adenocarcinoma. *Cancer Cell Int*. 2022;22(1):324.

doi: 10.1186/s12935-022-02749-x

118. Jin Y, Zhu H, Cai W, *et al*. B-Myb is up-regulated and promotes cell growth and motility in non-small cell lung cancer. *Int J Mol Sci*. 2017;18(6):860.

doi: 10.3390/ijms18060860

119. Turkowski K, Herzberg F, Günther S, *et al*. Fibroblast growth factor-14 acts as tumor suppressor in lung adenocarcinomas.

Cells. 2020;9(8):1755.

doi: 10.3390/cells9081755

120. Sun Y, Liu Z, Huang L, Shang Y. MiR-144-3p inhibits the proliferation, migration and invasion of lung adenocargen cancer cells by targeting COL11A1. *J Chemother*. 2021;33(6):409-419.

doi: 10.1080/1120009x.2021.1906031

121. Chen M, Zhang J, Zeng J, Yu Y, Gu C. Circular circRANGAP1 contributes to non-small cell lung cancer progression by increasing COL11A1 expression through sponging miR-653-5p. *Biochem Genet*. 2023;61(6):2580-2598.

doi: 10.1007/s10528-023-10393-x

122. Qiao H, Feng Y, Tang H. COL6A6 inhibits the proliferation and metastasis of non-small cell lung cancer through the JAK signalling pathway. *Transl Cancer Res*. 2021;10(10):4514-4522.

doi: 10.21037/tcr-21-2002

123. Ma Y, Qiu M, Guo H, *et al*. Comprehensive analysis of the immune and prognostic implication of COL6A6 in lung adenocarcinoma. *Front Oncol*. 2021;11:633420.

doi: 10.3389/fonc.2021.633420

124. Gong L, Wu D, Zou J, *et al*. Prognostic impact of serum and tissue MMP-9 in non-small cell lung cancer: A systematic review and meta-analysis. *Oncotarget*. 2016;7(14):18458-68.

doi: 10.18632/oncotarget.7607

125. Vandooren J, Van den Steen PE, Opdenakker G. Biochemistry and molecular biology of gelatinase B or matrix metalloproteinase-9 (MMP-9): The next decade. *Crit Rev Biochem Mol Biol*. 2013;48(3):222-272.

doi: 10.3109/10409238.2013.770819

126. Qiao X, Gu Y, Yu J, *et al*. The combination of CD147 and MMP-9 serum levels is identified as novel chemotherapy response markers of advanced non-small-cell lung cancer. *Dis Markers*. 2020;2020:8085053.

doi: 10.1155/2020/8085053

127. Han L, Chen Y, Huang N, *et al*. Cancer-educated neutrophils promote lung cancer progression via PARP-1-ALOX5-mediated MMP-9 expression. *Cancer Biol Med*. 2024;21(2):175-92.

doi: 10.20892/j.issn.2095-3941.2023.0248

128. Wang CY, Chen CL, Tseng YL, *et al*. Annexin A2 silencing induces G2 arrest of non-small cell lung cancer cells through p53-dependent and -independent mechanisms. *J Biol Chem*. 2012;287(39):32512-32524.

doi: 10.1074/jbc.M112.351957

129. Ling X, Qi C, Cao K, *et al*. METTL3-mediated deficiency of lncRNA HAR1A drives non-small cell lung cancer growth and metastasis by promoting ANXA2 stabilization. *Cell Death Discov*. 2024;10(1):203.

doi: 10.1038/s41420-024-01965-w

130. Wang Y, Wang Y, Liu W, *et al*. TIM-4 orchestrates mitochondrial homeostasis to promote lung cancer progression via ANXA2/PI3K/AKT/OPA1 axis. *Cell Death Dis*. 2023;14(2):141.

doi: 10.1038/s41419-023-05678-3

ACCSCIENCE PUBLISHING

Advances in Radiotherapy & Nuclear Medicine

PERSPECTIVE ARTICLE

Interventional radiotherapy: CT-sim guided modern minimally invasive technique

Qiman Han†, Yi Chen†, Bin Qiu, Zhe Ji, Ping Jiang*, and Junjie Wang*

Department of Radiation Oncology, Peking University Third Hospital, Beijing, China

Abstract

The concept of interventional radiology was introduced in 1976 as a new diagnostic and therapeutic method, relying on image guidance, such as X-ray, ultrasound, computed tomography (CT), and magnetic resonance imaging. Its indications mainly include obstructive diseases, and to a lesser extent, malignant tumors. Radiotherapy (RT) plays a pivotal role in the comprehensive treatment of cancer. The advent of the CT simulator has significantly enhanced the precision of RT and improvement outcomes and accelerated the development of a series of diagnostic and RT modalities, including puncture biopsy, fiducial marker implantation, high-dose rate after-loading after-loading brachytherapy, and radioactive seed implantation. The innovative concept of image-guidance interventional RT, inspired by interventional radiology, extends the benefits to not only cancer diagnosis but also RT. The image-guidance interventional RT advances the field of RT by expanding its indications and connotation.

Keywords: Intervention; Radiology; Radiotherapy; Carcinoma; Brachytherapy

†These authors contributed equally to this work.

***Corresponding authors:**
Junjie Wang
(junjiewang@pku.edu.cn)
Ping Jiang
(jiangping@bjmu.edu.cn)

Citation: Han Q, Chen Y, Qiu B, Ji Z, Jiang P, Wang J. Interventional radiotherapy: CT-sim guided modern minimally invasive technique. *Adv Radiother Nucl Med.* 2024;2(3):3781.
doi: 10.36922/arnm.3781

Received: May 28, 2024

Accepted: August 15, 2024

Published Online: September 11, 2024

1. Introduction

According to the statistics of the World Health Organization, radiotherapy (RT) plays a notable role in the treatment of cancer, providing options for radical cure, palliation, or as an adjuvant or neoadjuvant modality before or after surgery in 70% of cancer patients. A primary procedure in RT is the simulation of tumor positioning, which precisely identifies the tumor location using computed tomography (CT), magnetic resonance imaging (MRI), or positron emission tomography-CT, and then transfers these images into a treatment planning system (TPS) for designing the RT. The commonly utilized simulation positioning is the CT simulator (CT-sim), which primarily features: (i) X, Y, Z-axis three-dimensional (3D) laser positioning; (ii) patient immobilization using stabilization devices combined with CT couch; (iii) large-aperture diameter in the range of 80 – 85 cm; and (iv) CT-sim couch resembling that of linear accelerator, which minimizes errors in tumor positioning between CT-sim and RT.

With the rapid advancements of CT-sim, a novel percutaneous puncture biopsy has emerged, characterized by enhanced efficiency and accuracy. Regarding these developments, a pioneering concept, image-guidance interventional RT, was proposed. This concept encompasses various applications, including puncture biopsy, fiducial mark implantation, high-dose rate (HDR) after-loading brachytherapy, and radioactive

seed permanent implantation. This research aimed to significantly enhance the field and connotation of RT.

2. CT-sim guided puncture biopsy

Traditional tumor diagnosis primarily relies on bronchoscopy, gastroscopy, cholangioscopy, or CT-guided percutaneous biopsy. However, the application of these methods presents implementation and efficacy challenges, including low success rate, limited positivity rate, long-term learning curve, and operational complexity.[1-4] The CT-guided percutaneous biopsy is currently performed using diagnostic CT with small apertures and concave beds, which lack patient stabilization positioning systems. This deficiency makes patient positioning setup challenging. Moreover, the variability in individual physician practices significantly affects the accuracy of CT-guided percutaneous, making it difficult to establish standardized protocols.[5]

To overcome these challenges, a percutaneous biopsy fixation and navigation system was designed to integrate with the CT-sim. In addition, 3D-printing coplanar templates (3D-PCT) were developed to enhance puncture needle position precision, achieving accuracy within 1 mm, emerging to be particularly beneficial for targeting small pulmonary nodules with diameters <10 mm.[6-8] This integration of the CT-sim positioning facility, percutaneous biopsy navigation system, and 3D-PCT enhances standardized and uniform puncture biopsy, promoting widespread adoption and dissemination. The procedure encompasses the following 8 steps: (i) patient positioning setup and CT-sim scan; (ii) marking the puncture needles insertion site on the patient's skin; (iii) standard sterilization and draping procedures; (iv) installing navigation system and 3D-PCT; (v) subcutaneously inserting the puncture biopsy needle; (vi) conducting tissue sampling; (vii) CT-sim scan to confirm the occurrence of bleeding or pneumothorax; (viii) transferring patients back toward (Figures 1 and 2).

3. CT-sim guided fiducial mark implantation

RT can be categorized into two primary types: External beam RT (EBRT) and internal RT. EBRT can be further divided into conventional RT and stereotactic body RT (SBRT). EBRT involves delivering a dose of 180 – 200 cGy per fraction, five fractionations a week, for 4 – 6 weeks. In contrast, SBRT entails administering doses exceeding 5 Gy per fraction, typically given as 3 – 5 fractions. Stereotactic radiosurgery, which is mainly employed in the treatment of neurological tumors, requires only one or two fractions. The Gamma Knife and CyberKnife are examples of SBRT equipment utilized in clinical practice. The Gamma Knife employs multiple Co-60 radiation sources combined with rotational and focuses the radiation to the target for eliminating tumor cells.[9,10] On the other hand, the CyberKnife utilizes a robotic system to deliver radiation from various angles and directions in 3D space while employing real-time tracking facilitated by interactive X-ray identification of gold markers implanted in the tumor. Accurate identification of these markers is crucial for successful treatment due to factors, such as variability in gold marker positions due to respiratory motion, interference from bone structures, or the number of fiducial markers during real-time tracking irradiation procedures.[11-15]

Traditionally, fiducial mark implantation has been performed using ultrasound or CT guidance. However, studies indicated that ultrasound-guided gold markers implant deviates significantly from preoperative plans, leading to challenges in real-time tracking of fiducial marks and potentially impacting outcomes.[13,16] The 3D-PCT technique was developed for precise placement of fiducial markers implantation based on preoperative plan. Two key principles were proposed for successful fiducial mark implantation: Two puncture needles spaced 2 cm apart, and the insertion of two fiducial marks per needle while maintaining a 2 cm distance between gold markers. Notably, fiducial markers should be optimally implanted in the tumor or its periphery at a depth ranging from 2 to 3 cm.

The procedures involved include (i) pre-operative preparation; (ii) CT-sim scan to determine the needles entry point; (iii) standard sterilization; (iv) installing fixation stabilization navigator system and 3D-PCT; (v) insertion of needles at the pre-planned points; (vi) implantation of the fiducial markers; (vii) CT-sim scan to assess potential complications, such as pneumothorax or bleeding diligently; (viii) transferring patients back to the ward (Figures 3 and 4).

4. CT-sim guided high-dose-rate after-loading brachytherapy

Internal irradiation therapy comprises two main modalities: High-dose-rate brachytherapy (HDR-BT) and low-dose-rate interstitial brachytherapy (LDR-IBT), such as radioactive seed implantation. These methods involve the insertion of an applicator or radioactive seeds adjacent to or into carcinoma by interventional modality. HDR-BT is predominantly employed for the treatment of tumors in hollow organs, such as cervical and endometrial cancers, as well as solid tumors, including prostate, breast, and skin tumors.[17-26] LDR-IBT is primarily utilized in the treatment of early-stage prostate cancer, as well as in cases

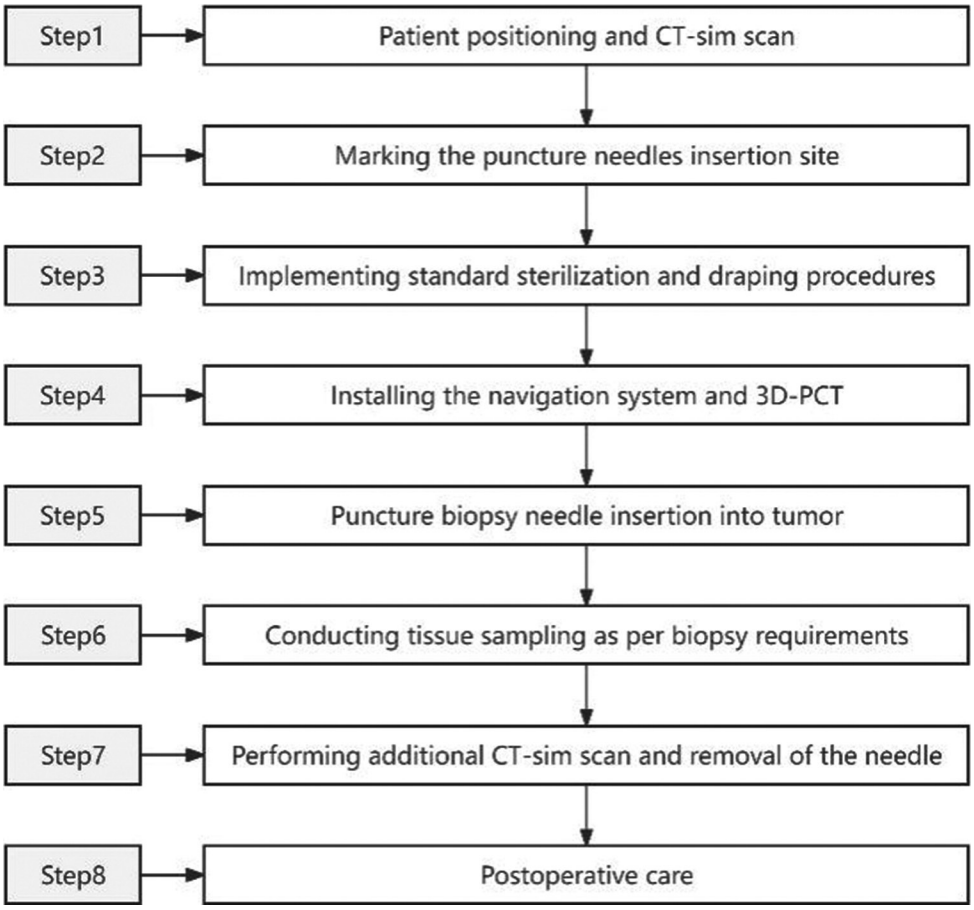

Figure 1. Flowchart of CT-sim guided puncture biopsy. Image provided by author.
Abbreviations: 3D-PCT: 3D-printing coplanar templates; CT-sim: Computed tomography simulator.

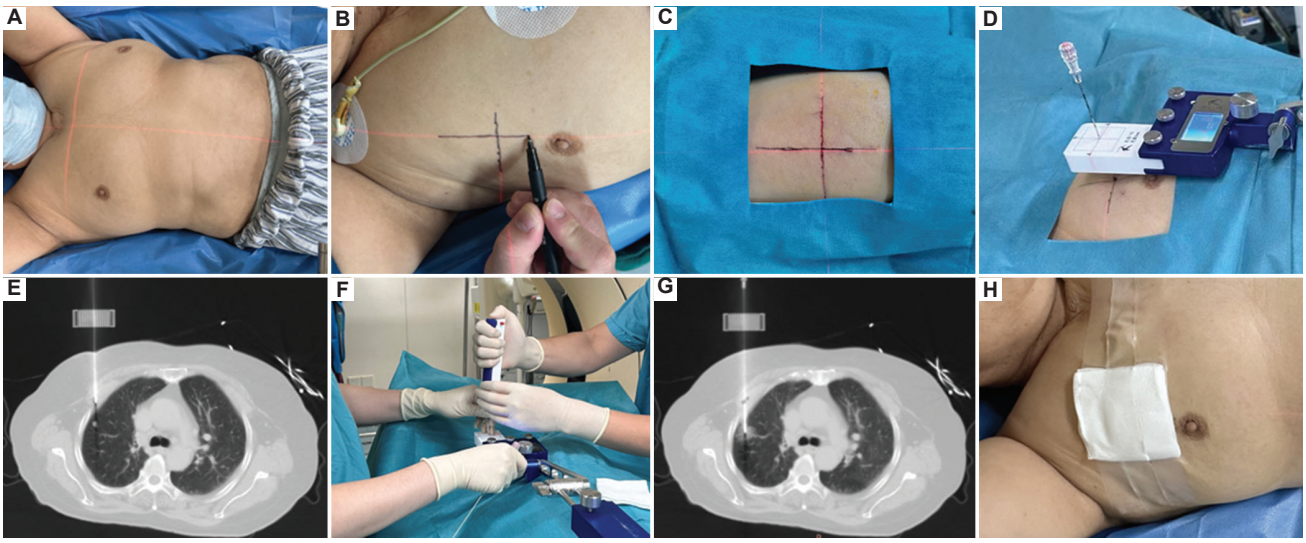

Figure 2. CT-sim guided puncture biopsy. (A) Patient positioning and CT-sim scan; (B) Puncture needles insertion site; (C) Implementing standard sterilization and draping procedures; (D) Installing the navigation system and 3D-PCT; (E) Puncture biopsy needle insertion into tumor; (F) Conducting tissue sampling; (G) CT-sim scan; (H) Post-operative care. Image provided by author.
Abbreviations: 3D-PCT: 3D-printing coplanar templates; CT-sim: Computed tomography simulator.

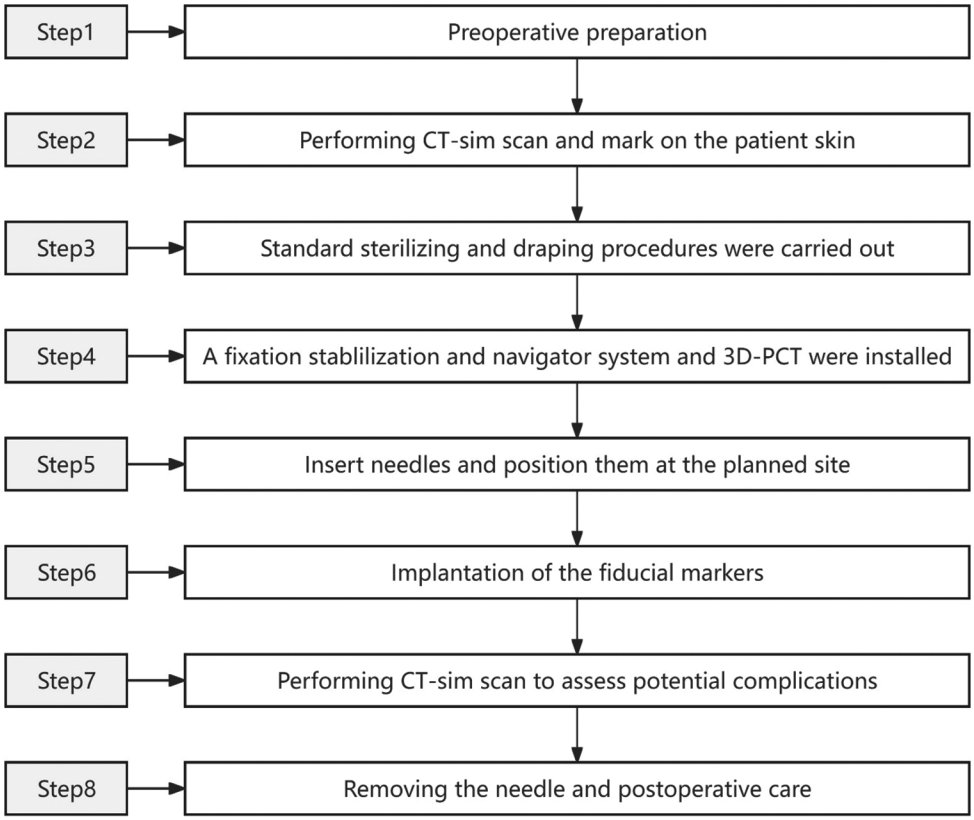

Figure 3. Flowchart of CT-guided fiducial mark implantation. Image provided by author.
Abbreviations: 3D-PCT: 3D-printing coplanar templates; CT-sim: Computed tomography simulator.

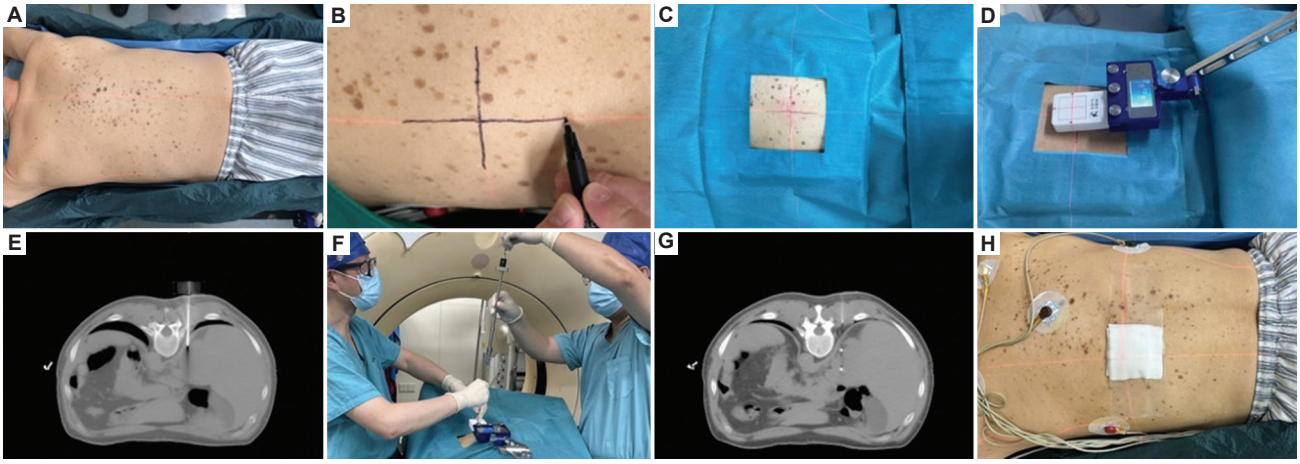

Figure 4. CT-sim guided fiducial mark implantation. (A) Preoperative preparation; (B) Performing CT-sim scan and mark on the patient skin; (C) Standard sterilization and draping procedures; (D) Installation of a fixation stabilization and navigator system and 3D-PCT; (E) Insertion of needles at the planned site; (F) Implantation of the fiducial markers; (G) Performing CT-sim scan to assess potential complications; (H) Post-operative care. Image provided by author.

of recurrent and metastatic solid tumors, by virtue of the minimal invasiveness benefit of the treatment.

The previous version of HDR-BT is a two-dimensional RT technique relying on X-ray simulation, which failed to meet precision radiation requirements, leading to diminished efficacy and increased incidence of adverse effects. With advancements in HDR-BT, patients require CT or MRI to ensure precise placement, orientation,

and alignment of the source applicator according to predetermined specifications. This evolution has propelled HDR-BT into a new era characterized by 3D treatment approaches, with CT-sim scan technology playing a pivotal role. Typically, HDR-BT entails 4 – 6 sessions administered biweekly over an extended therapy duration. However, the repeated insertions of the source applicator may pose a risk of cross-contamination and compromise patient tolerability. Attempts have been made to address these challenges by converting the CT simulation room into an operating theater equipped with aseptic lighting and imaging guidance devices, aligned with surgical standards requirements, to minimize nosocomial infections. In addition, the concept of "no pain HDR-BT" was introduced, involving the utilization of an anesthesia pump to administer spinal or epidural anesthesia, ensuring optimal patient position comfort during treatment. The procedure steps entailed include (i) preoperative preparation; (ii) patients' positioning setup, followed by anesthesia administration; (iii) implantation of the radiation source applicator or needles; (iv) CT-sim scan to verify applicator or needles position; (v) intraoperative TPS; (vi) transferal of the patients to HDR room to receive RT; (vii) returning patients to the CT-sim for removal of the radiation source applicator or needles; (viii) transferring patients to the ward for intravenous fluid administration, as well as anti-inflammatory and hemostatic treatments (Figures 5 and 6).

5. CT-sim guided radioactive seed implantation

The CT-guided radioactive 125I seed implantation brachytherapy utilizes imaging guidance techniques to accurately position radioactive iodine-125 seed (with a half-life of 59.6 days, size of 0.8 × 4.5 mm, energy of 27 – 35 keV, and encased in a nickel-titanium alloy) within or around tumors. The precise emission of low-energy gamma rays from iodine-125 seed effectively eradicates tumor cells. This approach is characterized by the delivery of localized high doses, rapid dose decay, and minimal damage to surrounding normal tissues, establishing it as an internationally recognized standard for the treatment of early-stage prostate cancer.[27-32]

In 2001, Professor Junjie Wang spearheaded the implementation of this technique in China with an initial emphasis on ultrasound-guided 125I seed implantation for prostate cancer. Thereafter, its utilization was broadened to include diverse malignancies, such as recurrent head-and-neck carcinoma, pulmonary carcinoma, pancreatic carcinoma, and hepatic cancer along with recurrent colorectal, cervical, and soft tissue neoplasms. This remarkable advancement signifies a pivotal milestone in the realm of 125I seed implantation brachytherapy.[33-45]

The standardized procedure for radioactive 125I seed implantation in prostate cancer involves transrectal

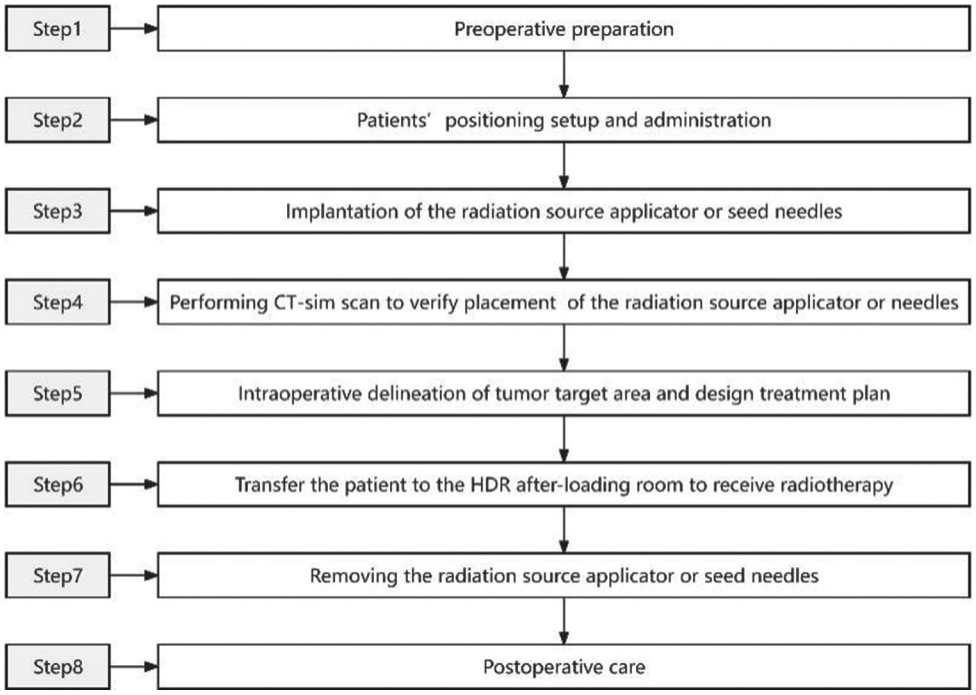

Figure 5. Flowchart of computed tomography (CT)-guided high-dose-rate (HDR) after-loading interstitial implantation. Image provided by author. Abbreviation: CT-sim: Computed tomography simulator.

ultrasound guidance, real-time intraoperative planning, and high-precision single-session completion.[46,47] CT-guided techniques were applied in the field of 125I seed implantation in 2002.[44,46-52] The advantages of CT guidance are as follows: (i) high-resolution CT scans; and (ii) unaffected by bone or gas interference, allowing treatment of lung cancer, head-and-neck, pelvis, and spinal cord with 125I seed implantation. Nonetheless, certain drawbacks must be acknowledged: (i) Preoperative planning poses challenges due to the presence of organ at risk (OAR), including bones, blood vessels, trachea, and intestines; (ii) Ultrasound-guided 125I seed implantation for prostate cancer mainly relies on two-dimensional plans with needles inserted parallelly, which could not apply to the other part of the body; (iii) The absence of a 3D planning system limits the ability to achieve 125I seed distribution in 3D space across different locations of the carcinoma. In 2015, Chinese physicians independently spearheaded the development of radioactive seed implant fixation and navigation brackets, in conjunction with 3D-printing non-coplanar template (3D-PNCT) or 3D-PCT, which features individual design and precise 125I seed implantation across diverse tumor location. In addition, brachytherapy-TPS (B-TPS) software compatible with 3D-PNCT or 3D-PCT and computer planning algorithms have been developed to ensure optimal 3D spatial distribution of radioactive 125I seeds in the tumor targets. This approach enables the fulfillment of preoperative target volume prescription dose, while minimizing radiation exposure to OAR. As a result of these advancements, 125I seed implantation has achieved standardization and uniformity in the treatment of solid tumors throughout the body, emerging as a widely applicable standardized protocol and possessing significant advantages in the management of recurrent head-and-neck cancer, lung cancer, pancreatic cancer, recurrent pelvic carcinoma, soft tissue tumors, and other conditions.[53-60]

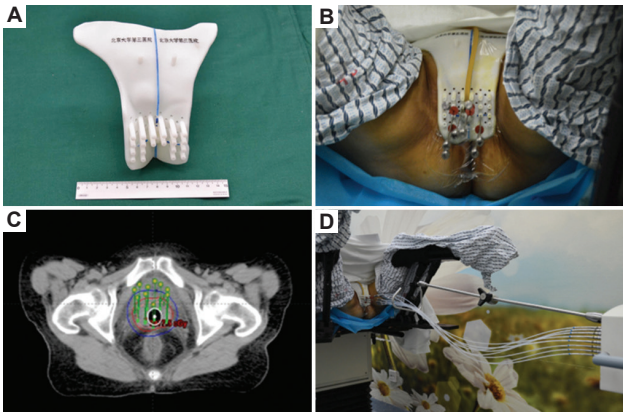

Figure 6. CT-sim guided HDR high-dose-rate after-loading brachytherapy. (A) Preoperative preparation; (B) Implantation applicator; (C) Target delineation and pre-planning; (D) Radiotherapy in high-dose-rate (HDR) after-loading room. Image provided by author.

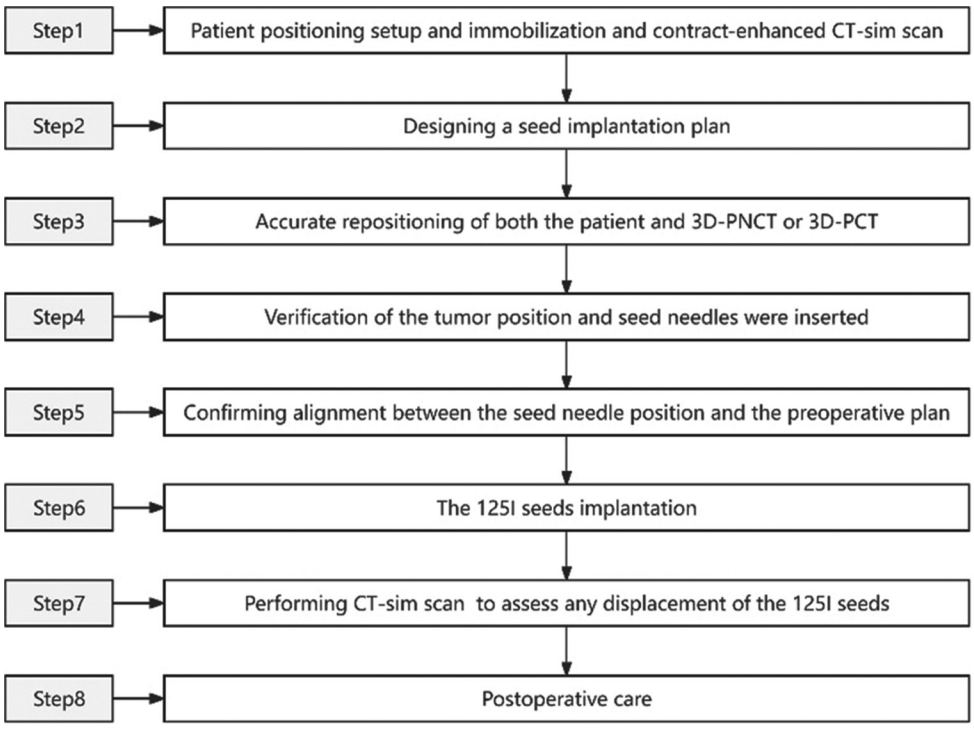

Figure 7. Flowchart of CT-sim guided radioactive seed implantation. Image provided by author.
Abbreviations: 3D-PCT: 3D-printing coplanar templates; 3D-PNCT: 3D-printing non-coplanar template; CT-sim: Computed tomography simulator.

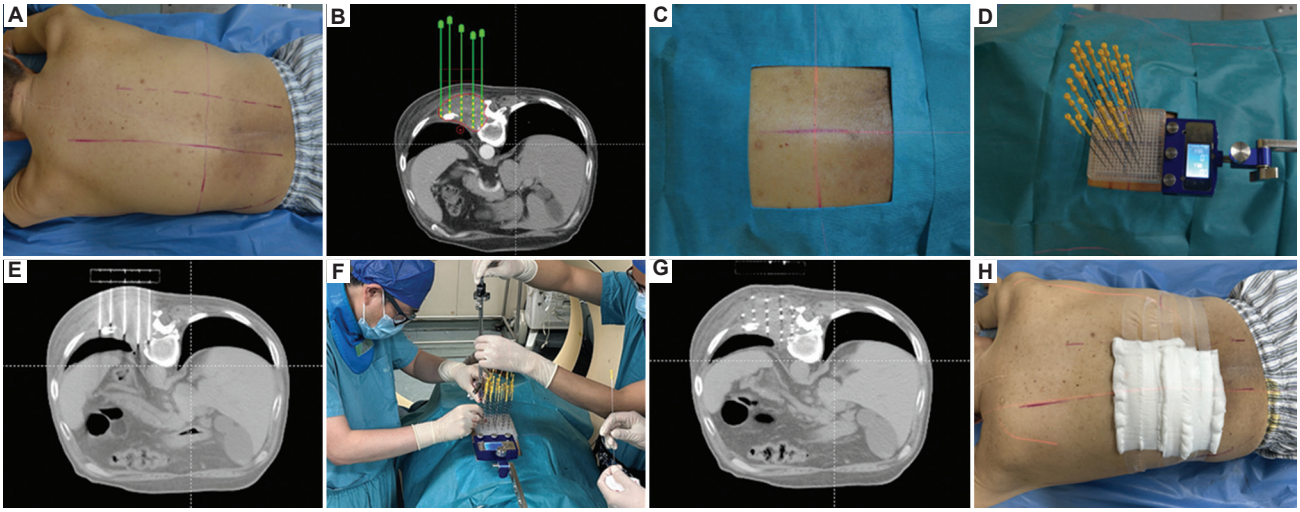

Figure 8. CT-simulator-guided radioactive seed implantation. (A) Patient setup and CT scan; (B) Pre-planning; (C) Repositioning 3D-PNCT or 3D-PCT; (D) Verification of seed needles position; (E) Confirming alignment between the seed needle position and pre-plan; (F) 125I seeds implantation; (G) Post-plan; (H) Post-operative care. Image provided by author.
Abbreviations: 3D-PCT: 3D-printing coplanar templates; 3D-PNCT: 3D-printing non-coplanar template; CT-sim: Computed tomography simulator.

The procedures of CT-sim guided radioactive seed implantation are as follows: (i) patient positioning setup, and contrast-enhanced CT-sim scan; (ii) transfer of CT-sim images to the B-TPS for designing pre-plan; (iii) accurate repositioning of 3D-PNCT or 3D-PCT; (iv) insertion of seed needles; (v) CT-sim scan to confirm alignment between seed needle position and pre-plan; (vi) 125I seeds implantation; (vii) CT-sim scan to assess the displacement of the 125I seeds, and supplementation of additional seeds, if necessary; and (viii) transferring patients back toward (Figures 7 and 8).

6. Conclusion

The advent of CT-sim has ushered in an era where interventional brachytherapy has attained swift advancements, bringing forth the establishment of standardized and harmonized technical systems that lay a concrete foundation for a revolutionary transformation in tumor diagnosis and RT.

Acknowledgments

None.

Funding

None.

Conflict of interest

Junjie Wang and Ping Jiang are the Editor-in-Chief and the Editorial Board Member of the journal, respectively, but were not in any way involved in the editorial and peer-review process conducted for this paper, directly or indirectly. Separately, other authors declared that they have no known competing financial interests or personal relationships that could have influenced the work reported in this paper.

Author contributions

Conceptualization: Junjie Wang, Ping Jiang
Writing – original draft: Qiman Han, Yi Chen
Writing – review & editing: Junjie Wang, Zhe Ji, Yi Chen, Bin Qiu

Ethics approval and consent to participate

Not applicable.

Consent for publication

Patients gave consent to publish their images in this study.

Availability of data

Not applicable.

References

1. Hwang EJ, Park CM, Yoon SH, Lim HJ, Goo JM. Risk factors for haemoptysis after percutaneous transthoracic needle biopsies in 4,172 cases: Focusing on the effects of enlarged main pulmonary artery diameter. *Eur Radiol.* 2018;28:1410-1419.

   doi: 10.1007/s00330-017-5101-8

2. Kawashima H, Ohno E, Ishikawa T, *et al.* Endoscopic management of perihilar cholangiocarcinoma. *Dig Endosc.* 2022;34:1147-1156.

doi: 10.1111/den.14317

3. Elmunzer BJ, Maranki JL, Gómez V, *et al.* ACG clinical guideline: Diagnosis and management of biliary strictures. *Am J Gastroenterol.* 2023;118:405-426.

doi: 10.14309/ajg.0000000000002190

4. Chung C, Kim Y, Park D. Transthoracic needle biopsy: How to maximize diagnostic accuracy and minimize complications. *Tuberc Respir Dis* (*Seoul*). 2020;83:S17-S24.

doi: 10.4046/trd.2020.0156

5. De Filippo M, Saba L, Silva M, *et al.* CT-guided biopsy of pulmonary nodules: Is pulmonary hemorrhage a complication or an advantage? *Diagn Interv Radiol.* 2014;20:421-425.

doi: 10.5152/dir.2014.14019

6. Ji Z, Jiang Y, Guo F, *et al.* Dosimetry verification of radioactive seed implantation for malignant tumors assisted by 3D printing individual templates and CT guidance. *Appl Radiat Isot.* 2017;124:68-74.

doi: 10.1016/j.apradiso.2016.12.009

7. Wang H, Ren T, Chen P, *et al.* Application of 3-dimensionally printed coplanar template improves diagnostic yield of CT-guided percutaneous core needle biopsy for pulmonary nodules. *Technol Cancer Res Treat.* 2022;21.

doi: 10.1177/15330338221089940

8. Haoran E, Chen J, Sun W, *et al.* Three-dimensionally printed navigational template: A promising guiding approach for lung biopsy. *Transl Lung Cancer Res.* 2022;11:393-403.

doi: 10.21037/tlcr-22-172

9. Desai R, Rich KM. Therapeutic role of gamma knife stereotactic radiosurgery in neuro-oncology. *Mo Med.* 2020;117:33-38.

10. Spina A, Garbin E, Albano L, Bisoglio A, Boari N, Mortini P. Gamma Knife radiosurgery for central neurocytoma: A quantitative systematic review and metanalysis. *Neurosurg Rev.* 2024;47:64.

doi: 10.1007/s10143-024-02301-7

11. Nemoto H, Saito M, Suzuki T, *et al.* Evaluation of computed tomography metal artifact and CyberKnife fiducial recognition for novel size fiducial markers. *J Appl Clin Med Phys.* 2023;24:e14142.

doi: 10.1002/acm2.14142

12. Suzuki T, Saito M, Onishi H, *et al.* Comparison of CT artifacts and image recognition of various fiducial markers including two types of thinner fiducial markers for CyberKnife treatment. *Rep Pract Oncol Radiother.* 2020;25:117-124.

doi: 10.1016/j.rpor.2019.12.005

13. Marsico M, Gabbani T, Lunardi S, Galli A, Biagini MR, Annese V. Percutaneous ultrasound-guided fiducial marker placement for liver cancer robotic stereotactic radio-surgery treatment: A comparative analysis of three types of markers and needles. *Arab J Gastroenterol.* 2017;18:83-86.

doi: 10.1016/j.ajg.2017.05.007

14. Scher N, Bollet M, Bouilhol G, *et al.* Safety and efficacy of fiducial marker implantation for robotic stereotactic body radiation therapy with fiducial tracking. *Radiat Oncol.* 2019;14:167.

doi: 10.1186/s13014-019-1373-2

15. Akasaka H, Mizonobe K, Oki Y, *et al.* Fiducial marker position affects target volume in stereotactic lung irradiation. *J Appl Clin Med Phys.* 2022;23:e13596.

doi: 10.1002/acm2.13596

16. Kim JH, Hong SS, Kim JH, *et al.* Safety and efficacy of ultrasound-guided fiducial marker implantation for CyberKnife radiation therapy. *Korean J Radiol.* 2012;13:307-313.

doi: 10.3348/kjr.2012.13.3.307

17. Ali ZS, Solomon E, Mann P, Wong S, Chan KKW, Taggar AS. High dose rate brachytherapy in the management of anal cancer: A review. *Radiother Oncol.* 2022;171:43-52.

doi: 10.1016/j.radonc.2022.03.019

18. Strouthos I, Karagiannis E, Zamboglou N, Ferentinos K. High-dose-rate brachytherapy for prostate cancer: Rationale, current applications, and clinical outcome. *Cancer Rep* (*Hoboken*). 2022;5:e1450.

doi: 10.1002/cnr2.1450

19. Miglierini P, Malhaire JP, Goasduff G, Miranda O, Pradier O. Cervix cancer brachytherapy: High dose rate. *Cancer Radiother.* 2014;18:452-457.

doi: 10.1016/j.canrad.2014.06.008

20. Viswanathan AN, Beriwal S, De Los Santos JF, *et al.* American Brachytherapy Society consensus guidelines for locally advanced carcinoma of the cervix. Part II: High-dose-rate brachytherapy. *Brachytherapy.* 2012;11:47-52.

doi: 10.1016/j.brachy.2011.07.002

21. Renard S, Salleron J, Py JF, *et al.* High-dose-rate brachytherapy for facial skin cancer: Outcome and toxicity assessment for 71 cases. *Brachytherapy*. 2021;20:624-630.

doi: 10.1016/j.brachy.2021.01.009

22. Itami J, Murakami N, Watanabe M, *et al.* Combined interstitial and intracavitary high-dose rate brachytherapy of cervical cancer. *Front Oncol.* 2021;11:809825.

doi: 10.3389/fonc.2021.809825

23. Zeng H, Dai J, Cao D, *et al.* Safety and efficacy associated with single-fraction high-dose-rate brachytherapy in localized prostate cancer: A systematic review and meta-analysis. *Strahlenther Onkol.* 2023;199:525-535.

doi: 10.1007/s00066-023-02063-z

24. Krzysztofiak T, Suchorzepka M, Tukiendorf A, Wojcieszek P, Kamińska-Winciorek G. Basal cell carcinoma after high dose rate brachytherapy: Medium-term dermoscopic evaluation of cancer's response. *Dermatol Ther* (*Heidelb*). 2023;13:2063-2078.

doi: 10.1007/s13555-023-00981-5

25. Yamazaki H, Masui K, Suzuki G, *et al.* Reirradiation for recurrent head and neck carcinoma using high-dose-rate brachytherapy: A multi-institutional study. *Brachytherapy*. 2022;21:341-346.

doi: 10.1016/j.brachy.2021.12.011

26. Dankulchai P, Petsuksiri J, Chansilpa Y, Hoskin PJ. Image-guided high-dose-rate brachytherapy in inoperable endometrial cancer. *Br J Radiol.* 2014;87:20140018.

doi: 10.1259/bjr.20140018

27. Henry A, Pieters BR, André Siebert F, Hoskin P. GEC-ESTRO ACROP prostate brachytherapy guidelines. *Radiother Oncol.* 2022;167:244-251.

doi: 10.1016/j.radonc.2021.12.047

28. Sanmamed N, Lee J, Berlin A, *et al.* Tumor-targeted dose escalation for localized prostate cancer using MR-guided HDR brachytherapy (HDR) or integrated VMAT (IB-VMAT) boost: Dosimetry, toxicity and health related quality of life. *Radiother Oncol.* 2020;149:240-245.

doi: 10.1016/j.radonc.2020.05.029

29. Corkum M, Loblaw A, Hasan Y, *et al.* Prostate high dose-rate brachytherapy as monotherapy for prostate cancer: Late toxicity and patient reported outcomes from a randomized phase II clinical trial. *Radiother Oncol.* 2021;156:160-165.

doi: 10.1016/j.radonc.2020.12.021

30. Alayed Y, Loblaw A, McGuffin M, *et al.* Single-fraction HDR brachytherapy as monotherapy in low and intermediate risk prostate cancer: Outcomes from two clinical trials with and without an MRI-guided boost. *Radiother Oncol.* 2021;154:29-35.

doi: 10.1016/j.radonc.2020.09.007

31. Chin J, Rumble RB, Kollmeier M, *et al.* Brachytherapy for patients with prostate cancer: American Society of Clinical Oncology/Cancer Care Ontario Joint Guideline Update. *J Clin Oncol.* 2017;35:1737-1743.

doi: 10.1200/jco.2016.72.0466

32. Mohler JL, Antonarakis ES. NCCN guidelines updates: Management of prostate cancer. *J Natl Compr Canc Netw.* 2019;17:583-586.

doi: 10.6004/jnccn.2019.5011

33. Wang J, Chai S, Wang R, *et al.* Expert consensus on computed tomography-assisted three-dimensional-printed coplanar template guidance for interstitial permanent radioactive ^{125}I seed implantation therapy. *J Cancer Res Ther.* 2019;15:1430-1434.

doi: 10.4103/jcrt.JCRT_434_19

34. Luo YJ, Liu ZL, Ye PC, *et al.* Safety and efficacy of intraoperative iodine-125 seed implantation brachytherapy for rectal cancer patients: A retrospective clinical research. *J Gastroenterol Hepatol.* 2016;31:1076-1084.

doi: 10.1111/jgh.13261

35. Wang J, Yuan H, Ma Q, *et al.* Interstitial 125I seeds implantation to treat spinal metastatic and primary paraspinal malignancies. *Med Oncol.* 2010;27:319-326.

doi: 10.1007/s12032-009-9212-1

36. Jiang YL, Ji Z, Tian SQ, *et al.* CT-guidance interstitial Iodine-125 seed brachytherapy as a salvage therapy for recurrent head and neck carcinoma. *Zhonghua yi xue za zhi*. 2018;98:3686-3691.

doi: 10.3760/cma.j.issn.0376-2491.2018.45.011

37. Wang H, Wang J, Jiang Y, *et al.* The investigation of ^{125}I seed implantation as a salvage modality for unresectable pancreatic carcinoma. *J Exp Clin Cancer Res.* 2013;32:106.

doi: 10.1186/1756-9966-32-106

38. Wang JJ, Yuan HS, Li JN, Jiang YL, Tian SQ, Yang RJ. CT-guided radioactive seed implantation for recurrent rectal carcinoma after multiple therapy. *Med Oncol.* 2010;27:421-429.

doi: 10.1007/s12032-009-9227-7

39. Huang M, Lin Q, Wang H, *et al.* Survival benefit of chemoembolization plus Iodine125 seed implantation in unresectable hepatitis B-related hepatocellular carcinoma with PVTT: A retrospective matched cohort study. *Eur Radiol.* 2016;26:3428-3436.

doi: 10.1007/s00330-015-4198-x

40. Yang M, Fang Z, Yan Z, *et al.* Transarterial chemoembolisation (TACE) combined with endovascular implantation of an iodine-125 seed strand for the treatment of hepatocellular carcinoma with portal vein tumour thrombosis versus TACE alone: A two-arm, randomised clinical trial. *J Cancer Res Clin Oncol.* 2014;140:211-219.

doi: 10.1007/s00432-013-1568-0

41. Sun H, Zhang M, Liu R, Liu Y, Hou Y, Wu C. Endovascular implantation of ^{125}I seed combined with transcatheter arterial chemoembolization for unresectable hepatocellular carcinoma. *Future Oncol.* 2018;14:1165-1176.

doi: 10.2217/fon-2017-0354

42. Mo Z, Zhang T, Zhang Y, *et al.* Feasibility and clinical value of CT-guided ^{125}I brachytherapy for metastatic soft tissue sarcoma after first-line chemotherapy failure. *Eur Radiol.* 2018;28:1194-1203.

doi: 10.1007/s00330-017-5036-0

43. Qu A, Jiang P, Sun H, *et al.* Efficacy and dosimetry analysis of image-guided radioactive ^{125}I seed implantation as salvage

treatment for pelvic recurrent cervical cancer after external beam radiotherapy. *J Gynecol Oncol.* 2019;30:e9.

doi: 10.3802/jgo.2019.30.e9

44. Tong L, Liu P, Huo B, Guo Z, Ni H. CT-guided ^{125}I interstitial brachytherapy for pelvic recurrent cervical carcinoma after radiotherapy. *Onco Targets Ther.* 2017;10:4081-4088.

doi: 10.2147/ott.S139571

45. Chen Y, Jiang Y, Ji Z, *et al.* Dosimetry, efficacy, and safety of three-dimensional printing noncoplanar template-assisted and CT-guided ^{125}I seed implantation for recurrent retroperitoneal lymphatic metastasis after external beam radiotherapy. *Brachytherapy.* 2020;19:380-388.

doi: 10.1016/j.brachy.2020.02.009

46. Davis BJ, Horwitz EM, Lee WR, *et al.* American Brachytherapy Society consensus guidelines for transrectal ultrasound-guided permanent prostate brachytherapy. *Brachytherapy.* 2012;11:6-19.

doi: 10.1016/j.brachy.2011.07.005

47. Yamada Y, Rogers L, Demanes DJ, *et al.* American Brachytherapy Society consensus guidelines for high-dose-rate prostate brachytherapy. *Brachytherapy*. 2012;11:20-32.

doi: 10.1016/j.brachy.2011.09.008

48. Li Q, Tian Y, Yang D, Liang Y, Cheng X, Gai B. Permanent Iodine-125 seed implantation for the treatment of nonresectable retroperitoneal malignant tumors. *Technol Cancer Res Treat*. 2019;18.

doi: 10.1177/1533033819825845

49. Liu Y, Shen Z, Qu A, Jiang P, Jiang Y, Wang J. A comparative study of dosimetric parameters of 3D-printed non-coplanar template-assisted CT-guided iodine-125 seed implantation brachytherapy in patients with inguinal lymph node metastatic carcinomas. *J Contemp Brachytherapy*. 2022;14:452-461.

doi: 10.5114/jcb.2022.121564

50. Yao L, Cao Q, Wang J, *et al.* CT-guided ^{125}I seed interstitial brachytherapy as a salvage treatment for recurrent spinal metastases after external beam radiotherapy. *Biomed Res Int.* 2016;2016:8265907.

doi: 10.1155/2016/8265907

51. Jiang W, Jiang P, Wei S, *et al.* The accuracy and safety of CT-guided iodine-125 seed implantation assisted by 3D non-coplanar template for retroperitoneal recurrent carcinoma. *World J Surg Oncol.* 2020;18:307.

doi: 10.1186/s12957-020-02087-0

52. Yan H, Mo Z, Xiang Z, *et al.* CT-guided ^{125}I brachytherapy for locally recurrent nasopharyngeal carcinoma. *J Cancer.* 2017;8:2104-2113.

doi: 10.7150/jca.19078

53. Ji Z, Jiang Y, Sun H, *et al.* 3D-printed template and optical needle navigation in CT-guided Iodine-125 permanent seed implantation. *J Contemp Brachytherapy.* 2021;13:410-418.

doi: 10.5114/jcb.2021.108595

54. Ji Z, Sun H, Jiang Y, *et al.* Comparative study for CT-guided ^{125}I seed implantation assisted by 3D printing coplanar and non-coplanar template in peripheral lung cancer. *J Contemp Brachytherapy.* 2019;11:169-173.

doi: 10.5114/jcb.2019.84503

55. Ji Z, Jiang Y, Guo F, *et al.* Safety and efficacy of CT-guided radioactive iodine-125 seed implantation assisted by a 3D printing template for the treatment of thoracic malignancies. *J Cancer Res Clin Oncol.* 2020;146:229-236.

doi: 10.1007/s00432-019-03050-7

56. Zhang F, Wang J, Guo J, *et al.* Chinese expert consensus workshop report: Guideline for permanent iodine-125 seed implantation of primary and metastatic lung tumors. *Thorac Cancer.* 2019;10:388-394.

doi: 10.1111/1759-7714.12912

57. Gai B, Zhang F. Chinese expert consensus on radioactive ^{125}I seeds interstitial implantation brachytherapy for pancreatic cancer. *J Cancer Res Ther.* 2018;14:1455-1462.

doi: 10.4103/jcrt.JCRT_96_18

58. Li W, Guan J, Yang L, Zheng X, Yu Y, Jiang J. Iodine-125 brachytherapy improved overall survival of patients with inoperable stage III/IV non-small cell lung cancer versus the conventional radiotherapy. *Med Oncol.* 2015;32:395.

doi: 10.1007/s12032-014-0395-8

59. Zhang S, Zheng Y, Yu P, *et al.* The combined treatment of CT-guided percutaneous 125I seed implantation and chemotherapy for non-small-cell lung cancer. *J Cancer Res Clin Oncol.* 2011;137:1813-1822.

doi: 10.1007/s00432-011-1048-3

60. Chen Y, Jiang Y, Ji Z, *et al.* Efficacy and safety of CT-guided ^{125}I seed implantation as a salvage treatment for locally recurrent head and neck soft tissue sarcoma after surgery and external beam radiotherapy: A 12-year study at a single institution. *Brachytherapy*. 2020;19:81-89.

doi: 10.1016/j.brachy.2019.09.006

ACCSCIENCE PUBLISHING

Advances in Radiotherapy & Nuclear Medicine

ORIGINAL RESEARCH ARTICLE

Neoadjuvant chemoradiotherapy for T3N0M0 esophageal squamous cell carcinoma

Ying Liu[1†], Yehan Zhou[2†], Xiaoding Zhou[1], Jingqiu Li[1], Jie Zhu[1], Yi Wang[1], Lei Wu[1], Gang Wan[1], Xuefeng Leng[3], Guangyuan Liu[3], Yongtao Han[3], Yang Liu[2], Lin Peng[3], and Qifeng Wang[1*]

[1]Department of Radiation Oncology, Sichuan Clinical Research Center for Cancer, Sichuan Cancer Hospital and Institute, Sichuan Cancer Center, Affiliated Cancer Hospital of University of Electronic Science and Technology of China, Chengdu, Sichuan, China

[2]Department of Pathology, Sichuan Clinical Research Center for Cancer, Sichuan Cancer Hospital and Institute, Sichuan Cancer Center, Affiliated Cancer Hospital of University of Electronic Science and Technology of China, Chengdu, Sichuan, China

[3]Department of Thoracic Surgery, Sichuan Clinical Research Center for Cancer, Sichuan Cancer Hospital and Institute, Sichuan Cancer Center, Affiliated Cancer Hospital of University of Electronic Science and Technology of China, Chengdu, Sichuan, China

Abstract

The optimal treatment for patients with pretreatment T3N0M0 (pre-T3N0M0) esophageal squamous cell carcinoma (ESCC) remains controversial. This study evaluated the impact of neoadjuvant chemoradiotherapy (NCRT) on the survival outcomes of individuals diagnosed with pre-T3N0M0 ESCC. A total of 443 patients with pre-T3N0M0 ESCC who underwent either NCRT plus surgery (NCRT + S) or surgery alone were included in the study. In the surgery group, patients with post-operative staging of pathological T3N0M0 (pT3N0M0) were classified as pre-T3N0M0. In the NCRT + S group, due to tumor downstaging after NCRT, patients with pre-treatment clinical T3 and post-operative pathology indicating lymph nodes without evidence of tumor involvement or regression were considered to have pre-T3N0M0. Univariate and multivariate Cox analyses were conducted to identify independent prognostic factors influencing overall survival (OS) in pre-T3N0M0 patients. Kaplan–Meier curves were employed to assess disparities in OS and disease-free survival (DFS) between the two groups. Compared to surgery alone, NCRT + S significantly enhanced the OS (Hazard ratio [HR] = 0.572, 95% Confidence interval [CI] = 0.407 – 0.804; P = 0.0059); however, it did not show a significant benefit in DFS (HR = 0.784, 95% CI = 0.564 – 1.09; P = 0.17). Compared with the surgery group, patients who achieved a pathologically complete response (pCR) after NCRT showed significantly improved OS (HR = 0.522, 95% CI = 0.339 – 0.804; P = 0.019). The overall and locoregional recurrence rates were significantly lower in the NCRT + S group than in the surgery group. Compared with surgery alone, NCRT + S significantly improved OS in patients with pre-T3N0M0 stage disease, especially in those who achieved pCR after NCRT.

Keywords: Esophageal cancer; Neoadjuvant chemoradiotherapy; Surgery; T3N0M0; Prognosis

[†]These authors contributed equally to this work.

***Corresponding author:**
Qifeng Wang
(wangqifeng@scszlyy.org.cn)

Citation: Liu Y, Zhou Y, Zhou X, *et al*. Neoadjuvant chemoradiotherapy for T3N0M0 esophageal squamous cell carcinoma. *Adv Radiother Nucl Med.* 2024;2(3):*3821*. doi: 10.36922/arnm.3821

Received: June 2, 2024

Accepted: July 8, 2024

Published Online: September 11, 2024

1. Introduction

Esophageal cancer is associated with high incidence and mortality rates.[1,2] Based on statistics, the 5-year survival rate for untreated esophageal cancer patients seldom surpasses 35 – 45%.[1,2] At present, neoadjuvant chemoradiotherapy (NCRT) followed by surgery is the standard therapeutic strategy for locally advanced esophageal cancer, according to the CROSS trial and the NEOCRTEC 5010 study.[3-5] However, in the NEOCRTEC 5010 study, 33.9% of patients in the surgery group had stage II disease, indicating that few patients had T3N0M0.[4] T3N0M0 and T2N0M0 are classified as stage II based on the eighth edition of the TNM classification; however, treatment strategies may differ across studies.[6-10] Therefore, the application of the NCRT treatment strategy to T3N0M0 patients remains a topic of debate.

Mantziari *et al.*[7] compared the survival outcomes between neoadjuvant treatment combined with surgery (NS) and primary surgery in patients with clinical T3N0M0 (cT3N0M0) and found that NS had a better curative effect. However, the proportion of patients with pathological N0 (pN0) in the surgery group was small, and approximately 64.3% of patients with lymph node (LN)-positive post-operative pathology had been misdiagnosed as N0 before treatment, indicating that clinical staging was not accurate. For this reason, the research results are controversial.

In the surgery-alone group, post-operative pathological staging typically represents the pretreatment staging. However, in the NCRT plus surgery (NCRT + S) group, due to tumor downstaging after NCRT,[11] post-operative pathological staging often cannot accurately represent pretreatment staging. Moreover, staging of LNs before treatment is often inaccurate.[7,12] To address this issue, many researchers have studied the effects of post-operative adjuvant therapy compared to surgery alone in patients with pathological T3N0M0 (pT3N0M0).[13,14] However, no studies have directly compared the efficacy of NCRT + S with surgery alone in patients with pretreatment T3N0M0 (pre-T3N0M0) status.

In this study, a new method was developed to accurately select patients with pre-T3N0M0. The objective was to assess the prognostic impact of NCRT + S compared to surgery alone in patients with pre-T3N0M0 esophageal squamous cell carcinoma (ESCC), with the aim of providing meaningful guidance for clinical practice.

2. Materials and methods

2.1. Patient selection

Patients who underwent esophagectomy at Sichuan Cancer Hospital between January 2008 and June 2021 were selected. The inclusion criteria were: (i) tumor located in the thoracic region, (ii) pathologically confirmed squamous cell carcinoma, (iii) treatment with either surgery alone or NCRT + S, and (iv) a pre-T3N0M0 stage. The exclusion criteria included: (i) the presence of other malignant tumors, (ii) incomplete resection (R1 and R2), (iii) positive node or organ metastasis (N1-3 or M1), and (iv) missing required data. A total of 443 patients were retrospectively reviewed.

2.2. Therapeutic strategy

The study population mainly underwent standard McKeown esophagectomy (n = 368) or Ivor Lewis esophagectomy (n = 69). The research cohort was divided into two groups based on treatment: the surgery (S) group and the NCRT + S group. Patients in the S group underwent surgery directly after diagnosis, whereas those in the NCRT + S group received chemoradiotherapy followed by surgery. The pathologic staging of patients was determined according to the eighth edition of the American Joint Committee on Cancer (AJCC) TNM classification for esophageal cancer.[15] In the NCRT + S group, the chemotherapy regimen typically included taxane combined with platinum. Patients received 40 – 50 Gy of external beam radiation in daily fractions of 1.8 – 2 Gy, 5 times a week, targeting the primary tumor and metastatic LNs for 4 – 5 weeks.

2.3. Evaluation of pre-treatment T3N0M0

In the S group, patients with pre-T3N0M0 status were selected based on post-operative pathological reports showing pT3N0M0 and complete tumor resection (R0). However, due to tumor downstaging after NCRT, evaluating the actual T3N0M0 before treatment in the NCRT + S group was challenging. Thus, a new method was developed to accurately assess patients with pre-T3N0M0 status. First, the eighth edition of the AJCC staging criteria was used to re-stage patients based on pretreatment endoscopic ultrasound and chest computed tomography (CT) scans. Subsequently, patients with clinical stage T3 (cT3) from the NCRT + S group were selected, and their excised LNs were subjected to pathological assessment. Based on previous studies,[16-18] a grading system was established to assess the treatment response of LNs after NCRT as follows: grade 0, no evidence of cancer involvement or regression (true negative LNs, Figure 1A); grade 1, complete regression of LNs (Figure 1B); grade 2, <10% cancer residual rate in LNs; grade 3, 10 – 50% cancer residual rate in LNs; and grade 4, >50% cancer residual rate in LNs. Grades 2 – 4 were considered non-pathological complete response (non-pCR) in LNs (Figure 1C). Patients with cT3 and LN grade 0 were ultimately considered to have been accurately staged as pre-T3N0M0.

2.4. Follow-up

During the treatment phase, patients were evaluated weekly. After completing treatment, they were monitored every 3 – 6 months for the 1st 2 years, every 6 – 12 months for the next 3 years, and annually thereafter. Recurrence was classified as local recurrence, distant metastasis, or death due to other causes. Local recurrence was characterized as the reappearance of cancer in the supraclavicular, mediastinal, or peritoneal regions, while distant metastasis referred to the recurrence of cancer in other parts of the body. All recurrences were confirmed through CT or magnetic resonance imaging scans, endoscopy, or positron emission tomography-CT examinations. Cytological or histological examinations were conducted when necessary, and the location and date of recurrence were documented.

2.5. Statistical analysis

Baseline characteristics of the study participants were compared using the Chi-squared test or Fisher's exact test, as appropriate. Overall survival (OS) was calculated from the date of diagnosis to the occurrence of the event or the last known follow-up date. Disease-free survival (DFS) was determined from the surgery date until the first sign of disease progression or the last known follow-up date. Actual survival was calculated using the Kaplan–Meier method and compared using the log-rank test. Prognostic factors were analyzed using univariate and multivariate Cox regression analyses. To mitigate potential confounding factors between the groups, propensity score matching (PSM) was also performed to balance the uneven variables between the two patient cohorts. A 1:1 nearest neighbor matching algorithm was applied using a caliper width of 0.02. The following variables were selected to generate the propensity score: age, sex, Karnofsky Performance Status (KPS), weight loss, tumor location, tumor length, lymphovascular invasion (LVI), perineural invasion (PNI), and total LNs excised. A $P < 0.05$ was considered statistically significant. All analyses were performed using R Statistical Software (Version 4.2.2, http://www.R-project.org, The R Foundation).

3. Results

3.1. Patient characteristics

After applying the inclusion and exclusion criteria, the records of 443 eligible patients treated between January

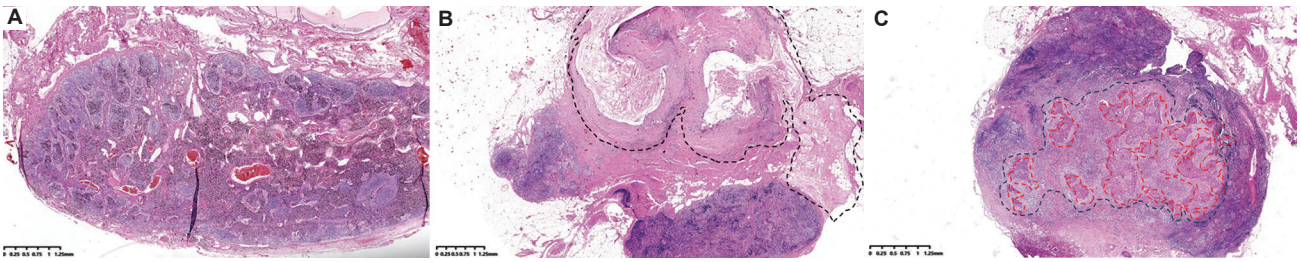

Figure 1. Pathological assessment images of the lymph nodes. The black dotted line indicates the lymph node tumor bed, while the red dotted line indicates the viable tumor. (A) Lymph node without evidence of cancer involvement or regression (true negative lymph node). (B) Lymph node complete regression. (C) No pathological complete regression of lymph node.

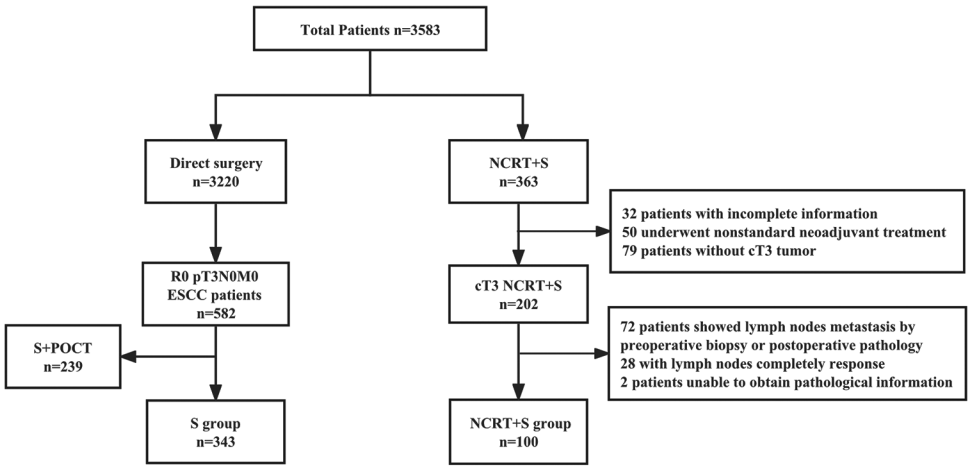

Figure 2. Flow chart for inclusion and exclusion of esophageal squamous cell carcinoma patients in this study
Abbreviations: cT3: Clinical T3; NCRT+S: Neoadjuvant chemoradiotherapy plus surgery; pT3N0M0: Pathological T3N0M0; S: Surgery; S+POCT: Surgery follows by post-operative adjuvant chemotherapy.

2008 and June 2021 were retrospectively reviewed. Of these, 343 patients were classified as pT3N0M0 and underwent surgery alone, while 100 patients with pre-T3N0M0 status received NCRT before surgery (Figure 2). The clinicopathological characteristics of the total population and the matched population are presented in Table 1. After PSM, baseline information was balanced between the two groups.

3.2. Univariate and multivariate analyses before and after PSM

In the univariate Cox regression analysis conducted on the entire population, age (>65 vs. ≤65, Hazard ratio [HR] = 1.41; 95% Confidence interval [CI] = 1.07 – 1.86, $P = 0.016$) and a KPS score of 80 (80 vs. ≥90; HR = 1.89; 95% CI = 1.35 – 2.63; $P < 0.001$) were associated with poorer OS. Conversely, total number of LNs excised (≥18 vs. <18; HR = 0.69; 95%

Table 1. Clinicopathological characteristics of the study population

Characteristic	Total (*n*=443)	Before PSM			After PSM		
		Surgery (*n*=343)	NCRT+S (*n*=100)	*P*-value	Surgery (*n*=85)	NCRT+S (*n*=85)	*P*-value
	n (%)	*n* (%)	*n* (%)		*n* (%)	*n* (%)	
Age (years)				0.017			0.748
≤65	269 (60.7)	198 (57.7)	71 (71.0)		54 (63.5)	56 (65.9)	
>65	174 (39.3)	145 (42.3)	29 (29.0)		31 (36.5)	29 (34.1)	
Sex				0.168			0.679
Male	360 (81.3)	274 (79.9)	86 (86.0)		70 (82.4)	72 (84.7)	
Female	83 (18.7)	69 (20.1)	14 (14.0)		15 (17.6)	13 (15.3)	
KPS				0.322			0.341
≥90	376 (84.9)	288 (84.0)	88 (88.0)		77 (90.6)	73 (85.9)	
80	67 (15.1)	55 (16.0)	12 (12.0)		8 (9.4)	12 (14.1)	
Weight loss				0.028			0.868
Yes	170 (38.4)	141 (41.1)	29 (29.0)		27 (31.8)	26 (30.6)	
No	273 (61.6)	202 (58.9)	71 (71.0)		58 (68.2)	59 (69.4)	
Tumor location				< 0.001			0.977
Upper	120 (27.1)	104 (30.3)	16 (16.0)		15 (17.6)	14 (16.5)	
Middle	218 (49.2)	187 (54.5)	31 (31.0)		30 (35.3)	30 (35.3)	
Lower	105 (23.7)	52 (15.2)	53 (53.0)		40 (47.1)	41 (48.2)	
Tumor length (cm)				< 0.001*			1.000*
≤5	354 (79.9)	260 (75.8)	94 (94.0)		82 (96.5)	82 (96.5)	
>5	86 (19.4)	83 (24.2)	3 (3.0)		3 (3.5)	3 (3.5)	
Unknown	3 (0.7)	0 (0)	3 (3.0)				
LVI				0.027			1.000*
Yes	24 (5.4)	23 (6.7)	1 (1.0)		1 (1.2)	1 (1.2)	
No	419 (94.6)	320 (93.3)	99 (99.0)		84 (98.8)	84 (98.8)	
PNI				0.120			0.823
Yes	86 (19.4)	72 (21.0)	14 (14.0)		11 (12.9)	12 (14.1)	
No	357 (80.6)	271 (79.0)	86 (86.0)		74 (87.1)	73 (85.9)	
Total lymph nodes excised				0.005			1.000
<18	202 (45.6)	144 (42.0)	58 (58.0)		48 (56.5)	48 (56.5)	
≥18	241 (54.4)	199 (58.0)	42 (42.0)		37 (43.5)	37 (43.5)	

Notes: *Fisher's exact test; $P<0.05$ indicates statistically significant differences.
Abbreviations: KPS: Karnofsky performance status; LVI: Lymphovascular invasion; NCRT+S: Neoadjuvant chemoradiotherapy plus surgery; PNI: Perineural invasion; PSM: Propensity score matching.

CI = 0.52 – 0.91; P = 0.008) and the implementation of NCRT + S (NCRT + S vs. surgery; HR = 0.56; 95% CI = 0.37 – 0.85; P = 0.004) were significantly correlated with better OS. The results of the multivariate analysis indicated that age (P = 0.013), KPS (P < 0.001), total LNs excised (P = 0.003), and NCRT + S (P = 0.005) were independent prognostic factors for OS (Table 2). Similarly, analysis of the sample after PSM revealed that age (P = 0.009), the total number of LNs excised (P = 0.004), and NCRT + S status (P = 0.028) were independent prognostic factors affecting OS (Table A1 in Appendix).

3.3. Survival

The median survival time for all patients was 80.8 months (range = 0.2 – 156.6 months). The overall study cohort's 5-year OS and DFS rates were 56% and 50.2%, respectively. The NCRT + S group (3-year OS = 74.7%; 5-year OS = 69.7%; HR = 0.572, 95% CI = 0.407 – 0.804; P = 0.0059) had significantly better OS than the surgery group (3-year OS = 64.5%; 5-year OS = 52.9%) in the overall population (Figure 3A). While the NCRT + S group (3-year DFS = 64.2%; 5-year DFS = 60.6%) demonstrated higher DFS than the surgery group (3-year DFS = 58.4%; 5-year DFS = 48.2%), the difference was not statistically significant (HR = 0.784, 95% CI = 0.564 – 1.09; P = 0.17; Figure 3B).

Consistent results were observed in the matched populations. Relative to the surgery group (3-year OS = 65.3%; 5-year OS = 50.3%), the NCRT + S group showed significantly better OS outcomes (3-year OS = 72.1%; 5-year OS = 68.6%; HR = 0.613, 95% CI = 0.383 – 0.981; P = 0.04; Figure 3C). In contrast to the surgery group (3-year DFS = 58.2%; 5-year DFS = 45.9%), the NCRT + S group did not show a statistically significant improvement in DFS (3-year DFS = 61.9%; 5-year DFS = 58.1%; HR = 0.830, 95% CI 0.537 – 1.283; P = 0.39; Figure 3D).

3.4. Subgroup analysis

Subgroup analyses were conducted to identify which subgroups could achieve survival benefits from NCRT + S. The NCRT + S group was divided into pCR and non-pCR groups, and their survival rates were compared to the surgery group. Patients in the pCR group showed a significant improvement in OS compared to surgery alone (HR = 0.522, 95% CI = 0.339 – 0.804; P = 0.019, Figure 3E). In contrast, the non-pCR group did not show any significant OS benefits (P = 0.093, Figure 3E). Although the DFS of patients in the pCR group was longer than those who only underwent surgery, the difference was not statistically significant (P = 0.054, Figure 3F). Similarly, the non-pCR group did not show any significant benefit

Table 2. Univariate and multivariate Cox regression analyses for the overall survival of the entire cohort before propensity score matching

Variables	Univariate		Multivariate	
	HR (95% CI)	*P*-value	HR (95% CI)	*P*-value
Age (years) >65 versus≤65	1.41 (1.07 – 1.86)	0.016	1.42 (1.08 – 1.88)	0.013
Sex: Female versus Male	0.78 (0.54 – 1.13)	0.182		
KPS: 80 versus≥90	1.89 (1.35 – 2.63)	< 0.001	1.88 (1.34 – 2.62)	< 0.001
Weight loss: No versus Yes	1.09 (0.82 – 1.45)	0.548		
Tumor location		0.073		
Upper	1.00 (reference)			
Middle	0.77 (0.57 – 1.06)			
Lower	0.64 (0.43 – 0.95)			
Tumor length (cm)		0.418		
≤5	1.00 (reference)			
>5	1.25 (0.9 – 1.73)			
Unknown	0.83 (0.12 – 5.93)			
LVI: No versus Yes	1.26 (0.64 – 2.46)	0.486		
PNI: No versus Yes	0.72 (0.52 – 1.01)	0.063		
Total lymph nodes excised: ≥18 versus<18	0.69 (0.52 – 0.91)	0.008	0.65 (0.49 – 0.87)	0.003
Group: NCRT+S versus Surgery	0.56 (0.37 – 0.85)	0.004	0.55 (0.36 – 0.84)	0.005

Note: P<0.05 indicated statistically significant differences.
Abbreviations: CI: Confidence intervals; HR: Hazard ratio; KPS: Karnofsky Performance Status; LVI: Lymphovascular invasion; NCRT+S: Neoadjuvant chemoradiotherapy plus surgery; PNI: Perineural invasion.

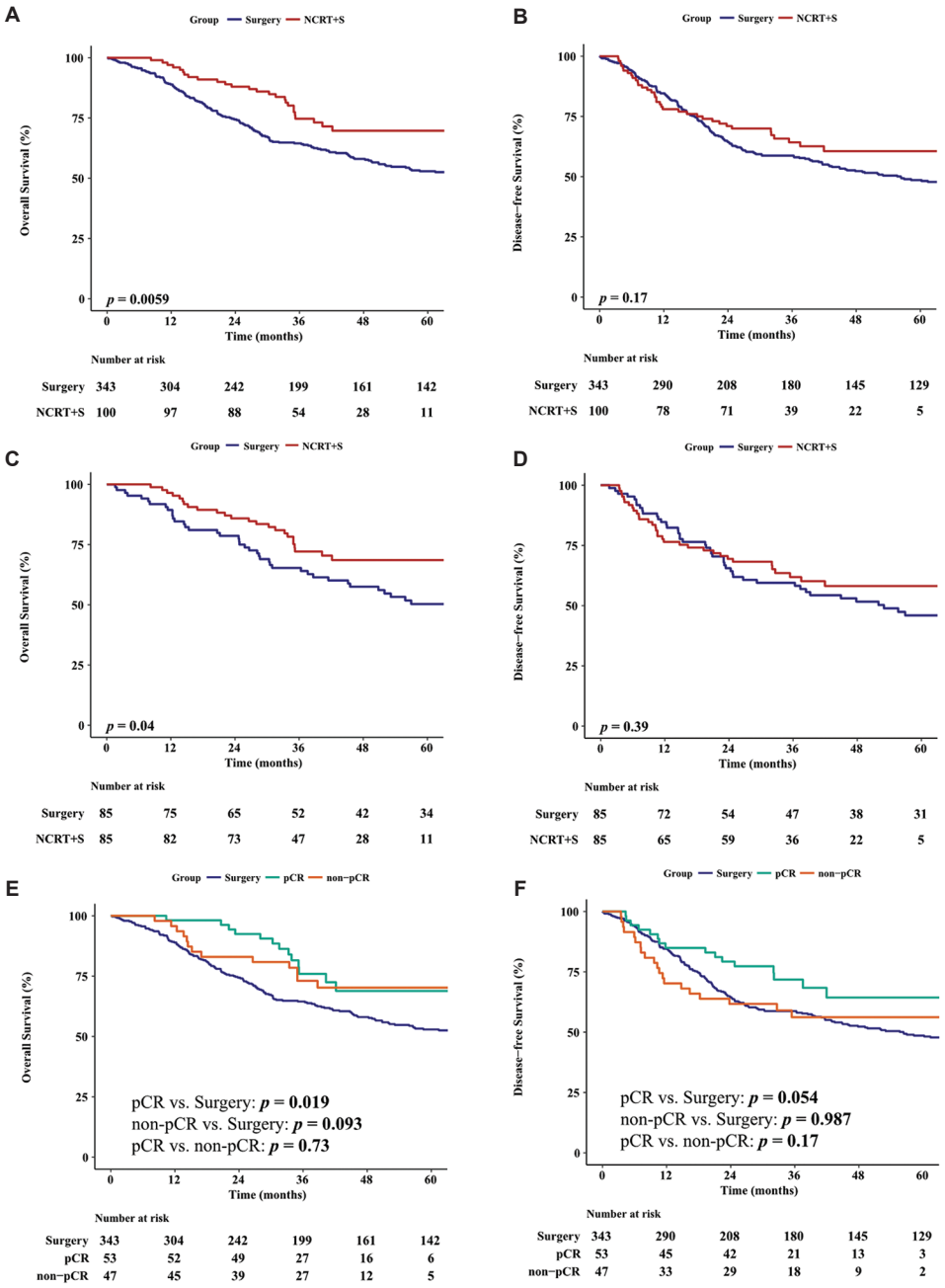

Figure 3. Kaplan–Meier curves for survival analysis in the study cohort and subgroup. (A) Overall survival across the entire population. (B) Disease-free survival across the entire population. (C) Overall survival in the matched sample. (D) Disease-free survival in the matched sample. (E) Overall survival in the subgroup. (F) Disease-free survival in the subgroup.
Abbreviations: NCRT+S: Neoadjuvant chemoradiotherapy plus surgery; pCR: Pathologically complete response.

regarding DFS (P = 0.987, Figure 3F). Within the NCRT + S group, neither the pCR nor the non-pCR groups showed any benefits regarding OS (P = 0.73, Figure 3E) or DFS (P = 0.17, Figure 3F).

Subgroups were also created based on age, gender, KPS, presence of weight loss, tumor location, tumor length, presence of LVI, presence of PNI, and the number of LNs excised, and a COX subgroup analysis was performed. The results showed that in the overall population, patients aged ≤65 years, male patients, those with KPS of 80, without weight loss, with tumor length ≤5 cm, without LVI, without PNI, and with fewer than 18 LNs excised significantly benefited from NCRT + S (all $P < 0.05$). Patients with LVI who underwent NCRT

+ S had an increased risk of death (HR = 10.99; 95% CI = 1.00 – 121.25), while in other subgroups, NCRT + S reduced the risk of death (Table 3). Patients with tumors located in the lower segment (HR = 1.17; 95% CI = 0.65 – 2.12), tumor length >5 cm (HR = 1.54; 95% CI = 0.37 – 6.39), or with vascular invasion had a significantly increased risk of progression when undergoing NCRT + S (Table 4).

Table 3. Subgroup analysis related to overall survival in the overall population

Subgroup S versus NCRT+S	Total	HR (95% CI)	*P*-value	*P*-value for interaction
Age (years)				0.939
≤65	269	0.58 (0.35 – 0.99)	0.045	
>65	174	0.59 (0.30 – 1.19)	0.142	
Sex				0.174
Male	360	0.60 (0.39 – 0.92)	0.020	
Female	83	0.19 (0.03 – 1.37)	0.098	
KPS				0.181
≥90	376	0.64 (0.41 – 1.01)	0.055	
80	67	0.30 (0.09 – 0.98)	0.046	
Weight loss				0.482
Yes	170	0.67 (0.32 – 1.40)	0.287	
No	273	0.51 (0.31 – 0.84)	0.009	
Tumor location				0.563
Upper	120	0.51 (0.20 – 1.29)	0.154	
Middle	218	0.46 (0.20 – 1.05)	0.065	
Lower	105	0.73 (0.38 – 1.40)	0.340	
Tumor length (cm)				0.74
≤5	354	0.56 (0.36 – 0.87)	0.009	
>5	86	0.85 (0.12 – 6.21)	0.872	
Unknown	3	NA (NA – NA)	NA	
LVI				0.045
Yes	24	10.99 (1.00 – 121.25)	0.050	
No	419	0.54 (0.35 – 0.82)	0.004	
PNI				0.719
Yes	86	0.65 (0.25 – 1.65)	0.362	
No	357	0.56 (0.35 – 0.90)	0.016	
Total lymph nodes excised				0.435
<18	202	0.43 (0.25 – 0.73)	0.002	
≥18	241	0.68 (0.35 – 1.32)	0.257	

Abbreviations: CI: Confidence intervals; HR: Hazard ratio; KPS: Karnofsky Performance Status; LVI: Lymphovascular invasion; NCRT+S: Neoadjuvant chemoradiotherapy plus surgery; PNI: Perineural invasion; S: Surgery.

3.5. Failure patterns in the whole population

At the final follow-up, the total number of failures (comprising local recurrences, distant metastases, and deaths) was 228/443 (51.5%). The NCRT + S and S groups included 36 and 192 patients, respectively. Of the 103 (103/443, 23.3%) local recurrences, 84 were intrathoracic local-regional recurrences, 12 were in the supraclavicular LNs, and seven were in the intraabdominal LNs. The NCRT + S group, with a rate of 14 (14/100), showed a significant reduction in local recurrence compared to the S group (89/343, 25.9%, $P = 0.013$). Fifty-two patients had distant metastases, including 13 with metastasis in the lung, four in the liver, three in the bone, three in the brain, 24 with two or more metastatic sites, and five with other metastatic locations. No significant differences were observed between the NCRT + S and S groups (11/100 vs. 41/343, $P = 0.794$). Thirteen patients experienced both local recurrences and distant metastases. Thirty-one deaths occurred due to fistulas, hematemesis, hemoptysis, and other non-tumor-related internal medical conditions. Twenty-one patients had unknown reasons for disease progression and cause of death; in contrast, eight patients developed a second primary tumor. The results are presented in Table 5.

4. Discussion

This study introduced a novel approach to evaluating patients with pre-T3N0M0 status and is the first to compare survival outcomes between NCRT + S and surgery alone in this specific group. The results confirmed that NCRT + S significantly improved OS in patients with pre-T3N0M0 status.

Patients in the NCRT + S group were selected based on their pretreatment clinical T stage (cT) rather than the post-operative pathological T (pT) stage. Previous studies[4,5,11] have confirmed that NCRT leads to tumor downstaging, so the post-operative pT staging does not accurately represent the pretreatment T stage in the NCRT + S group. Since endoscopic ultrasonography (EUS) and CT are widely used in clinical practice, this study utilized cT staging determined through EUS and CT. Both Lightdale and Kulkarni[19] and a meta-analysis[20] reported that the accuracy of EUS in diagnosing cT3 tumors in esophageal cancer was ≥90%. The accuracy of CT in distinguishing T3 lesions was 86.7%.[21] Therefore, the selection of patients with cT3 tumors in this study's NCRT + S group closely represented the actual pretreatment T3 status.

Due to the limited accuracy of CT in LN staging,[21] clinical N (cN) staging before treatment is often less reliable. A previous study[12] reported that approximately 50% of patients with ESCC who underwent surgery alone

Table 4. Subgroup analysis related to disease-free survival in the overall population

Subgroup S versus NCRT+S	Total	HR (95% CI)	crude.*P*_value	*P*-value for interaction
Age (years)				0.65
≤65	269	0.77 (0.49 – 1.2.0)	0.247	
>65	174	0.89 (0.48 – 1.64)	0.707	
Sex				0.024
Male	360	0.88 (0.61 – 1.28)	0.500	
Female	83	0.15 (0.02 – 1.07)	0.058	
KPS				0.114
≥90	376	0.90 (0.61 – 1.32)	0.586	
80	67	0.39 (0.14 – 1.09)	0.073	
Weight loss				0.429
Yes	170	0.95 (0.50 – 1.80)	0.875	
No	273	0.71 (0.46 – 1.09)	0.119	
Tumor location				0.193
Upper	120	0.53 (0.21 – 1.32)	0.174	
Middle	218	0.64 (0.32 – 1.26)	0.196	
Lower	105	1.17 (0.65 – 2.12)	0.594	
Tumor length (cm)				0.363
≤5	354	0.76 (0.52 – 1.11)	0.157	
>5	86	1.54 (0.37 – 6.39)	0.552	
Unknown	3	NA (NA – NA)	NA	
LVI				0.095
Yes	24	72004889078.07 (0 – Inf)	1.000	
No	419	0.76 (0.52 – 1.09)	0.134	
PNI				0.625
Yes	86	0.96 (0.40 – 2.27)	0.921	
No	357	0.77 (0.51 – 1.14)	0.191	
Total lymph nodes excised				0.234
<18	202	0.58 (0.36 – 0.94)	0.027	
≥18	241	0.98 (0.56 – 1.70)	0.935	

Abbreviations: CI: Confidence intervals; HR: Hazard ratio; KPS: Karnofsky Performance Status; LVI: Lymphovascular invasion; NCRT+S: Neoadjuvant chemoradiotherapy plus surgery; PNI: Perineural invasion; S: Surgery.

exhibited nodal overstaging (cN > pN). Although the pretreatment T stage could not be accurately determined through pathology, the LN status after NCRT can be assessed through pathological examination. Based on previous studies,[17,18] LNs without evidence of tumor involvement or regression were considered as true negative. In this context, patients with LN regression after NCRT and those diagnosed with LN metastasis through needle biopsy before treatment were excluded to reduce diagnostic errors. Therefore, this study successfully identified patients with an actual pretreatment N0 status through the pathological evaluation of LNs. In addition, a method to precisely identify patients with pN0 status before treatment is needed to ensure optimal care for those with pre-T3N0M0 status.

To account for the potential confounding effects of tumor downstaging and clinical mis-staging, a previous study[22] matched the clinical LN status with the pathological LN status to identify true LN-negative patients. They compared the efficacy of NCRT + S versus surgery alone in patients with true LN-negativity. The results indicated that in the true LN-negative group, NCRT + S did not significantly improve OS. However, that study only included patients with esophageal adenocarcinoma, and the proportion of patients with T3 status in the true LN-negative group was unknown. Gao *et al.*[23] conducted a similar study, which

Table 5. Failure patterns in the entire population

Variables	Total	Surgery	NCRT+S	*P*-value
	(*n*=443)	(*n*=343)	(*n*=100)	
Total failure, *n* (%)				<0.001
None	215 (48.5)	151 (44.0)	64 (64.0)	
Yes	228 (51.5)	192 (56.0)	36 (36.0)	
Failure patterns, *n* (%)				0.002*
None	215 (48.5)	151 (44.0)	64 (64.0)	
LR	103 (23.3)	89 (25.9)	14 (14.0)	
DM	52 (11.7)	41 (12.0)	11 (11.0)	
LR+DM	13 (2.9)	9 (2.6)	4 (4.0)	
Others	60 (13.5)	53 (15.5)	7 (7.0)	
LR, *n* (%)				0.013
Absent	340 (76.7)	254 (74.1)	86 (86.0)	
Present	103 (23.3)	89 (25.9)	14 (14.0)	
DM, *n* (%)				0.794
Absent	391 (88.3)	302 (88.0)	89 (89.0)	
Present	52 (11.7)	41 (12.0)	11 (11.0)	
LR and DM, *n* (%)				0.502*
Absent	430 (97.1)	334 (97.4)	96 (96.0)	
Present	13 (2.9)	9 (2.6)	4 (4.0)	
Others, *n* (%)				0.030
Absent	383 (86.5)	290 (84.5)	93 (93.0)	
Present	60 (13.5)	53 (15.5)	7 (7.0)	

Notes: *Fisher's exact test; $P<0.05$ indicates statistically significant differences.
Abbreviations: DM: Distant metastasis; LR: Local recurrences.

indicated that NCRT + S could provide survival benefits to true LN-negative patients. It was suspected that the inconsistency in the results of these two studies stems from inaccurate clinical staging. Although some researchers[7] found that NCRT + S significantly improved DFS and OS in patients with cT3N0M0 compared to surgery alone, they relied on clinical staging, and the N staging of patients in the surgery group was inconsistent with post-operative pathological staging, leading to controversial results. This study accurately identified patients with a true LN-negative status before treatment through pathological assessment, making the findings more reliable. Furthermore, this study also confirmed that patients with pre-T3N0M0 stage disease who underwent NCRT + S had superior OS outcomes, and even after PSM analysis, these patients still demonstrated similar survival outcomes. In addition, the survival rate in this study surpassed previous results,[4,5,7,22-25] likely due to the selection of patients accurately staged as pre-T3N0M0. However, the survival rate of the surgery group was in line with findings from other studies.[26,27] Age and the number of LNs removed were also identified as independent prognostic factors for OS, which has been reported in earlier research.[27,28]

Previous research[29,30] suggests that among patients undergoing NCRT + S, those achieving pCR have a significant survival advantage over patients with non-pCR. To better identify beneficiaries in the NCRT + S group, the patients were divided into pCR and non-pCR groups, and their prognosis was compared with that of the surgery group. It was found that compared with surgery alone, the pCR group showed improved OS; however, the non-pCR group did not. This result has not been reported previously. This study suggests that NCRT + S should be recommended for patients likely to achieve pCR after NCRT. Direct surgery might be advised if pCR cannot be achieved because the survival rates are similar. This is crucial for patients intolerant to chemoradiotherapy. Moreover, although NCRT + S treatment is relatively expensive for patients, it is still recommended for those who can benefit from NCRT, despite the high cost. For patients who cannot benefit from NCRT, opting for surgery alone can help avoid the high expenses, making it a better option for those with financial constraints. Nonetheless, there remains an urgent need for non-invasive pretreatment methods to predict whether patients can achieve a pCR after undergoing NCRT. At present, potential biomarkers for predicting NCRT treatment response in esophageal cancer include genetic markers and metabolic markers such as levels of lactic acid and glucose metabolism-related substances, which can reflect changes in tumor metabolic status and thus predict treatment response. In addition, imaging markers such as tumor volume changes obtained through imaging studies or tumor features extracted through radiomics methods to predict treatment response can be further researched in the future.

Considering the lack of significant benefit of NCRT + S on DFS in patients with pre-T3N0M0 disease, the failure patterns in the entire cohort were further analyzed. The results showed that NCRT + S significantly reduced the local recurrence rate. Previous studies[13,14] found that surgery alone significantly increased the local recurrence rate compared to post-operative adjuvant therapy. Similarly, the research confirmed that surgery alone significantly increased the local recurrence rate compared to NCRT + S. Therefore, local treatment is crucial for patients with pre-T3N0M0 esophageal cancer to reduce the risk of local recurrence.

This study had some limitations. First, being a single-center retrospective study, the findings require validation through multicenter prospective studies. Second, the status of the LNs that were not excised during surgery could not be assessed. Moreover, since NCRT + S treatment for T3N0M0 has only recently been widely adopted in clinical practice, the follow-up period for these patients remains

relatively short. Although post-operative pN0 is accurate, current pretreatment diagnostics struggle to identify pN0 disease. Developing methods to identify patients with pN0 disease through pretreatment diagnostics is essential to ensure that patients diagnosed with T3N0M0 receive the most appropriate treatment.

5. Conclusion

This study demonstrated that NCRT + S improves OS in patients with pre-T3N0M0 stage disease compared to surgery alone, especially in those who achieve pCR after NCRT. Moreover, NCRT + S reduces the local recurrence rate in patients with pre-T3N0M0 ESCC. NCRT + S is recommended for patients with pre-T3N0M0 who are likely to achieve pCR after NCRT. There is a demand for a noninvasive pretreatment method to accurately determine patients who are likely to achieve pCR.

Acknowledgments

We gratefully acknowledge Sichuan Cancer Hospital and Institute for the clinical data supported.

Funding

This work was supported by the Science and Technology Department of Sichuan Province (2023YFS0488 and 2023YFQ0055), Sichuan.

Conflict of interest

The authors declare no conflicts of interest.

Author contributions

Conceptualization: Qifeng Wang
Investigation: Ying Liu, Yehan Zhou, Xiaoding Zhou, Jingqiu Li, Jie Zhu, Yi Wang, Lei Wu, Gang Wan, Xuefeng Leng, Guangyuan Liu, Yongtao Han, Yang Liu, Lin Peng
Methodology: Yehan Zhou
Writing – original draft: Ying Liu
Writing – review & editing: Yehan Zhou, Qifeng Wang

Ethics approval and consent to participate

Ethical approval permission has been obtained from the Regional Ethical Committee (Nos: SCCHEC-02-2023-029).

Consent for publication

Not applicable.

Availability of data

This study retrospectively collected clinicopathological data of ESCC patients who underwent either NCRT or surgery alone from the electronic medical record system of Sichuan Cancer Hospital. In addition, for patients who underwent NCRT, pathological assessments of LNs were conducted using their pathology slides.

References

1. Sung H, Ferlay J, Siegel RL, *et al*. Global cancer statistics 2020: GLOBOCAN estimates of incidence and mortality worldwide for 36 cancers in 185 countries. *CA Cancer J Clin*. 2021;71(3):209-249.

   doi: 10.3322/caac.21660

2. Cao W, Chen HD, Yu YW, Li N, Chen WQ. Changing profiles of cancer burden worldwide and in China: A secondary analysis of the global cancer statistics 2020. *Chin Med J (Engl)*. 2021;134(7):783-791.

   doi: 10.1097/CM9.0000000000001474

3. Eyck BM, Van Lanschot JJ, Hulshof M, *et al*. Ten-year outcome of neoadjuvant chemoradiotherapy plus surgery for esophageal cancer: The randomized controlled CROSS trial. *J Clin Oncol*. 2021;39(18):1995-2004.

   doi: 10.1200/JCO.20.03614

4. Yang H, Liu H, Chen Y, *et al*. Neoadjuvant chemoradiotherapy followed by surgery versus surgery alone for locally advanced squamous cell carcinoma of the esophagus (NEOCRTEC5010): A phase III multicenter, randomized, open-label clinical trial. *J Clin Oncol*. 2018;36(27):2796-2803.

   doi: 10.1200/JCO.2018.79.1483

5. Shapiro J, Van Lanschot JJ, Hulshof M, *et al*. Neoadjuvant chemoradiotherapy plus surgery versus surgery alone for oesophageal or junctional cancer (CROSS): Long-term results of a randomised controlled trial. *Lancet Oncol*. 2015;16(9):1090-1098.

   doi: 10.1016/S1470-2045(15)00040-6

6. Markar SR, Gronnier C, Pasquer A, *et al*. Role of neoadjuvant treatment in clinical T2N0M0 oesophageal cancer: Results from a retrospective multi-center European study. *Eur J Cancer*. 2016;56:59-68.

   doi: 10.1016/j.ejca.2015.11.024

7. Mantziari S, Gronnier C, Renaud F, *et al*. Survival benefit of neoadjuvant treatment in clinical T3N0M0 esophageal cancer: Results from a retrospective multicenter European study. *Ann Surg*. 2017;266:805-813.

   doi: 10.1097/sla.0000000000002402

8. Rhodin KE, Raman V, Jawitz OK, *et al*. Patterns of use of induction therapy for t2n0 esophageal cancer. *Ann Thorac Surg*. 2021;111(2):440-447.

   doi: 10.1016/j.athoracsur.2020.05.089

9. Goense L, Visser E, Haj Mohammad N, *et al*. Role of

neoadjuvant chemoradiotherapy in clinical T2N0M0 esophageal cancer: A population-based cohort study. *Eur J Surg Oncol*. 2018;44(5):620-625.

doi: 10.1016/j.ejso.2018.02.005

10. Mariette C, Dahan L, Mornex F, *et al*. Surgery alone versus chemoradiotherapy followed by surgery for stage I and II esophageal cancer: Final analysis of randomized controlled phase III trial FFCD 9901. *J Clin Oncol*. 2014;32(23):2416-2422.

    doi: 10.1200/jco.2013.53.6532

11. Robb WB, Dahan L, Mornex F, *et al*. Impact of neoadjuvant chemoradiation on lymph node status in esophageal cancer. *Ann Surg*. 2015;261(5):902-908.

    doi: 10.1097/sla.0000000000000991

12. Dijksterhuis WP, Hulshoff JB, Van Dullemen HM, *et al*. Reliability of clinical nodal status regarding response to neoadjuvant chemoradiotherapy compared with surgery alone and prognosis in esophageal cancer patients. *Acta Oncol*. 2019;58(11):1640-1647.

    doi: 10.1080/0284186X.2019.1648865

13. Wang Q, Peng L, Li T, *et al*. Postoperative chemotherapy for thoracic pathological T3N0M0 esophageal squamous cell carcinoma. *Ann Surg Oncol*. 2020;27(5):1488-1495.

    doi: 10.1245/s10434-019-08112-1

14. Yang J, Zhang W, Xiao Z, *et al*. The impact of postoperative conformal radiotherapy after radical surgery on survival and recurrence in pathologic T3N0M0 esophageal carcinoma: A propensity score-matched analysis. *J Thorac Oncol*. 2017;12(7):1143-1151.

    doi: 10.1016/j.jtho.2017.03.024

15. Rice TW, Gress DM, Patil DT, Hofstetter WL, Kelsen DP, Blackstone EH. Cancer of the esophagus and esophagogastric junction-Major changes in the American joint committee on cancer eighth edition cancer staging manual. *CA Cancer J Clin*. 2017;67(4):304-317.

    doi: 10.3322/caac.21399

16. Davies AR, Myoteri D, Zylstra J, *et al*. Lymph node regression and survival following neoadjuvant chemotherapy in oesophageal adenocarcinoma. *Br J Surg*. 2018;105(12):1639-1649.

    doi: 10.1002/bjs.10900

17. Hsu PK, Yeh YC, Chien LI, Huang CS, Hsu HS. Clinicopathological significance of pathologic complete lymph node regression after neoadjuvant chemoradiotherapy in esophageal squamous cell carcinoma. *Ann Surg Oncol*. 2021;28(4):2048-2058.

    doi: 10.1245/s10434-020-09363-z

18. Hagi T, Makino T, Yamasaki M, *et al*. Pathological regression of lymph nodes better predicts long-term survival in esophageal cancer patients undergoing neoadjuvant chemotherapy followed by surgery. *Ann Surg*. 2022;275(6):1121-1129.

    doi: 10.1097/SLA.0000000000004238

19. Lightdale CJ, Kulkarni KG. Role of endoscopic ultrasonography in the staging and follow-up of esophageal cancer. *J Clin Oncol*. 2005;23(20):4483-4489.

    doi: 10.1200/JCO.2005.20.644

20. Puli SR, Reddy JB, Bechtold ML, Antillon D, Ibdah JA, Antillon MR. Staging accuracy of esophageal cancer by endoscopic ultrasound: A meta-analysis and systematic review. *World J Gastroenterol*. 2008;14(10):1479-1490.

    doi: 10.3748/wjg.14.1479

21. Lee G, Hoseok H, Kim SJ, *et al*. Clinical implication of PET/MR imaging in preoperative esophageal cancer staging: Comparison with PET/CT, endoscopic ultrasonography, and CT. *J Nucl Med*. 2014;55(8):1242-1247.

    doi: 10.2967/jnumed.114.138974

22. Gabriel E, Attwood K, Du W, *et al*. Association between clinically staged node-negative esophageal adenocarcinoma and overall survival benefit from neoadjuvant chemoradiation. *JAMA Surg*. 2016;151(3):234-245.

    doi: 10.1001/jamasurg.2015.4068

23. Gao HJ, Wei YC, Gong L, *et al*. Neoadjuvant chemoradiotherapy plus surgery versus surgery alone for clinical node-negative esophageal carcinoma. *Thorac Cancer*. 2020;11(9):2618-2629.

    doi: 10.1111/1759-7714.13586

24. Van Hagen P, Hulshof MC, Van Lanschot JJ, *et al*. Preoperative chemoradiotherapy for esophageal or junctional cancer. *N Engl J Med*. 2012;366(22):2074-2084.

    doi: 10.1056/NEJMoa1112088

25. Speicher PJ, Wang X, Englum BR, *et al*. Induction chemoradiation therapy prior to esophagectomy is associated with superior long-term survival for esophageal cancer. *Dis Esophagus*. 2015;28(8):788-796.

    doi: 10.1111/dote.12285

26. Li T, Fu X, Xiao L, *et al*. The long-term impact of tumor burden in pT3N0M0 esophageal squamous cell carcinoma. *Medicine*. 2019;98(42):e17637.

    doi: 10.1097/md.0000000000017637

27. Situ D., Wei W, Lin P, *et al*. Do tumor grade and location affect survival in esophageal squamous cell carcinoma? Survival analysis of 302 cases of pT3N0M0 esophageal squamous cell carcinoma. *Ann Surg Oncol*. 2012;20(2):580-585.

    doi: 10.1245/s10434-012-2656-0

28. Ho HJ, Chen HS, Hung WH, *et al*. Survival impact of total

resected lymph nodes in esophageal cancer patients with and without neoadjuvant chemoradiation. *Ann Surg Oncol*. 2018;25(13):3820-3832.

doi: 10.1245/s10434-018-6785-y

29. Wong IY, Chung JC, Zhang RQ, *et al*. A novel tumor staging system incorporating tumor regression grade (TRG) with lymph node status (ypN-category) results in better prognostication than ypTNM stage groups after neoadjuvant therapy for esophageal squamous cell carcinoma. *Ann Surg*. 2022;276(5):784-791.

doi: 10.1097/SLA.0000000000005636

30. Steffen T, Dietrich D, Schnider A, *et al*. Recurrence patterns and long-term results after induction chemotherapy, chemoradiotherapy, and curative surgery in patients with locally advanced esophageal cancer. *Ann Surg*. 2019;269(1):83-87.

doi: 10.1097/SLA.0000000000002435

Appendix

Table A1. Univariate and multivariate Cox regression analyses for the overall survival of the entire cohort after PSM

Variables	Univariate		Multivariate	
	HR (95% CI)	*P*-value	HR (95% CI)	*P*-value
Age (years) >65 versus≤65	1.91 (1.18 – 3.07)	0.009	1.89 (1.17 – 3.06)	0.009
Sex: Female versus Male	1.12 (0.60 – 2.08)	0.729		
KPS: 80 versus≥90	1.31 (0.67 – 2.57)	0.450		
Weight loss: No versus Yes	0.85 (0.51 – 1.41)	0.524		
Tumor location		0.545		
Upper	1.00 (reference)			
Middle	0.75 (0.39 – 1.43)			
Lower	0.70 (0.38 – 1.30)			
Tumor length (cm): >5 versus≤5	2.10 (0.66 – 6.70)	0.261		
LVI: No versus Yes	0.86 (0.12 – 6.25)	0.886		
PNI: No versus Yes	0.98 (0.49 – 1.98)	0.958		
Total lymph nodes excised: ≥18 versus<18	0.49 (0.30 – 0.82)	0.005	0.47 (0.28 – 0.79)	0.004
Group: NCRT+S versus surgery	0.59 (0.36 – 0.98)	0.039	0.57 (0.34 – 0.94)	0.028

Note: $P<0.05$ indicates statistically significant differences.
Abbreviations: CI: Confidence intervals; HR: Hazard ratio; KPS: Karnofsky Performance Status; LVI: Lymphovascular invasion; NCRT+S: Neoadjuvant chemoradiotherapy plus surgery; PNI: Perineural invasion.

ACCSCIENCE PUBLISHING

Advances in Radiotherapy & Nuclear Medicine

ORIGINAL RESEARCH ARTICLE

Association between ^{82}Rb positron emission tomography-derived regional myocardial blood flow, severity of angiographic coronary artery stenosis, and mortality in patients with chest pain

Cesia Gallegos[1]*, Camila Trejo Paredes[1†], Jiun-Ruey Hu[1†], Edith L. Posada[2], Yuichi Saito[3], Alexandra Lansky[1], Samit Shah[1], Yi-Hwa Liu[1], Kim G. Smolderen[1,4], Carlos Mena-Hurtado[1], Albert J. Sinusas[1], and Edward J. Miller[1]

[1]Department of Medicine, Yale School of Medicine, Yale University, New Haven, Connecticut, United States of America

[2]Department of Cardiology, National Institute of Cardiology Ignacio Chávez, Mexico City, Mexico

[3]Department of Cardiology, School of Medicine, Teikyo University, Tokyo, Japan

[4]Department of Psychiatry, Yale School of Medicine, Yale University, New Haven, Connecticut, United States of America

[†]*These authors contributed equally to this work.*

***Corresponding author:**
Cesia Gallegos
(cesia.gallegoskattan@yale.edu)

Citation: Gallegos C, Paredes CT, Hu J, *et al*. Association between ^{82}Rb positron emission tomography-derived regional myocardial blood flow, severity of angiographic coronary artery stenosis, and mortality in patients with chest pain. *Adv Radiother Nucl Med*. 2024;2(3):3786.
doi: 10.36922/arnm.3786

Received: May 29, 2024

Accepted: July 27, 2024

Published Online: September 23, 2024

Abstract

Impairment in global myocardial flow reserve (MFR) on rubidium-82 (^{82}Rb) positron emission tomography (PET) stress testing predicts cardiovascular events; however, the relationship between regional coronary artery territory myocardial blood flow (MBF) and invasive coronary angiography is unknown. In this study, patients with acute chest pain who were referred for coronary angiography after abnormal PET stress testing were evaluated. Both global and regional coronary territory stress and rest MBF were derived using ^{82}Rb PET. Coronary artery stenosis severity was assessed using quantitative coronary angiography (QCA) performed within 3 months of PET. A total of 189 patients were followed for a median of 4.1 years. The results showed a weak correlation between regional MFR impairment (<1.7) and stenosis severity in the left descending artery (r = –0.20, P = 0.005), left circumflex artery (r = –0.15, P = 0.042), and right coronary artery (r = –0.26, P < 0.001). In addition, a weak correlation was observed between global MFR and stenosis in any vessel, in both binary and continuous analyses. However, impairment in MFR within any territory was associated with increased all-cause mortality in both unadjusted and adjusted analyses. In conclusion, this is the first large-scale study to examine the relationship between regional coronary territory MBF, coronary artery stenosis severity as assessed using QCA, and mortality. Although coronary territory MFR demonstrated a weak correlation with coronary stenosis severity, impairment in per-territory MFR was significantly associated with increased all-cause mortality, suggesting that mechanisms such as diffuse atherosclerosis and/or microvascular disease may be contributing factors.

Keywords: Myocardial blood flow; Myocardial flow reserve; Positron emission tomography; Perfusion; Coronary microvascular disease

1. Introduction

Positron emission tomography (PET) myocardial perfusion imaging (MPI) is highly accurate for the diagnosis of coronary artery disease (CAD) and risk assessment.[1] Multiple studies have evaluated the diagnostic accuracy of PET MPI in CAD, demonstrating that the sensitivity of PET for detecting obstructive CAD is 92% and 95% for single-vessel and multivessel CAD, respectively.[2-5] PET also allows for non-invasive quantification of absolute global and regional myocardial blood flow (MBF; expressed as ml/min/g) and myocardial flow reserve (MFR; ratio of stress/rest MBF) using tracers such as rubidium-82 (^{82}Rb). Measurement of MBF has been shown to improve diagnostic accuracy and provides incremental prognostic information compared to measures of relative perfusion alone, particularly in multivessel disease.[6-10]

Global and regional MBF are also important prognostic tools in patients with and without obstructive CAD.[9,11-16] PET MPI with MBF quantification is the non-invasive gold-standard modality for the diagnosis of coronary microvascular dysfunction[10] by quantifying reductions in hyperemic MBF and/or MFR,[10] thus avoiding costly and repeated invasive testing.

Despite all the advances in the understanding of invasive and non-invasive coronary physiology assessment and global ^{82}Rb-derived MBF, there is a paucity of data on the correlation between regional MBF and angiographic severity of CAD, its implications for revascularization, and its relationship to all-cause mortality. To date, there are no large studies evaluating the correlation between regional MBF/MFR and angiographic stenoses to validate its widespread use for referral for invasive procedures. With this background, our study seeks to determine the relation between ^{82}Rb-derived regional MBF indices and percent area stenosis through quantitative coronary angiography (QCA), and their relationship to all-cause mortality.

2. Methods

We performed a retrospective review of consecutive adult patients from the Yale Nuclear Cardiology PET lab who underwent cardiac dynamic three-dimensional (3D) ^{82}Rb PET/computed tomography (CT) with regadenoson stress, followed by coronary angiography within 3 months. We excluded patients with low-quality angiographic films (unable to perform QCA), uninterpretable MBF measurements, previous coronary artery bypass graft (CABG), heart transplant, and dobutamine or adenosine stress. A schematic of the study design is presented in Figure 1.

2.1. PET/CT imaging protocol

Dynamic rest and stress ^{82}Rb PET MPI was performed on a 3D PET/CT camera with a 64-slice CT scanner (Discovery 690, GE Healthcare, USA). The stress and imaging protocols used have been described in previous work by our group.[17]

2.2. QCA

Standard coronary angiographic images were analyzed with at least two projections obtained per vessel distribution and angles of projection optimized for the cardiac position. In each patient, luminal diameter stenoses of the major epicardial coronary arteries were clinically graded by subjective visual consensus of two experienced operators and then analyzed using two-dimensional QCA at the Yale Cardiovascular Research Group Angiographic Core Laboratory (QAngio XA; 7.4 MEDIS, Netherlands), which was applied to both obstructive and non-obstructive atherosclerotic plaques from the reference vessel. Either isocenter or catheter calibration was applied. Coronary lesions were analyzed for qualitative atherosclerotic plaque characteristics. Diameter and length (mm) of obstruction and area (mm^2), along with percent stenosis, were measured and then compared to visual stenosis grading. Percent stenosis was calculated as:

([1-minimal lumen diameter]/reference vessel diameter) × 100 (I)

Other characteristics, such as symmetry and area of plaque and the distal and proximal stenosis measurements were also obtained. All traced lesions were manually

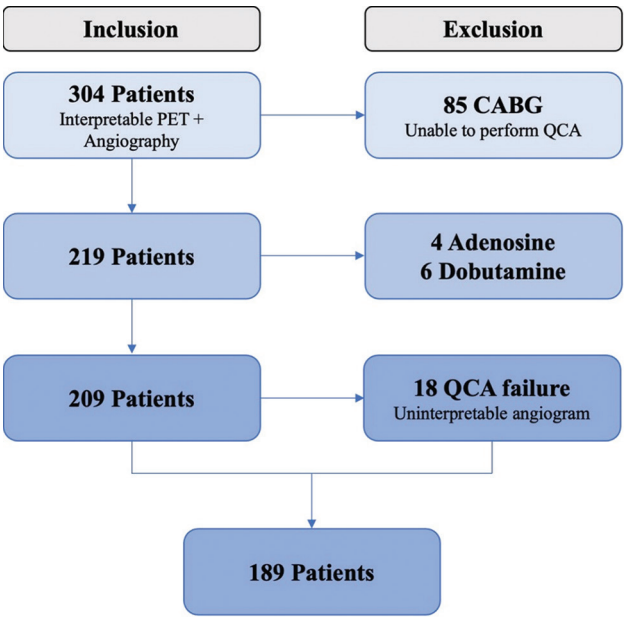

Figure 1. Study flow diagram
Abbreviations: CABG: Coronary artery bypass graft; QCA: Quantitative coronary angiography.

corrected for magnification distortion and pincushion. Two trained technicians evaluated all QCA measurements to reduce interobserver variability. A significant stenosis was defined as ≥50% of luminal obstruction, given the overall low number of events in the population.

2.3. Statistical analysis

Categorical variables were compared with Chi-square tests or Fisher's exact tests as appropriate. Heterogeneity was evaluated through the coefficient of variance (standard deviation [SD]/mean). Continuous variables were analyzed using pairwise comparisons with paired *t*-tests or Wilcoxon signed-rank tests as appropriate. A two-tailed $P < 0.05$ was considered statistically significant. The association of impaired regional and global flow reserve (MFR-cutoffs defined below) and significant stenosis (≥50% on QCA) was first assessed as binary variables. The sensitivity, specificity, positive and negative predictive value, accuracy, and positive and negative likelihood ratio were calculated for the ability of MFR impairment to predict ≥50% stenosis on QCA. The association between per vessel degree of stenosis and flow reserve was assessed using the Spearman correlation of continuous variables. The vital status of all patients was assessed through chart review in September 2022 (3 years after the last PET was done). The relationship between regional MFR impairment (defined below) and all-cause mortality was evaluated in unadjusted and adjusted survival analyses. Kaplan–Meier curves were compared with log-rank tests. Cox proportional hazards regression was performed with adjustment for age, sex, body mass index (BMI), diabetes history, CAD history, heart failure (HF) history, smoking, and need for subsequent revascularization. Subsequent revascularization was coded as a binary variable based on whether the patient underwent subsequent percutaneous coronary intervention (PCI) or CABG. Statistical analysis was performed in R (R Foundation for Statistical Computing, Vienna, Austria).

2.4. Determination of regional coronary territory MFR cutoff values

We first ascertained the level of regional coronary territory MFR that would optimally distinguish between the presence and absence of significant (≥50%) stenosis in the corresponding vessel (binary variables): left descending artery (LAD) MFR <1.7 had the optimal sensitivity (69%) and specificity (60%) for significant LAD stenosis, right coronary artery (RCA) MFR <1.4 had the optimal sensitivity (46%) and specificity (80%) for significant RCA stenosis, and left circumflex artery (LCX) MFR <1.5 had the optimal sensitivity (65%) and specificity (66%) for significant LCX stenosis (Table S1, top).

We then ascertained the level of global MFR that would optimally distinguish between the presence and absence of significant (≥50%) stenosis in each vessel (binary variable). A global MFR <1.7 had the optimal sensitivity (66%) and specificity (56%) for significant LAD stenosis, a global MFR <1.7 had the optimal sensitivity (57%) and specificity (55%) for significant RCA stenosis, and a global MFR <1.6 had the optimal sensitivity (65%) and specificity (65%) for significant LCX stenosis (Table S1, bottom). We performed survival analysis based on whether patients had MFRs above or below the coronary territory-specific MFR cutoffs.

3. Results

3.1. Patient characteristics

A total of 304 patients underwent dynamic ^{82}Rb PET MPI and were clinically referred to coronary angiography by their treating clinicians during the study period. A total of 115 patients were excluded from the analysis due to prior CABG precluding accurate assessment of QCA and MFR, poor angiographic films and/or uninterpretable QCA, and/or non-regadenoson stress (Figure 1). Among the 189 patients that were included, 43% (82/189) were women, the median age was 66 years (interquartile range [IQR]: 56, 74), and the mean BMI was 34.5 kg/m^2 (SD: 8.8). 51% (97/189) of patients had a perfusion defect of ³10% of the left ventricle (LV). The baseline characteristics of the included group are summarized in Table 1. There was no statistical difference in the baseline characteristics in the patients who did or did not have a baseline perfusion defect of ≥10% of the LV. The distribution of the percentage of perfusion defects is shown in Figure S1. Median regional MFR was reduced in all coronary territories: 1.75 (IQR: 1.40, 2.19) in the LAD territory, 1.76 (IQR: 1.36, 2.27) in the RCA territory, and 1.71 (IQR: 1.30, 2.16) in the LCX territory. The median global MFR was 1.73 (IQR: 1.36, 2.20).

3.2. Quantitative coronary analysis

Table 2 shows the characteristics of the vessels through QCA. For the LAD, the median obstruction diameter was 1.6 mm [1.21, 1.93] and the median percent stenosis was 29.81% [24.61, 45.00]; for the RCA, the median obstruction diameter was 1.73 mm [1.27, 2.30] and median percent stenosis was 28.57% [21.53, 45.09]; and for the LCX, the median obstruction diameter was 1.73 mm [1.30, 2.15] and median percent stenosis was 27.51% [23.02, 36.67]. 17% (32/187) of patients had LAD stenosis >50%; 20% (37/183) of patients had RCA stenosis >20%; 9% (17/186) of patients had LCX stenosis >50%.

Table 1. Baseline patient characteristics (*n*=189)

Variables	Value (%)
Gender (*n*[%])	
Female	82 (43)
Male	107 (56.6)
Age (Median [IQR], year)	66 (56,74)
BMI	34.5
Race (*n*[%])	
Black/African American	38 (20.1)
White/Caucasian	130 (68.8)
Hispanic/Latino	15 (7.9)
Other	6 (3.1)
Hypertension (*n*[%])	145 (77.5)
Diabetes (*n*[%])	87 (46.5)
Hyperlipidemia (*n*[%])	126 (67.4)
Smoking (*n*[%])	38 (20.3)
Chronic renal disease (*n*[%])	25 (13.4)
Peripheral vascular disease (*n*[%])	16 (8.6)
Family history of CAD (*n*[%])	22 (11.8)

Abbreviations: BMI: Body mass index; CAD: Coronary artery disease; IQR: Interquartile range.

Table 2. Characteristics of stenosis in each vessel on quantitative coronary angiography in the full sample

Vessels	Obstruction diameter (mm)	Obstruction length (mm)	Stenosis percent (%)
LAD	1.60 (1.21, 1.93)	7.71 (5.13, 11.33)	29.81 (24.61, 45.00)
RCA	1.73 (1.27, 2.30)	7.38 (5.45, 11.23)	28.57 (21.53, 45.09)
LCX	1.73 (1.39, 2.15)	6.30 (4.55, 10.34)	27.51 (23.02, 36.67)

Note: Values are expressed as median (interquartile range).
Abbreviations: LAD: Left descending artery; LCX: Left circumflex artery; RCA: Right coronary artery.

3.3. Relationship between regional MFR and severity of angiographic stenosis

To further explore the relationship between regional coronary territory MFR and angiographic stenosis, we examined both features as continuous variables using the cutoff values previously described. There was a weak correlation between LAD territory MFR and LAD percent stenosis (r = −0.20, P = 0.005), RCA territory MFR and RCA percent stenosis (r = −0.26, P < 0.001), and to a lesser extent, between LCX territory MFR and LCX percent stenosis (r = −0.15, P = 0.042) (Figure 2). The regional coronary territory MFR was not strongly correlated with per-vessel percent stenosis on cubic spline modeling (Figure S2). We also calculated the positive and negative predictive values of regional coronary territory MFR. The

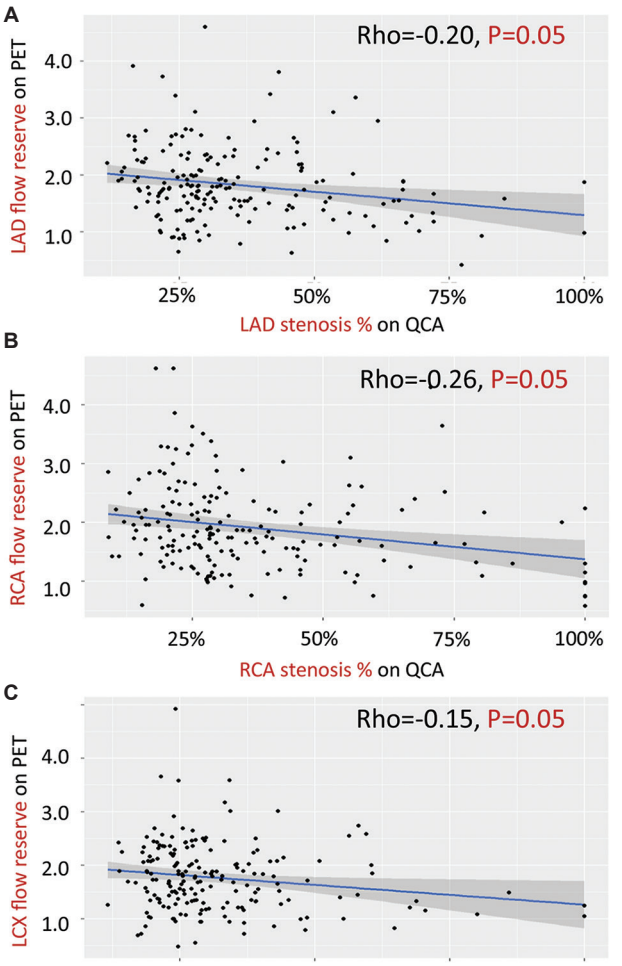

Figure 2. Correlation between regional coronary territory myocardial flow reserve and per-vessel angiographic percent stenosis as continuous variables in the (A) LAD, (B) RCA, and (C) LCX
Abbreviations: LAD: Left descending artery; LCX: Left circumflex artery; RCA: Right coronary artery.

regional MFR cutoffs had a low positive predictive value (0.26, 0.37, and 0.16 for LAD, RCA, and LCX, respectively) but a high negative predictive value (0.90, 0.85, and 0.95) for significant per-vessel stenosis (Table S2, top).

There was a weak correlation between global MFR and LAD percent stenosis (r = −0.17, P = 0.018), global MFR and RCA percent stenosis (r = −0.19, P = 0.009), and to a lesser extent, between global MFR and LCX percent stenosis (r = −0.15, P = 0.047) (Figure 3). The global MFR was not strongly correlated with per-vessel percent stenosis on cubic spline modeling (Figure S3). These global MFR cutoffs had a low positive predictive value (0.24, 0.24, and 0.16 for the LAD, RCA, and LCX, respectively) but a high negative predictive value (0.89, 0.83, and 0.95) for significant per-vessel stenosis (Table S2, bottom).

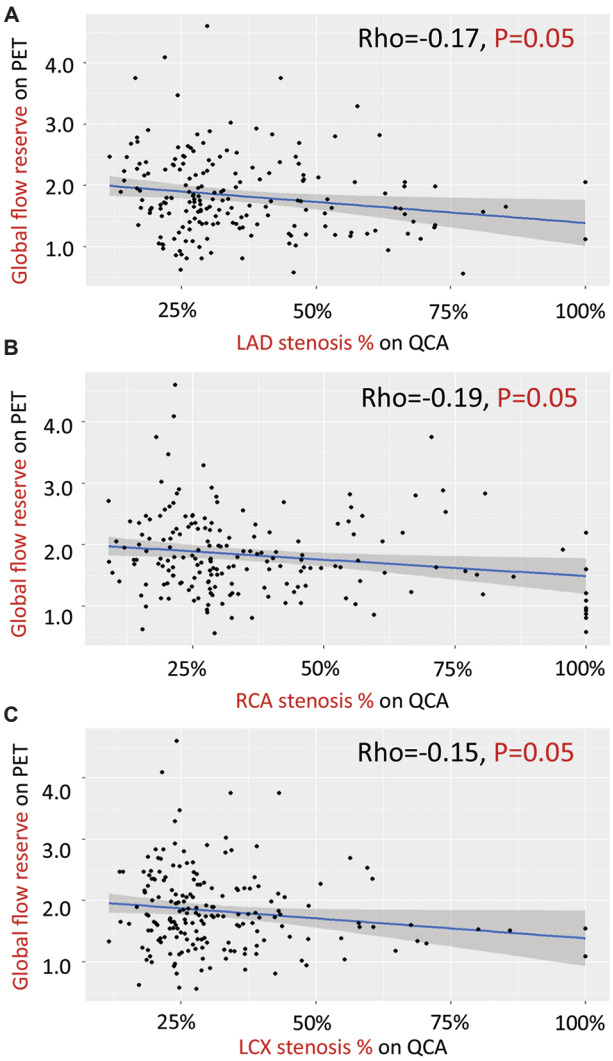

Figure 3. Correlation between global myocardial flow reserve and per-vessel angiographic percent stenosis as continuous variables in the (A) LAD, (B) RCA, and (C) LCX
Abbreviations: LAD: Left descending artery; LCX: Left circumflex artery; RCA: Right coronary artery.

3.4. Unadjusted all-cause mortality associated with impaired regional MFR

We then sought to ascertain if impairment in regional coronary territory MFR had any prognostic implication despite its weak correlation with angiographic percent stenosis. Median survival in our cohort was 4.1 years (IQR: 3.7, 4.5). A total of 38/189 (20%) individuals died. Individuals with LAD MFR <1.7 had poorer survival ($P_{log\text{-}rank}$ = 0.007) compared to those without impaired LAD MFR (Figure 4A). This was also true for individuals with RCA MFR <1.7 ($P_{log\text{-}rank}$ <0.001) compared to those without impaired RCA MFR (Figure 4B) and those with LCX MFR <1.7 ($P_{log\text{-}rank}$ = 0.002) compared to those without impaired LCX MFR (Figure 4C). Individuals with global MFR <1.7 had overall poorer survival ($P_{log\text{-}rank}$ = 0.002) compared to those without impaired global MFR (Figure 4D). Note that 59/189 (31%) patients had impairment in all four MFR parameters (LAD, RCA, LCX, and global) (Figure S4).

3.5. Unadjusted all-cause mortality associated with perfusion defects in ≥10% of territory

To ascertain the role of epicardial versus microvascular disease, we examined the survival of patients with and without baseline perfusion defects spanning ≥10% and <10% of LV segments. There was no significant difference ($P_{log\text{-}rank}$ = 0.56) in all-cause mortality of patients whose perfusion defects were ≥10% and <10% of the LV (Figure 5). There was no significant difference in LAD territory MFR, RCA territory MFR, LCX territory MFR, or global MFR between patients whose perfusion defects were ≥10% and <10% of the LV (Table S3).

3.6. Adjusted all-cause mortality associated with impaired MFR

We adjusted for age at the time of PET MPI, sex, BMI, presence of Type 2 diabetes, CAD, HF, smoking history, and need for subsequent revascularization to further account for the possibility of confounders in patient survival. 3% (6/189) of patients underwent subsequent CABG, and 6% (11/189) of patients underwent subsequent PCI. After adjustment for covariates, all parameters (regional and global MFR <1.7) were associated with higher mortality: LAD territory MFR (adjusted hazard ratio [aHR] = 2.1, 95% confidence interval [CI] = 1.048 – 4.3, P_{Cox} = 0.037); RCA territory MFR (aHR = 3.4, 95% CI = 1.6 – 7.1, P_{Cox} = 0.001); LCX territory (aHR = 2.8, 95% CI = 1.4 – 5.9, P_{Cox} = 0.006); global MFR <1.7 (aHR = 2.7, 95% CI = 1.3 – 5.7, P_{Cox} = 0.007).

4. Discussion

To the best of our knowledge, this is the first large study to examine the relationship between regional coronary territory MBF and MFR and coronary artery stenosis through QCA, and its relationship to all-cause mortality. Furthermore, we assessed whether there is an optimal threshold of hyperemic MBF or MFR that can be used routinely to predict stenosis severity. Current data support that a global hyperemic MBF of >2 mL/min/g and MFR of more than >2 reliably excludes the presence of high-risk angiographic CAD.[9,11,16] Multiple studies also support that global MFR <1.5 is suggestive of higher-risk CAD.[8,12,13]

Our research yielded several important findings. First, it found that while a regional LAD territory MFR of <1.7 is suggestive of obstructive disease in the LAD, there was significant heterogeneity in this association,

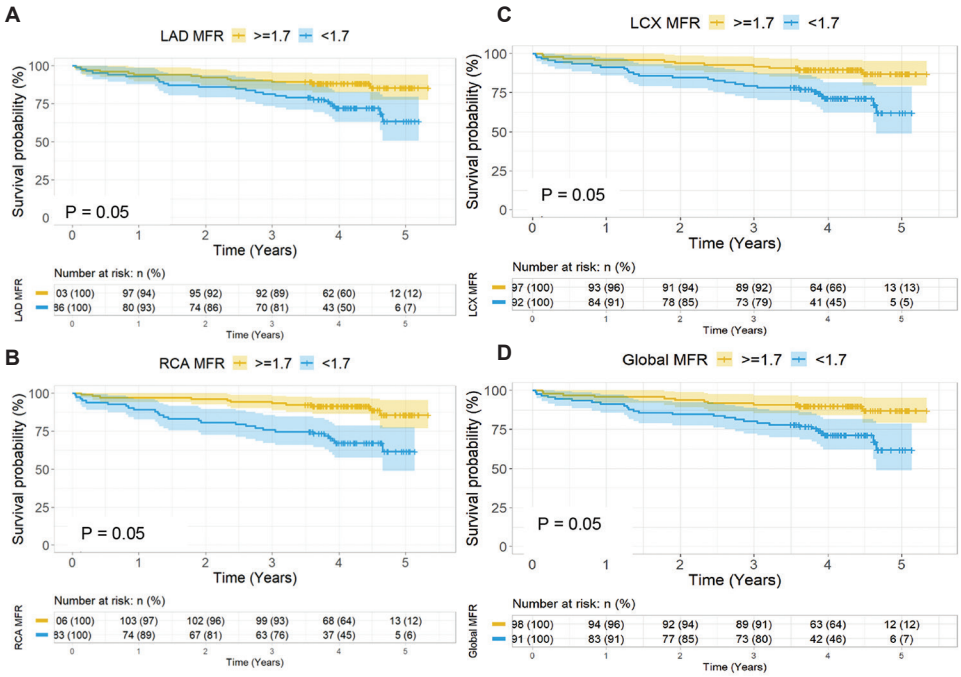

Figure 4. Kaplan–Meier plots depicting survival (all-cause mortality inverse) of patients according to whether they had impairments in MFR of the coronary territories of the (A) LAD, (B) RCA, (C) LCX, (D) globally < 1.7. Patients with impaired MFR are denoted in blue, while patients with preserved MFR are denoted in yellow

Abbreviations: LAD: Left descending artery; LCX: Left circumflex artery; MFR: Myocardial flow reserve; RCA: Right coronary artery.

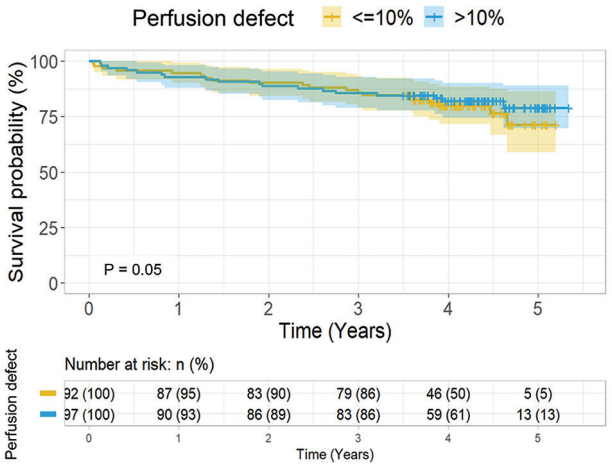

Figure 5. Kaplan-Meier plot depicting survival (all-cause mortality inverse) of patients according to whether they had resting perfusion defects spanning >10% (in blue) or ≤10% (in yellow) of left ventricular myocardial segments

suggesting regional MFR and MBF are overall modest indicators of regional obstructive CAD. Second, this study also demonstrates that regional coronary territory MBF is only weakly associated with stenoses ≥50% across all three vessels, even when accounting for baseline perfusion defects at rest. In our study, we defined significant stenosis as ≥50%, as it has also been used in other studies.[18] Lesions >40% are recognized in the literature as intermediate and have been associated with variability in hyperemic MBF and MFR, which is concordant with our data. Small cohorts have shown a close correlation between MBF and MFR estimates with quantitative measurements of stenosis severity on coronary in stenosis >40%.[19,20] Unsurprisingly, our findings suggest a multifactorial discordance between regional coronary territory MBF and QCA, likely due to the fact that MBF indices integrate not only epicardial CAD but also microvascular function.[21] Other pathophysiologic processes that may explain this discordance include interindividual variability in hyperemic blood flows and flow reserve, stenosis location within the vessel (mid, proximal, distal, entrance, and exit angles),[22,23] concomitant microvascular disease,[21] presence of collaterals, or significant stenoses in other vessels leading to coronary steal.

Our study also has significant implications for decisions on downstream testing with coronary angiography. Our results show that a normal regional coronary territory MBF has an excellent negative predictive value for obstructive epicardial CAD ranging from 85 to 95% in all three vessels and was similar to the range of 83 – 95% for global MFR. These findings are in line with other studies previously published[24] and add to the evidence that the addition of regional coronary territory MBF indices to

perfusion data could be a strong tool to reduce potentially unnecessary downstream invasive testing. Conversely, regional MFR had a low positive predictive value to detect true obstructive disease per vessel, likely secondary to the vascular and anatomic considerations described earlier. This may be overcome with the use of hybrid imaging, as described by Javadi *et al.*[25]

It is known that globally reduced MFR is a relevant marker for predicting short-term cardiovascular events.[26] Our study expands this concept by showing that regional coronary territory MFR at or below the cutoffs described were associated with increased all-cause mortality compared to those without impaired regional MFR, even after adjusting for known risk factors, including revascularization. The integration of this important finding into anatomical and perfusion data could be used to guide treatment, including the decision for medical management versus revascularization, as well as preventive measures.

Our study has several potential methodological limitations that might have influenced our results. Although this is the largest study to date reporting on the applicability of regional coronary territory MBF indices on the prediction of significant coronary stenosis, this was a single-center, retrospective, non-randomized study, which carries inherent limitations to this design, including referral bias. Another limitation is that the study is underpowered to detect "true negatives" and specificity since the angiographic referral was clinically decided. In addition, despite the large amount of data collected over 2 years, the number of events (stenoses ≥50%) was low, limiting the power. The inclusion of patients with prior myocardial infarction also confounds the relationship between flow and stenosis, as it may reduce stress flow and regional MFR depending on the degree of injury and total LV mass affected. Though this was accounted for in the subgroup analysis, it further decreased the number of events per group (prior infarction versus no prior infarction). Important angiographic characteristics, such as shape, serial stenosis, and vessel morphology that may significantly affect resistance, were not evaluated. Finally, a good proportion of patients had decreased MFR without significant lesions, which raises the question of the presence of isolated microvascular dysfunction in this population. Studies have reported that these patients constitute ≤20% of patients with angina and no obstructive disease.[27] Hence, the presence of microvascular disease in our cohort is likely a significant contributor to decreased regional blood follow, which is currently being investigated.

5. Conclusion

Data are lacking regarding the correlation of regional MBF and MFR with angiographically defined CAD, which could, therefore be used to guide revascularization decision-making. Our study suggests that at different cutoff MFR values per coronary territory, for example, ≤1.7 in the LAD, ^{82}Rb PET regional MFR has a specificity of 65% and negative predictive value of 89% to predict ≥50% stenosis across all vessels. Although there is heterogeneity in the association between regional coronary territory MFR and the degree of stenosis, our data suggest that regional MFR performs best in predicting normal tests and decreasing downstream invasive testing. Larger studies with an increased number of events (stenosis ≥50%) and incorporation of individual coronary anatomy are crucial in elucidating this relationship.

Acknowledgments

None.

Funding

None.

Conflict of interest

Kim G. Smolderen is a consultant for Happify, Hook, and UnitedHealthcare. Carlos Mena Hurtado is a consultant for Cook and Abbott. Edward J. Miller is a consultant for Alnylam, Pfizer, GE, and CSL Behring. The other authors have no conflicts of interest to declare.

Author contributions

Conceptualization: Cesia Gallegos, Edward J. Miller, Albert J. Sinusas
Formal analysis: Jiun-Ruey Hu, Edith L. Posadas
Investigation: Cesia Gallegos, Camila Trejo Paredes, Edward J. Miller, Albert J. Sinusas, Carlos Mena-Hurtado, Alexandra Lansky, Yuichi Saito
Methodology: Cesia Gallegos, Camila Trejo Paredes, Edward J. Miller, Kim G. Smolderen, Samit Shah
Writing – original draft: Cesia Gallegos, Camila Trejo Paredes, Jiun-Ruey Hu
Writing – review & editing: All authors

Ethics approval and consent to participate

This study was approved by the Yale Institutional Review Board (IRB) (Approval ID: 2000021621).

Consent for publication

Not applicable.

Availability of data

The data underlying this article will be shared on reasonable request to the corresponding author.

References

1. Murthy VL, Bateman TM, Beanlands RS, *et al*. Clinical quantification of myocardial blood flow using PET: Joint position paper of the SNMMI Cardiovascular council and the ASNC. *J Nucl Med*. 2018;59(2):273-293.

   doi: 10.2967/jnumed.117.201368

2. Sampson UK, Dorbala S, Limaye A, Kwong R, Di Carli MF. Diagnostic accuracy of rubidium-82 myocardial perfusion imaging with hybrid positron emission tomography/ computed tomography in the detection of coronary artery disease. *J Am Coll Cardiol*. 2007;49(10):1052-1058.

   doi: 10.1016/j.jacc.2006.12.015

3. Parker MW, Iskandar A, Limone B, *et al*. Diagnostic accuracy of cardiac positron emission tomography versus single photon emission computed tomography for coronary artery disease: A bivariate meta-analysis. *Circ Cardiovasc Imaging*. 2012;5(6):700-707.

   doi: 10.1161/circimaging.112.978270

4. Lee JM, Kim CH, Koo BK, *et al*. Integrated myocardial perfusion imaging diagnostics improve detection of functionally significant coronary artery stenosis by 13N-ammonia positron emission tomography. *Circ Cardiovasc Imaging*. 2016;9(9):e004768.

   doi: 10.1161/circimaging.116.004768

5. Valenta I, Quercioli A, Schindler TH. Diagnostic value of PET-measured longitudinal flow gradient for the identification of coronary artery disease. *JACC Cardiovasc Imaging*. 2014;7(4):387-396.

   doi: 10.1016/j.jcmg.2014.01.001

6. Joutsiniemi E, Saraste A, Pietilä M, *et al*. Absolute flow or myocardial flow reserve for the detection of significant coronary artery disease? *Eur Heart J Cardiovasc Imaging*. 2014;15(6):659-665.

   doi: 10.1093/ehjci/jet274

7. Hajjiri MM, Leavitt MB, Zheng H, Spooner AE, Fischman AJ, Gewirtz H. Comparison of positron emission tomography measurement of adenosine-stimulated absolute myocardial blood flow versus relative myocardial tracer content for physiological assessment of coronary artery stenosis severity and location. *JACC Cardiovasc Imaging*. 2009;2(6):751-758.

   doi: 10.1016/j.jcmg.2009.04.004

8. Fiechter M, Ghadri JR, Gebhard C, *et al*. Diagnostic value of N-13 ammonia myocardial perfusion PET: Added value of myocardial flow reserve. *J Nucl Med*. 2012;53(8):1230-1234.

   doi: 10.2967/jnumed.111.101840

9. Ziadi MC, DeKemp RA, Williams K, *et al*. Does quantification of myocardial flow reserve using rubidium-82 positron emission tomography facilitate detection of multivessel coronary artery disease? journal article. *J Nucl Cardiol*. 2012;19(4):670–680.

   doi: 10.1007/s12350-011-9506-5

10. Schindler TH, Fearon WF, Pelletier-Galarneau M, *et al*. Myocardial perfusion PET for the detection and reporting of coronary microvascular dysfunction: A JACC: cardiovascular imaging expert panel statement. *JACC Cardiovasc Imaging*. 2023;16:536-548.

    doi: 10.1016/j.jcmg.2022.12.015

11. Parkash R, Ruddy T, Kitsikis A, Hart R, Beauschene L, Williams K. Potential utility of rubidium 82 PET quantification in patients with 3-vessel coronary artery disease. *J Nucl Cardiol*. 2004;11:440-449.

    doi: 10.1016/j.nuclcard.2004.04.005

12. Murthy VL, Naya M, Foster CR, *et al*. Improved cardiac risk assessment with noninvasive measures of coronary flow reserve. *Circulation*. 2011;124(20):2215-2224.

    doi: 10.1161/CIRCULATIONAHA.111.050427

13. Ziadi MC, Dekemp RA, Williams KA, *et al*. Impaired myocardial flow reserve on rubidium-82 positron emission tomography imaging predicts adverse outcomes in patients assessed for myocardial ischemia. *J Am Coll Cardiol*. 2011;58(7):740-748.

    doi: 10.1016/j.jacc.2011.01.065

14. Herzog BA, Husmann L, Valenta I, *et al*. Long-term prognostic value of 13N-ammonia myocardial perfusion positron emission tomography added value of coronary flow reserve. *J Am Coll Cardiol*. 2009;54(2):150-156.

    doi: 10.1016/j.jacc.2009.02.069

15. Murthy VL, Naya M, Foster CR, *et al*. Coronary vascular dysfunction and prognosis in patients with chronic kidney disease. *JACC Cardiovasc Imaging*. 2012;5(10):1025-1034.

    doi: 10.1016/j.jcmg.2012.06.007

16. Murthy VL, Bateman TM, Beanlands RS, *et al*. Clinical quantification of myocardial blood flow using PET: Joint position paper of the SNMMI cardiovascular council and the ASNC. *J Nucl Cardiol*. 2018;25(1):269-297.

    doi: 10.1007/s12350-017-1110-x

17. Feher A, Srivastava A, Quail MA, *et al*. Serial assessment of coronary flow reserve by rubidium-82 positron emission tomography predicts mortality in heart transplant recipients. *JACC Cardiovasc Imaging*. 2020;13(1_Part_1):109-120.

    doi: 10.1016/j.jcmg.2018.08.025

18. Meijboom WB, Van Mieghem Carlos AG, Van Pelt N, *et al*. Comprehensive assessment of coronary artery stenoses. Computed tomography coronary angiography versus conventional coronary angiography and correlation with fractional flow reserve in patients with stable angina. *J Am Coll Cardiol*. 2008;52(8):636-643.

doi: 10.1016/j.jacc.2008.05.024

19. Di Carli M, Czernin J, Hoh Carl K, *et al*. Relation among stenosis severity, myocardial blood flow, and flow reserve in patients with coronary artery disease. *Circulation*. 1995;91(7):1944-1951.

    doi: 10.1161/01.CIR.91.7.1944

20. Uren NG, Melin JA, De Bruyne B, Wijns W, Baudhuin T, Camici PG. Relation between myocardial blood flow and the severity of coronary-artery stenosis. *N Engl J Med*. 1994;330(25):1782-1788.

    doi: 10.1056/NEJM199406233302503

21. Gould KL, Nakagawa Y, Nakagawa K, *et al*. Frequency and clinical implications of fluid dynamically significant diffuse coronary artery disease manifest as graded, longitudinal, base-to-apex myocardial perfusion abnormalities by noninvasive positron emission tomography. *Circulation*. 2000;101(16):1931-1939.

    doi: 10.1161/01.cir.101.16.1931

22. Goldstein RA, Kirkeeide RL, Demer LL, *et al*. Relation between geometric dimensions of coronary artery stenoses and myocardial perfusion reserve in man. *J Clin Invest*. 1987;79(5):1473-1478.

    doi: 10.1172/jci112976

23. Kirkeeide RL, Gould KL, Parsel L. Assessment of coronary stenoses by myocardial perfusion imaging during pharmacologic coronary vasodilation. VII. Validation of coronary flow reserve as a single integrated functional measure of stenosis severity reflecting all its geometric dimensions. *J Am Coll Cardiol*. 1986;7(1):103-113.

    doi: 10.1016/s0735-1097(86)80266-2

24. Naya M, Murthy VL, Taqueti VR, *et al*. Preserved coronary flow reserve effectively excludes high-risk coronary artery disease on angiography. *J Nucl Med*. 2014;55(2):248-255.

    doi: 10.2967/jnumed.113.121442

25. Javadi MS, Lautamäki R, Merrill J, *et al*. Definition of vascular territories on myocardial perfusion images by integration with true coronary anatomy: A hybrid PET/CT analysis. *J Nucl Med*. 2010;51(2):198-203.

    doi: 10.2967/jnumed.109.067488

26. Fukushima K, Javadi MS, Higuchi T, *et al*. Prediction of short-term cardiovascular events using quantification of global myocardial flow reserve in patients referred for clinical 82Rb PET perfusion imaging. *J Nucl Med.* 2011;52(5):726-732.

    doi: 10.2967/jnumed.110.081828

27. Panza JA. Myocardial ischemia and the pains of the heart. *N Engl J Med*. 2002;346(25):1934-1935.

    doi: 10.1056/NEJMp020047

ACCSCIENCE PUBLISHING

Advances in Radiotherapy & Nuclear Medicine

ORIGINAL RESEARCH ARTICLE

Multislit gamma camera for external beam radiotherapy assistance: Experimental proof of concept

Hugo Simões[1]*, Luís Lopes[1], Paulo J. B. M. Rachinhas[2], and Paulo Crespo[1,3]

[1]Laboratory of Instrumentation and Experimental Particle Physics, Rua Larga, Coimbra, Portugal

[2]Department of Radiotherapy, Coimbra Hospital and University Center, Praceta Mota Pinto, Coimbra, Portugal

[3]Department of Physics, Faculty of Science and Technology, University of Coimbra, Rua Larga, Coimbra, Portugal

Abstract

The orthogonal computed tomography (OrthoCT) concept, based on orthogonal ray imaging, is a low-dose imaging technique currently under investigation to potentially aid in external-beam radiation therapy treatments. This technique involves detecting radiation scattered within the patient and emitted at approximately 90° from the direction of the incoming beam. This scattered radiation can be collected by a 1D-detector system with a multisliced collimator positioned perpendicular to the incident beam axis. Such a system holds promise for on-board imaging with the patient positioned and prepared for treatment, as well as for real-time treatment monitoring. In this study, a multi-slice OrthoCT detector prototype was developed and tested under in-beam irradiation. The system utilizes gadolinium orthosilicate scintillator crystals coupled to photomultiplier tubes and a collimator made of lead slices. Experimental measurements were conducted using a heterogeneous phantom made of acrylic with an air cavity inside. The phantom was irradiated with a TrueBeam™ linac operating at 6 MV in the flattening-filter-free mode. The findings of this study indicate that this innovative imaging technique is capable of providing morphological images of the phantom. This accomplishment is achieved without the need to rotate the X-ray source around the object to be irradiated, demonstrating the feasibility of such a system.

Keywords: Orthogonal computed tomography; Low-dose imaging for radiotherapy; Rotation-free megavoltage tomography; X-ray detection; Image-guided radiotherapy

***Corresponding author:**
Hugo Simões
(hugo.simoes@coimbra.lip.pt)

Citation: Simões H, Lopes L, Rachinhas PJBM, Crespo P. Multislit gamma camera for external beam radiotherapy assistance: Experimental proof of concept. *Adv Radiother Nucl Med.* 2024;2(3):4099.
doi: 10.36922/arnm.4099

Received: July 1, 2024

Accepted: August 23, 2024

Published Online: September 24, 2024

1. Introduction

External beam radiotherapy is one of the primary modalities prescribed for cancer treatments. The most recently developed techniques allow for more conformal treatments, which are directly correlated with the therapeutic outcome.[1] However, this increase in dose conformality requires an even more precise positioning of the patient and knowledge of their anatomy and morphology at the moment of irradiation so that underdosage of tumor or overdosage of the surrounding healthy tissues can be minimized. Examples of factors that may compromise this treatment conformality

include (1) formation of edema in the irradiated area, (2) tumor regression/progression, (3) filling of cavities with edematous tissue (*e.g.*, due to inflammation), (4) change in tissue permeability, (5) weight loss/gain, and (6) misalignment of patient positioning, among others.[2-6]

Image-guided radiation therapy (IGRT) allows for more precise tumor targeting, thereby reducing the side effects of eventual morphological and/or anatomical changes. Cone-beam computed tomography is one of the most commonly used IGRT techniques for treatment monitoring, as it provides visualization of the target with volumetric imaging and relatively high-resolution soft-tissue information.[7] However, this technique results in an increase in the dose delivered to the patient due to sequential and repetitive imaging.[8] Portal imaging is also an IGRT technique, but it provides either two-dimensional (2D) imaging or three-dimensional (3D) imaging after rotation around the patient (not prone to real-time imaging).[9]

In this work, we investigated experimentally the orthogonal computed tomography (OrthoCT) concept, which had been described in our previous work.[10] This imaging technique, shown schematically in Figure 1 for monitoring a lung irradiation, entails detection of radiation dispersed in the patient and emitted at right angles with respect to the beam axis. Since photon scattering in the patient occurs with higher intensity in tissues of higher density, a detection system (made of a multi-slat collimator followed by a photon detector) positioned perpendicularly to the beam axis yields a signal proportional to the photons that escaped the patient (*i.e.*, a signal correlated with patient morphology). The OrthoCT provides images without the need to rotate the X-ray source around the imaging patient, as it is based on the detection of photons emitted at almost right angles with respect to the incoming photon flux. Using a small, pencil-like beam scanned in one or more known directions, the triggered detector slice corresponds to the third point where the interaction occurred. Our simulation results demonstrate that this technique enables the acquisition of images of the morphology of an anthropomorphic phantom with a dose of 10 mGy.[10] This was achieved by irradiating only a small part of the phantom, as it is not necessary to rotate the X-ray source around the patient, suggesting that such a low-dose morphological imaging technique can potentially be useful for (1) on-board imaging to assist in radiotherapy or (2) real-time radiotherapy monitoring.

To investigate the feasibility of such a system in a radiotherapy environment, a small-scale detector prototype was designed, built, and tested experimentally. Figure 2 shows a schematic of the system designed in

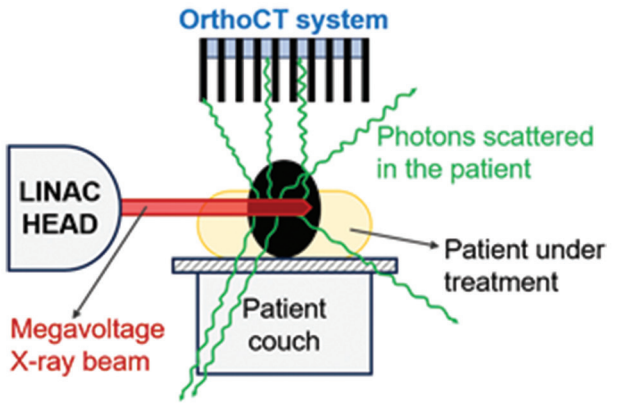

Figure 1. The orthogonal computed tomography concept.[10] The radiation scattered within the patient and emitted at right angles with respect to the beam axis yields a signal correlated with its morphology. Image created by author.

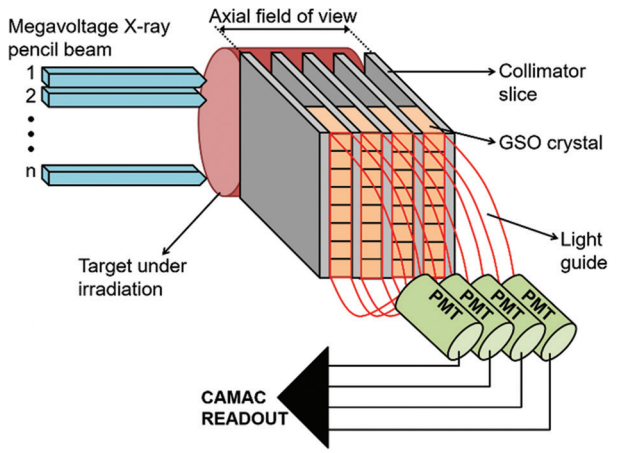

Figure 2. Schematic of the prototype developed and built as part of this work Abbreviation: GSO: Gadolinium orthosilicate.

this work. It consists of four slabs of scintillation crystals (in this case gadolinium orthosilicate [GSO]) separated by slices of lead. Photomultiplier tubes (PMTs) were used as light detectors, one for each slab of crystals. The scintillation light was directed from the crystals to the PMTs by custom-made acrylic light guides. The results of measurements performed with the prototype in a radiotherapy environment are reported here. It should be noted that this work represents a very preliminary proof-of-concept that requires further investigation before clinical translation can be considered.

2. Experimental setup and methodology

2.1. The OrthoCT detector

Figure 3 shows photographs of the detector prototype developed and tested within this study. It consisted of four

lines of GSO scintillator crystals separated by 3-mm-thick slices of lead. Each GSO line consisted of 47 crystals with a 4 mm × 4 mm cross-section and 30 mm length, individually wrapped with Teflon tape (Figure 4, top-left). Each line of crystals was placed inside an aluminum box to maintain the crystals all together and aligned. In total, 188 scintillator crystals were used. The aluminum box had a thickness of 1 mm at the radiation entrance region. The total length of each scintillator line was approximately 200 mm. The lead slices had dimensions of 200 mm × 200 mm. The collimator slices, along with the GSO lines, were enclosed inside a second aluminum box to ensure stability in the geometry (Figure 4, top-right). The thickness of this aluminum box at the radiation entrance region was 2 mm. To maintain the structure of the collimator, the space between the lead slices was filled with pieces of extruded polystyrene, each with a thickness of 4.6 mm. The distance between the centers of two consecutive GSO lines (*i.e.*, the detector pitch) was 7.6 mm. The scintillation light from the GSO lines was directed to the PMTs (specifically, the model XP5602 from Photonis Imaging Sensors, France) using custom-made acrylic light guides (Figure 4, bottom).

The prototype was mounted on a 10-mm-thick aluminum base. In addition, it was enclosed by 10-mm-thick polyvinyl chloride walls, with its top covered (Figure 3), to prevent it from being exposed to external light. The total dimensions of the system are 1200 mm in length and 800 mm in width. It has a height of 320 mm and weighs approximately 75 kg.

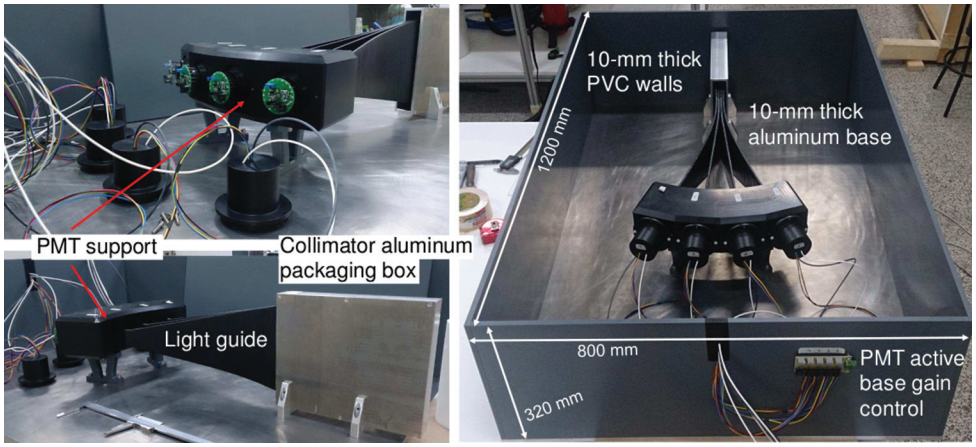

Figure 3. Photographs of the prototype developed and tested in this work. The final prototype includes four lines of gadolinium orthosilicate crystals separated by lead slices with a thickness of 3 mm. The scintillation light is directed to the photomultiplier tube by means of acrylic light guides
Abbreviation: PVC: Polyvinyl chloride.

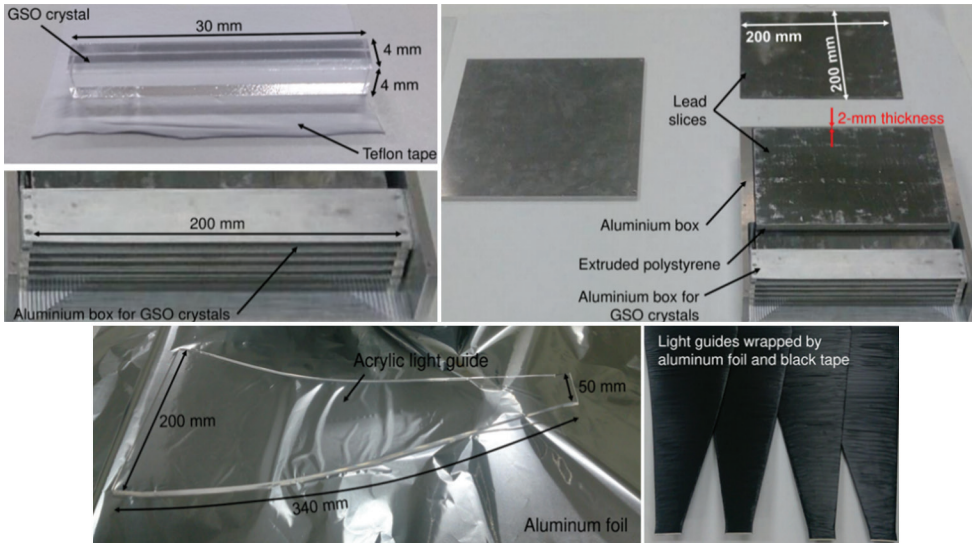

Figure 4. Detector prototype parts. Top-left: gadolinium orthosilicate scintillator crystals; top-right: lead collimator inside the aluminum box; bottom: custom-made acrylic light guides.

2.2. Data acquisition system and digital analysis

Figure 5 shows a schematic diagram of the electronic setup used to acquire the experimental measurements. The Nuclear Instrumentation Module (NIM) CAEN N471 high-voltage source was used. It is capable of delivering 3 mA of current at 3 kV output voltages, enabling the four PMTs to be powered simultaneously. A voltage splitter was used to replicate the input voltage and make it available to four outputs. With this configuration, any variation in the supply voltage would be common to all the channels, resulting in an approximately zero relative variation between them. The PMTs were supplied with a voltage of −982 V, consuming a total current of 479 μA.

Each PMT has an integrated amplification system that allows for the control of its gains. Its active elements require a differential supply of ±6 V, where the gain is controlled by applying a voltage in the range of 0 – 6 V. For this purpose, a small circuit board based on a potentiometer was built, using the 6 V and ground voltages provided by the NIM crate to generate the gain control voltage for each PMT. The active base gain control voltage used for each PMT was set at 5.30 V (the same voltage for all the PMTs).

The output signal from the active base of the PMT has a positive polarity. However, both the gate generator and the analog-to-digital converter (ADC) used in the measurements require a signal with negative polarity as input. The NIM LeCroy 428F Linear FAN-IN/FAN-OUT module, which features four independent channels, was employed to invert the polarity of the signal. Each output of the LeCroy 428F module was routed to the Computer Automated Measurement and Control (CAMAC) LeCroy 2259B Peak Sensing ADC.

ADC module channels 8 – 11 were used. The signal from channel 4 of the LeCroy 428F module was used to feed the gate generator, the NIM CAEN 2255B Dual Timer module. The gate signal was configured to have a duration of 5 μs, starting approximately 100 ns after an event occurred.

The CAMAC system was controlled by the 3988 GPIB Crate Controller module developed by Kinetic Systems (Illinois, USA). The GPIB protocol was utilized for

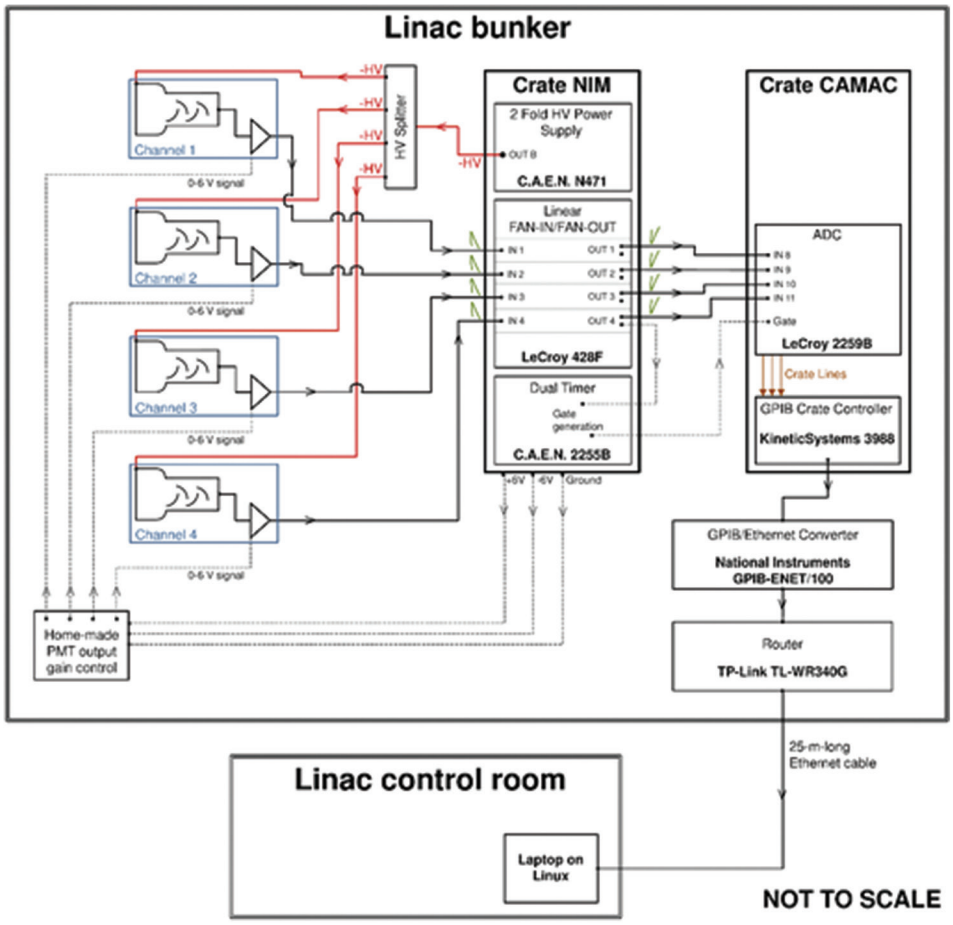

Figure 5. Schematic diagram of the electronics used for data acquisition. Image created by the author.

communication with the computer through the GPIB/Ethernet converter (GPIB-ENET/100 model, National Instruments, Austin, Texas, USA). This converter was connected to the computer through a local network established by a TP-Link TL-WR340G router. For the experimental measurements in a radiotherapy environment, all the NIM and CAMAC electronics described here, along with the GPIB/Ethernet converter and router, were placed inside the treatment room. The acquisition system was controlled from the linear accelerator (linac) control room using a laptop computer running the Linux OpenSuse 11.3 operating system with custom-made C/C++ routines. A 25-meter Ethernet cable was used to establish the connection with the router inside the treatment room. The total dead time of the data acquisition system was approximately 85%.

Once the data were collected during the irradiation, the corresponding counts spectra were constructed. It should be noted that the information collected by the CAMAC system during irradiation consists of a data vector for each channel of the prototype. Each sample in this vector represents the maximum amplitude value of an event detected by that channel. To build the count profiles, we first created a histogram of the values obtained for each of the channels for a given measurement. Each histogram was divided into 128 bins, with values ranging from 0 to 2047 (this value was chosen based on the fact that the ADC used in the acquisition has a dynamic range of 11 bits). The resulting histogram is then fitted to a Gaussian curve according to the Equation I:

$$y = A \times e^{\frac{(x-\mu)^2}{2\sigma^2}} \quad \text{(I)}$$

where A, μ, and σ represent the amplitude, mean, and standard deviation of the Gaussian curve, respectively. This procedure was implemented in MATLAB (MathWorks, Massachusetts, USA), using the *fminsearch* function to calculate the best-fit parameters. The profile value for a given channel at a certain irradiation position is then given by the value of μ, obtained from the Gaussian fit.

2.3. Linear accelerator

The linac used in this experimental study was the TrueBeam™ (Varian Medical Systems, Inc., Palo Alto, CA, USA) installed in the Radiotherapy Department of the Coimbra Hospital and University Center. It was operated at 6MV in flattening filter-free mode with a dose rate of 800 monitor units per minute (MU/min). A field size of 5 mm × 5 mm at the isocenter was used. This size was achieved by the combined setting of the jaws and the multi-leaf collimator (MLC). Figure 6 illustrates the configuration used during the irradiation process. The

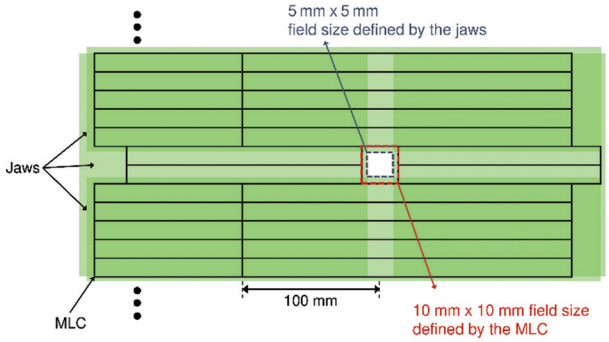

Figure 6. Configuration of the jaws and MLC leaves used during irradiation. The field size defined by the MLC and the jaws was 10 mm × 10 mm and 5 mm × 5 mm at the isocenter, respectively. The junction between the MLC leaves was offset by 100 mm from the center. Abbreviation: MLC: Multi-leaf collimator.

MLC was positioned to define a field of 10 mm × 10 mm at the isocenter. Note that the junction between the leaves of the same pair of the MLC had an offset of 100 mm from the isocenter, as depicted in the diagram. This arrangement of the jaws and the MLC aimed to minimize the impact of radiation that escapes through the linac head window and falls outside the field of interest. The jaws were set to define a field size of 5 mm × 5mm at the isocenter.

Figure 7 displays the time macrostructure of the linac beam measured with the prototype and acquired with a PicoScope 2203 oscilloscope (Pico Technology, UK). Examining the persistence graph obtained from 100 waveforms plotted on a time scale that allows two pulses to be observed simultaneously (left), the period of the macrostructure is 4.85 ms, corresponding to a frequency of approximately 206 Hz. From the analysis of a single pulse (persistence plot at the middle and average pulse waveform at right), it exhibits a fast rise in amplitude (approximately 0.85 µs), followed by a slower rise (for about 3.25 µs), and a sharp decay at around 1.40 µs. After approximately 5.5 µs, the event approaches values very close to zero and continues with a gradual decay that persists until around 10 µs (when the signal returns to the baseline).

2.4. Mitigation of the out-of-field radiation effect

It is well established that there exists a background flux of photons (and other particles) emanating from the linac head. Studies have been conducted to examine the influence of such out-of-field flux on the development of secondary oncological diseases.[11] Different types of accelerators yield varying doses outside the treatment field due to differences in their shielding.[12] The background radiation escaping from the linac head presents technological challenges for orthogonal ray imaging, as it can lead to signal saturation when penetrating the detector. In addition, this out-of-

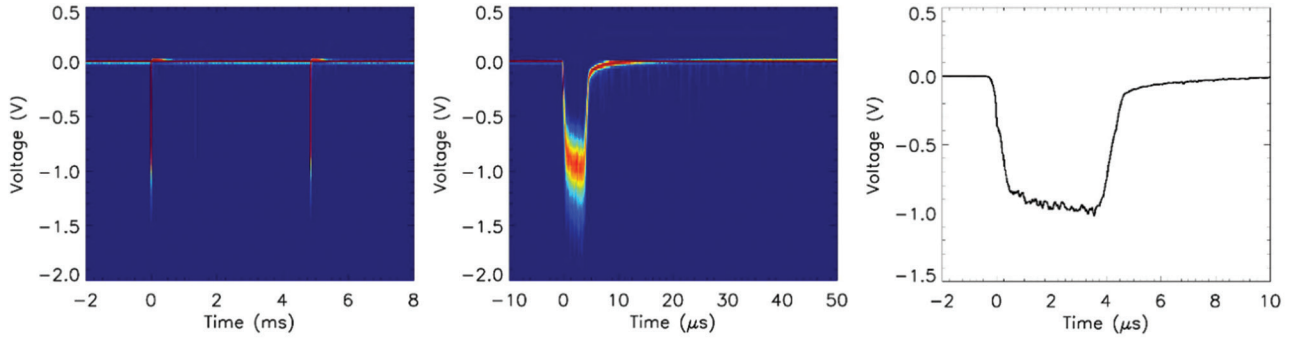

Figure 7. Macrostructure of the linear accelerator (linac) beam measured with the prototype. Left and middle: persistence graph obtained from 100 waveforms with different time scales. The period between beam pulses is 4.85 ms. Right: impulse obtained from the average of 100 waveforms.

field flux significantly diminishes the signal-to-noise ratio, potentially compromising the ability to detect the signal of interest originating from radiation scattered on the target. Eliminating the background escaping the linac head poses a challenge. However, its impact on the detector can be mitigated by the introduction of shielding material.[13] To this end, several blocks of Cerrobend™ and lead (with a density of 9.38 g/cm^3 and 11.34 g/cm^3, respectively) were positioned around the detector. Various configurations were tested, and the one yielding the best results is illustrated in Figure 8. Approximately 315 kg of shielding material was used.

To analyze the influence of the shielding on the performance of the prototype, preliminary measurements were conducted in the linac room. Figure 9 shows the dose equivalent values measured with the AT1123 dosimeter (ATOMTEX, Minsk, Republic of Belarus) at various positions of the prototype after the positioning of the shielding material. Upon analysis of the values, it is evident that the shielding configuration employed significantly reduces the impact of background radiation on the system. The comparison of the values measured at positions A and D reveals a reduction in background by a factor of approximately 250. Figure 10 displays the spectra obtained with (blue) and without (red) a polymethylmethacrylate (PMMA) target positioned in front of the detector, using different geometric configurations of the shielding material placement. As illustrated, inadequate shielding leads to the masking of the target signal (left), with <30 bins of variation between the two spectra. Improved shielding enhances the ability to detect the target (right), increasing the difference to approximately 270 bins

2.5. Experimental procedure

Figure 11 illustrates the experimental setup implemented in the radiotherapy environment, including the experimental phantom and the linac head. The prototype was positioned

Figure 8. Views from different angles of the shielding configuration employed to mitigate the out-of-field radiation escaping from the linear accelerator (linac) head.

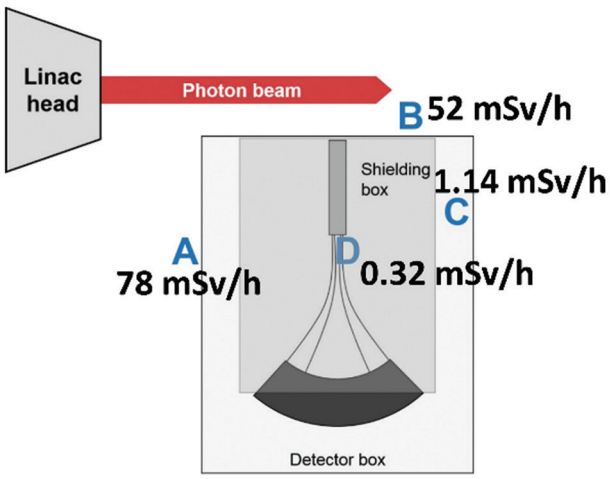

Figure 9. Dose equivalent values were measured at various positions of the prototype system. The comparison of the values measured at positions A and D reveals a reduction in background influence by a factor of approximately 250.

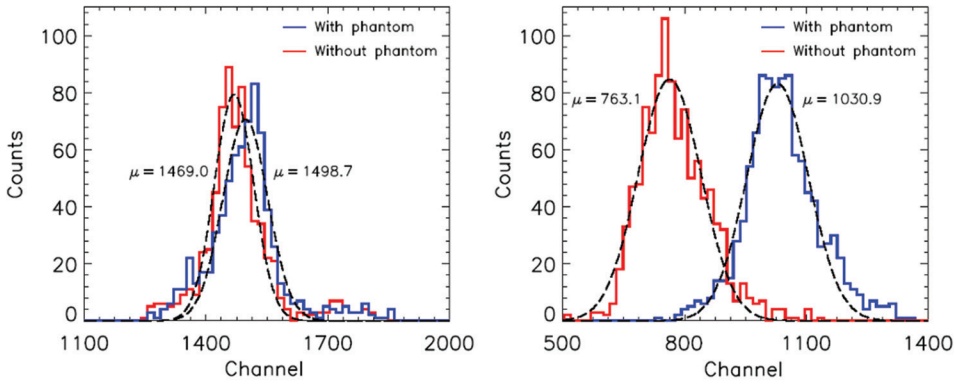

Figure 10. Counts spectra were obtained with different geometries of the shielding material, with (blue curve) and without (red curve) the polymethylmethacrylate target positioned in front of the detector. Inadequate shielding results in the masking of the signal from the target (left), while improved shielding enhances the ability to detect the target (right).

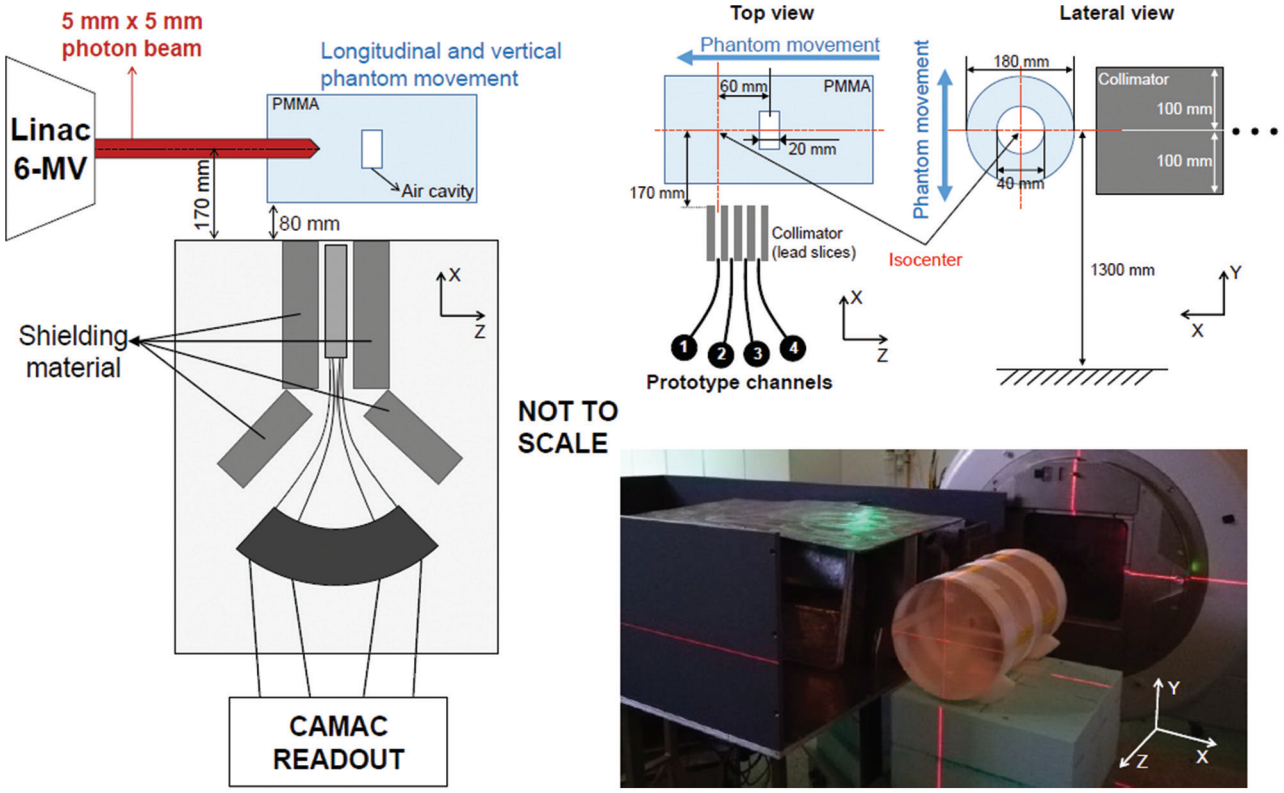

Figure 11. Scheme of the setup implemented in the experiments. A cylindrical polymethylmethacrylate phantom was irradiated by a 5 mm × 5 mm (at isocenter) X-ray beam. The position of the detector prototype remained fixed during the measurements, while the phantom was placed on the patient couch and moved to acquire longitudinal and/or vertical scans. The origin of the scan axis coincides with the center of the phantom air cavity.

perpendicular to the direction of the beam emitted from the linac, at a distance of 170 mm from its axis. Due to its geometry and weight, as well as the weight of the shielding material used, the position of the prototype system remained fixed during the irradiation. The center of crystal line 1 was aligned with the isocenter plane. A PMMA cylinder with a diameter of 180 mm and a length of 300 mm was utilized as the phantom. At its center, the phantom contained an air cavity with a diameter of 40 mm and a length of 20 mm. It was placed on the patient couch, initially positioned with its center shifted 60 mm away from the isocenter. The patient couch was used to aid in positioning the phantom in the different positions for data acquisition, as described in the following sections. The distance between

the phantom and the collimator surface was 80 mm. The phantom was irradiated with a 5 mm × 5 mm beam at the isocenter (as described in **section 2.3**) with the linac head positioned at 270° (*i.e.*, the beam entered from the left side of the phantom). Each acquisition lasted 45 s to acquire at least 1000 events for each phantom position. This long-time irradiation was due to the dead time of the acquisition system. However, the aim of this work was to demonstrate the concept of the OrthoCT technique. Therefore, optimizing the acquisition system, including considerations of dead time, was not considered within the scope of this study.

2.5.1. Relative gain of each prototype channel

To proceed with the calibration, the relative gain of each channel was determined. The diagram in Figure 12 outlines the procedure used. The phantom was initially irradiated at the −60 mm position (coincident with the isocenter) and then shifted 7.6 mm to the right (*i.e.*, away from the linac head). This distance corresponds to the pitch value of the detector. As illustrated in the diagram, the phantom region covered by channel 1 in the first irradiation position corresponds to the area of channel 2 in the second irradiation position. The same relationship is verified between channels 2 and 3 and channels 3 and 4. Thus, it is possible to relate the gain of the fourth channel to the gain of the third one. Similarly, the gain of channel 2 can be related to that of channel 3, and finally, that of channel 1 to channel 2. Five measurements were taken for each phantom position, and the average value was obtained for each channel.

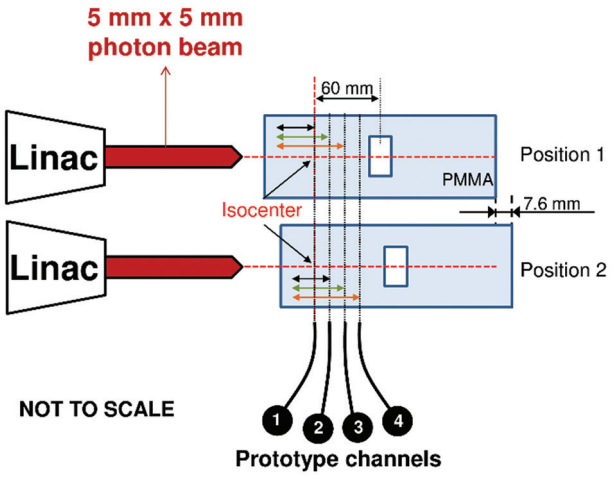

Figure 12. Scheme of the procedure used to determine the relative gain of each channel. The phantom was irradiated at two different positions: it was first irradiated at Z = −60 mm and then moved 7.6 mm to the right (*i.e.*, away from the linac head).

2.5.2. Longitudinal scan along the phantom

To obtain a longitudinal scan, the phantom was moved from Z = −60 mm to Z = +60 mm in steps of 10 mm (distances as defined in the experimental setup depicted in Figure 11).

2.5.3. 2D scan of air cavity region

A 2D image of the air cavity region was obtained. For this purpose, longitudinal scans were performed at different heights, effectively creating a 2D scan in the region of the air cavity. The longitudinal scans covered an area between Z = −62 mm and Z = +70 mm with steps of ΔZ = 22.8 mm. In the vertical direction, the step size was ΔY = 5 mm, encompassing the region from Y = −30 mm to Y = +30 mm. It is important to note that Z represents the longitudinal direction, while Y expresses the vertical one. The prototype channels 1, 2, and 3 were used to obtain the 2D scan, while channel 4 was solely employed to generate the gate signal.

2.5.4. Profiles with background subtraction

The influence of subtracting a background measurement on the technique's ability to detect variations between PMMA and air was analyzed. The background measurement involved obtaining count spectra without the phantom positioned in front of the detector. All parameters were kept the same as described in Figure 11, except for the presence of the phantom. Five irradiations were performed without the phantom, and the average value obtained from these five spectra was used as the background measurement for the corresponding channel. The background-subtracted profiles were then obtained using the data acquired in sections 2.5.2 and 2.5.3.

3. Results and discussion

3.1. Relative gain of each prototype channel

The μ values obtained for each irradiation position and the corresponding average value are shown in Table 1. Taking G_1, G_2, G_3, and G_4 as the gains of channels 1, 2, 3, and 4, respectively, the relative gains can be expressed as follows:

$$\frac{G_1}{G_2}=\frac{1034.74}{877.59}\leftrightarrow G_1=1.1791G_2,$$

$$\frac{G_2}{G_3}=\frac{867.42}{764.63}\leftrightarrow G_2=1.1344G_3\leftrightarrow\frac{G_1}{1.1791}$$
$$=1.1344G_3\leftrightarrow G_1=1.3376G_3,$$

$$\frac{G_3}{G_4}=\frac{759.73}{872.25}\leftrightarrow G_3=0.8710G_4\leftrightarrow\frac{G_1}{1.3376}=$$
$$0.8710G_4\leftrightarrow G_1=1.1650G_4. \quad \text{(II)}$$

Table 1. Determination of the relative gain of each channel: Value obtained for each irradiation position and the corresponding average

Position 1	Irradiation #	Channel 1	Channel 2	Channel 3	Channel 4
	1	1030.94	865.85	760.38	860.28
	2	1037.98	867.30	760.27	867.34
	3	1035.00	866.08	762.08	862.40
	4	1034.38	871.09	756.20	861.28
	5	1035.38	866.77	759.73	861.21
	Average	1034.74	867.42	759.73	862.50
Position 2	1	1043.04	875.81	763.28	868.45
	2	1043.13	875.51	762.99	870.87
	3	1035.89	879.55	763.80	873.44
	4	1035.89	875.89	762.01	875.11
	5	1040.27	881.16	771.06	873.38
	Average	1039.64	877.59	764.63	877.25

This means that using channel 1 as the reference, the values obtained for channels 2, 3, and 4 must be multiplied by 1.1791, 1.3376, and 1.1650, respectively, to calibrate the relative gains. It should be noted that as the position of the phantom varies, the geometry of the system changes, including the distance from the source to the surface of the phantom. In addition, the cross-sectional area of the beam changes due to its divergence. This could potentially change the relative gain between the two channels. However, the induced variations were considered to be minimal and therefore were not taken into account in the approach used to calculate the relative gains.

3.2. Longitudinal scan along the phantom

The profile obtained from the longitudinal shift of the phantom is shown in Figure 13: the red squares depict channel 1, the green triangles represent channel 2, and the blue diamonds and black circles correspond to channels 3 and 4, respectively. The profiles of channels 2, 3, and 4 were multiplied by the corresponding gain calibration values. In addition, the profile was normalized to the point at the most proximal position, in this case obtained with channel 1 (Z = −60 mm). The relative statistical errors were calculated as follows:

$$\varepsilon_r(\%) = \frac{\sigma}{\mu\sqrt{N}} \times 100 \quad \text{(III)}$$

where μ and σ correspond to the mean and standard deviation, respectively, obtained from a Gaussian fit of N samples. The error values were all below 0.31%. Analysis of the plots shows a good correlation between the depth profile and the position of the air cavity. In other words, the air cavity is clearly distinguishable, even though there

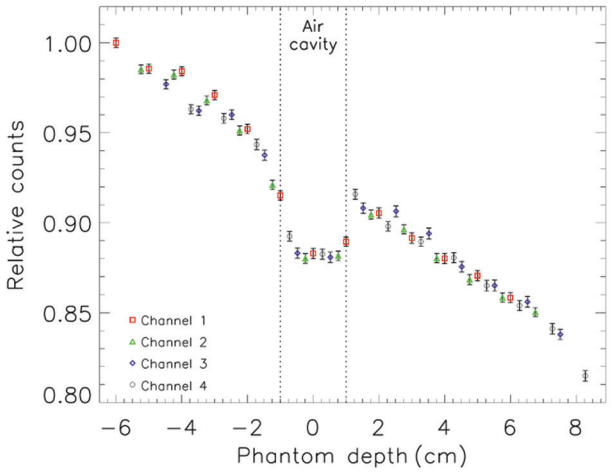

Figure 13. The profile obtained from the longitudinal scan along the phantom: the red squares depict channel 1, the green triangles represent channel 2, and the blue diamonds and black circles correspond to channels 3 and 4, respectively.

is a variation in the relative counts of about 12% (in approximately 50 mm of PMMA). It can also be seen that the number of counts decreases along the phantom depth due to the decrease in intensity of the X-ray beam as it penetrates the target.

3.3. Two-dimensional scan of air cavity region

Figure 14 depicts the experimental results obtained from the 2D scan of the air cavity region. The upper left panel shows the raw data obtained from the experiments. The upper right panel shows the count distribution obtained after data normalization in the horizontal direction (i.e., all the measured data points were divided by the value obtained by averaging the values represented in the first column).

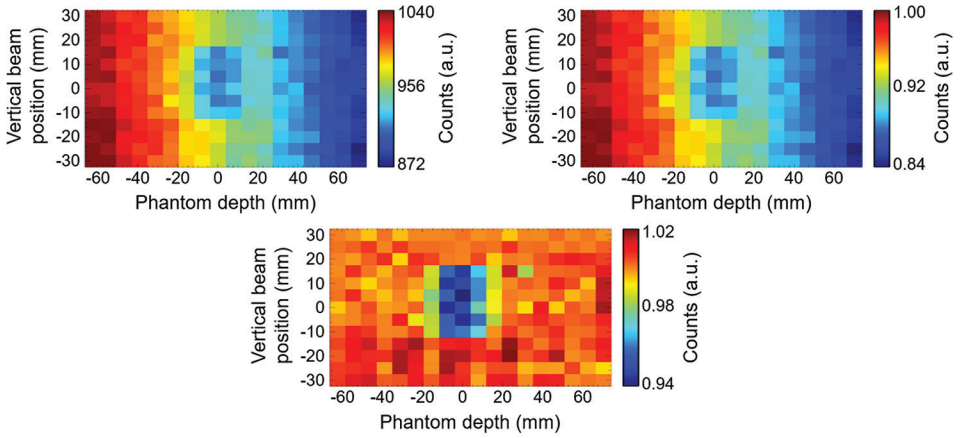

Figure 14. Results obtained from 2D scanning in the air cavity region. The top panels show the results obtained directly from the measured data (left) and after applying normalization to the data in the horizontal direction (right). The bottom panel shows the result obtained after applying vertical normalization to the measured data.

It should be noted that the area covered by the scan in the horizontal and vertical direction is 132 mm and 60 mm, respectively. The pixel size is 7.6 mm in the x-plane (*i.e.*, along the beam direction) and 5 mm in the y-plane (vertical direction). In both images, it is possible to observe the decay progression as the radiation penetrates through the phantom in the longitudinal direction. The air cavity region is also clearly visible. The lower part of the image shows the result of applying vertical normalization to the acquired data. The normalization factor used for each column was the average value obtained from the measurements at the two highest beam positions (*i.e.*, positions Y = 30 mm and Y = 25 mm). The implementation of such a procedure yields an image with a homogeneous intensity (*i.e.*, reducing the effect of beam intensity decay along the depth of the phantom in the OrthoCT image), facilitating a direct analysis of the obtained intensities in PMMA and air. In this case, the maximum relative error for each beam position was lower than 0.33%. Furthermore, in this scan, the air cavity is clearly visible. Nevertheless, the sensitivity of the system is low, as the relative variation in counts between the homogeneous region of the phantom (calculated by averaging the intensities in the Y = 0 mm and Z = −60 mm region of the vertically normalized image) and the air cavity (averaging the intensities in the Y = 0 mm and Z = 0 mm region of the same image) is only about 5% (it drops from values close to 1 to around 0.95).

3.4. Profiles with background subtraction

Table 2 presents the measured background values for each channel. The values for channels 1, 2, 3, and 4 were determined to be 761.77, 650.36, 576.98, and 641.78, respectively. The relative gains of the channels were recalculated, taking into account the background subtraction. The values in Table 1 were used with the corresponding background subtraction, resulting in the following relative gain values:

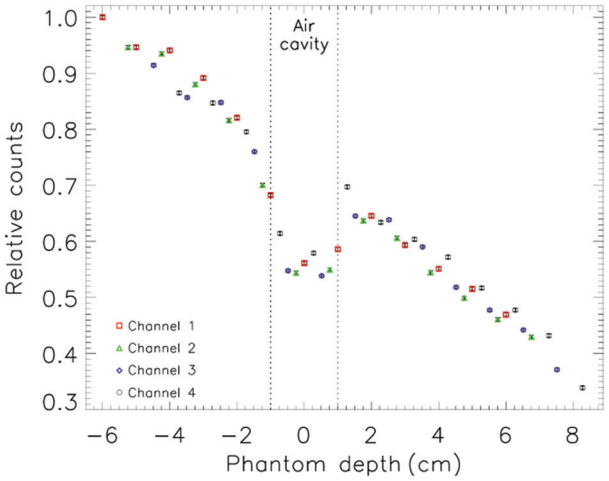

Figure 15. The profile obtained from the longitudinal scan along the phantom with background subtraction: the red squares depict channel 1, the green triangles represent channel 2, and the blue diamonds and black circles correspond to channels 3 and 4, respectively.

Table 2. Determination of the background of each channel: values obtained for each irradiation and the corresponding average

Irradiation #	Channel 1	Channel 2	Channel 3	Channel 4
1	763.08	644.70	573.04	641.64
2	760.82	649.59	579.90	641.63
3	762.22	655.75	571.46	642.27
4	765.42	647.83	579.10	641.27
5	757.33	653.91	581.41	641.67
Average	761.77	650.36	576.41	641.78

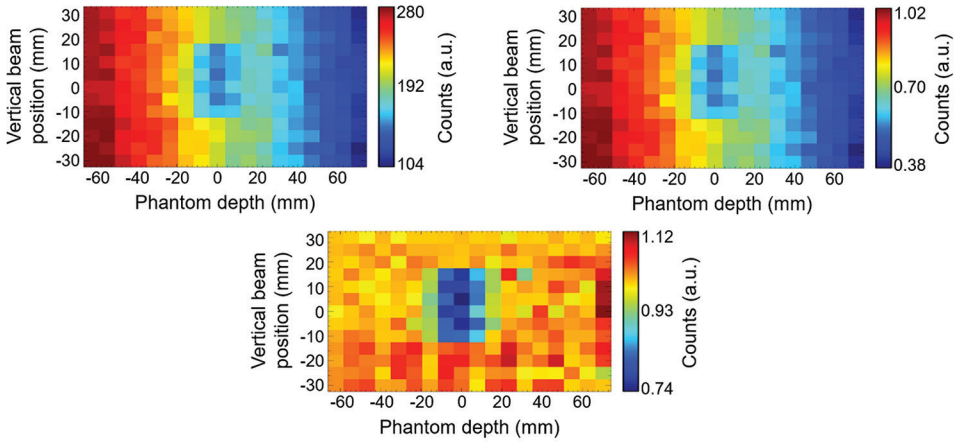

Figure 16. Results obtained from 2D scanning in the air cavity region, after background subtraction. The top panels show the results obtained directly from the measured data (left) and after applying normalization to the data in the horizontal direction (right). The bottom panel shows the result obtained after applying vertical normalization to the measured data.

$G_1 = 1.2013\ G_2$; $G_1 = 1.3896\ G_3$; $G_1 = 1.1019\ G_4$

Figures 14 and 15 display the scans obtained after background subtraction. It is noteworthy that the profiles with background subtraction were derived from the data detailed in sections 3.2 and 3.3. In Figure 15, the profile from the longitudinal scan along the phantom is presented. The red squares depict channel 1, the green triangles represent channel 2, and the blue diamonds and black circles correspond to channels 3 and 4, respectively. The profiles from channels 2, 3, and 4 were multiplied by their corresponding gain factors. All data points were normalized to the point at the most proximal position, obtained with channel 1 (Z = −60 mm). The maximum observed relative error was $\varepsilon_{r,t}$=0.32%, calculated as follows:

$$\varepsilon_{r,t}(\%) = \sqrt{\varepsilon_r^2 + \varepsilon_{r,b}^2} \quad \text{(IV)}$$

Where ε_r was calculated according to Equation III, and $\varepsilon_{r,b}$ refers to the background measurement error and is given by

$$\varepsilon_{r,b}(\%) = \frac{\bar{\sigma}}{\bar{\mu} \times \sqrt{\frac{N_1 + N_2 + N_3 + N_4 + N_5}{5}}} \times 100 \quad \text{(V)}$$

Where $\bar{\alpha}$ and $\bar{\sigma}$ represent the average values of the mean and standard deviation obtained from the five background measurement profiles, respectively, and N_1, N_2, N_3, N_4, and N_5 are the numbers of samples measured in each dataset.

Figure 16 depicts the results of the 2D scan in the air cavity region after background subtraction. The image in the top left corner shows the results obtained directly from the measured data. The top-right image displays the results after horizontal normalization. The bottom image represents the results after vertical normalization of the measured data. The normalization factors used were similar to those specified in section 3.3. The maximum relative error was $\varepsilon_{r,t}$ = 0.33%.

The analysis of the two figures indicates an enhancement in the capability to distinguish the air cavity. The longitudinal scan exhibited an average decrease of approximately 45% compared to the maximum point. In the scenario without background subtraction, this variation was around 12%. In the vertically normalized 2D scan, the relative variation in counts between the homogeneous region of the phantom (calculated by averaging the intensities in the Y = 0 mm and Z = −60 mm region of the vertically normalized image) and the air cavity (averaging the intensities in the Y = 0 mm and Z = 0 mm region of the same image) is approximately 23% (it drops from values close to 1 to values around 0.77). This result is notably higher than the 5% value obtained in the scenario without background subtraction. Therefore, subtracting the background measurement from the profiles enhances the ability of orthogonal ray imaging to distinguish between PMMA and air.

4. Conclusion

This paper presents the prototype developed and constructed as part of this study, along with the results of testing conducted in a radiotherapy environment. The experiments were performed using the TrueBeam™ linac installed at Coimbra Hospital and University Centre, operating at 6 MV in the flattening filter-free mode. The background radiation emanating from the linac head hinders the detector's proper operation by obscuring the signal emitted from the irradiated target. It is worth noting

that this background has a more pronounced impact on orthogonal ray imaging measurements due to the utilization of very small irradiation fields (5 mm × 5 mm). Although impossible to eliminate entirely, the impact of this background on the obtained profiles has been significantly reduced. This was achieved through the utilization of approximately 315 kg of shielding material, consisting of Cerrobend™ and lead. The necessity for such a substantial amount of shielding material was also influenced by the geometry of the system. Building a more compact system, using, for example, silicon photomultipliers directly coupled to the scintillation crystals, will decrease the quantity of shielding material needed.

Obtaining background-subtracted profiles improved the ability to discriminate the air cavity placed at the center of the PMMA phantom. This work experimentally demonstrated the capability of OrthoCT to obtain 2D images of the morphology of targets in the region of interest without the need to rotate the linac around them.

To ensure sufficient statistics, the 2D images were acquired with an irradiation time of 45 s per phantom position. This was due to the dead time of the acquisition system and the use of the absolute maximum amplitude of each detected event to create the corresponding profiles. For example, analyzing the signals in the current integration mode can enhance the statistical significance of the collected data. This is because it integrates a signal that is correlated with the energy of all events detected by the system. Simulation results indicate that 10 mGy is sufficient for obtaining OrthoCT images.[10] Therefore, in the current integration mode, similar images to those shown in Figure 16 can be obtained with a total irradiation time of only 1.3 s. This statement is based on the fact that the TrueBeam™ linac delivers approximately 10 mGy every 100 ms, and the images were obtained from 13 vertical beam positions.

Acknowledgments

The authors gratefully acknowledge the staff from the detector laboratory and mechanical workshop of the laboratory of instrumentation and experimental particle physics (Alberto Blanco, Rui Alves, Nuno Dias, Carlos Silva, Douglas Lima, Américo Pereira, Orlando Cunha, and Nuno Carolino) for their support in the construction and assembly of the detector prototype. The authors also acknowledge Andreas Wagner (Institute of Radiation Physics Helmholtz-Zentrum Dresden-Rossendorf, Dresden, Germany) for lending some of the electronics modules used in data acquisition.

Funding

This study was partly funded by Project POCI-01-0145-FEDER-0073334, supported through FCT/MCTES national funds and FEDER, in accordance with Parceria PT2020 LIP - FIS/50007.

Conflict of interest

The authors declare that they have no competing interests.

Author contributions

Conceptualization: Hugo Simões & Paulo Crespo
Investigation: All authors
Methodology: All authors
Writing–original draft: Hugo Simões
Writing–review & editing: All authors

Ethics approval and consent to participate

Not applicable.

Consent for publication

Not applicable.

Availability of data

Data are available from the corresponding author upon reasonable request.

References

1. Berger T, Seppenwoolde Y, Pötter R, *et al.* Importance of technique, target selection, contouring, dose prescription, and dose-planning in external beam radiation therapy for cervical cancer: Evolution of practice from EMBRACE-I to II. *Int J Radiat Oncol Biol Phys.* 2019;104(4):85-94.
doi: 10.1016/j.ijrobp.2019.03.020

2. De Crevoisier R, Tucker SL, Dong L, *et al.* Increased risk of biochemical and local failure in patients with distended rectum on the planning CT for prostate cancer radiotherapy. *Int J Radiat Oncol Biol Phys.* 2005;62(4):965-973.
doi: 10.1016/j.ijrobp.2004.11.032

3. Thieke C, Malsch U, Schlegel W, *et al.* Kilovoltage CT using a linac-CT scanner combination. *Br J Radiol.* 2006;79(1):S79-S86.
doi: 10.1259/bjr/88849490

4. Lee C, Langen KM, Lu W, *et al.* Evaluation of geometric changes of parotid glands during head and neck cancer radiotherapy using daily MVCT and automatic deformable registration. *Radiother Oncol.* 2008;89(1):81-88.
doi: 10.1016/j.radonc.2008.07.006

5. Serduc R, van de Looij Y, Francony G, *et al.* Characterization and quantification of cerebral edema induced by synchrotron x-ray microbeam radiation therapy. *Phys Med Biol.* 2008;53(5):1153.
doi: 10.1088/0031-9155/53/5/001

6. Sterzing F, Engenhart-Cabillic R, Flentje M, Debus J. Image-guided radiotherapy: A new dimension in radiation oncology. *Dtsch Arztebl Int.* 2011;108(16):274-280.

doi: 10.3238/arztebl.2011.0274

7. Albarakati H, Jackson P, Gulal O, *et al.* Dose assessment for daily cone-beam CT in lung radiotherapy patients and its combination with treatment planning. *Phys Eng Sci Med.* 2022;45:231-237.

doi: 10.1007/s13246-022-01105-7

8. Kan MW, Leung LH, Wong W, Lam N. Radiation dose from cone beam computed tomography for image-guided radiation therapy. *Int J Radiat Oncol Biol Phys.* 2008;70(1):272-279.

doi: 10.1016/j.ijrobp.2007.08.062

9. Van Elmpt W, McDermott L, Nijsten S, Wendling M, Lambin P, Mijnheer B. A literature review of electronic portal imaging for radiotherapy dosimetry. *Radiother Oncol.* 2008;88(3):289-309.

doi: 10.1016/j.radonc.2008.07.008

10. Simões H, Lopes AL, Travassos C, *et al.* Monitoring tumor lung irradiation with megavoltage patient-scattered radiation: A full system simulation study. *IEEE Trans Radiat Plasma Med Sci.* 2017;1(5):452-459.

doi: 10.1109/TRPMS.2017.2724139

11. Taylor ML, Kron T. Consideration of the radiation dose delivered away from the treatment field to patients in radiotherapy. *J Med Phys.* 2011;36(2):59-71.

doi: 10.4103/0971-6203.79686

12. Reft CS, Runkel-Muller R, Myrianthopoulos L. *In vivo* and phantom measurements of the secondary photon and neutron doses for prostate patients undergoing 18 MV IMRT. *Med Phys.* 2006;33(10):3734-3742.

doi: 10.1118/1.2349699

13. Simões H, Cunha M, Pinto M, *et al.* Dose-free monitoring of radiotherapy treatments with scattered photons: First experimental results at a 6-MV linac. *IEEE Trans Nucl Sci.* 2013;60(4):3110-3118.

doi: 10.1109/TNS.2013.2265137

ACCSCIENCE PUBLISHING

Advances in Radiotherapy & Nuclear Medicine

MINI-REVIEW

Cancer radiotherapy with mini neutron/gamma-ray generators

Ka-Ngo Leung[1,2]* and James K. Leung[2]

[1]Department of Nuclear Engineering, University of California, Berkeley, California, United States of America

[2]Berkion Technology LLC, Berkeley, California, United States of America

Abstract

Recent advancements in negative hydrogen (H-) or negative deuterium (D-) ion source technology as well as the commercial availability of high-frequency AC high-voltage power supplies have enabled the development of mini neutron/gamma-ray generators using low-energy nuclear reactions. These generators can provide a useful flux of high-energy neutrons or gamma photons in either pulsed or continuous operations. With the new mini generator, intraoperative radiotherapy as well as treatment of tumors in the brain, skin, breast, salivary gland, pancreas, liver, and kidney can be performed using external or internal neutron/gamma-ray beams. The new radiotherapy system is very compact and requires very low power for operation, enabling its location inside an operation room of a hospital or clinical facility.

Keywords: Neutron; Gamma-ray; Cancer therapy; Intraoperative radiotherapy; Brain tumor; Boron neutron capture therapy

***Corresponding author:**
Ka-Ngo Leung
(kangoleung@pacbell.net)

Citation: Leung K, Leung JK. Cancer radiotherapy with mini neutron/gamma-ray generators. *Adv Radiother Nucl Med.* 2024;2(3):3920. doi: 10.36922/arnm.3920

Received: June 12, 2024

Accepted: July 23, 2024

Published Online: September 5, 2024

1. Introduction

Radiotherapy tools based on photons or electrons are commonly used in clinical facilities. Most superficial cancers have been treated with low- or high-energy X-ray machines and electron accelerators, unfortunately, with little effectiveness. Neutron radiation therapy is a high linear energy transfer (LET) type of radiation with a higher relative biological effectiveness (RBE) compared to conventional X-ray therapy. Fast neutrons are very effective in the treatment of some types of tumors such as refractory Merkel cell carcinoma[1] and malignant salivary gland tumors.[2] So far, the neutrons used for radiation therapy are mostly provided by fission reactors or accelerator-based neutron sources. Since these systems are large and accessibility is difficult, neutrons are not commonly employed in cancer therapy treatments.

The development of compact and high-flux neutron/gamma-ray generators for radiotherapy has only occurred in recent years. Martellini *et al.* have recently reported a radiofrequency (RF)-driven D^+ ion-based d-d neutron generator for intraoperative radiotherapy (IORT) purposes.[3] Persuad *et al.* tested a tandem accelerator-based gamma generator for producing 6- and 7-MeV gammas from the p-^{19}F reaction.[4] However, the size of this gamma generator is not small and the flux is too low to be useful for radiotherapy. Recent experimental investigations demonstrated that a substantial amount of H^-/D^- ions can be produced by thermal desorption processes.[5] Based on

these new findings, mini neutron/gamma-ray tubes are now being developed which can eliminate most issues from the larger positive H^+/D^+ ion-based neutron/gamma-ray generators. Using a high-frequency AC high-voltage supply, short pulses of high-intensity neutron or gamma-ray beams can be generated using the d-d, d-^{10}B, d-^{7}Li, p-^{7}Li, or p-^{19}F nuclear reactions.[6] This article describes the design and development of these mini tubes and their applications for neutron or gamma-ray cancer therapy.

2. Mini neutron tube for external neutron beam therapy

Figure 1 shows a schematic diagram of the mini neutron tube design. This neutron tube is made of Pyrex glass with a diameter and length of 2.5 cm and 8 cm, respectively. A slotted thin titanium foil (0.1-mm thick and 2 cm in diameter), used as a H^-/D^- ion emitter, is located at one end of the tube while a beam target electrode is located at the opposite end. The beam target electrode (~2 cm in diameter) is positively biased with respect to the emitter foil. To produce H^-/D^- ions by thermal desorption processes, hydrogen or deuterium gas and cesium vapor are initially introduced into the glass tube. The temperature of the titanium foil can be varied by adjusting the heating current. When the temperature of the titanium foil reaches 250°C, copious amounts of D^- ions are emitted.[5] These D^- ions are accelerated to the titanium target electrode where 2.45 MeV neutrons will be produced by the d-d fusion reaction. Titanium is used as the target material because it is capable of absorbing a large number of deuterium atoms on the surface, thereby enabling more d-d reactions to occur and enhancing the neutron yield. Without an ion source chamber, the size of the neutron generator is significantly reduced. In addition, complex power sources such as an RF or microwave generator and its matching network are eliminated,[7] and a simple heater power supply is all that is required to produce the H^-/D^- ion.

For low ion beam current, the neutron tube can be operated with a DC high voltage (~100 kV) power supply. To achieve a high neutron yield, a higher D^- ion beam energy is needed. Today, commercial high-frequency AC high-voltage supplies are readily available. These compact AC high-voltage power sources are commonly found in portable dental X-ray machines. Peak voltage between 500 kV and 2 MV (with peak current in tens of mA) can be obtained with these power supply units. Using these high-voltage power sources, the mini d-d neutron tube can produce a high peak flux of 2.45 MeV neutrons suitable for cancer therapy. The average neutron yield depends on the duty factor (DF) of the ion beam operation. As an example, if the mini tube is operated with 500 kV, 10 mA of D^- beam power, the peak neutron yield is 5×10^{10} n/s. The average neutron yield is 5×10^{8} n/s if the DF is 1%. If the D^- beam power is increased to 1 MV, 10 mA, then the peak neutron

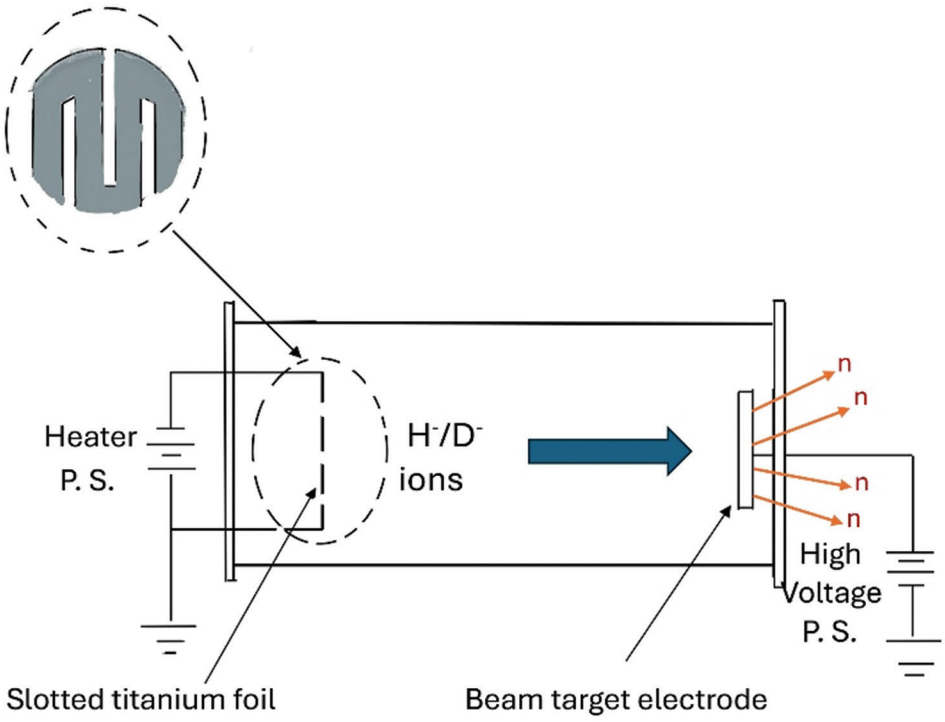

Figure 1. The mini neutron tube based on thermally emitted H^-/D^- ions. Diagram created by the authors.

yield becomes 2×10^{11} n/s and the average neutron yield is 2×10^{9} n/s for 1% DF operation.

The beam target for the d-d neutron tube is a round copper disk. It is coated with a thin layer of titanium on the one side. Deuterium atoms are absorbed on the titanium surface. Under ion beam bombardment, the temperature of the target electrode will increase. If the temperature exceeds 250°C, most of the deuterium atoms will evaporate away. The probability for the d-d fusion reaction to occur becomes smaller. To maintain a high neutron yield, the target electrode must be cooled by compressed air. For a 1 MV, 10 mA D^- ion beam, the power density on the target electrode with a diameter of 2 cm is about 3 kW/cm^2 for continuous operation. For 1% DF pulsed operation, the power density is only 30 W/cm^2. Air cooling can easily maintain the target temperature below 250°C. Figure 2 shows a prototype mini d-d neutron tube. The D^- ion emitting foil is located at the one end while the titanium target is at the opposite end of the glass tube. The titanium target electrode is housed inside a high-density polyethylene cylinder for high-voltage insulation and air cooling arrangement. The tubings for the gas inlet and outlet are both installed at the center of the glass tube. The entire assembly is about 17-cm long.

Neutron therapy can be administered to a cancer patient either in the form of an external or an internal neutron beam. If the tumor is located near the surface of the body, a neutron beam can be applied externally to the tumor. In this case, a single mini d-d neutron tube can be employed. For 2.45 MeV d-d neutrons, the absorbed dose as a function of depth in water should be quite similar to those of the d-Be neutrons. The peak of the absorption curve occurs at ~2 cm.[8] By placing the target electrode of the d-d neutron tube adjacent to the skin or breast tumor, one can deliver the highest available neutron dose to the tumor. With the diameter of the beam target electrode properly optimized, one can control the neutron irradiation area without performing beam scanning.

If the neutron dose for a single neutron tube is not adequate, then a multi-D^- ion emitter system can be employed to enhance the neutron output. Figure 3 shows the design of a more intense neutron source where seven D^- ion beams from separate emitters are impinging on a single target electrode. Using a hemispherical shape titanium electrode, the target area will increase by a factor of two, thereby reducing the beam power density by the same factor while maintaining the neutron source size of 2 cm in diameter. With this arrangement, the total D^- beam power density on the target electrode is ~100 W/cm^2 for a 1 MV, 70 mA, and 1% DF operation. Using forced-air cooling, the temperature of the hemispherical target electrode can be kept below 250°C.

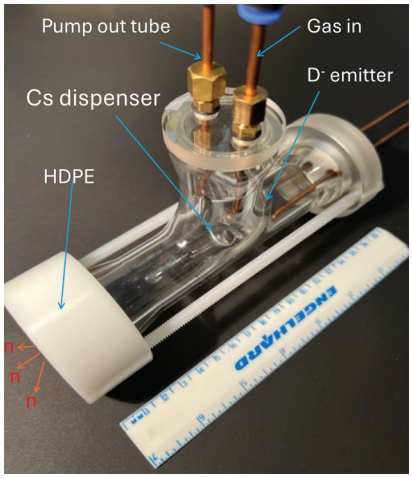

Figure 2. A prototype mini d-d neutron tube with the titanium target enclosed by a high-density polyethylene cylinder

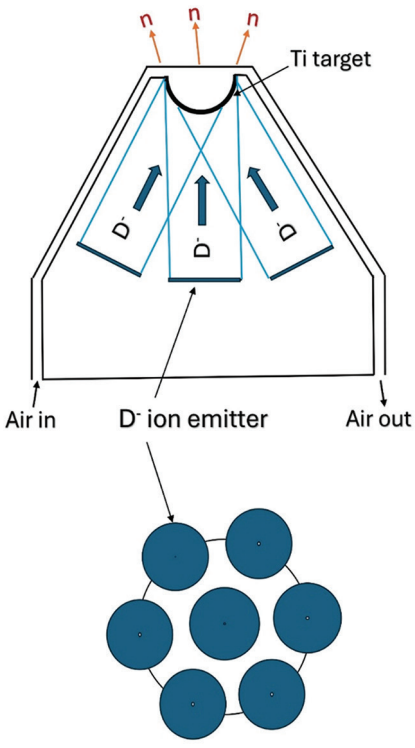

Figure 3. Schematic diagram of the intense d-d neutron tube with seven D^- ion emitters and a common titanium target electrode. Diagram created by the authors.

3. Mini neutron tubes for internal neutron beam irradiation

An RF-driven D^+ ion-based d-d neutron generator has recently been applied for IORT through irradiation of tumor bed with 2.45 MeV d-d neutrons after removal of the solid cancer tumor.[3] Monte Carlo simulations have

demonstrated that operating the d-d neutron generator in continuous wave (CW), with a beam power of 100 kV and 10 mA, can generate a neutron yield of 3.3×10^9 n/s with a neutron flux ~ 8×10^7 n/cm^2/s at the center of the irradiation window. The delivered dose rate is about 2 Gray (RBE)/min, resulting in 4 – 9 min of treatment time.[3] The new mini d-d neutron tube can provide high peak neutron doses in pulsed mode operation. By operating the mini neutron tube at 500 kV and 10 mA of D^- ion beam current, the peak neutron yield is 5×10^{10} n/s. The average neutron yield becomes 5×10^9 n/s for a 10% DF (1 ms, 100 Hz) operation. Thus, the treatment time should be about the same as the larger D^+ ion-based d-d neutron generator. By positioning the beam target near the center of the tumor bed, one can further increase the neutron flux on the cavity wall. The near isotropic neutron emission will permit the irradiation or "sterilization" of the surrounding side walls of the cavity, therefore reducing the chance of cancer recurrences.

The surgical removal of a tumor is usually followed by an IORT procedure. Radiation in the form of photons, electrons, protons, or neutrons can be applied. It is essential to allow these radiation particles to reach all corners of the surrounding walls. In addition, the irradiation should be uniform on the cavity walls. The design of the mini neutron tube can be tailored to meet these requirements. Figure 4 shows the emission profile for the d-d neutrons when the interaction energy is 500 keV.[9] The emission is not isotropic with the neutron yield in the forward direction (that is at 0°) being four times higher than that at 90°. On the other hand, the neutron flux varies as $1/R^2$ where R is the distance between the cavity wall and the target electrode. To compensate for this difference in neutron emission, the titanium target cannot be planar in shape. Instead, a conical target electrode design should be employed. This conical target is located inside the spherical end of the applicator as shown in Figure 5. The shape and the position of the conical target can be optimized so that at any point on the target surface, the ratio of R(0°)/R(90°) maintains at 2. With this conical target arrangement, the d-d neutron flux on the spherical surface of the applicator will be uniform. A prototype of the mini neutron tube with the applicator arrangement is shown in Figure 6.

Since the neutron beam in this mini tube can be generated either in CW or in short-pulsed mode, one can investigate the so-called FLASH effect in neutron therapy.[10] It has been observed that FLASH treatment in X-ray photon, electron, or proton therapy (using very high doses in very short pulses) can destroy the tumor cells but not the surrounding healthy tissue.[10] The FLASH effect for neutron radiotherapy can be explored with the mini neutron tube for *in vitro* studies. If the results are successful,

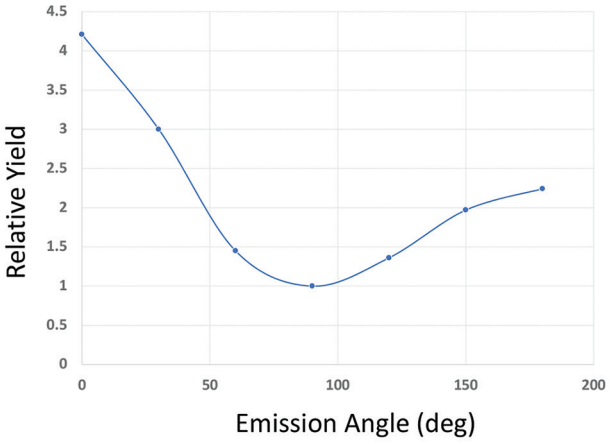

Figure 4. Relative angular distribution for the d-d neutrons at 500 keV deuteron energy. Modified based on data from Csikai.[9]

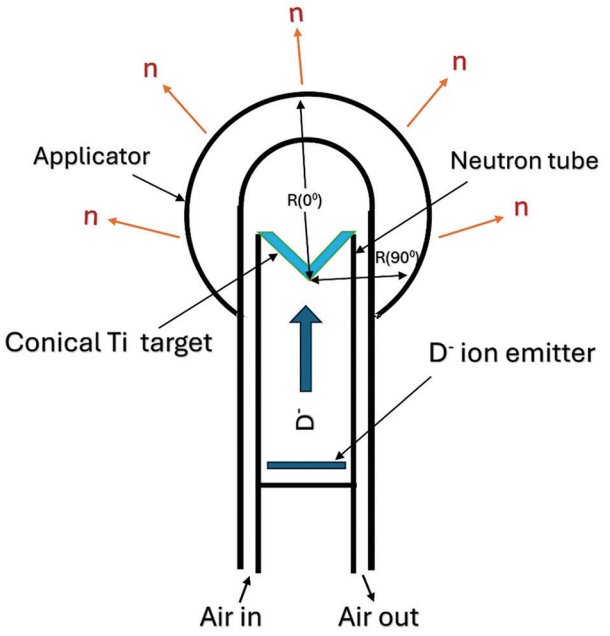

Figure 5. Schematic diagram of the mini d-d neutron tube and applicator arrangement for intraoperative radiotherapy. Diagram created by the authors.

and irradiation is uniform on the surrounding walls, the mini neutron tube should be an ideal tool for performing IORT in cancer patients. The mini d-d neutron tube and its associated power supplies can all be mounted on a robotic arm, similar to a low-energy dental X-ray machine.

4. Mini neutron tubes for direct production of epithermal neutron

Epithermal neutrons in the range of 0.4 – 20 keV are desirable for some cancer treatments and to produce medical radioisotopes.[6,7,11] They can be formed by

moderating the 2.5 MeV d-d neutrons or the 10 and 13 MeV d-^{7}Li neutrons. Alternatively, they can be directly produced by employing the ^{7}Li(p,n)^{7}Be reaction near the threshold interaction energy (1.881 MeV).[12,13] This approach to forming epithermal neutrons offers several advantages. First, as no moderation is needed, the epithermal neutron flux is higher. Second, the epithermal neutrons formed at near-threshold energy are directional with a mean neutron angle of approximately 20^{0}. Therefore, shielding is not needed on the side and at the back of the neutron generator. Third, the d-d and the d-^{7}Li neutrons are emitted isotropically, therefore more than 50% of these neutrons produced are wasted but not the near-threshold produced p-^{7}Li neutrons. In the past, this approach of generating epithermal neutrons was only carried out with a large 2 MV accelerator system such as a linac or a tandem accelerator. Using the new mini p-^{7}Li neutron tube (Figure 1) and employing an AC high-voltage power supply, a compact high-yield epithermal neutron source can be developed for boron neutron capture therapy (BNCT) applications.[14]

BNCT is based on the high probability of a stable isotope ^{10}B capturing a thermal neutron, thereby releasing two high-energy ions (^{4}He^{2+} and ^{7}Li^{+}). Because of the high LET and RBE of these ions, only cells in close proximity to the reaction ^{10}B(n, α)^{7}Li are damaged, leaving adjacent cells unaffected. The enhanced uptake of the boron-labeled agent in tumor cells versus normal cells results in selective killing of tumor cells. Using the mini p-^{7}Li neutron tube, a high flux of epithermal neutrons can be directly produced by operating the generator near the threshold interaction energy. On entering the patient's body, these epithermal neutrons are moderated to thermal neutrons when they arrive at the tumor site. The distribution of epithermal and thermal neutron flux inside the body has been studied in detailed by Nakagawa in one chapter of the book.[14] Using a 1.9 MV and 10 mA H^{-} ion beam with a diameter of 2 cm, the total neutron yield is 1.5×10^{11} n/s with mean neutron energy of 38 keV and a mean neutron angle of 23^{0}.[12] For a H^{-} ion beam with a diameter of 5 cm and an ion beam current of 70 mA, the average neutron yield for a 1% DF operation is approximately 1×10^{10} n/s, or an average epithermal neutron flux of 5×10^{8} n/cm^{2}/s, which is the recommended value for BNCT treatment.[15]

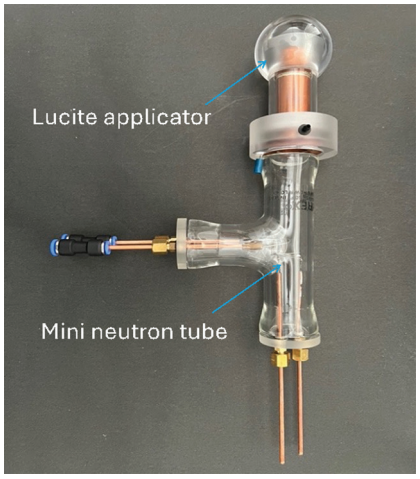

Figure 6. A prototype mini neutron tube with an applicator enclosing the conical titanium target. The spherical applicator head is changeable. The mini neutron tube and applicator system are approximately 25-cm long.

A single p-^{7}Li neutron tube with a 5-cm diameter beam target can provide the required epithermal neutron flux for BNCT. Alternatively, one can employ a cluster of mini neutron tubes each operated with a 2-cm diameter target. Figure 7 shows a schematic diagram of a multi-neutron tube arrangement. There are six tubes surrounding the center one. These six neutron tubes are focused on the tumor providing the highest flux of thermal neutrons at the tumor site. With a total H^{-} beam current of 70 mA (i.e., 10 mA from each neutron tube), the combined epithermal neutron yield is 1×10^{10} n/s for a 1% DF operation. Since the orientation of these neutron tubes can be adjusted independently, the epithermal neutron beam from each tube can be focused onto the tumor. As a result, the thermal neutron flux reaching the tumor site will be higher than a single large tube. With recent advancements in boron drug development,[16] the mini p-^{7}Li neutron tubes should be the most compact and versatile tool for the treatment of cancer through BNCT.

5. Mini gamma-ray tube for the generation of 6 MeV photons

High-energy photons have found important applications in explosive and special nuclear materials detection, medical imaging, cancer therapy, radioisotope production, and structural analysis. Bremsstrahlung photons (or X-rays) with a continuum energy distribution are generated by high-energy electron accelerators. The end-point energy

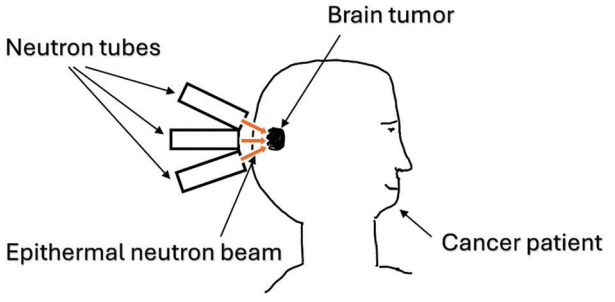

Figure 7. Treatment of brain tumor with multiple epithermal neutron tubes. Diagram created by the authors.

of these X-ray photons is the acceleration voltage of the electron beam. Since most Bremsstrahlung photons have energies much lower than the end-point energy,[8] they may not be useful for the intended application and contribute significant doses to the surroundings while producing unwanted background radiation. The thick shielding needed to remove these lower energy photons results in an accelerator system that is generally quite large and not suitable for some applications. High-energy gamma photons (or gamma rays) can be produced by the decay of some radioisotopes. For example, cesium-137 emits 662-keV gamma-rays and cobalt-60 emits a pair of 1.13 and 1.33 MeV gammas. Due to their high activities, these radioisotopes are very compact and intense gamma sources. The drawbacks are that they are always "on," require thickly shielded containers for safety purposes, and are regulated radioactive materials. The Gamma Knife device incorporates 201 cobalt-60 sources housed in the central body of the unit. These sources produce 201 collimated beams directed to a single focal point (machine isocenter). A newly loaded Gamma Knife has a total activity of the order of 220 TBq (6000 Ci) providing a gamma flux between 2.8 to 7×10^9 γ/cm²/s at the isocenter.[8] In its main application for the treatment of brain cancer, the Gamma Knife provides a typical dose rate on the order of 1 – 2 Gray/min at the tumor site.[8]

Alternatively, megavolt-energy gamma rays can also be produced by bombarding a target with accelerated ions (e.g., protons or deuterons) to create nuclear reactions in the target. Of all these reactions, the $^{19}F(p,\alpha\gamma)^{16}O$ reaction can produce high-energy gamma-rays of 6.1, 6.9, and 7.1 MeV, which are suitable for radiotherapy applications.[8] Using the p-^{19}F reaction, coupled with a mini gamma-ray generator, one can produce a useful gamma yield and energy for the radiotherapy treatment of cancer. The mini gamma-ray tube has a similar design and operation as the mini neutron tube. A schematic diagram of an axial-type mini gamma-ray tube is shown in Figure 8. A slotted thin titanium foil is used as the H^- ion emitter. The emitted H^- ions are then accelerated to the target electrode where the p-^{19}F gammas are produced.

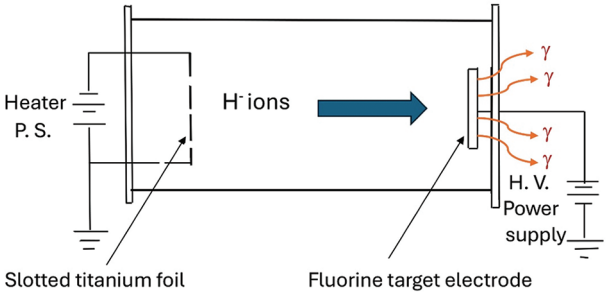

Figure 8. The mini p-^{19}F gamma-ray generator based on thermally emitted H^- ions. Diagram created by the authors.

The p-^{19}F reaction has a high resonance cross-section of 160 mb at 340 keV proton energy. It also has two resonances at ~900 keV proton energy. To take advantage of the high resonance cross-section for gamma production, the H^- ions need to be accelerated to energies of 1 MeV or higher. Thin layers of CaF_2 or MgF_2 can serve as the target materials. The thick-target gamma yields have been measured for incident proton energies between 1.5 and 4 MeV.[17,18] From the result of these measurements, the thick-target gamma yield for a 1 MeV proton beam is estimated to be about 2×10^{10} γ/mA/s. By operating the mini gamma-ray tube at 10% DF, the average gamma-ray yield is 2×10^9 γ/mA/s. Assuming the tumor is located 2 cm from the surface, the gamma flux at the tumor site will become 4×10^7 γ/mA/cm²/s. This flux can be greatly increased by employing the multiple tube arrangement as illustrated in Figure 7. With seven mini tubes (each operating at 1 MV, 10 mA, and 10% DF), the total gamma flux at the tumor site can exceed 2.8×10^9 γ/cm²/s. This estimated gamma flux at the tumor site is approximately the same as that of the Gamma Knife.

There are several advantages in using multiple mini tubes for brain tumor treatment. First, the gamma beams can be turned off when they are not in use. Second, the energy of the p-^{19}F gamma photon is higher than that of the Gamma Knife. They have better tumor penetration ability. Therefore, cancer treatment is more effective for the gamma tube system.[8] Third, since the gamma beams are operating in short pulses, FLASH photon therapy can be performed in the mini gamma tube system.[10] Fourth, the machine and maintenance cost for the single or multiple gamma tube system is much lower than that of the Gamma Knife. Fifth, the gamma tubes can be mounted on a robotic arm. Besides brain tumors, they can be used to treat other types of cancer in the body. As the entire gamma tube system is very compact, it can be conveniently located in any hospital or medical clinic.

6. Conclusion

Mini neutron/gamma-ray tubes based on thermal emission of H^-/D^- ions can provide a high flux of neutrons/gamma-photons in pulsed mode operation. The mini neutron/gamma-ray tube can be operated from hundreds of kilo-volts to 1.9 mega-volts to generate high-flux and high-energy neutrons or gamma-photons. These new mini neutron/gamma-ray tubes can be used in IORT, skin and breast cancer treatment, as well as treatment of brain and other types of tumors. A prototype of the mini tube is being assembled. It will be evaluated for neutron/gamma-

ray production before being employed for therapeutic uses. The mini neutron/gamma-ray tube system can be conveniently located in a clinical facility or inside the operational room of a hospital. If neutron/gamma radiotherapy is proven successful in removing all common types of tumors, it may become a standard therapeutic tool for cancer treatment.

Acknowledgments

Fruitful discussions with Maurizio Martellini and members of the Theranosti Centre (Milan, Italy) and the technical support by C&E Enterprises are deeply acknowledged.

Funding

This work is supported by Berkion Technology's internal funding. This work is supported by Berkion Technology's internal funding. The authors are currently affiliated with Berkion Technology, which was involved in designing and conducting the study.

Conflict of interest

The authors are currently affiliated with Berkion Technology. However, the authors declared that they have no known competing financial interests or personal relationships that could have influenced the work reported in this paper.

Author contributions

Conceptualization: All authors
Writing – original draft: Ka-Ngo Leung
Writing – review & editing: James K. Leung

Ethics approval and consent to participate

Not applicable.

Consent for publication

Not applicable.

Availability of data

Not applicable.

References

1. Macomber MW, Tarabadkar ES, Mayr NA, *et al*. Neutron radiation therapy for treatment of refractory merkel cell carcinoma. *Int J Part Ther*. 2017;3:485-491.

   doi: 10.14338/IJPT-17-0003.1

2. Krull A, Schwarz R, Brackrock S, *et al*. Neutron therapy in malignant salivary gland tumors: Results at European Centers. *Recent Results Cancer Res*. 1998;150:88-99.

3. Martellini M, Sarotto M, Leung KN, Gherardi G. A compact neutron generator for the Niort treatment of severe solid cancers. *Med Res Arch*. 2023;11(3).

   doi: 10.18103/mra.v11i3.3799

4. Persuad A, Kwan JW, Leitner M, *et al*. A tandem-based compact dual-energy gamma generator. *Rev Sci Instrum*. 2010;81:02B904.

   doi: 10.1063/1.3258028

5. Leung KN. Production of H- ions by thermal desorption process. *AIP Adv*. 2023;13:075123.

   doi: 10.1063/5.0162487

6. Leung KN. New mini neutron tubes with multiple applications. *J Nucl Eng*. 2024;5:197-208.

   doi: 10.3390/jne5030014

7. Leung KN. New compact neutron generator system for multiple applications. *Nucl Technol*. 2020;206:1607-1614.

8. National Research Council. *Radiation Source Use and Replacement: Abbreviated Version*. Washington, DC: The National Academies Press; 2008.

   doi: 10.17226/11976

9. Csikai J, editor. *CRC Handbook of Fast Neutron Generator*. Vol. 1. Boca Raton, Florida: CRC Press Inc.; 1987.

10. Bin J, Obst-Huebl I, Mao JH, *et al*. A new platform for ultra-high dose rate radiobiological research using the BELLA PW laser proton beamline. *Sci Rep Nat Portfolio*. 2022;12:1484.

    doi: 10.1038/s41598-022-05181-3

11. Leung KN, Leung JK, Melville G. Feasibility study on medical isotope production using a compact neutron generator. *Appl Radiat Isot*. 2018;137C:23-27.

    doi: 10.1016/j.apradiso.2018.02.026

12. Lee CL, Zhou XL. Thick target yields for the 7Li(p,n)7Be reaction near threshold. *Nucl Instrum Methods Phys Res B*. 1999;152:1-11.

13. Tanaka K, Kobayashi T, Sakurai Y, Nakagawa Y, Ishikawa M, Hoshi M. Irradiation characteristics of BNCT using Near-Threshold ^{7}Li(p,n)^{7}Be direct neutrons: Application to intra-operative BNCT for malignant brain tumors. *Phys Med Biol*. 2002;47:3011-3032.

    doi: 10.1088/0031-9155/47/16/315

14. Sauerwein WAG, Wittig A, Moss R, Nakagawa Y, editors. *Neutron Capture Therapy*. Berlin: Springer-Heidelberg; 2012.

15. Durisi E, Zanini A, Manfredotti C, *et al*. Design of an epithermal column for BNCT based on D-D fusion neutron facility. *Nucl Instrum Methods Phys Res A*. 2007;574:363-369.

16. Wang S, Blaha C, Santos R, *et al*. Synthesis and initial biological evaluation of boron-containing prostate-specific

membrane antigen ligands for treatment of prostate cancer using boron neutron capture therapy. *Mol Pharm.* 2019;16:3831-3841.

doi: 10.1021/acs.molpharmaceut.9b00464

17. Fessler A, Massey TN, Micklich BJ, Smith DL. Thick target photon yields and angular distributions for the $^{19}F(p,\alpha\gamma)^{16}O$ source reaction at incident proton energies between 1.5 and 4.0 MeV. *Nucl Instrum Methods Phys Res A*. 2000;450:353-359.

18. Micklich BJ, Smith DL, Massey TN, Fink CL, Ingram D. Measurement of thick-target high-energy γ-ray yields from the $^{19}F(p,\alpha\gamma)^{16}O$ reaction. *Nucl Instrum Methods Phys Res A*. 2003;505:1-4.

doi: 10.1016/S0168-9002(03)01006-4

ACCSCIENCE PUBLISHING

Advances in Radiotherapy & Nuclear Medicine

SHORT COMMUNICATION

Determining beta radiation doses from Y-90 microsphere for the treatment of hepatic tumors by using Monte Carlo and analytical methods

Leonardo Pessoa da Silva[1], Henrique Trombini[2], and Eduardo De Paiva[1]*

[1]Division of Medical Physics, Institute of Radiation Protection and Dosimetry, Rio de Janeiro, Brazil

[2]Department of Exact and Applied Social Sciences, Federal University of Health Sciences of Porto Alegre, Porto Alegre, Rio Grande do Sul, Brazil

Abstract

The very short range of beta radiation is a potential radiation treatment for tumor, which can preserve sensitive structures. However, due to the limited range of beta radiation, practical dosimetry of beta sources may be a point of concern, and theoretical dosimetry methods play an important role. A resin microsphere loaded with the Yttrium-90 (Y-90) radionuclide can be applied in the radioembolization of hepatic tumors. In this work, we present initial calculations of dose rates around a microsphere loaded with the Y-90 radionuclide uniformly distributed on its exterior surface. Two approaches were used to carry out the estimations: the first one by means of Monte Carlo simulations using the PENELOPE code and the second one by means of the beta-point dose function formalism. A Fortran code was developed to handle with the various quantities necessary to perform the numerical integration of the beta-point dose function. A comparison between results obtained by means of both methods indicated a maximum difference of ~5% up to the 0.3 cm distance from the center of the sphere.

Keywords: Radioembolization; Beta particles; Yttrium-90; Monte Carlo method; Beta-point dose function

***Corresponding author:**
Eduardo De Paiva
(eduardo.paiva@ird.gov.br)

Citation: da Silva LP, Trombini H, De Paiva E. Determining beta radiation doses from Y-90 microsphere for the treatment of hepatic tumors by using Monte Carlo and analytical methods. *Adv Radiother Nucl Med*. 2024;2(3):3639. doi: 10.36922/arnm.3639

Received: May 12, 2024

Accepted: June 26, 2024

Published Online: August 13, 2024

1. Introduction

Beta radiation plays an important role in the treatment of several kinds of diseases.[1] The short range of beta particles and their high dose gradient make them an attractive clinical option for brachytherapy treatments. In particular, there is an increasingly use of radioembolization with Yttrium-90 or Holmium-166 to treat primary and metastatic liver tumors.[2-12] Radioembolization consists of the administration of radioactive microspheres to the target region through a catheter in a hemodynamic procedure.[13] By lodging in the dysfunctional tissue through the local vasculature, in addition to producing sufficient doses of radiation to promote the death of tumor cells, the embolization generated prevents the arrival of oxygen and nutrients to this region, enhancing the desired effect.[14] There are two commercial types of microspheres loaded with Y-90: those of resin (Sir-Spheres®, Sirtex Medical Ltd., Sydney, Australia) and those of glass (Therasphere®, Boston Scientific, Boston, MA, USA); and there are also the microspheres of PLLA (poly-L-lactic acid) loaded with Ho-166 (QuiremSpheres®, Quirem Medical B.V., Deventer, The Netherlands).[2]

In this study, estimations of the beta dose rates alongside the radial distance of a microsphere containing the Yttrium-90 radionuclide were performed. Yttrium-90 has a physical half-life of 2.7 days and emits beta particles with a maximum energy of 2.28 MeV (mean energy of 0.933 MeV) and with a mean range of 0.25 cm. These properties make it a suitable beta emitter to be used in brachytherapy treatment of hepatic tumors.[2-12]

In this work, we present initial calculations of dose rates around a microsphere of radius *R* loaded with the Y-90 radionuclide uniformly distributed on its exterior surface (Figure 1). Two approaches were used to carry out the estimations: first by means of Monte Carlo (MC) simulations using the PENELOPE code, version 2014;[15,16] and second by means of the beta-point dose function formalism.[17-19] A Fortran code (some versions of compiler can be freely downloaded from the web) was developed to perform the numerical integration of the beta-point dose function.[20,21] A comparison between the calculations obtained by MC simulation and the results obtained by means of the beta-point dose function was made, and a good agreement was found between the results considering these two calculation methods.

It should be noticed that the dosimetric evaluation of a single microsphere provides essential insights into the fundamental behavior of the beta radiation emitted by Y-90 at a micro-scale. This foundational knowledge is crucial for understanding the dose distribution around individual microspheres, which is a building block for modeling more complex systems involving multiple microspheres.

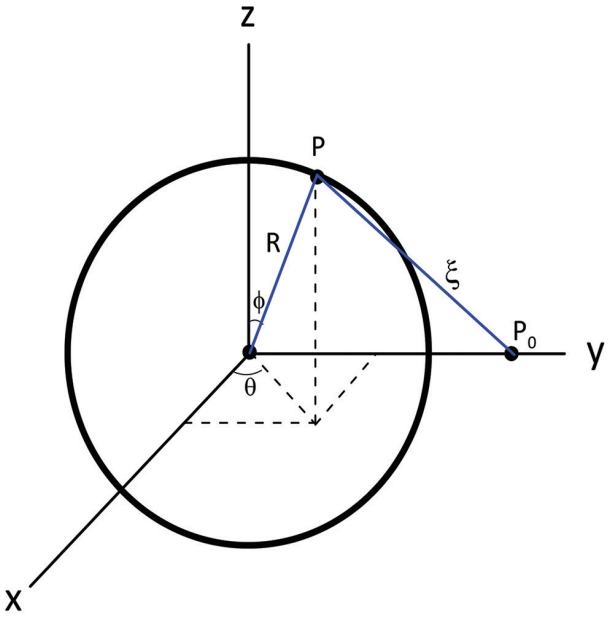

Figure 1. The geometry of the sphere with the Yttrium-90 radionuclide distributed on its surface used throughout calculations

2. Materials and methods

In this study, we consider a unique sphere containing the Y-90 radioisotope distributed uniformly over its external surface, as well as SIR-spheres microspheres which are manufactured from resin [poly(styrene-co-divinylbenzene)] and biocompatible material, and are intended for permanent application (SIR-Spheres®, Sirtex Medical Ltd., Sydney, Australia).[2]

In clinical practice, Y-90 microspheres are often distributed heterogeneously within the liver. Understanding the dose distribution from a single microsphere allows for better modeling of scenarios where clusters of microspheres form regions of varying radiation intensities. This knowledge can improve the accuracy of dose calculations in heterogeneous distributions, leading to more precise treatment planning.

2.1. Monte carlo calculation

In this work, the dose rates along the radial distances of the resin Y-90 microsphere were simulated using the PENELOPE code, version 2014.[15,16] With the PENELOPE code, it is possible to simulate negative beta particles, positrons, and photons cascades initiated by a primary incident particle.

All simulated materials were generated using the *material.f* program, which is part of the PENELOPE package. Once the information about the materials is known, the program interface prompts the user to enter relevant information such as the number of chemical elements in the material, their atomic numbers, their stoichiometry or mass fraction per element and density. Once the main data is provided, the software calculates the average excitation energy, the estimated oscillator strength, and the plasmon energy.

In the *in.in* input file, the necessary parameters were defined for the simulation to occur as expected, considering the variables of the simulated problem and computational time optimization criteria. When building this file, important aspects were defined, such as the type of simulated particle and its energies, the spatial arrangement of the emitting source and the target material, the geometry file name that contains the information about the emitting body and its dimensions, the emission direction, the desired output files, among other important parameters, such as simulation time and number of simulated stories.

The target material for simulated energy deposition was the liver tissue described by the ICRU report 44,[22] with a density of 1.06 g/cm^3. To generate the sphere, the PENGEOM package was used, which is capable of producing objects to be included in the simulation from quadric surfaces, which means that from a set of second-degree equations, it is possible to reproduce objects that are part of the simulation, like the analyzed microsphere.

In the case of the resin microsphere, in which the radioactivity is only found in more superficial layers of the microsphere,[14] we decided to create a second spherical surface around an inactive core, thus creating a body of the type of spherical shell in which the emission of radiation was defined, with a chemical composition identical to that of the nucleus. Due to the absence of specifications in the literature or manufacturer, the shell thickness was set as 1 μm.

The Y-90 beta emission spectra used for the simulations, in which we have curves of intensity (dN/dE) as a function of energy, were obtained through the Evaluated Nuclear Structure Data File database, which has updated information on more than 3000 nuclides and its properties.[23] The obtained spectrum was integrated and normalized to represent the energy spectrum in terms of probabilities, ensuring that the sum of individual probabilities equaled to one.

The GRIDR tally was chosen, in which spherical symmetry was assumed and the energy per unit of mass was integrated radially as a function of the distance from the origin of the system. As the center of the microsphere and the target tissue coincide with this point, the function provides exactly the radiation dose as a function of the distance from the microsphere.

Since the PENELOPE code allows the resumption of interrupted or already completed processes by changing the stopping criterion, the number of simulated primary particles was increased until the statistical uncertainty (3 standard deviations – presented in the output file) relating to the absorbed dose of each of the bins presented a value of <1% in relation to the dose absorbed into this mass element. The final number of simulated primary particles was 10^9.

2.2. Beta-point source dose function calculation

The function that describes the absorbed dose rate $J(\xi)$ around a beta-point source as a function of the distance ξ can be expressed by Vynckier and Wambersie.[18,19]

$$J(\xi)=\frac{B}{(\rho\upsilon\xi)^2}\left\{\begin{array}{l} c\left[\left(1-\frac{\rho\upsilon\xi}{c}\exp\right)\right]X_1(\xi)+ \\ \left(1-\frac{\rho\upsilon\xi}{c}\right) \\ \rho\upsilon\xi exp(1-\rho\upsilon\xi)- \\ \rho\upsilon\xi\left(1-\frac{\rho\upsilon\xi}{2}-\frac{f}{2}\right) \end{array}\right\}X_2(\xi), \quad \text{(I)}$$

Where ρ is the medium density and ν is the absorption coefficient, with

$$X_1(\xi)=0 \quad \text{if} \quad \rho\upsilon\xi \geq c \text{ and } \quad X_2(\xi)=0$$

$$\text{if} \quad \rho\upsilon\xi \geq f \quad \text{(II)}$$

The parameter B is a normalization constant given as a function of the dimensionless parameters c and f by the following expression:

$$B=\frac{0.046\rho^2\upsilon^3\bar{E}_\beta}{3c^2-(c^2-1)\exp(1)+(3+f)\exp(1-f)-4\exp\left(1-\frac{f}{2}\right)}, \quad \text{(III)}$$

where $\bar{E}_\beta$ is the mean kinetic energy of the beta particles.

Equation I was obtained by Vynckier and Wambersie[18,19] from the expression firstly proposed by Loevinger[17] to obtain a better fit of the beta function to new experimental and theoretical data.

In Equation I, we consider that the medium has density ρ = 1 g/cm^3, and the radioactive material is uniformly distributed on its surface. Thus, considering spherical coordinates, the absorbed dose rate $\dot{D}$ at point $P_0(x_0, y_0, z_0)$ along y-axis (Figure 1) can be written as:

$$\dot{D}=a_S\iint J(\xi).dS=R^2a_S\iint J(\xi).\sin\phi d\phi d\theta, \quad \text{(IV)}$$

Where a_s is the area activity. The angle θ is the azimuthal angle in the xy-plane from the x-axis with $0 \leq \theta \leq 2\pi$; ϕ is the polar angle from the positive z-axis with $0 \leq \phi \leq \pi$; and the radial coordinate is the constant radius R.

The distance from the point source on the sphere to the point of interest P_0 is related to the spherical coordinates given by:

$$\xi^2=R^2+x_0^2+y_0^2+z_0^2-2R^*$$
$$\left(x_0\sin\phi\cos\theta+y_0\sin\phi\sin\theta+z_0\cos\phi\right) \quad \text{(V)}$$

The dose rate given by Equation IV was numerically evaluated by means of a Fortran code, and results were compared to simulation data obtained using the PENELOPE code.

A Fortran code was developed to perform the numerical integration of the beta-point source dose function according to the above equations to obtain the absorbed dose rates along the radial distance of a microsphere containing the Y-90 radioisotope distributed over its area. The radius of the sphere was 16 μm and its activity was 50 Bq, and in the above equations, the parameters c, f, υ, and $\bar{E}_\beta$ are, respectively, 0.95, 4.48, 5.05 cm^2/g, and 0.933 MeV for Y-90.[20,21]

3. Results and discussion

In Figure 2, the absorbed dose rates in water are shown for the Y-90 microsphere as a function of the radial distance from the center of the microsphere, from 0.03 cm up to 1 cm. Results were normalized to the 0.03 cm radial distance, and values obtained from both approaches (MC and Loevinger formalism) clearly indicate a pronounced reduction in dose rate along the radial distance. Dose rates dropped to 50% of the reference value at 0.042 cm, to 20% at 0.066 cm, to just 5% at 0.129 cm, and became negligible from 0.27 cm onward. These findings showed that a considerable amount of beta energy is absorbed by tissue stretching for a short distance. Differences between results from the two theoretical methods were at most ~5% up to a distance of 0.3 cm from the sphere's center.

The short range of beta particles in tissue can be an advantage in radiotherapy treatments of hepatic tumors.

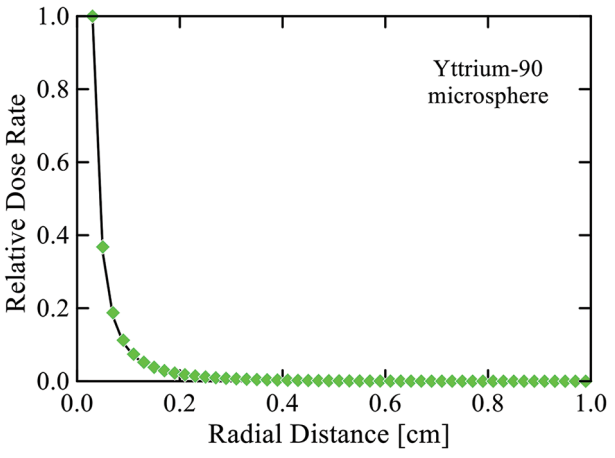

Figure 2. The dose rates as a function of the radial distance from the center of the microsphere with the Yttrium-90 radionuclide distributed on its external surface obtained by the beta-point dose function (solid line) and by Monte Carlo simulations (lozenges). Results are normalized to 0.03 cm distance.

Because of the rapid dose decline in tissue, the beta source can deliver a high dose of radiation to the target volume, while sparing the adjacent healthy structures. However, because of the experimental limitations of beta radiation dosimetry, simulation and analytical calculation methods can be used to estimate the radiation doses of beta emitters. In this work, we used the MC technique (PENELOPE code) and the beta-point dose function formalism to evaluate the radiation doses from a microsphere intended to be used in the treatment of hepatic tumors, and the results of the two approaches were compared. Although MC simulation, mainly because of its higher accuracy, is the method of choice in evaluating the interaction of ionizing radiation with matter and estimating the radiation dose, the beta-point dose function calculation showed a good agreement with the simulation method used in this study, mainly at relevant clinical distances. This may encourage the use of analytical calculation as a dosimetry method for beta-emitting nuclides, mostly because the calculation method produces the result faster than the simulation technique, making it a good dosimetry option for clinical practices. When considering the beta-point dose function as a dose calculation method, complex geometries should not be considered because of the inaccurate results. In this case, the MC methods eclipse the analytical methods. While point source approximations are commonly used, they may not always capture the nuances of the actual dose distribution from a microsphere. By comparing the detailed dosimetric profile of a single microsphere to that of a point source approximation, our study can identify potential discrepancies and provide more accurate dose predictions, enhancing the precision of dosimetric assessments, particularly in areas with high microsphere concentrations.

Insights from single-microsphere dosimetry can inform the optimization of microsphere distribution strategies. For example, understanding the dose fall-off and penetration characteristics of a single microsphere can help in planning the spatial arrangement of multiple microspheres to achieve uniform dose distribution while minimizing healthy tissue exposure. Our findings can be integrated into multi-microsphere dosimetry models to refine the overall dose calculations. Accurate single-sphere dosimetry data can serve as inputs for Monte Carlo simulations or analytical methods that account for the cumulative effect of multiple microspheres. This approach ensures that the complex interactions between microspheres and their collective dose distribution are modeled more accurately.

4. Conclusion

In this work, two theoretical calculation methods were used to estimate the dose rates around a microsphere

containing the Y-90 radioisotope, and a simple numerical calculation of beta particles radiation dose rates from one Y-90 microsphere that can be used in the treatment of hepatic tumors was performed. Despite the simplified assumptions adopted in the analytical/numerical method and the inherent computational limitations of the MC method, the calculation methods were able to reproduce the general trend of dose rate values on the radial distance of the Y-90 microsphere and may be used as an auxiliary tool in dose planning and also serve as a reference in future works concerning this kind of beta sources. However, it should be mentioned that there is a downside to the MC simulation techniques, which is their consumption time and heavy computation, which may hinder their use in clinical practice. Alternatively, although analytical calculation methods can estimate the radiation dose faster than the simulation techniques, there is no possibility to simulate more complex geometries and consider different types of materials. Results of a more complete study considering also the Thera (Yttrium-90, glass) and Quirem (Holmium-166, PLLA) microspheres will be reported soon.

This study focuses specifically on the dosimetric evaluation of a single microsphere loaded with the Y-90 radioisotope, which, in some extent, has not been extensively explored. While it is valid to point out the practicality of evaluating dose estimates for different beta applicators, our work addresses an important aspect of microsphere-based treatments. By analyzing the beta dose from a single microsphere, we provide insights that could be valuable for refining treatment strategies and optimizing dose delivery in targeted therapies. Beyond its immediate applications, our methodology can influence broader research in pharmacokinetics and pharmacodynamics, potentially leading to innovations in drug development and therapeutic strategies. In summary, our study provides a foundational advancement in dose calculation that not only addresses current challenges but also opens up new avenues for research and application in dosimetry. The principles of dose distribution and their implications for treatment planning are applicable to different radioisotopes, making our study valuable for a wide range of radionuclide therapies.

Acknowledgments

The authors thank IRD/CNEN and UFCSPA for their support. The author Leonardo Pessoa da Silva would like also to thank for the partial financial support given by the Brazilian CAPES.

Funding

None.

Conflict of interest

The authors declare that they have no competing interests.

Author contributions

Conceptualization: Leonardo Pessoa da Silva, Henrique Trombini
Investigation: Leonardo Pessoa da Silva
Methodology: All authors
Writing – original draft: Eduardo De Paiva
Writing – review & editing: All authors

Ethics approval and consent to participate

Not applicable.

Consent for publication

Not applicable.

Availability of data

Data are available from the corresponding author upon reasonable request.

References

1. ICRU Report 72. Dosimetry of beta rays sources and low-energy photons for brachytherapy with sealed sources. *J ICRU*. 2004;4:2.

   doi: 10.1093/jicru/ndh018

2. Aliseda D, Rotellar F, Sancho L, *et al*. Surgery and radioembolization of liver tumors. *Rev Esp Med Nucl Imag Mol (Engl Ed)*. 2023;42(4):265-271.

   doi: 10.1016/j.remnie.2023.06.002

3. Burrel M, Bermúdez P, Forner González A. Perspectives for yttrium-90 radioembolization as therapeutic option for hepatocellular carcinoma. *Rev Esp Enferm Dig*. 2022;114(4):195-197.

   doi: 10.17235/reed.2022.8775/2022

4. Lüdemann W, Kahn J, Pustelnik D, *et al*. Yttrium-90 radioembolization for unresectable hepatocellular carcinoma: Predictive modeling strategies to anticipate tumor response and improve patient selection. *Eur Radiol*. 2022;32(7):4687-4698.

   doi: 10.1007/s00330-022-08585-x

5. Choi JW, Kim HC. Radioembolization for hepatocellular carcinoma: What clinicians need to know. *J Liver Cancer*. 2022;22(1):4-13.

   doi: 10.17998/jlc.2022.01.16

6. Oliván-Sasot P, Pérez-Enguix D, Bello-Arques P, *et al*. Radioembolization in patients with hepatocellular carcinoma: a series of 53 cases. *Radiologia* (*Engl Ed*). 2023;65(1):12-21.

doi: 10.1016/j.rx.2020.09.012

7. Lee HM, Alder L, Nguyen M, *et al*. Long-term outcome analysis of Y90 radioembolization in hepatocellular carcinoma. *J Gastrointest Oncol*. 2023;14(3):1378-1391.

   doi: 10.21037/jgo-22-882

8. Anbari Y, Veerman FE, Keane G, *et al*. Current status of yttrium-90 microspheres radioembolization in primary and metastatic liver cancer. *J Interv Med*. 2023;6(4):153-159.

   doi: 10.1016/j.jimed.2023.09.001

9. Yu CY, Huang PH, Tsang LL, *et al*. Yttrium-90 radioembolization as the major treatment of hepatocellular carcinoma. *J Hepatocell Carcinoma*. 2023;10:17-26.

   doi: 10.2147/JHC.S385478

10. Yu Q, Khanjyan M, Fidelman N, Pillai A. Contemporary applications of Y90 for the treatment of hepatocellular carcinoma. *Hepatol Commun*. 2023;7(10):e0288.

    doi: 10.1097/HC9.0000000000000288

11. Jiang Z, Yang F, Wang W. Applications of Yttrium-90 (^{90}Y) in hepatocellular carcinoma. *Onco Targets Ther*. 2024;17: 149-157.

    doi: 10.2147/OTT.S445898

12. Busse NC, Al-Ghazi MS, Abi-Jaoudeh N, *et al*. AAPM medical physics practice guideline 14.a: Yttrium-90 microsphere radioembolization. *J Appl Clin Med Phys*. 2024;25(2):e14157.

    doi: 10.1002/acm2.14157

13. Weber M, Lam M, Chiesa C, *et al*. EANM procedure guideline for the treatment of liver cancer and liver metastases with intra-arterial radioactive compounds. *Eur J Nucl Med Mol Imag*. 2022;49:1682-1699.

    doi: 10.1007/s00259-021-05600-z

14. Pasciak AS. *Handbook of Radioembolization: Physics, Biology, Nuclear Medicine, and Imaging*. United States: CRC PRESS; 2016. p. 330.

15. Salvat F. *PENELOPE-2014: A Code System for Monte Carlo Simulation of Electron and Photon Transport*; 2015. Available from: https://www.oecd-nea.org/upload/docs/application/pdf/2020-01/nsc-doc2015-3.pdf [Last accessed on 2023 Jun 15].

16. Salvat F. The penelope code system. Specific features and recent improvements. *Ann N Energy*. 2013;82:98-109.

    doi: 10.1016/j.anucene.2014.08.007

17. Loevinger R. The dosimetry of beta sources in tissue. The point-source function. *Radiology*. 1956;66(1):55-62.

    doi: 10.1148/66.1.55

18. Vynckier S, Wambersie A. Dosimetry of beta sources in radiotherapy. I. The beta point source dose function. *Phys Med Biol*. 1982;27:1339-1347.

    doi: 10.1088/0031-9155/27/11/004

19. Vynckier S, Wambersie A. Dosimetry of beta sources in radiotherapy: Absorbed dose distributions around plane sources. *Radiat Prot Dos*. 1986;14:169-173.

    doi: 10.1093/oxfordjournals.rpd.a079641

20. Pashazadeh A, De Paiva E, Mahmoodian N, Friebe M. Calculation of beta radiation dose of a circular Y-90 skin patch: Analytical and simulation methods. *Radiat Phys Chem*. 2020;166:108491.

    doi: 10.1016/j.radphyschem.2019.108491

21. De Paiva, E, Robatjazi M, Pashazadeh A. Calculations of beta radiation doses from multiwell Phosphorus-32 and Yttrium-90 applicators designed to be used in the treatment of superficial skin tumors: Comparison of Monte Carlo and analytical methods. *Eur Phys J Plus*. 2022;137:916.

    doi: 10.1140/epjp/s13360-022-03116-5

22. White, DR. ICRU Report 44, Tissue substitutes in radiation dosimetry and measurement. *J ICRU*. 1989;23:1-189.

23. *Evaluated Nuclear Structure Data File*. Available from: https://www.nndc.bnl.gov/ensdf [Last accessed on 2023 Jun 20].

ACCSCIENCE PUBLISHING

Advances in Radiotherapy & Nuclear Medicine

CASE REPORT

Co-occurrence of rectal and lung cancers: A case report

Phuong Cam Pham[1,2,3], Khuy Minh Doan[4], Thuy Phuong Ngo[2], Hien Minh Nguyen[2], Ha Thanh Le[2], Lanh Minh Pham[4], and Khoa Trong Mai[1,2,3]*

[1]The Nuclear Medicine and Oncology Center, Bach Mai Hospital, Hanoi, Vietnam

[2]Department of Oncology and Nuclear Medicine, University of Medicine and Pharmacy, Vietnam National University, Hanoi, Vietnam

[3]Department of Nuclear Medicine, Hanoi Medical University, Hanoi, Vietnam

[4]The Pathology and Cytology Center, Bach Mai Hospital, Hanoi, Vietnam

Abstract

Co-occurrence of two types of cancers, especially lung and colorectal cancers is rare. This study investigated patients at Bach Mai Hospital who were diagnosed with two or three cancers. Only a few patients concurrently had two cancers. Positron emission tomography (PET)/computed tomography (CT) was used for the staging of cancer, especially synchronous malignancies. In this report, we have presented the case of a patient diagnosed with rectal and lung cancer based on CT, magnetic resonance imaging, and PET/CT scans as well as immunohistochemistry. Managing terminal synchronous cancers is challenging. The efficacy of the preferred anticancer therapy must be considered to ensure patients' quality of life. Although the combination of tyrosine kinase inhibitor-targeted therapy and chemotherapy is promising, its toxicity remains unknown. Our patient received two cycles of mFOLFOX6, afatinib, and bisphosphonate. However, the treatment was discontinued due to grade 3 stomatitis and grade 2 anemia. Despite recovery and partial response in terms of symptom and tumor marker reduction, the patient refused further treatment and chose palliative care.

Keywords: Two types of cancers; Lung and colorectal cancers; Tyrosine kinase inhibitors plus chemotherapy; Synchronous cancer; Afatinib plus mFOLFOX6

***Corresponding author:**
Khoa Trong Mai
(maitrongkhoa@hmu.edu)

Citation: Pham PC, Doan KM, Ngo TP, *et al.* Co-occurrence of rectal and lung cancers: A case report. *Adv Radiother Nucl Med.* 2024;2(3):3887.
doi: 10.36922/arnm.3887

Received: June 6, 2024

Accepted: August 14, 2024

Published Online: October 7, 2024

1. Introduction

While lung and colon cancers are two common malignancies, their co-occurrence is relatively rare, accounting for <1% of all cases of lung cancer. Moreover, bone metastasis in patients with colorectal cancer is rare.[1] Positron emission tomography (PET)/computed tomography (CT) has been proven to improve the diagnostic performance of synchronous multiple cancers and expose more primary tumors and metastatic lesions. This study aims to report a rare case of a patient with synchronous lung and rectal cancer who was diagnosed with bone metastases from rectal cancer at the beginning. However, the understanding of the mechanisms implicated in multiple synchronous cancers remains limited, and

no guidelines for the management and treatment of this condition have been established. Recently, the combination of epidermal growth factor receptor (EGFR) tyrosine kinase inhibitors and chemotherapy has been investigated, especially in non-small cell lung cancer. The efficacy and safety profile of the afatinib plus 5-fluorouracil (5-FU) regimen has been evaluated in several studies. However, to the best of our knowledge, studies on the efficacy of the combination of mFOLFOX6 and afatinib are limited.

2. Case presentation

A 66-year-old male carpenter was admitted for severe low back pain and weakness in the lower extremities for over 1 month with no history of injuries or physical labor. He had a history of smoking (20 pack years) and a family history of a cousin with liver cancer (no relatives had colorectal or lung cancer). Clinical examination revealed limited lumbar mobility, reduced motor function of the lower extremities, and autonomic dysfunction.

Figure 1 shows a lumbar magnetic resonance imaging (MRI) scan with multiple osteolytic lesions of the lumbosacral vertebrae, which invaded the soft tissues and compressed the spinal cord and cauda equina.

A whole-body CT scan revealed a 25 × 28-mm solid nodule, with spiculated margin and pleural retraction, in the lower lobe of the right lung, indicating the presence of a primary malignant tumor; no abnormal regional lymphadenopathy was detected (Figure 2). Several enlarged focal hypodense presacral lymph nodes were also detected along the inferior mesenteric artery (IMA). The largest short-axis diameter of the lymph nodes was 10 mm, with an uncertain gastrointestinal wall thickness (Figure 3). Multifocal osteolytic lesions were also detected, including a rib lesion that invaded the adjacent soft tissues (Figure 4).

Colonoscopy revealed an endoluminal ulcerated mass occupying half of the lumen circumference, which was located 10 cm from the anal verge (Figure 5). A pelvic MRI scan showed a thickened high rectal wall with serosal invasion and multiple enlarged presacral lymph nodes along the IMA (Figure 6). The carcinoembryonic antigen (CEA) level was 323.2 ng/mL (normal range: 0 – 3.4 ng/mL). The Cyfra 21 – 1 level was 11.11 ng/mL (normal range: 0 – 3.3 ng/mL).

Histopathological report of lung biopsy revealed that the primary lung adenocarcinoma was positive for thyroid transcription factor-1 (TTF-1) and napsin A and negative for cytokeratin 20 (CK20) and caudal-type homeobox 2 (CDX2). Rectal biopsy samples revealed that the rectal adenocarcinoma was positive for CDX2 and negative for TTF-1. The biopsy specimen in the lesion of the rib showed adenocarcinoma, which originated from the gastrointestinal tract and was positive for CK20 and CDX2. These findings were consistent with the characteristics of synchronous lung and colon adenocarcinomas (Table 1 and Figure 7).

Further gene testing revealed an absence of Rat sarcoma (RAS), *BRAF* mutations, and proficient mismatch repair (pMMR) on rectal tumors, whereas lung lesions showed EGFR mutations in exon 18 and PD-L1 clone SP263 with a TPS of 80%.

The CT scan did not show any enlarged hilar or mediastinal lymph nodes. However, on the PET/CT, we detected a malignant mass measuring 31 × 22 mm in the right lower lobe of the lung (arrow), with a SUVmax of 9.0, right hilar lymph nodes measuring 13 × 8 mm with a

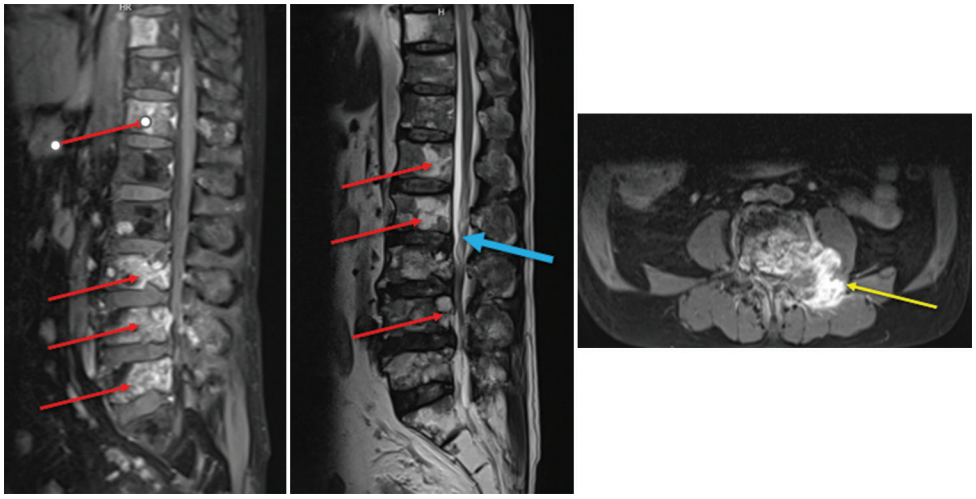

Figure 1. Lumbar magnetic resonance imaging shows multiple osteolytic lesions of the lumbosacral vertebrae (red arrow) invading the soft tissues (yellow arrow) and compressing the spinal cord and cauda equina (blue arrow)

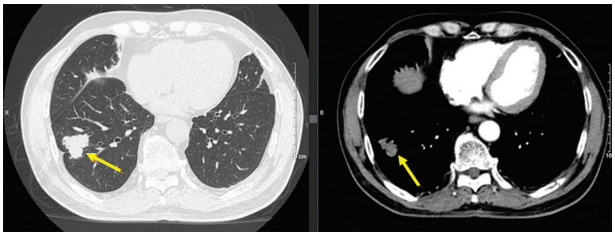

Figure 2. Computed tomography scan of the chest shows a 25 × 28-mm mass, with spiculated margin and pleural retraction and no abnormal regional lymphadenopathy, in the lower lobe of the right lung (arrow)

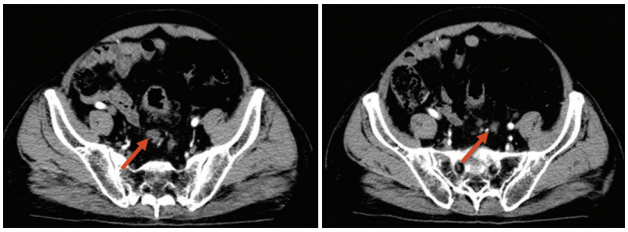

Figure 3. Abdominal-pelvic computed tomography scan shows several presacral lymph nodes along the inferior mesenteric artery, and their largest short-axis diameter was 10 mm

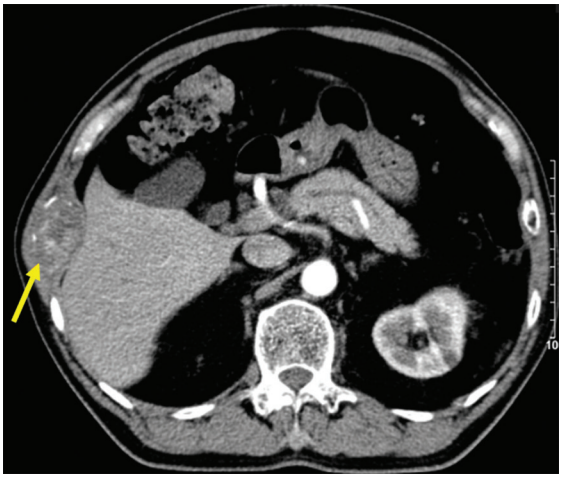

Figure 4. Computed tomography scan shows a metastatic lesion on the right rib, which invaded the adjacent soft tissues (arrow)

SUVmax of 5.7, thickened high rectal wall with a SUVmax of 9.0 with serosal invasion, three colorectal lymph nodes, three inferior IMA lymph nodes with a SUVmax of 7.2, and increased metabolism of 18F-fluodeoxyglucose in the whole skeletal system (Figure 8).

After consulting with multidisciplinary tumor boards, the patient was treated with a second generation of tyrosine kinase inhibitors (TKIs; afatinib) combined with mFOLFOX6 and bisphosphonate.

However, before treatment, the patient experienced autonomic dysfunction and complete paralysis of the lower

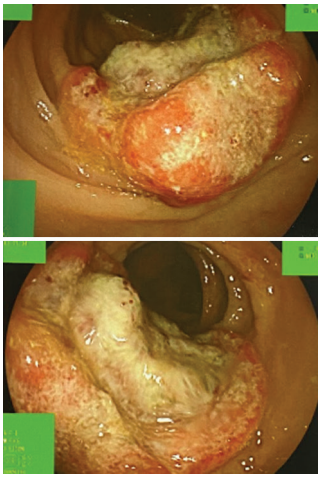

Figure 5. Colonoscopy revealed that an ulcerated mass occupied half of the lumen circumference, which was located 10 cm from the anal verge

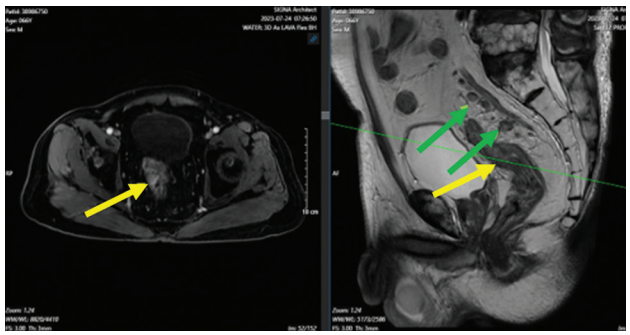

Figure 6. A pelvic magnetic resonance imaging scan shows a high rectal tumor (yellow arrow) and multiple inferior mesenteric artery lymph node chains (green arrow)

extremities. Following two cycles of chemotherapy and afatinib, although the patient's tumor markers and pain significantly reduced, his paralysis symptoms persisted and grade 2 anemia and grade 3 stomatitis occurred. Therefore, the anticancer treatment was discontinued, and the patient underwent blood transfusions and received medication supplements for a week. Nevertheless, the patient then refused further treatment and opted for palliative care at home.

3. Discussion

The diagnosis and management of synchronous malignancies have been a challenge. This study reported a rare case of synchronous lung cancer and rectal cancer, the latter being classified in the advanced stage with bone metastases. The co-occurrence of lung and colon cancers is rare. A study in Japan that was conducted from April 2009 to July 2016 reported that only 17 out of 3102 (0.54%) patients with lung cancer were diagnosed with colorectal cancer.[2] Similar findings were observed in another UK study, which found

Table 1. Histopathology information

Location	Histopathology	Immunohistochemistry				Conclusion
		TTF-1	Napsin A	CDX2	CK20	
Lung tumor	Adenocarcinoma	+	+	-	-	Primary lung cancer
Rectal tumor	Mucinous adenocarcinoma	-		+	-	Primary rectal cancer
Rib tumor	Adenocarcinoma	-		+	+	Origin from the digestive system

Abbreviations: TTF-1: Thyroid transcription factor-1; CDX: Caudal-type homeobox 2; CK20: Cytokeratin 20.

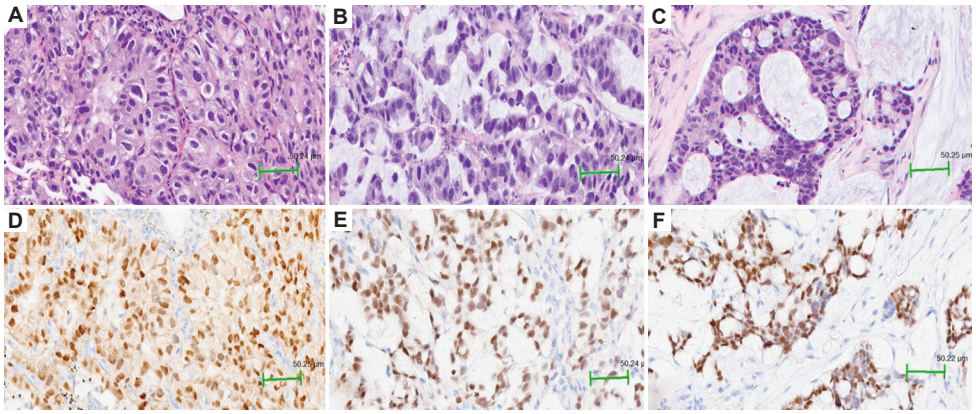

Figure 7. Images of histopathology and immunohistochemistry. H&E stain indicated adenocarcinoma of the lung tumor (A), rectal tumor (B) and rib tumor (C). Immunohistochemical examination revealed staining was positive for thyroid transcription factor-1 in lung tumor (D), caudal-type homeobox 2 in rectal tumor (E), and rib tumor (F). Magnification: 400×

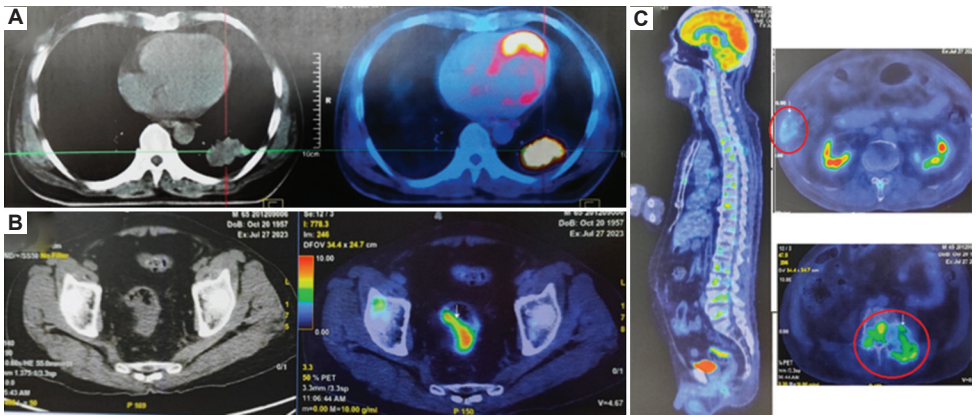

Figure 8. Positron emission tomography/computed tomography image. (A) Right lung tumor. (B) Rectal tumor. (C) Multiple bone lesions (red circle)

that 0.6% of patients had simultaneous colorectal and lung cancer.[3] Furthermore, approximately 1.24% of colon cancer cases have been reported to have metastasized to the bone at the time of diagnosis, making it a significantly unusual occurrence.[1]

If rectal lesions are neglected, the patient's condition can be easily mistaken for lung cancer with bone metastases or rectal cancer with lung and bone metastases. Therefore, it is crucial to screen for additional cancers and emphasize the value of PET/CT in patients with cancer. PET/CT can identify a significant number of second primary cancers in patients with known primary cancer and plays an important role in the management of metachronous malignancies.[4] Our patient's stage was increased from T1N0 to T1N1 due to the detection of ipsilateral hilar lymph nodes in PET/CT, which was also contraindicated for stereotactic body radiation therapy.[5]

When treating synchronous cancers, it is important to determine which of them should be handled first or whether they should be managed simultaneously according to several criteria, such as whether the cancers are more hazardous, have a higher probability of spreading, or are

life-threatening and need urgent intervention as well as the associated mobilities.[6] Treatment for both types of cancer must be considered during the entire course of the treatment. Furthermore, toxicities can arise if different combinations of therapeutic alternatives are administered.

Our patient was in the advanced stage and received treatment to extend survival and enhance his quality of life. Upon initial diagnosis, he uncomfortably complained of low back pain and limb weakness due to bone metastases. Thus, treatment for primary malignancies that cause bone metastases should take precedence. Although rectal cancer was identified as the source of the metastasis to the rib, the possibility of bone metastatic lung cancer could not be ruled out in this case because of the significant amount of bone damage. Accordingly, we decided to simultaneously treat the lung and colorectal cancers.

Based on the immunohistochemistry and molecular biology analyses, we concurred that patients with rectal cancer and lung cancer who do not have *RAS* or *BRAF* gene mutations and pMMR tend to have *EGFR* gene mutations. For our patient, we selected a therapy regimen that included a combination of mFOLFOX6 and afatinib. Several studies have investigated the safety of the combination of TKI therapy and chemotherapy.[7,8] In terms of gastrointestinal cancer, a phase II study on patients with advanced gastric cancer treated with afatinib in combination with 5-FU and cisplatin revealed acceptable toxicities, including skin and hematological toxicities and diarrhea.[9] After two cycles of treatment, we observed grade 3 oral stomatitis and grade 2 anemia, indicating the first instance of adverse reaction to the combination treatment of afatinib and mFOLFOX6 in the literature. The absence of diarrhea, which is a common adverse effect of both afatinib and mFOLFOX6, and the combination regimen of afatinib and chemotherapy,[10] might be due to the patient's symptoms of autonomic dysfunction. Owing to the increased incidence of stomatitis associated with afatinib, TKIs were discontinued. Moreover, before the third cycle, grade 2 anemia was observed. Stomatitis is typically observed with both afatinib and mFOLFOX6 therapies and combination treatment may exacerbate this condition. Anemia can result not only from chemotherapy but also from bone marrow metastasis. However, a bone marrow biopsy was not performed as it is invasive and would not alter the treatment approach. Although we planned to resume chemotherapy following blood transfusions, the patient declined further treatment and chose palliative care at home.

4. Conclusion

Our patient with synchronous lung and rectal cancers was evaluated through MRI and PET/CT and was classified in the advanced stage with bone metastasis. He was treated with a combination of afatinib and mFOLFOX6. This is one of the few cases of the co-occurrence of rectal and non-small cell lung cancers. Advanced-stage synchronous cancers are challenging to manage. Furthermore, the toxicities of afatinib in combination with the mFOLFOX6 regimen were evaluated.

Acknowledgments

The authors would like to thank the participating patients, as well as colleagues who made this work possible.

Funding

None.

Conflict of interest

Phuong Cam Pham serves as the Editorial Board Member of the journal, respectively, but was not in any way involved in the editorial and peer-review process conducted for this paper, directly or indirectly. Separately, the authors declare that they have no known competing financial interests or personal relationships that could have appeared to influence the work reported in this paper.

Author contributions

Conceptualization: Phuong Cam Pham, Khoa Trong Mai, Lanh Minh Pham
Investigation: All authors
Writing–original draft: Thuy Phuong Ngo, Hien Minh Nguyen, Ha Thanh Le, Lanh Minh Pham
Writing–review & editing: Khuy Minh Doan, Phuong Cam Pham, Khoa Trong Mai

Ethics approval and consent to participate

This study was approved by the Ethics Committee of Bach Mai Hospital (approval no:. 4459/BM-HĐĐĐ).

Consent for publication

Informed consent from the patient to publish his data was obtained.

Availability of data

The original data of the study are included in the article. Further inquiries can be directed to the author.

References

1. Huang JF, Shen J, Li X, *et al*. Incidence of patients with bone metastases at diagnosis of solid tumors in adults: A large population-based study. *Ann Transl Med*. 2020;8(7):482.
doi: 10.21037/atm.2020.03.55

2. Kurishima K, Miyazaki K, Watanabe H, *et al*. Lung cancer patients with synchronous colon cancer. *Mol Clin Oncol*. 2018;8(1):137-140.

doi: 10.3892/mco.2017.1471

3. Alghanmi HA. Successful treatment of synchronous double lung primary malignancies and colon cancer. *Cureus*. 2022;14(2):e22552.

doi: 10.7759/cureus.22552

4. Chirila ME, Piciu D, Larg MI, Barbus E. Synchronous and metachronous cancers on F18-FDG PET-CT. A tertiary cancer center experience. *Int J Radiat Oncol Biol Phys*. 2019;105(1):E464.

doi: 10.1016/j.ijrobp.2019.06.1427

5. Vlaskou Badra E, Baumgartl M, Fabiano S, Jongen A, Guckenberger M. Stereotactic radiotherapy for early stage non-small cell lung cancer: Current standards and ongoing research. *Transl Lung Cancer Res*. 2021;10(4):1930-1949.

doi: 10.21037/tlcr-20-860

6. Vogt A, Schmid S, Heinimann K, *et al*. Multiple primary tumours: Challenges and approaches, a review. *ESMO Open*. 2017;2(2):e000172.

doi: 10.1136/esmoopen-2017-000172

7. Wu Q, Luo W, Li W, Wang T, Huang L, Xu F. First-generation EGFR-TKI plus chemotherapy versus EGFR-TKI alone as first-line treatment in advanced NSCLC with EGFR activating mutation: A systematic review and meta-analysis of randomized controlled trials. *Front Oncol*. 2021;11:598265.

doi: 10.3389/fonc.2021.598265

8. Planchard D, Jänne PA, Cheng Y, *et al*. Osimertinib with or without chemotherapy in EGFR-mutated advanced NSCLC. *N Engl J Med*. 2023;389:1935-1948.

doi: 10.1056/NEJMoa2306434

9. Makatsoris T, Samantas E, Manousou K, *et al*. Afatinib in combination with cisplatin and 5-fluorouracil (5-FU) as first line treatment in inoperable gastric and gastro-esophageal junction (GEJ) cancer: A phase II study by the hellenic cooperative oncology group. *Ann Oncol*. 2018;29:viii227-viii228.

doi: 10.1093/annonc/mdy282.061

10. Fukuhara T, Nagashima H, Utsumi Y, *et al*. A phase II study of afatinib in combination with pemetrexed and carboplatin in patients with EGFR mutation positive non-squamous, advanced non-small-cell lung cancer (NSCLC) refractory to first-line osimertinib treatment: NEJ025B. *J Clin Oncol*. 2023;41(16_suppl):9044-9044.

doi: 10.1200/JCO.2023.41.16_suppl.9044

Our Journals

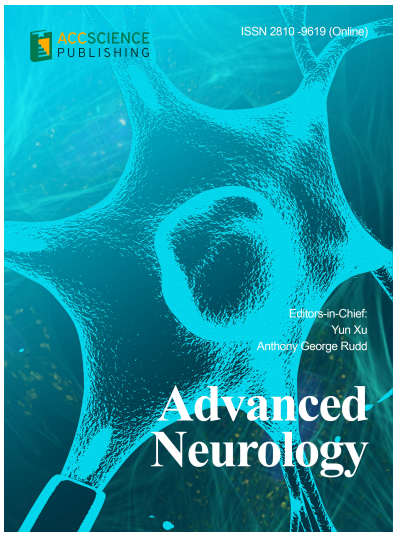

Advanced Neurology is a peer-reviewed and open-access journal that aims to publish and disseminate novel research in the breadth of neurology and neuroscience. The journal aims to advance our understanding in the nervous system and provide a platform to neuroscientists and physicians to showcase their findings in original fundamental and clinical research as well as to present new ideas that highlight the changes in the neurological clinical practice.

Advanced Neurology covers subject areas, including but not limited to the following:

- Neurological disorders
- Neurodegenerative disease
- Cerebrovascular disease
- Epilepsy and movement disorders
- Neuroimmune disease
- Neurological infections
- Muscle disease
- Molecular and cellular neuroscience
- Systems neuroscience
- Cognitive neuroscience
- Computational modeling of nervous system

Global Translational Medicine is a quarterly journal that focuses on medicine, biological sciences, and biomaterials engineering. The goal of *Global Translational Medicine* is to provide a platform to researchers for showcasing their latest research works in translational medicine so as to advance the field towards the betterment of human health. Despite the advancement of omics and new technologies, the process of transforming these technologies and scientific research results into effective therapies and putting them into clinical use still has a long way to go. *Global Translational Medicine* provides a platform to fill the gaps in preclinical and inter-disciplinary research, to promote clinical translation of scientific research results, and to contribute to the conception of new and improved preventive measures as well as diagnostic and therapeutic techniques of diseases.

Global Translational Medicine covers the following themes: cardiovascular disease, metabolism/diabetes/obesity, neuroscience/neurology, cancer, biomaterials and their applications in medicine, proteomics/metabolomics, pharmacogenomics, biomarkers, bioinformatics and data mining, animal and clinical research, and medical methods arising from interdisciplinary crossover.

Start a new journal

Write to us via email if you are interested to start a new journal with AccScience Publishing. Please attach your CV, professional profile page and a brief pitch proposal in your email. We shall inform you of our decision whether we are interested to collaborate in starting a new journal.

Contact: info@accscience.com

https://accscience.com/journal/ARNM

Contact
www.accscience.com
8 Burn Road, #15-03 Trivex, Singapore 369977
Email: editorial@accscience.com
Phone: +65 8182 1586